Breakup and instability analysis of compound liquid jets

by

Muhammad Faheem Afzaal

A thesis submitted to
The University of Birmingham
for the degree of
DOCTOR OF PHILOSOPHY

School of Mathematics
The University of Birmingham
June 2014

UNIVERSITYOF
BIRMINGHAM

University of Birmingham Research Archive

e-theses repository

Abstract

This study deals with the temporal instability of compound liquid jets. The presence of an outer column of liquid which is totally immiscible from the inner fluid introduces many interesting features in jet breakup dynamics. The governing equations which model the behavior of a compound jet are in general rather complex due to the presence of multiple free surfaces and different fluids. However, an asymptotic approach can be used to yield a set of one dimensional equations which greatly simplify the resulting analysis. We perform linear and nonlinear analysis to reveal many interesting features of the compound liquid jets. The influence of gravity on the instability and breakup of inviscid and viscous compound jets is also considered. Additionally, we estimate the theoretical breakup lengths, breakup time and droplet sizes of such jets for varying key parameters.

ACKNOWLEDGEMENTS

I am highly grateful to almighty Allah for giving me the strength and courage to complete this research work. I would like to thank my supervisor Dr. Jamal Uddin, for his guidance and support throughout the thesis, without whom this project was impossible.

I am also grateful to my parents Muhammad Afzaal and Azra Bibi for their moral, emotional and financial support at each and every step of my life. My special thanks to my friends, Muhammad Tausif and Abdullah Alsharif for encouraging and motivating me throughout my studies. Lastly, I would like to thank my wife Saman Riaz for her tender, love and care during my whole Ph.D.

CONTENTS

List of Figures

CHAPTER 1

INTRODUCTION AND LITERATURE REVIEW

1.1   Introduction

The formation and rupture of liquid jets have been studied on scales ranging from the micro scale to the typical sizes of galaxies. A liquid jet emanates from a nozzle or orifice into an ambient gas and takes the shape of a long cylindrical column. This process plays an important role in many practical applications, for example, ink jet printing, diesel engine technology, coating, manufacturing, agriculture, DNA sampling and nuclear fission [26]. Furthermore, the applications of liquid jet can be found in cooling of microchip components [91] and targeted delivery of drugs to the site of disease [65]. We can easily explore common occurrences of this phenomena many times in our daily life such as kitchen taps, irrigation system, showers, perfumes or deodorants and sprayers. An example of higher speed water jets is shown in Fig. 1.1, which are used to cut meat, tissues and metal plates [26].

A jet of liquid belongs to the special class of free surface flows which are amongst the most complicated flow situations found in fluid mechanics. It is very important to define

Figure 1.1: Higher speed water jets, courtesy of Eggers & Villermaux [26]

the position of a fluid particle in free surface flow problems. The kinematic condition is constructed to prescribe the position of a particle and mathematically it can be written as

$$\frac{D}{Dt}\left(r - S(x,t)\right) = 0, \quad \text{where} \quad \frac{D}{Dt} = \frac{\partial}{\partial t} + u \cdot \nabla \tag{1.1}$$

and $S(x,t)$ is the free surface which is the function of time and spatial coordinates. The above equation (1.1) illustrates that a particle keeps its position on the free surface for all time. In addition, dynamical conditions are essential to set the equilibrium on the free surface. When the molecules of a fluid migrate from high energy to low energy levels the surface area of jet is contracted. This process provides surface tension to a liquid which is taken as energy per unit area of interface. Regarding to free interface the stresses due to surface tension are balanced by the stresses produced by viscous forces and pressure. The tangential stress condition on the free surface is formulated as

$$\mathbf{n} \cdot \mathbf{\Pi} \cdot \mathbf{t} = \mathbf{t} \cdot \nabla \sigma \tag{1.2}$$

2
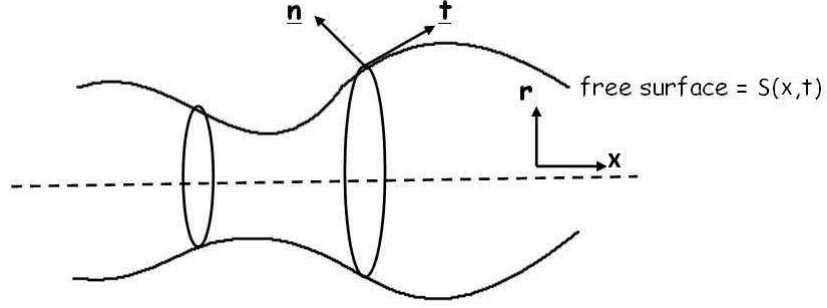
Figure 1.2: The figure shows the geometry of a free surface in cylindrical coordinate system and dotted line represent the axis of symmetry.

where $\mathbf{\Pi}$ is the total stress tensor, σ is the surface tension, $\boldsymbol{n}$ and $\boldsymbol{t}$ are the normal and tangent vectors to the free surface respectively which are shown in Fig. 1.2. Generally the surface tension is taken to be constant unless a surfactant is present. The second stress condition acting normal to the free surface is written as

$$\mathbf{n} \cdot \mathbf{\Pi} \cdot \mathbf{n} = \sigma \kappa \tag{1.3}$$

where κ is the mean curvature of free surface.

The instability in a liquid jet occurs due to the continuous disturbances (caused by, for example, fluctuations in pressure or density) which grow along its free surface and finally lead to its disintegration into a series of droplets. During this process the radius of the jet near the breakup point becomes infinitesimally small, whereas the associated velocity diverges to infinity. Consequently singularities occur in the equation of motion because of the topological transitions at rupture.

The phenomenon of liquid jet breakup is categorized into four types of regime [47], namely the Rayleigh regime, the first wind induced regime, the second wind induced regime and the atomization regime. The images of these different regime are shown in the Fig. 1.3. Usually the atomization regime and second wind induced regime are referred as

3
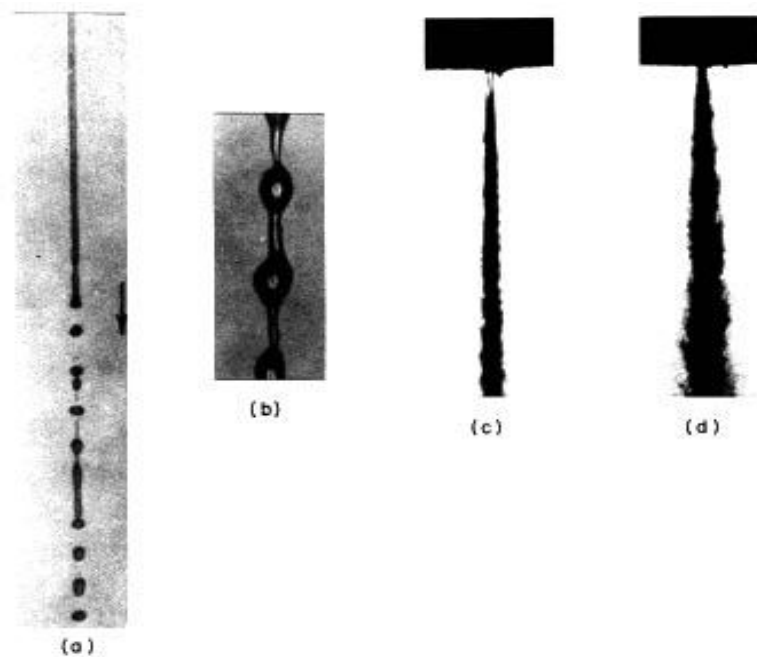
Figure 1.3: Four types of breakup regime, (a). Rayleigh regime (b). First wind induced regime (c). Second wind induced regime (d). Atomization regime, are shown in the figure. It is taken from Lin & Reitz [46].

high speed regime, while the other two are low speed regime. The breakup of lower speed regime has been found away from the orifice and the size of the droplets are similar to the diameter of orifice. But in the case of high speed regime the droplets produced are much smaller than the size of orifice and breakup occurs very close to the orifice. Moreover, the liquid will not form a jet if the exit velocity is very low and furthermore viscosity enhances this effect.

1.2 Classical work on liquid jets

In the late seventeenth century, the earliest work on jets appears in a book by the French scientist E. Mariotte [51]. He explained that gravity is the main factor of liquid jet breakup. It was Savart [77] who performed the earliest experiments on liquid jets. He illuminated the jets with the sheet of light and examined the decay of liquid jet into droplets. As a result he observed tiny modulations growing on the surface of jet which

Figure 1.4: The image is taken from the Savart's original papar [77] which shows the perturbations growing on a water jet

are shown in the Fig. 1.4. In his experiments smaller droplets, which are often called satellite droplets, are also seen between the main droplets. Savart concluded that break up of liquid jet depends on inherent property of fluid motion but failed to identify the surface tension the source of instability, despite it being discovered three decades prior to his analysis. The first qualitative work on jet breakup has been done by Plateau [64] who discovered that surface tension is the actual source which reduces the surface area of jet and thus converts it into droplets.

The review of early work on liquid jets is given by Bogy [8] with more detailed reviews by Eggers [24] and Eggers & Villermaux [26]. The literature regarding to the liquid jets can also be found in the books of Anno [3], Middleman [53], Yarin [90] and Lin [48].

1.2.1 Inviscid jets

The first significant mathematical analysis of the mechanism of instability in liquid jets was performed by Rayleigh [70] who showed that capillary jet break-up is caused by surface tension and the wave mode which grow quicker with the time (*i.e.* mode of maximum instability). He realized that an optimal wavelength existed at which the perturbations grew the fastest. The theoretical results of Rayleigh matched within a good degree of accuracy with the experimental results of Savart. In this section we will summarize the key findings of Rayleigh.

The linear instability of an infinitely long column of incompressible inviscid fluid can be modeled by assuming a cylindrical jet in equilibrium state to which small disturbance are imposed. Hence the radius of the jet takes the form,

$$r = s + \delta \cos(kx) \cos(m\theta) \tag{1.4}$$

where s is the radius, k is the wave number, m is an integer, δ is small initial disturbance, θ is azimuthal co-ordinate and x is the axial length. By using the standard equation of motion and considering the wave mode of the form $exp(\lambda t + i(kx + m\theta))$, where t is the time and λ is wavelength, Rayleigh was able to get an eigenvalue relation given by

$$\lambda^2 = \frac{\sigma(ks)}{\rho s^3}(1 - m^2 - (ks)^2)\frac{I'_m(ks)}{I_m(ks)}. \tag{1.5}$$

Here ρ is the density of the fluid, σ is surface tension, $Re(\lambda)$ is the growth rate, $Im(\lambda)$ is the frequency of the wave and $I_m(ks)$ is a modified Bessel function of order m. For $m \neq 0$, we can say that disturbances are neutrally stable for $Re(\lambda) = 0$ which means that λ is purely imaginary and waves are stable for $Re(\lambda) > 0$. The positive values of $Re(\lambda)$ are obtained by putting $m = 0$ in equation (1.5). In this case the waves are unstable for

$0 < ks < 1$ and the mode is axisymmetric. The recurrence formulas of Bessel function;

$$I_{m-1}(x) + I_{m+1}(x) = \frac{2m}{x} I_m(x) \quad , \quad I_m'(x) = \frac{1}{2}(I_{m-1}(x) + I_{m+1}(x)), \tag{1.6}$$

can be used to obtain

$$\lambda^2 = \frac{\sigma(ks)}{\rho s^3}(1 - (ks)^2)\frac{I_1(ks)}{I_0(ks)}, \tag{1.7}$$

which is the Rayleigh's classical formula for axisymmetric disturbances. The famous Rayleigh mode which is most unstable mode and indicates the most unstable wave number $ks \approx 0.697$ corresponds to the maximum growth rate having wavelength $\lambda_w \approx 9.02s$. The characteristic breakup time, t_b can be found by taking the inverse of growth rate $Re(\lambda) = 0.34(\sigma/\rho s^3)^{\frac{1}{2}}$, which is $t_b = 2.94(\rho s^3/\sigma)^{\frac{1}{2}}$.

1.2.2 Viscous jets

The instability of liquid jets in the presence of viscosity was investigated by Weber [88]. He concluded that the size of droplets become larger by increasing the viscosity which consequently delay the process of break up. The characteristic equation derived by Weber is given by

$$\lambda^2 + \lambda \frac{2\mu k^2}{I_0(kR)}\left[I_1'(kR) - \frac{k\tilde{k}I_1(kR)I_1'(\tilde{k}R)}{(k^2 + \tilde{k}^2 I_1(\tilde{k}R)}\right] = \frac{\sigma R}{\rho\mu^2}\frac{kR(k^2 - \tilde{k}^2)I_1(kR)}{(k^2 + \tilde{k}^2)I_0(kR)}(1 - k^2R^2), \tag{1.8}$$

where $\tilde{k}^2 = k^2 + \frac{\lambda}{\mu}$.

1.3 A review on linear theory of jet instability

The purpose of studies on liquid jet instabilities is to investigate the growth rate of initial disturbances, unstable wavenumbers, breakup lengths of jets, break up time and to verify post rupture behavior. The phenomenon of jet break up is nonlinear in nature but linear

analysis can be used to yield a good approximation for many aspects, for example, the break up length and the size of main droplets produced and it indeed shows a good degree of accuracy when compared with experiments. In linear temporal instability analysis positive values of $Re(\lambda)$ lead to perturbations which grow with the time and remain uniform in space. In this case λ is taken to be complex i.e. $\lambda = \lambda_r + i\lambda_i$, where λ_r is temporal growth rate and amplitude of disturbances will grow with the positive values of λ_r. The wave number k will be real in temporal instability analysis and $\frac{\lambda_i}{k}$ is wave speed where λ_i is frequency of oscillations.

Tomotika [85] extended Rayleigh's original analysis by taking into account of very viscous fluid surrounded by another viscous fluid to analyze the ratios of viscous forces to the surface tension forces between the two fluids. The spatial instability of liquid jets is introduced by Keller et $al.$ [38]. They observed that the disturbances grow not only at $t = 0$ but also grow along the surface of jet for later times. Also it was the experimental observation of Lieb & Goldstein [43] that disturbances are minimal close to the orifice and propagate as they travel along the jet. Keller et $al.$ used the complex wave number i.e. $k = k_r + ik_i$, where k_r is wave number and k_i is spatial growth rate, the real part of λ is taken to be zero which means λ is purely imaginary i.e. $\lambda = i\omega$. The Rayleigh's temporal mode is also described in this analysis; therefore we can say that the disturbances grow temporally and spatially on the jet surface.

Recently, Amini & Dolatabadi [2] performed temporal and spatial instability analysis of elliptic liquid jets. They used the one dimensional Cosserat equations which are systematically derived by Bechtel et $al.$ [7]. This study reveals that elliptic jets are more unstable than that of circular jets with growth rates being increased by enlarging the ellipticities.

The Weber number is defined as, $We = \rho s U^2 / \sigma$, where σ is surface tension, ρ is density, U is exit velocity of jet and s is the radius of orifice. It is evident that the stability of a liquid jet is strongly dependent on Weber number and several authors observed a singularity in their stability analysis at $We = 1$. Baird & Davidson [6] considered the annular straight jets without gravity and found a discontinuity at $We = 1$. They observed that singularity occurred due to large menisci at the nozzle. Finnicum *et al.* [27] described the two dimensional liquid curtain under the influence of gravity. They also noticed the singularity at $We = 1$ but it can be removed if the curtain leaves the nozzle in a given direction. They demonstrated that the stability of a jet is affected by the angle with which curtain leaves the orifice.

Spatial and temporal instabilities are also called convective instabilities, such instabilities grow and propagate beyond the point of origin leading to disintegration of the jet. Lieb & Goldstein [43] realized a new form of disturbances which grow more quickly than the Rayleigh mode. This kind of instability is also called absolute instability and we can observe it in the case of slow moving jets. Jets becomes absolutely unstable below the critical Weber number which is dependent on the Reynolds number [45]. Moreover, it was shown that the disturbances grow away from the point of origin as well at the point origin.

1.4 A review on nonlinear jet dynamics

Linear theory reveals that the jet breakup should be uniform along its axis and the droplet formed to be almost equal to the wavelength of any initial disturbance. But the formation of satellite droplets (which are produced due to the fine threads between the primary droplets) is not predicted by linear theory. Hence, we need nonlinear analysis to study the complete dynamics of jet break up. Yuen [93] was the first who took into account the nonlinear effects of disturbances on the jet surface. The growth rate and cut-off wave

number observed by Yuen are different from that taken in linear analysis. The theoretical survey of Chaudhary & Redekopp [11] indicates the formation of satellite droplets which can be controlled by forcing the jet to some suitable harmonics. Using higher order perturbation theory, the qualitative prediction of unequal drop sizes is presented by Chaudhary & Maxworthy [9, 10] but fails to identify the shape of fluid close to pinch-off.

We need to use the full Navier-Stokes equations to illustrate nonlinear jet dynamics but it is very difficult to get the full numerical solution in the presence of free boundary conditions. Keeping this fact in mind Eggers [25] obtained the one dimensional model using a long wavelength approximation. Although, Ambravaneswaran *et al.* [1] and Moseler & landman [57] described the jet by presenting two dimensional and three dimensional model respectively.

Lee [42] solved the one dimensional momentum equation of an inviscid jet numerically and found non-uniformity in jet breakup due to satellites. The theoretical and experimental analysis is executed by Lee & Pimbley [62] and predict that the satellites can disappear if the distance between main drops is five to seven times the jet diameter. A different approach is used by Schulkes [78] to investigate the nonlinear instability on the surface of liquid jets. The equations derived by Schulkes are more accurate from those presented by Lee. He obtained the numerical solution of a nonlinear set of equations and mentioned the formation of satellite droplets.

Eggers & Dupont [25] studied the one dimensional model in the presence of viscosity and investigated the bifurcation of a drop suspended from an orifice. The aim of their study is to analyze the behavior of the singularity close to the neck region in the final stage of rupture. The experimental photographs of Peregrine *et al.* [60] compared with simulations of droplets of water suspended from an orifice and good agreement is found between theory and experiment. A boundary element method is applied by Hilbing &

Heister [35] to examine the evolutions of straight liquid jets and the formation of main and satellite droplets for fixed wavelength. According to this analysis, a change in Weber number, wavelength and magnitude of disturbances alter the size of droplet.

1.5   Instability analysis of compound jets

The two fluid jet or compound jet is the simple extension of a single jet which is composed of an inner thread of fluid which is completely covered by outer immiscible liquid. This type of fluid system contains two interfaces, an inner interface separating the core and annular fluid while the outer one separates the annular and ambient gas region. The mechanics of compound jet breakup into droplets is similar to single fluid jet but the complication arises in the dynamics of compound jets. The applications of compound jets can be found in fiber spinning and particle sorting [34]. The compound jets were used by Hertz & Hermanrud [33] to develop a new method for ink jet printing. In addition, encapsulation of one substance by another is one of the main application of compound jets which relates to encapsulation and development of food additives [30], targeted delivery of drugs [36, 52] and improvement of insecticides [61].

One dimensional temporal instability analysis of an inviscid compound jet is considered by Sanz & Masueger [76]. They studied the influence of surface tension ratios, density ratios and radii ratios of inner to outer fluids and established the breakup regimes and finally compared the theoretical results with the experiment performed by Hertz & Hermanrud [33]. The capillary instability of compound jets in the presence of viscosity is presented by Radev & Tchavdarov [67]. By using two dimensional equation of motion the influence of secondary fluid layer on the instability is investigated numerically and three types of breakup regimes are identified in this analysis. Shkadov & Sisoev [81] analyzed the two-layer axisymmetric capillary jet and applied the boundary layer approximation to full Navier-Stoke equation to calculate the stationary mean flow. Furthermore, they

examined the two types of axisymmetric disturbances related to the interface between the layers and jet surface.

The spatial and temporal instability of an inviscid compound jet has been discussed by Chauhan *et al.* [12]. The set of equations are solved in Fourier-Laplace domain and then inverted back into real domain. Two types of growing modes (stretching mode and squeezing mode) are found in temporal analysis, but the spatial analysis reveals that the jet is absolutely unstable, with the development of convective instabilities for higher velocities. Chauhan *et al.* [13] carried out the temporal instability of viscous compound jet to control the drop size in jet breakup and compound drop formation. Numerical and analytical approach is used to solve dispersion relation for two different cases.

Craster *et al.* [19] investigated the instability of compound liquid jets with a large viscosity contrast between annular and core regions. Both linear theory and numerical simulations are used to study the effect of viscosity in the neighbouring fluids. Compound and annular jets at low Reynolds number has been studied by Ramos [69]. Craster *et al.* [18] and Kwak & Pozrikidis [41] conducted the instability of compound liquid jet in the presence of insoluble surfactants.

The absolute instability of an inviscid compound jet is reported by Chauhan *et al.* [14], whereas Suryo *et al.* [83] examined the compound jet numerically. Rou *et al.* [73] investigated the linear instability of nonaxisymmetric viscous compound emanating in an inviscid ambient gas. They solved the dispersion relation by direct numerical procedure and concluded that the gas-to-shell density ratio and the Weber number which is defined at outer interface (i.e. ambient gas and shell liquid layer) have large influences on the growth of nonaxisymmetric instability modes.

Uddin & Decent [86] studied the instability of inviscid axisymmetric compound jets falling under gravity. They considered one dimensional model of jet breakup by using

slender jet approximation and steady-state solutions of falling compound jet were determined. Moreover, a two-step finite difference scheme was used to study the effects of key parameters on breakup and drop formation. More recently, the breakup of a non-Newtonian shear thinning compound jet obeying Carreau model has been investigated by Mohsin *et al.* [54]. Other related studies are reported by Radev & Gospodinov [66] and Yoshinaga & Maeda [92].

Compound drops can be produced through co-extrusion process which requires understanding of the channel flow of extruded liquids. Wilson & Rallison [89] considered Oldroyd-B fluids to understand the stability of co-extruded elastic liquids. Furthermore, Loscertales *et al.* [50] used electrified liquid jets for the production of Micro and Nano capsules (with diameter 10 & 0.15 micrometer) and the capillary break up of viscous fluid encased by another viscous fluid has been demonstrated by Lister & Stone [49].

1.6 Experimental investigation on jets

Experimental observations suggest that the phenomenon of breakup and drop formation in axisymmetric liquid jets is remarkably complex. During the first half of nineteenth century experiments on free surface flows were performed by Savart [77] and Plateau [63]. Later on, Lenard [44] and Rayleigh [71] analyzed the structure appearing on free surface evolutions with the help of photography which are shown in Figs. 1.5 and 1.6 respectively. However, Hauser et. al. [32] and Edgerton [22] were able to study the jet dynamics in time and more accurately by using high speed cameras.

In twentieth century many researchers followed the Savart's idea to study the jet instability and different techniques were used to impose the frequency at the nozzle. Crane *et al.* [17] applied disturbances of different wavelengths on the orifice through electrical vibrator, whilst Donnely & Glabberson [21] introduced disturbances by using loud speaker and found growth of surface waves as a function of time.
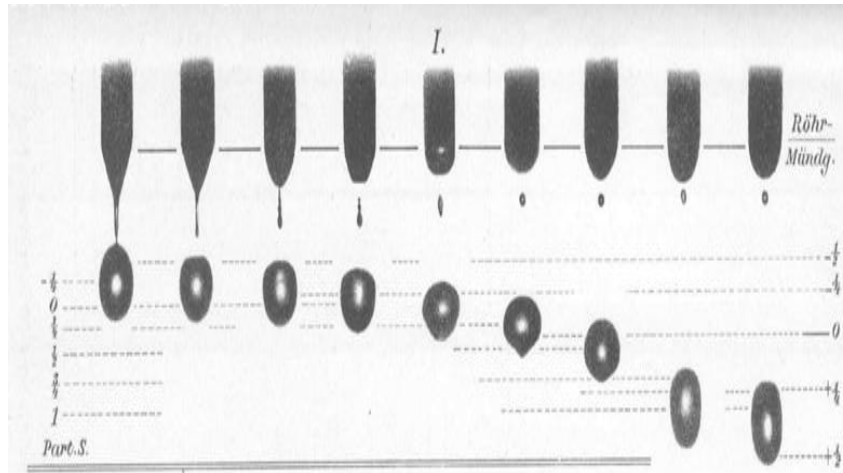
Figure 1.5: A sequence of pictures of a drop of water falling from a pipette [44], it is one of the first series of photographs of drop formation.

Goedde & Yuen [29] scrutinized the behavior of the neck and swell region of the jet through different ways. They calculated the diameter of the neck and swell region as a function of time and demonstrated the dominance of nonlinear effects. Rutland & Jameson [74] compared their experimental results with the nonlinear theory presented by Yuen [93]. Although it was a good agreement but the satellites were seen at wave number greater than 0.7 which was the contradiction between theory and experiment.

In modern research, high resolution equipments are used at microscale level to give more details about the post rupture behavior, especially in the case of secondary filaments. The appearance of secondary filament between the primary thread and departing drop has been analyzed by Shi *et al.* [80] while observing a drop falling from faucet. Other background references related to faucet dripping are Tate [84], Rayleigh [72] and Harkin & Brown [31]. Similar kind of phenomenon was discussed by Kowalewski [40] in the case of jet issuing from orifice and compared the results with Eggers 1D model [23]. Although, the shape of pinch-off region matched with the experiment but post rupture results were contrary to the experimental observation.
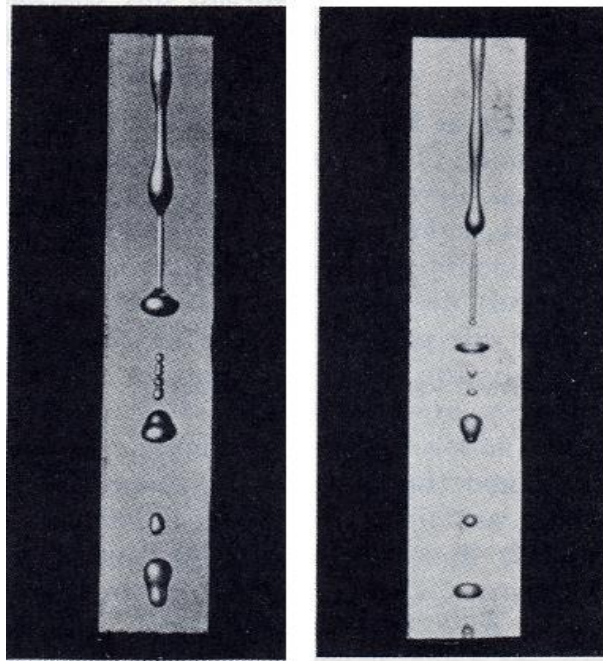
Figure 1.6: A photograph of jet breakup which is reproduce from Rayleigh's paper [71].

The experiments on compound liquid jets are performed by Hertz & Hermanrud [33] and Kendall [39] who considered gas in a core region; hence the droplets formed upon the breakup are hollow spheres. Recently, the experiment on the breakup of compound jet to periodic excitations has been done by Chiu & Lin [16] and showed six patterns of breakup.

1.7   Structure of thesis

In this thesis we focus on the instability and breakup of compound liquid jets. This system of fluids has been given less attention in the literature as compared to the single fluid jets and many interesting features arise when the rupture of inner and outer liquids coincides. The preceding sections of this chapter contain the brief introduction and a detailed review on the instability of single and compound jets.

In the next chapter, we review the work of Uddin [87] and reproduce the dispersion relation to describe the linear instability analysis of an inviscid compound liquid jet. We

15

also give the brief description of Lax-Wendroff method applied by Uddin [87] to examine the non-linearity in an inviscid compound jet and discuss the results in more detail.

Chapter three is related to the non-uniform compound liquid jets. In this chapter, we discuss some important results obtained in [55], where we considered an inviscid compound jet falling under gravity. The dispersion relation is solved numerically using Ferrari's method and the numerical results are also checked using Muller's method. Moreover, we provide the nonlinear analysis of similar problem studied by Uddin & Decent [86]. In both these cases, the steady state solutions for the centreline of the jet were found using Newton's method but we apply Runge-Kutta method to find the steady state solutions.

Chapter four deals with the two dimensional axisymmetric compound moving in a vertical downward direction. We perform the linear instability analysis using full set of governing equation which describe the evolution of interfaces of the compound liquid jet. We then solve the resulting dispersion relation in a long wavelength limits and give the graphical comparison between them.

In chapter five, we examine the instability of a two dimensional axisymmetric inviscid compound jet falling vertically downwards under the influence of gravity. The steady state equations are derived using an asymptotic method and the temporal instability is determined using a multiple scale approach. The results are analyzed to investigate the key features of the jet including theoretical breakup lengths.

In chapter six, we formulate the governing equations which describe the evolution of the interfaces of an inviscid compound jet in a surrounding gas. We then perform the linear temporal instability analysis to investigate the most unstable wavenumber and its associated growth rate of disturbance. We also examine how gas-to-shell liquid density ratio affects the dynamics of the jet.

In chapter seven, we aim to investigate the behavior and instability of an inviscid compound jet which falls vertically under gravity in the presence of a surrounding gas. The governing equations are formulated and then reduced into one dimensional form using an asymptotic expansion. We solve this set of equations using Newton's method to determine a steady state. Thereafter, we consider the temporal instability of the jet around this steady state. Furthermore, we investigate how key parameters, including the surrounding gas density, alter the growth rate and most unstable wavenumber. Finally, we use an approximation to estimate breakup lengths of the jet.

In chapter eight, we investigate the instability of viscous compound jet using linear theory of instability and apply asymptotic method to reduce the set of equation into one dimension and obtain dispersion relation to analyze the behavior of the jet with different surface tension ratios, density ratios, radii ratios and viscosity ratios.

We examine the viscous compound jet falling under the influence of gravity in chapter nine. The governing equations are formulated and one dimensional set of equations are obtained using an asymptotic approach. The steady-state solutions are found using modified Newton method. In addition, we present linear temporal analysis to study the effects of key parameters on the surface of compound jet and breakup lengths are also calculated. Finally, we performed the nonlinear analysis of one dimensional viscous compound jet falling under gravity using finite difference scheme based on Lax-Wendroff method to study the formation of satellite droplets.

In chapter ten, we give the conclusions of this work and suggest the future work related to the compound liquid jets.

CHAPTER 2

UNIFORM COMPOUND LIQUID JETS

2.1 Introduction

Whether it is the investigation of single liquid jets or compound liquid jets the surface instabilities play an important role in the jet breakup. The liquid jet emerging from the orifice is inherently unstable and continuous growing disturbances lead to disintegration of the jet into droplets. In the case of a single jet the free interface exists between the fluid and surrounding gas but in compound liquid jet there are two interfaces; one separates the inner and outer immiscible fluid and the other one lies between the outer fluid and ambient gas.

A compound liquid jet contains core and annular regions; the fluid flow in the core region is totally encased by the annulus of second liquid. Like the single jets, compound jets have contribution in scientific developments and are important in many practical applications, such as particle encapsulation, food manufacturing, targeted delivery of drugs and ink jet printing. Most importantly, there are two types of modes namely, a stretching mode and squeezing mode, which are found by considering the disturbances in temporal mode but the stretching mode is dominant in compound jet instability [13]. A sketch of stretching and squeezing mode is displayed in Fig. 2.1.
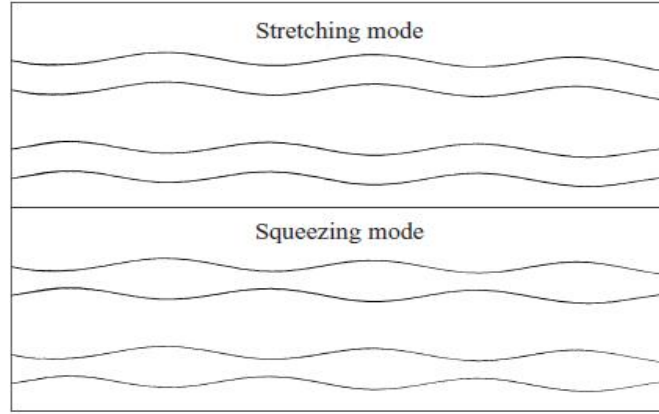
Figure 2.1: Stretching and squeezing mode in compound jet, courtesy of Chauhan *et al.* [13]

2.2   Linear Analysis

This section deals with a detailed review on the linear instability analysis of a uniform inviscid compound liquid jet carried out by Uddin [87]. An inviscid compound jet issuing from a concentric tube with the exit velocity U was considered (See Fig. 2.2). It was assumed that the inner fluid is totally enclosed by the outer immiscible liquid and the outer radius of the compound jet was denoted by a and the inner one was χa, where $(0 < \chi < 1)$. Both the fluids were taken as incompressible and were considered in the cylindrical co-ordinate system. The conservation of mass and the momentum equations were taken by Uddin [87] as

$$\nabla \cdot \mathbf{u}^{[\mathbf{z}]} = 0, \tag{2.1}$$

$$\frac{\partial \mathbf{u}^{[\mathbf{z}]}}{\partial t} + \mathbf{u}^{[\mathbf{z}]} \cdot \nabla \mathbf{u}^{[\mathbf{z}]} = -\frac{1}{\rho^{[z]}} \nabla p^{[z]}, \tag{2.2}$$

where $z = I, O$, subscripts I and O used for inner and outer fluids respectively. The

19
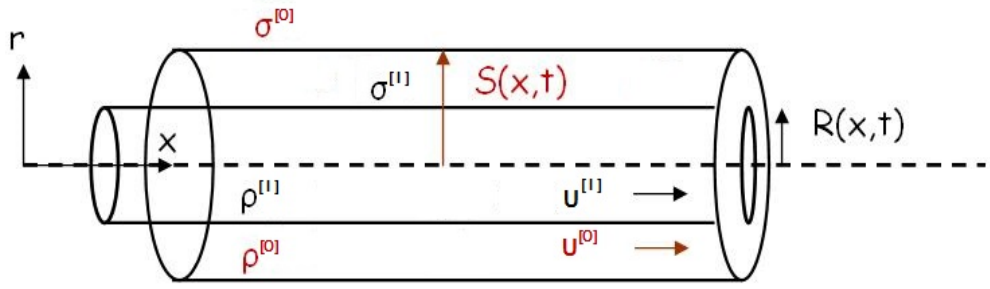
Figure 2.2: Profile of a compound jet

kinematic conditions obtained at the interfaces of compound jet are

$$\frac{\partial f}{\partial t} + \mathbf{u}^{[\mathbf{z}]}.\nabla f = 0 \quad \text{on} \quad r = R(x,t), \tag{2.3}$$

$$\frac{\partial f}{\partial t} + \mathbf{u}^{[\mathbf{O}]}.\nabla f = 0 \quad \text{on} \quad r = S(x,t) \tag{2.4}$$

and the normal stress conditions are

$$p^{[I]} - p^{[O]} = \sigma^{[I]}\kappa \quad \text{on} \quad r = R(x,t), \tag{2.5}$$

$$p^{[O]} = \sigma^{[O]}\kappa \quad \text{on} \quad r = S(x,t), \tag{2.6}$$

where $p^{[z]}$ is the pressure, t is the time, $\rho^{[z]}$ is the density of the fluids, κ is the curvature of the free surface, $\sigma^{[I]}$ and $\sigma^{[O]}$ are the surface tensions at the inner and outer interfaces, $f = r - R(x,t)$ and $f = r - S(x,t)$ define the free surface at the inner and the outer interface respectively. Equations $(2.1) - (2.6)$ were non-dimensionized using the following

scales

$$\bar{x} = \frac{x}{L}, \quad \bar{u}^{[z]} = \frac{u^{[z]}}{U}, \quad \bar{w}^{[z]} = \frac{w^{[z]}}{U},$$

$$\bar{t} = \frac{tU}{L}, \quad \bar{r} = \frac{r}{a}, \quad \bar{p}^{[z]} = \frac{p^{[z]}}{\rho^{[O]}U^2}, \quad \text{and} \quad \varepsilon = \frac{a}{L}.$$

Additionally, the dimensionless form of inner and outer radii of the jet at the nozzle are $R(0,t) = \chi$ and $S(0,t) = 1$ respectively. Dropping the overbears for the ease of convenience, Uddin [87] found the one dimensional set equations by posing the asymptotic expansions, which are given by

$$u^{[z]} = u_0^{[z]}(x,t) + (\varepsilon r)u_1^{[z]}(x,t) + O((\varepsilon r)^2), \tag{2.7}$$

$$w^{[z]} = (\varepsilon r)w_1^{[z]}(x,t) + O((\varepsilon r)^2), \tag{2.8}$$

$$p^{[z]} = p_0^{[z]}(x,r,t) + (\varepsilon r)p_1^{[z]}(x,t) + O((\varepsilon r)^2), \tag{2.9}$$

$$R = R_0(x,t) + \varepsilon R_1(x,t) + O(\varepsilon^2), \tag{2.10}$$

$$S = S_0(x,t) + \varepsilon S_1(x,t) + O(\varepsilon^2). \tag{2.11}$$

21

Substituting the above expansions into the original dimensionless equations and after some considerable algebra, we are able to get the resulting equations

$$\frac{\partial u_0^{[I]}}{\partial t} + u_0^{[I]}\frac{\partial u_0^{[I]}}{\partial x} = -\frac{1}{\rho We}\frac{\partial}{\partial x}\left(\frac{\sigma}{R} + \frac{1}{S}\right), \tag{2.12}$$

$$\frac{\partial u_0^{[O]}}{\partial t} + u_0^{[O]}\frac{\partial u_0^{[O]}}{\partial x} = -\frac{1}{We}\frac{\partial}{\partial x}\left(\frac{1}{S}\right), \tag{2.13}$$

$$\frac{\partial R_0^2}{\partial t} + \frac{\partial(R_0^2 u_0^{[I]})}{\partial x} = 0, \tag{2.14}$$

$$\frac{\partial}{\partial t}(S_0^2 - R_0^2) + \frac{\partial}{\partial x}((S_0^2 - R_0^2)u_0^{[O]}) = 0, \tag{2.15}$$

where $\rho = \rho^{[I]}/\rho^{[O]}$ is the density ratio between inner and outer fluids, $\sigma = \sigma^{[I]}/\sigma^{[O]}$ is the ratio between inner and outer interfaces and $We = \rho^{[O]}aU^2/\sigma^{[O]}$ is the Weber number.

Linear instability analysis was then performed by assuming the small perturbations in terms of $0 < \delta << \varepsilon$, that is,

$$u_0^{[I]}(x,t) = u_0^{[I]}(x) + \delta \ exp(ik\overline{x} + \lambda\overline{t}) \ \widehat{u}^I, \tag{2.16}$$

$$u_0^{[O]}(x,t) = u_0^{[O]}(x) + \delta \ exp(ik\overline{x} + \lambda\overline{t}) \ \widehat{u}^O, \tag{2.17}$$

$$R_0(x,t) = R_0(x) + \delta \ exp(ik\overline{x} + \lambda\overline{t}) \ \widehat{R}, \tag{2.18}$$

$$S_0(x,t) = S_0(x) + \delta \; exp(ik\overline{x} + \lambda \overline{t}) \; \widehat{S}, \qquad (2.19)$$

where $\overline{x} = x/\varepsilon$ and $\overline{t} = t/\varepsilon$. Here, $u^{[I]}(x) = u^{[O]}(x) = S_0(x) = 1$ and $R_0(x) = \chi$ were assumed as the steady-state solutions. The disturbances were considered in temporal mode, so λ, which is the growth rate, taken in complex form that is $\lambda = \lambda_r + i\lambda_i$ and wave number k assumed as a real number. By introducing the small perturbations in equations $(2.12) - (2.15)$ and choosing the linear terms in δ, the following characteristic equation was obtained

$$\lambda^4 - \frac{k^2}{2We}[(\frac{\chi^2}{\rho} + (1 - \mu^2))(1 - k^2) + \frac{\sigma \chi k^2}{\rho}(\frac{1}{\chi^2} - k^2)]\lambda^2$$

$$+ \frac{k^4 \sigma \chi}{4\rho We^2}(1 - k^2)(\frac{1}{\chi^2} - k^2)(1 - \chi^2) = 0, \qquad (2.20)$$

which is quartic in λ. The numerical results of equation (2.20) for the growth rate of disturbances λ_r against the wavenumber k have been shown in Fig. 2.3, where we can see two types of growing modes. The curve with the smallest growth rate is called squeezing mode and the curve with the largest growth rate is known as stretching mode which is responsible for the breakup.

2.3 Nonlinear Instability Analysis

Linear theory provides us an estimation of breakup lengths and drop sizes but unable to reveal an accurate description of post rupture behavior of the jet. Therefore, we need an approach to investigate the non-uniformity in the breakup and the formation of satellite droplets which are experimentally observed processes. For this purpose, we will use a numerical method to review the nonlinear analysis of an inviscid compound jet developed
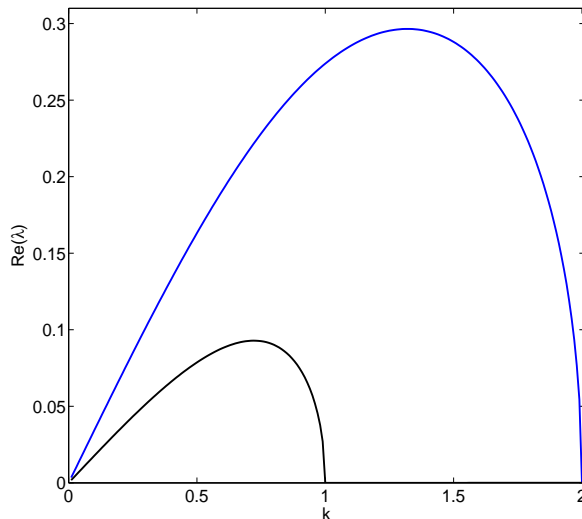
Figure 2.3: Growth rate of disturbances versus wavenumber, The parameters used here are $We = 10$, $\sigma = 1$, $\rho = 1$, and $\chi = 0.5$

by Uddin [87] with some more numerical results.

In order to perform the nonlinear analysis of the uniform inviscid compound jet, Uddin [87] modified the leading order pressure terms (that is $p_0^{[I]} = 1/We[\sigma/R_0 + 1/S_0)]$ and $p_0^{[O]} = 1/(WeS_0))$ of equations (2.12) and (2.13) by including the full expression for the curvature, which are given by

$$p_0^{[I]} = \frac{\sigma}{We} \left[\frac{1}{R_0(1 + \varepsilon^2 R_{0_x}^2)^{1/2}} - \frac{\varepsilon^2 R_{0_{xx}}^2}{(1 + \varepsilon^2 R_{0_x}^2)^{3/2}} \right] + \frac{1}{We} \left[\frac{1}{S_0(1 + \varepsilon^2 S_{0_x}^2)^{1/2}} - \frac{\varepsilon^2 S_{0_{xx}}^2}{(1 + \varepsilon^2 S_{0_x}^2)^{3/2}} \right] \qquad (2.21)$$

and

$$p_0^{[O]} = \frac{1}{We} \left[\frac{1}{S_0(1 + \varepsilon^2 S_{0_x}^2)^{1/2}} - \frac{\varepsilon^2 S_{0_{xx}}^2}{(1 + \varepsilon^2 S_{0_x}^2)^{3/2}} \right]. \qquad (2.22)$$

Although this technique is not asymptotically correct it is necessary to produce a correct equilibrium shape at breakup. Furthermore, the jet is unstable at arbitrary small

wavelengths if we ignore the full expression of curvature terms.

A finite difference method was applied to solve the equations $(2.12) - (2.15)$ by keeping the fixed and uniform grid points. In addition, time integration method applied is an explicit scheme which is based on two step Lax-Wendroff method. We first discuss the two step Lax-Wendroff method in the following section. Since we will require such a method in the chapter nine of this thesis.

2.3.1 Two step Lax-Wendroff Method

The Lax-Wendroff method is based on a finite difference scheme and it can be used to solve the PDEs of the form

$$\frac{\partial \mathbf{u}}{\partial t} = \frac{\partial \mathbf{F}(\mathbf{u})}{\partial x},$$ (2.23)

where $\mathbf{F}$ is the flux vector which generally depends upon $\mathbf{u}$ and spatial derivative of $\mathbf{u}$. The time derivative can be written as

$$\frac{\partial \mathbf{u}}{\partial t} = \frac{\mathbf{u}_i^{n+1} - \mathbf{u}_i^n}{\triangle t},$$ (2.24)

whereas the space derivative is denoted by

$$\frac{\partial \mathbf{F}}{\partial x} = \frac{\mathbf{F}_{i+1}^n - \mathbf{F}_{i-1}^n}{2 \triangle x}.$$ (2.25)

Here $\mathbf{u}_i^n = \mathbf{u}(x_0 + i\triangle x, t_0 + n\triangle t)$ and $\mathbf{F}_n^i = \mathbf{F}(x_0 + i\triangle x, t_0 + n\triangle t)$. In this case, i is the time node, n is the space node, $\triangle x$ is the spatial step size, $\triangle t$ is an appropriate time step, x_0 is the initial value of x and t_0 is the initial time. Hence, the resulting finite

approximation takes the following form

$$\frac{\mathbf{u}_i^{n+1} - \mathbf{u}_i^n}{\triangle t} = \frac{\mathbf{F}_{i+1}^n - \mathbf{F}_{i-1}^n}{2\triangle x}. \tag{2.26}$$

The above method is known to be unstable, therefore we use the approximation of the form

$$\mathbf{u_i^n} = \frac{1}{2}(\mathbf{u}_{i+1}^n - \mathbf{u}_{i-1}^n), \tag{2.27}$$

which implies

$$\mathbf{u}_i^{n+1} = \frac{1}{2}(\mathbf{u}_{i+1}^n - \mathbf{u}_i^n) + \frac{\triangle t}{2\triangle x}(\mathbf{F}_{i+1}^n - \mathbf{F}_{i-1}^n). \tag{2.28}$$

Finally, intermediate points at the half time step $t_{n+1/2}$ and the half mesh points $x_{i+1/2}$ are introduced and the whole solution is moved one step to two step of the the Lax-Wendroff scheme as

$$\mathbf{u}_{i+1/2}^{n+1/2} = \frac{1}{2}(\mathbf{u}_{i+1}^n - \mathbf{u}_{i-1}^n) + \frac{\triangle t}{2\triangle x}(\mathbf{F}_{i+1}^n - \mathbf{F}_i^n), \tag{2.29}$$

$$\mathbf{u}_i^{n+1} = \mathbf{u}_i^n + \frac{\triangle t}{\triangle x}(\mathbf{F}_{i+1/2}^{n+1/2} - \mathbf{F}_{i-1/2}^{n+1/2}). \tag{2.30}$$

The Fluxes $\mathbf{F}_{n+1/2}^{i+1/2}$ are computed from the values of $\mathbf{u}_{n+1/2}^{i+1/2}$ and this system will be solved for all the points on the compound jet.

2.3.2   Nonlinear Temporal Solution

To obtain the nonlinear temporal solution, we can re-write the equations $(2.12) - (2.15)$, after substituting the full curvature terms and choosing $A(x,t) = R^2$ and $B(x,t) = S^2$,

26
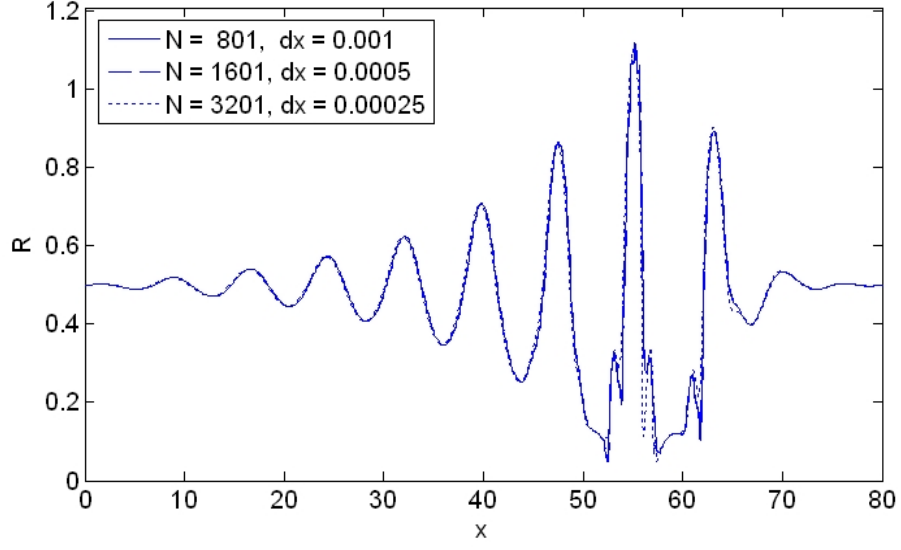
Figure 2.4: Radius of the compound jet at various mash points to check the accuracy. The parameters are $We = 31.2$, $K = 0.38$, $\sigma = 0.22$, $\rho = 1.2$, $\varepsilon = 0.01$, $\delta = 0.01$, $\chi = 0.5$ and $\triangle t = 10^{-6}$

as

$$u_t^{[I]} + \left(\frac{(u^{[I]})^2}{2}\right)_x = -\frac{1}{\rho We}\left(\sigma\frac{4(2A + (\varepsilon A_x)^2 - \varepsilon^2 AA_{xx})}{(4A + (\varepsilon A_x)^2)^{3/2}} + \frac{4(2B + (\varepsilon B_x)^2 - \varepsilon^2 BB_{xx})}{(4B + (\varepsilon B_x)^2)^{3/2}}\right)_x,$$
(2.31)

$$u_t^{[O]} + \left(\frac{(u^{[O]})^2}{2}\right)_x = -\frac{1}{We}\left(\frac{4(2B + (\varepsilon B_x)^2 - \varepsilon^2 BB_{xx})}{(4B + (\varepsilon B_x)^2)^{3/2}}\right)_x,$$
(2.32)

$$A_t = (Au^{[I]})_x,$$
(2.33)

and

$$(B - A)_t = ((B - A)u^{[O]})_x.$$
(2.34)

27
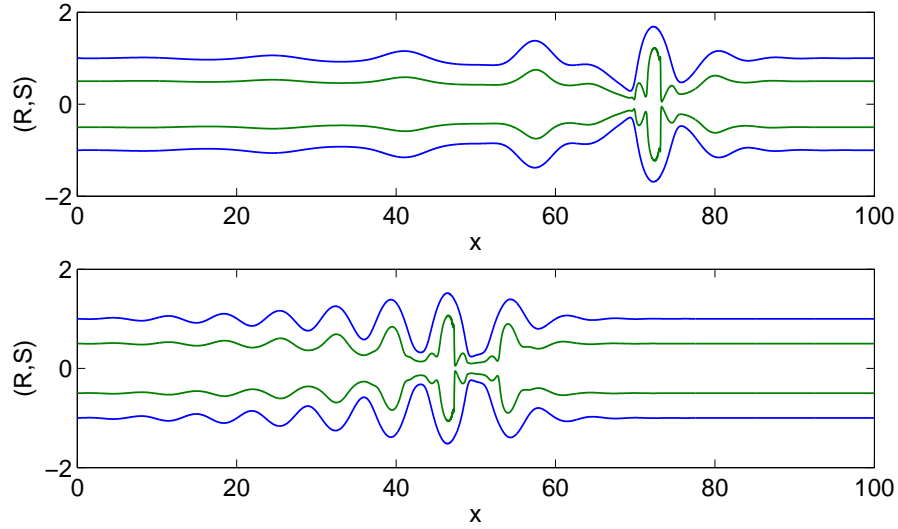
Figure 2.5: Profiles of an inviscid compound jet at the point of breakup for two different disturbance wavenumber $K = 0.38$ ($first$) and $K = 0.89$ ($second$). The other parameters are $We = 31.2$, $\sigma = 0.22$, $\rho = 1.2$, $\varepsilon = 0.01$, $\delta = 0.01$ and $\chi = 0.5$

This system of equations is solved for $x \in [0, L]$, where L is the entire length of the jet. The initial conditions for the uniform inviscid compound jet are taken as $u^{[I]} = u^{[O]} = S = 1$ and $R = \chi$. The imposed upstream boundary conditions at the nozzle are given by

$$u^{[I]}(0, t) = u^{[O]}(0, t) = 1 + \delta \, cos \left(\frac{Kt}{\varepsilon} \right), \quad R(0, t) = \chi \quad \text{and} \quad S(0, t) = 1 \qquad (2.35)$$

where δ is dimensionless initial amplitude and K is the wavenumber of imposed sinusoidal disturbance. The downstream boundary conditions for $u^{[I]}$, $u^{[O]}$, R and S are obtained by quadratic extrapolation of last interval mesh points. In this numerical simulation of the evolution of compound jet, our stopping criteria was taken to be the time at which the minimum dimensionless inner jet radius was 0.05 due to consistency with previous work [59]. Using a value smaller than this, for example, 0.01 will not alter the resulting observations as close to breakup the evolution of the jet, in particular the radius, changes exponentially. Therefore, we took the location of this minimum point to be the location

28
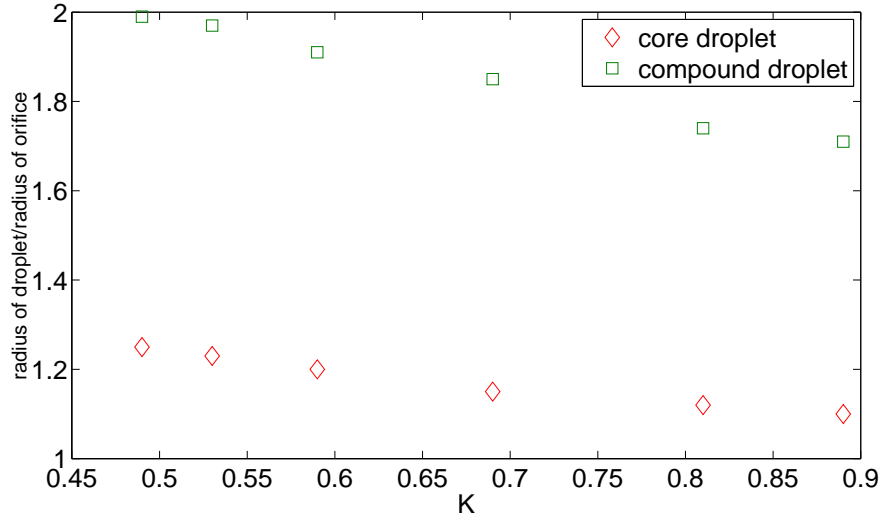
Figure 2.6: Inner and outer droplet sizes when the disturbance wavenumber K is varied. Here, we have $We = 32.2$, $\sigma = 0.28$, $\rho = 1.2$, $\varepsilon = 0.01$, $\delta = 0.01$ and $\chi = 0.5$

of breakup. It is important to mention that, in some cases, when the outer fluid radius may not be relatively small we assume that the the compound jet will break at this point. Moreover, the size of the droplet can be measured by evaluating the volume of the fluid between the breakup point and the closest adjacent minimum of the compound jet, which is mathematically expressed as

$$V_{drop} = \pi \int R^2 dx \qquad (2.36)$$

and drop radius will be equalled to the radius of sphere, that is,

$$\widehat{R} = \left(\frac{3V_{drop}}{4\pi} \right)^{\frac{1}{3}}. \qquad (2.37)$$

An example of checking the accuracy of the numerical scheme by refining the mesh points has been given in Fig. 2.4. In this figure, we are showing the inner radius of the
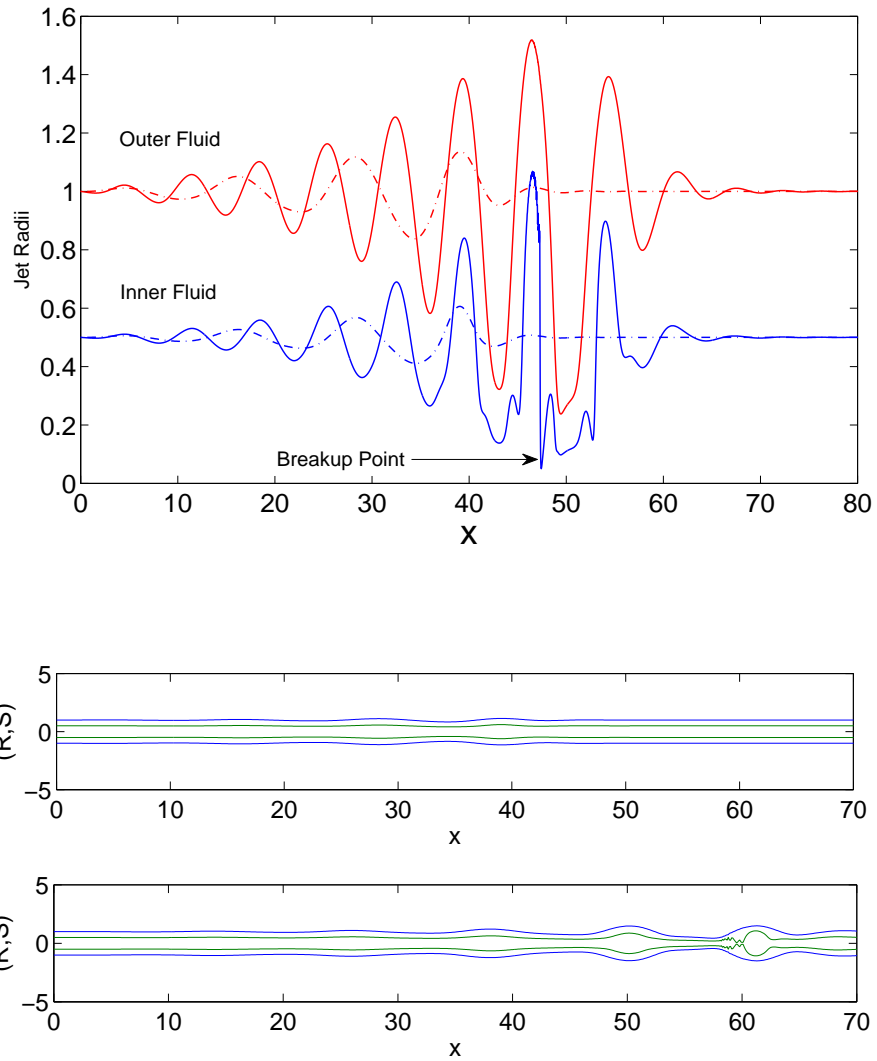
Figure 2.7: The evolution of the compound jet radius in time consisting two inviscid fluids (*top*). The profiles of the compound jet at different times are also manifested, $t = 0.4$ (*middle*) and $t = 0.619$ (*bottom*). Here, we have $We = 32.2$, $\sigma = 0.28$, $\rho = 1.2$, $K = 0.52$, $\varepsilon = 0.01$, $\delta = 0.01$ and $\chi = 0.5$
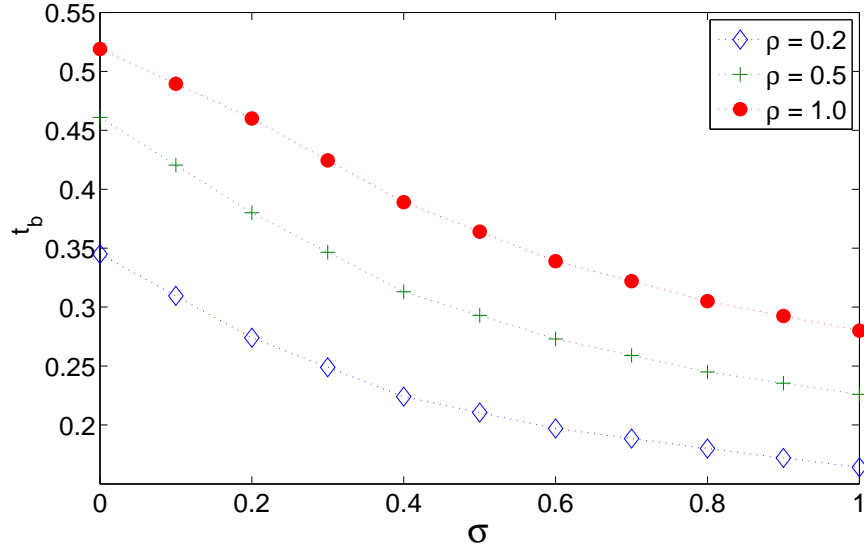
Figure 2.8: Breakup time of the compound versus density ratios and surface tension ratios. Here, we have $We = 40$, $K = 0.48$, $\varepsilon = 0.01$, $\delta = 0.01$ and $\chi = 0.5$

compound jet at the point of breakup. The formation of multiple cores with compound droplets for different disturbance wavenumber K is shown in Fig. 2.5, where we can observe that the multiple core formation is most conspicuous. The size of compound droplet and the core droplet for various values of the disturbance wavenumber is depicted in Fig. 2.6, where we notice the decrease in the size of compound and core droplets with increasing the wavenumber. In Fig. 2.7, we have shown the evolution of an inviscid compound jet and we can clearly see that the inner thread behaves qualitatively different at the time of breakup. Figures 2.8 and 2.9 are extensions of some of the figures found in Uddin [87].

In Fig. 2.8, we present the breakup time of the compound jet for the given values of the surface tension ratios σ the density ratios ρ. It is observed that the breakup time is increased with ρ and is reduced for larger values of σ. Fig. 2.9 shows that the compound jet takes more time to breakup for the higher values of the radii ratio χ. Moreover, the optimum wavenumber is found to increase by decreasing the inner to outer radii ratio of

31
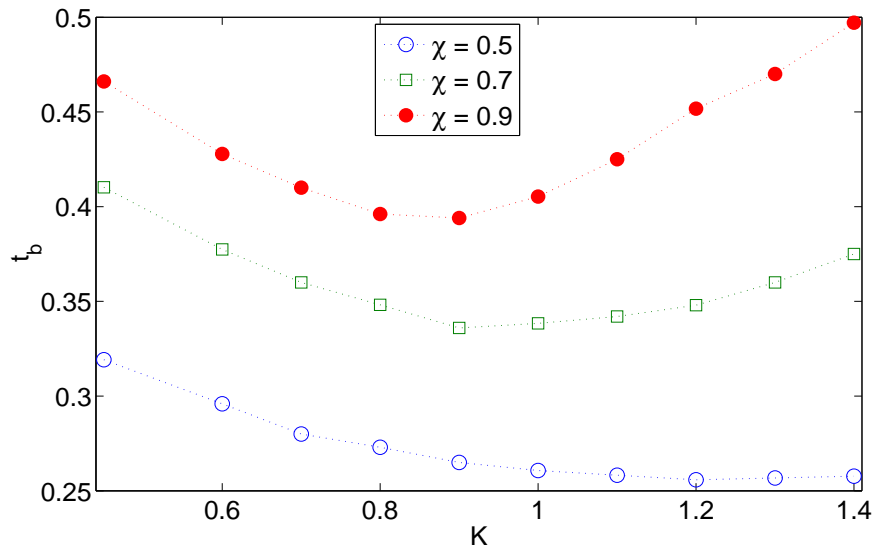
Figure 2.9: Breakup time of the compound for the given inner to outer radii ratio χ. The other parameters are $We = 40$, $\sigma = 0.25$, $\rho = 0.34$, $\varepsilon = 0.01$ and $\delta = 0.01$.

the compound jet.

CHAPTER 3

NON-UNIFORM COMPOUND LIQUID JETS

3.1 Introduction

In the preceding chapter we have reviewed the linear and nonlinear instability analysis of a uniform inviscid compound jet. The effects of gravity on the instability and the dynamics of the compound jet were neglected and therefore the compound jet was constrained to move in a parallel plane to its initial direction of motion. So, in this chapter, we describe the theoretical investigations on a compound jet emerging from circular orifice and falling under the influence of gravity.

Mohsin *et al.* [55] and Uddin & Decent [86] performed the linear and nonlinear analysis respectively by assuming the compound jet in a cylindrical co-ordinate system. The exit effects were assumed to be ignored and velocity profile was taken as $\mathbf{u}^{[\mathbf{z}]} = (w^{[z]}, 0, u^{[z]})$, where the superscripts $z = I$ and $z = O$ refer to the inner and the outer fluids respectively. Both the fluids were assumed to be incompressible and immiscible. It was denoted that $r = R(x, t)$ is the interface of inner fluid with the outer liquid, $r = S(x, t)$ is the interface of outer fluid with the quiescent gas, $\sigma^{[I]}$ is the surface tension at the interface $r = R(x, t)$ and $\sigma^{[O]}$ is the surface tension at the interface $r = S(x, t)$. The density of the fluids was denoted by $\rho^{[z]}$, and the pressure and the time were denoted as $p^{[z]}$ and t respectively.

The gravity was taken as $\mathbf{g} = (0, 0, g)$. In addition, the surface tensions $\sigma^{[I]}$ and $\sigma^{[O]}$ were assumed to be constant at the inner and the outer interface respectively.

The continuity equation and the momentum equation were formulated as

$$\frac{\partial u^{[z]}}{\partial x} + \frac{\partial w^{[z]}}{\partial r} + \frac{w^{[z]}}{r} = 0, \tag{3.1}$$

$$\frac{\partial u^{[z]}}{\partial t} + u^{[z]}\frac{\partial u^{[z]}}{\partial x} + w^{[z]}\frac{\partial u^{[z]}}{\partial r} = -\frac{1}{\rho^{[z]}}\frac{\partial p^{[z]}}{\partial x} + g \tag{3.2}$$

and

$$\frac{\partial w^{[z]}}{\partial t} + u^{[z]}\frac{\partial w^{[z]}}{\partial x} + w^{[z]}\frac{\partial w^{[z]}}{\partial r} = -\frac{1}{\rho^{[z]}}\frac{\partial p^{[z]}}{\partial r}. \tag{3.3}$$

These equations were complemented by the kinematic conditions and the normal stress conditions. The kinematic conditions, at the interface $r = R(x, t)$, can be written as

$$w^{[z]} = \frac{\partial R}{\partial t} + u^{[z]}\frac{\partial R}{\partial x}, \tag{3.4}$$

where $z = I, O$. Similarly, the kinematic conditions, at the interface $r = S(x, t)$, were

$$w^{[z]} = \frac{\partial S}{\partial t} + u^{[z]}\frac{\partial S}{\partial x}, \tag{3.5}$$

where $z = O$. The normal stress conditions, at the interfaces $r = R(x, t)$ and $r = S(x, t)$, were given as

$$p^{[I]} - p^{[O]} = \sigma^{[I]}\kappa^{[I]}, \tag{3.6}$$

34

and

$$p^{[O]} = \sigma^{[O]} \kappa^{[O]} \tag{3.7}$$

respectively, where

$$\kappa^{[I]} = \frac{\left(1 + \left(\frac{\partial R}{\partial x}\right)^2\right)^{-\frac{1}{2}}}{R} - \frac{\frac{\partial^2 R}{\partial x^2}}{\left(1 + \left(\frac{\partial R}{\partial x}\right)^2\right)^{\frac{3}{2}}}, \tag{3.8}$$

$$\kappa^{[O]} = \frac{\left(1 + \left(\frac{\partial S}{\partial x}\right)^2\right)^{-\frac{1}{2}}}{S} - \frac{\frac{\partial^2 S}{\partial x^2}}{\left(1 + \left(\frac{\partial S}{\partial x}\right)^2\right)^{\frac{3}{2}}}. \tag{3.9}$$

The variables were nondimensionalized in a following way:

$$\overline{x} = \frac{x}{L}, \quad \overline{u}^{[z]} = \frac{u^{[z]}}{U}, \quad \overline{w}^{[z]} = \frac{w^{[z]}}{U},$$

$$\overline{t} = \frac{tU}{L}, \quad \overline{r} = \frac{r}{a}, \quad \overline{p}^{[z]} = \frac{p^{[z]}}{\rho^{[O]} U^2}, \quad \text{and} \quad \varepsilon = \frac{a}{L}.$$

The dimensionless forms of inner and outer radii of the jet at the nozzle were taken as $R(0, t) = \chi$ and $S(0, t) = 1$ respectively.

3.2 Asymptotic Method

The variables were expanded, after dropping the overbars, using an asymptotic slender jet expansion of the form

$$\{u^{[z]}, w^{[z]}, p^{[z]}\} = \{u_0^{[z]}(x, t), 0, p_0^{[z]}(x, r, t)\} \quad + (\varepsilon r)\{u_1^{[z]}(x, t), w_1^{[z]}(x, t), p_1^{[z]}(x, t)\} + O((\varepsilon r)^2), \tag{3.10}$$

$$\{R, S\} = \{R_0(x, t), S_0(x, t)\} + \varepsilon\{R_1(x, t), S_1(x, t)\} + O(\varepsilon^2). \tag{3.11}$$

After substituting the above asymptotic expansions in the equations $(3.1) - (3.9)$, the leading order continuity equation for the inner and outer fluids gives

$$w_1^{[z]} = -\frac{1}{2} \frac{\partial u_0^{[z]}}{\partial x}, \tag{3.12}$$

where $z = I, O$. The leading order kinematic conditions, at $r = R(x)$ and $r = S(x)$, give

$$\frac{\partial}{\partial t} \left(R_0^2 \right) + \frac{\partial}{\partial x} \left(R_0^2 u_0^{[I]} \right) = 0, \tag{3.13}$$

and

$$\frac{\partial}{\partial t} \left(S_0^2 - R_0^2 \right) + \frac{\partial}{\partial x} \left((S_0^2 - R_0^2) u_0^{[O]} \right) = 0, \tag{3.14}$$

respectively. The leading order normal stress conditions, at $r = S(x, t)$ and $r = R(x, t)$, yield

$$p_0^{[O]} = \frac{1}{S_0 We} \text{ and } p_0^{[I]} = \frac{1}{We} \left(\frac{\sigma}{R_0} + \frac{1}{S_0} \right) \tag{3.15}$$

respectively, where $\sigma = \sigma^{[I]}/\sigma^{[O]}$ is the ratio of surface tension between inner and outer fluid interfaces and $We = \rho^{[O]} U^2 a / \sigma^{[O]}$ is the Weber number. By using equations (3.12) and (3.15), the radial momentum equation (3.3) gives $\partial p_0^{[z]}/\partial r = 0$, that is automatically satisfied. Substituting equation (3.15) in the axial momentum equation (3.2) for the inner and the outer fluids, which implies

$$\frac{\partial u_0^{[I]}}{\partial t} + u_0^{[I]} \frac{\partial u_0^{[I]}}{\partial x} = -\frac{1}{\rho We} \frac{\partial}{\partial x} \left(\frac{\sigma}{R_0} + \frac{1}{S_0} \right) + \frac{1}{F^2} \tag{3.16}$$

36

and

$$\frac{\partial u_0^{[O]}}{\partial t} + u_0^{[O]} \frac{\partial u_0^{[O]}}{\partial x} = -\frac{1}{We} \frac{\partial}{\partial x} \left(\frac{1}{S_0} \right) + \frac{1}{F^2}, \tag{3.17}$$

where $\rho = \rho^{[I]}/\rho^{[O]}$ is the density ratio of the inner fluid to the outer fluid and $F = U/\sqrt{Lg}$ is the Froude number, which gives a measure of the relative importance of gravitational forces.

3.3   Steady State solutions

The steady state form of equations (3.13), (3.14), (3.16) and (3.17) is given by

$$\frac{\partial}{\partial x} \left(R_0^2 u_0^{[I]} \right) = 0, \tag{3.18}$$

$$\frac{\partial}{\partial x} \left((S_0^2 - R_0^2) u_0^{[O]} \right) = 0, \tag{3.19}$$

$$u_0^{[I]} \frac{\partial u_0^{[I]}}{\partial x} = -\frac{1}{\rho We} \frac{\partial}{\partial x} \left(\frac{\sigma}{R_0} + \frac{1}{S_0} \right) + \frac{1}{F^2}, \tag{3.20}$$

$$u_0^{[O]} \frac{\partial u_0^{[O]}}{\partial x} = -\frac{1}{We} \frac{\partial}{\partial x} \left(\frac{1}{S_0} \right) + \frac{1}{F^2}. \tag{3.21}$$

Uddin & Decent [86] and Mohsin *et al.* [55] solved the above system of equations using Newton's method but this can also be solved with the help of Runge-Kutta method. The results using both the methods are identical and we therefore use the Runge-Kutta method in this chapter. The initial conditions at the nozzle were specified as $u_0^{[I]} = u_0^{[O]} = S_0 = 1$ and $R_0 = \chi$. By using the initial conditions and dropping subscripts zeros from the

37
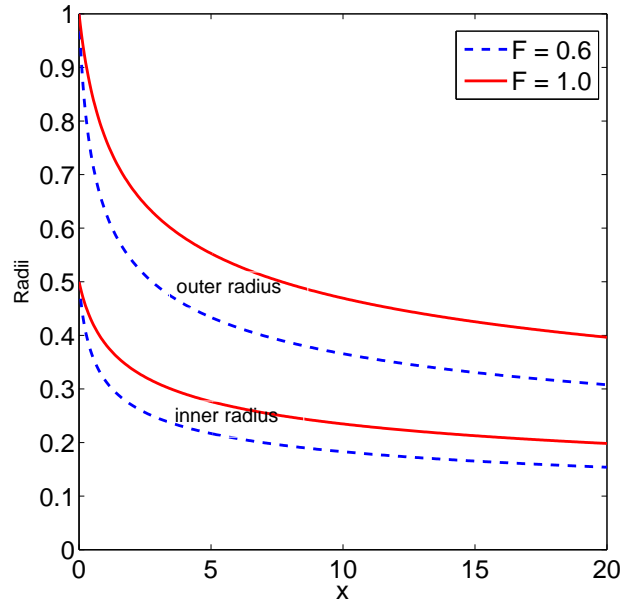
Figure 3.1: The steady state solutions for inner and outer jet radii for various Froude numbers. Other parameters are $\rho = 1$, $\sigma = 1$, $\chi = 0.5$ and $We = 100$.

variables for ease of convenience, we apply Runge-Kutta method to find the steady state solutions. We present the steady state solutions, for various values of Froude number, for the inner and outer radii of the compound jet in Fig. 3.1. We notice that a decrease in Froude number, which corresponds to a greater influence of gravitational forces, leads to a more rapid decay of jet radii along the jet which is expected due to the increased acceleration in the vertical direction.

3.4 Linear instability Analysis

Linear instability analysis was then performed by assuming the small perturbations in terms of δ, that is,

$$u_0^{[I]}(x,t) = u_0^{[I]}(x) + \delta \ exp(ik\overline{x} + \lambda \overline{t}) \ \widehat{u}^I, \tag{3.22}$$

38

$$u_0^{[O]}(x,t) = u_0^{[O]}(x) + \delta \ exp(ik\overline{x} + \lambda\overline{t}) \ \widehat{u}^O, \tag{3.23}$$

$$R_0(x,t) = R_0(x) + \delta \ exp(ik\overline{x} + \lambda\overline{t}) \ \widehat{R}, \tag{3.24}$$

$$S_0(x,t) = S_0(x) + \delta \ exp(ik\overline{x} + \lambda\overline{t}) \ \widehat{S}, \tag{3.25}$$

where $\overline{x} = x/\varepsilon$ and $\overline{t} = t/\varepsilon$. The disturbances were considered in temporal mode, so λ, which is the growth rate, taken in complex form, that is, $\lambda = \lambda_r + i\lambda_i$ and wave number k assumed as a real number. By introducing the small perturbations in equations $(3.13) - (3.17)$ and choosing the linear terms in δ, the following characteristic equation was obtained

$$[4RS]\lambda'^4 - [8RS(ik(u^{[O]} - u^{[I]}))]\lambda'^3$$

$$+ \left[\frac{2ikR^3}{\rho We}\left(\frac{ik}{S^2} - ik^3\right) + \sigma S\left(\frac{ik}{R^2} - ik^3\right) - (4RS(ik(u^{[O]} - u^{[I]}))^2)\right]\lambda'^2$$

$$+ \left[\frac{2ikR(\frac{ik}{S^2} - ik^3)}{We}(S^2 - R^2)\right]\lambda'^2 + \left[\frac{4k^2R(\frac{ik}{S^2} - ik^3)(u^{[O]} - u^{[I]})}{We}(S^2 - R^2)\right]\lambda'$$

$$+ \frac{R(\frac{ik}{S^2} - ik^3)}{We}\left(2k^2(u^{[O]} - u^{[I]}))^2 - \frac{\sigma k^2R(\frac{ik}{R^2} - ik^3)}{\rho We}\right)(S^2 - R^2) = 0. \tag{3.26}$$

where $\lambda' = \lambda + iku^{[O]}$.
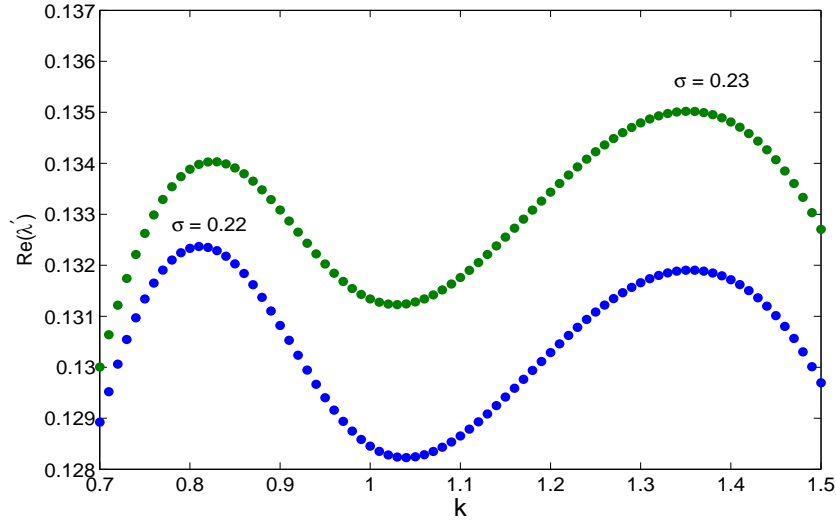
Figure 3.2: Growth rate of disturbances versus wavenumber for two different surface tension ratios σ. The other parameters are $We = 10$, $\rho = 1$, and $\chi = 0.5$

We solve the dispersion relation (3.26) by applying Ferrari's method [4] (we have also checked our results using Muller's method [58]) and examine the instability and the breakup of the compound jet. The purpose to solve this dispersion in a temporal mode is to obtain the growth rate of disturbances for the given values of wavenumber k. We choose the maximum value of growth rate of disturbances λ'_{max} and its correspondent value of wavenumber K_{max} and both of these values give us the information about the droplet size and the breakup of the jet.

As the compound jet is accelerating in the vertical direction, the steady state solutions are the function of x, that is axial distance along the jet. The major results from this section have been published by the author in *Physics of Fluids*, (see Mohsin *et al.* [55]) and here we summarize the key observations. In Fig. 3.2, we plot the growth rate of disturbances against the wavenumber k for two different values of the surface tension ratio σ. We notice that the growth rate of disturbances becomes large if we increase the value of surface tension ratio σ. Moreover, we find a competing mode at $\sigma = 0.22$ and
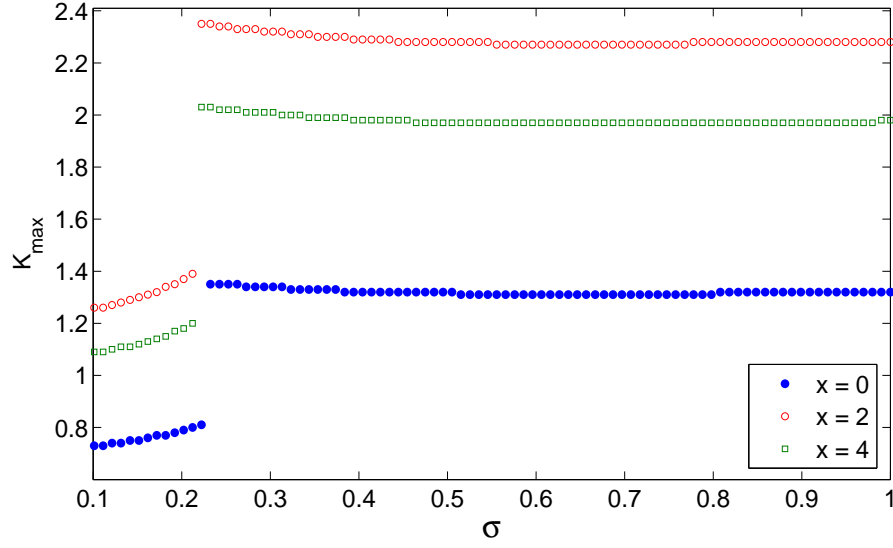
Figure 3.3: Maximum wavenumber versus surface tension ratios σ at different locations of the compound jet. The other parameters are $We = 10$, $\rho = 1$, and $\chi = 0.5$

$\sigma = 0.23$. In Fig. 3.3, we find a large difference in maximum wavenumber k_{max} and it is due to the competing mode propagating along the jet. It exists for a smaller value of the surface tension ratio σ which we refer to a threshold surface tension ratio σ^*. We obtain k_{max} at three different positions of the jet by increasing the surface tension ratio σ. It can be seen that the there is a jump in the values of values of k_{max} at $\sigma = 0.23$ and k_{max} increases when $\sigma < \sigma^*$ and then it decreases slightly when $\sigma > \sigma^*$. This trend is found to be similar for all the values of x. Using the results of linear instability analysis, we obtain the theoretical breakup lengths which are shown in Fig. 3.4. The breakup lengths are found by varying the inner to outer radii ratio χ for two different values of the Weber number. It is clearly noticed that the compound jet take more time to breakup for higher values of the Weber number. In addition, the breakup length increase with the increases in χ and we also observe the outer jet breakup at $\chi = 0.94$ for $We = 20$ and $\chi = 0.91$ for $We = 100$.

41
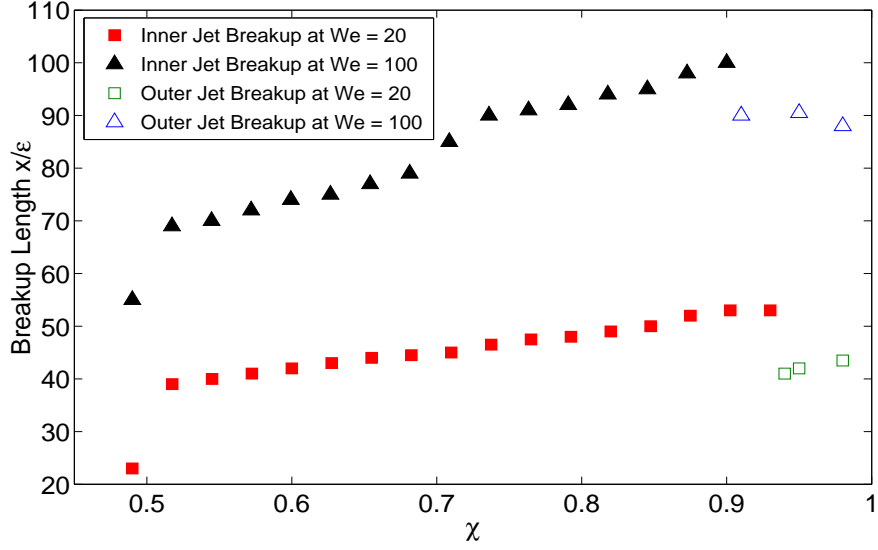
Figure 3.4: Theoretical breakup lengths of compound jet. The parameters used here are $\sigma = 1$, $\varepsilon = 0.01$, $\rho = 1$, $F = 1$ and $\delta = 0.002$

3.5 Nonlinear Analysis

In order to perform the nonlinear analysis, we first re-write the equations (3.13), (3.14), (3.16) and (3.17), after substituting the full curvature terms and choosing $A(x,t) = R^2$ and $B(x,t) = S^2$, as

$$u_t^{[I]} + \left(\frac{(u^{[I]})^2}{2}\right)_x = -\frac{1}{\rho We}\left(\sigma\frac{4(2A + (\varepsilon A_x)^2 - \varepsilon^2 AA_{xx})}{(4A + (\varepsilon A_x)^2)^{3/2}} + \frac{4(2B + (\varepsilon B_x)^2 - \varepsilon^2 BB_{xx})}{(4B + (\varepsilon B_x)^2)^{3/2}}\right)_x + \frac{1}{F^2},$$
(3.27)

$$u_t^{[O]} + \left(\frac{(u^{[O]})^2}{2}\right)_x = -\frac{1}{We}\left(\frac{4(2B + (\varepsilon B_x)^2 - \varepsilon^2 BB_{xx})}{(4B + (\varepsilon B_x)^2)^{3/2}}\right)_x + \frac{1}{F^2},$$
(3.28)

$$A_t = (Au^{[I]})_x,$$
(3.29)
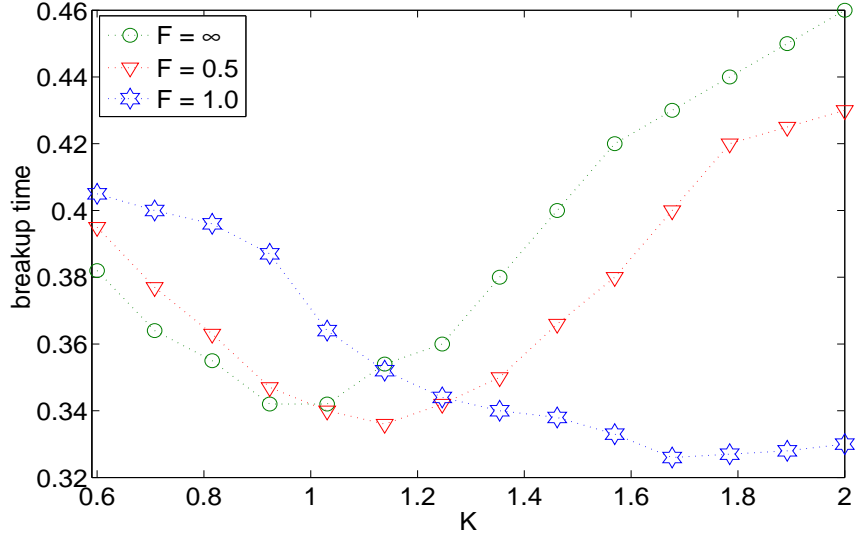
Figure 3.5: Breakup time of compound jet against wavenumber of disturbance at nozzle for different values of Froude number, where $\sigma = 1.0$, $\rho = 1.0$, $\delta = 0.01$, $\varepsilon = 0.01$, $\chi = 0.5$, and $We = 20$.

and

$$(B - A)_t = ((B - A)u^{[O]})_x. \tag{3.30}$$

This system of equations is solved for $x \in [0, L]$, where L is the entire length of the jet. The initial conditions are the steady state solutions found in the previous section. The imposed upstream boundary conditions at the nozzle are given by

$$u^{[I]}(0, t) = u^{[O]}(0, t) = 1 + \delta \, cos\left(\frac{Kt}{\varepsilon}\right), \quad R(0, t) = \chi \text{ and } S(0, t) = 1 \tag{3.31}$$

where δ is dimensionless initial amplitude and K is the wavenumber of imposed sinusoidal disturbance. The downstream boundary conditions for $u^{[I]}$, $u^{[O]}$, R and S are obtained by quadratic extrapolation of last interval mesh points.

43
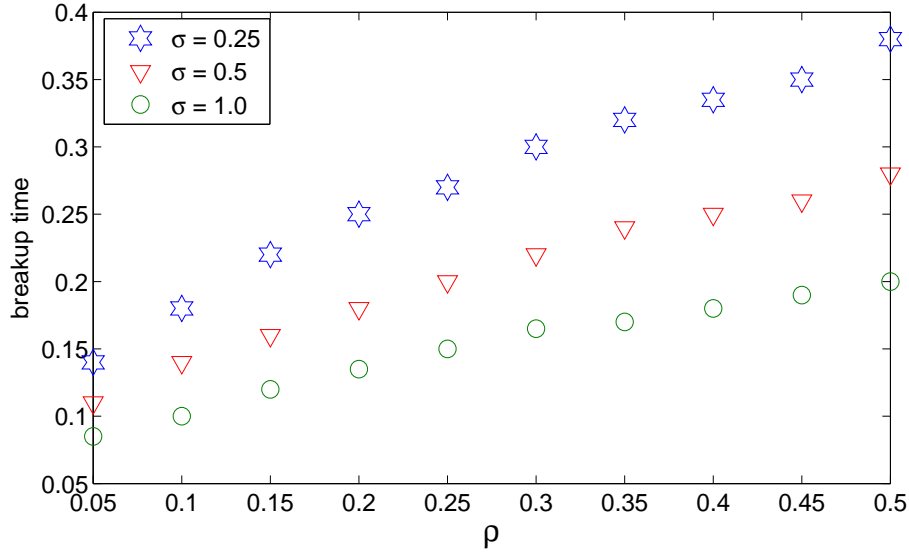
Figure 3.6: Breakup time of compound jet against density ratios for different values of surface tension ratios, where $K = 1.0$, $F = 0.707$, $\delta = 0.01$, $\chi = 0.01$, $\varepsilon = 0.01$, and $We = 25$.

Here, we provide some numerical results found by Uddin & Decent [86] to study the dynamics of inner and outer fluids. From Fig. 3.5, we can see that the compound jet falling under the gravity will be longer and more stable for small disturbance wavenumber but if we increase the wavenumber at the nozzle the compound jet falling without the influence of gravity takes more time to breakup as compare to the compound jet falling with gravity. It is also noticed that the wavenumber at which the breakup time is minimal decreases by increasing the Froude number.

In Fig. 3.6, the graph is presented between the breakup time of compound jet falling under the gravity and the density ratios for different values of surface tension ratios. It is observed that the breakup time is increased with ρ for different values of σ. Furthermore, the breakup time reduces for larger values of σ. The profiles of an inviscid compound jet for two different disturbance amplitude are shown in the Fig. 3.7 and the size of the inner droplet in the presence of gravity and for the case of zero gravity by varying the disturbance amplitude δ is shown in Fig. 3.8. It can be noticed that the droplet becomes

44
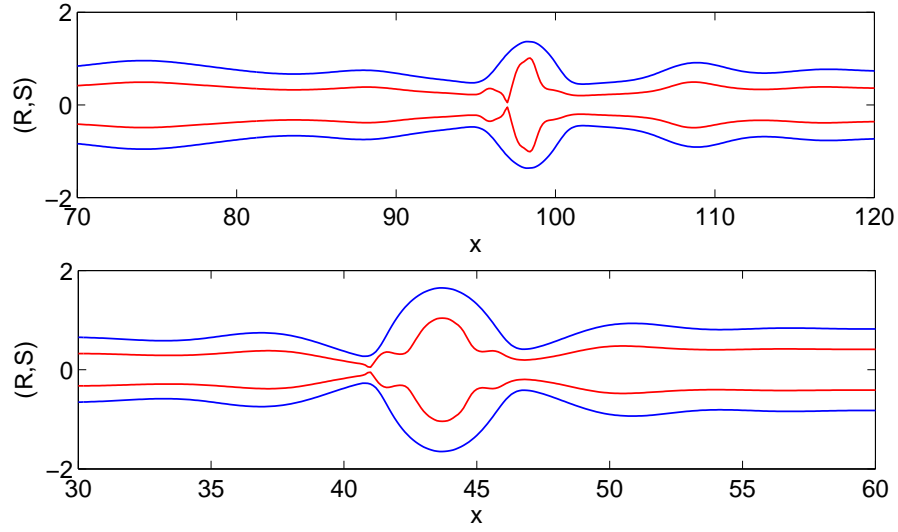
Figure 3.7: Profiles of the compound jet for two different values of disturbance amplitude, that is, $\delta = 0.01$ ($first$) and $\delta = 0.05$ ($second$), where $\sigma = 0.22$, $\rho = 1.2$, $K = 0.38$, $\varepsilon = 0.01$, $\chi = 0.5$, and $We = 31.2$.

large for the higher disturbance amplitude δ. Furthermore, we observe that the size of the droplet reduces due to the presence of gravity.

Lastly, we can conclude that an increase in the Froude number lead to decrease the optimum wavenumber and the compound jet falling under gravity takes more time to breakup by increasing the density ratios and decreasing the surface tension ratios.
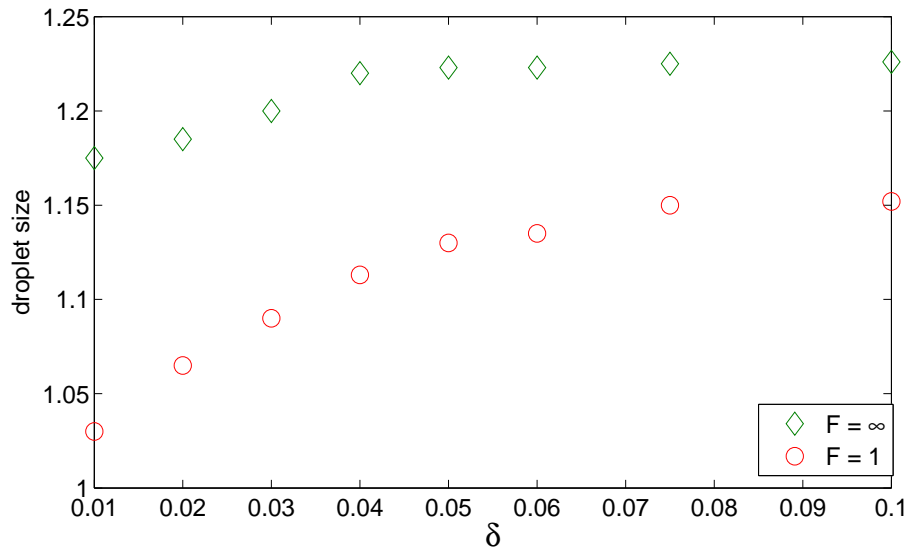
Figure 3.8: Droplet size produced by the inner jet for different disturbance amplitude, where $\sigma = 0.22$, $\rho = 1.2$, $K = 0.38$, $\varepsilon = 0.01$, $\mu = 0.5$, and $We = 31.2$.

CHAPTER 4

TWO DIMENSIONAL INVISCID COMPOUND

JET

4.1 Introduction

We have so far described the instability analysis of a compound liquid jet using a one dimensional model to capture the relationship between the jet radius and the jet axial velocity. In this chapter, we aim to examine the linear instability analysis of a two dimensional inviscid compound liquid jet. Basically, we are extending the analysis of Uddin [87] and are including effects due to the flow in the radial direction. Therefore, we require the full set of dimensionless equations to perform the linear instability analysis of the compound jet. For ease of reference, we present the dimensionless continuity and momentum equations, which are given by

$$\frac{\partial u^{[z]}}{\partial x} + \varepsilon \frac{\partial w^{[z]}}{\partial r} + \frac{w^{[z]}}{r} = 0, \tag{4.1}$$

$$\frac{\partial u^{[z]}}{\partial t} + u^{[z]} \frac{\partial u^{[z]}}{\partial x} + \frac{w^{[z]}}{\varepsilon} \frac{\partial u^{[z]}}{\partial r} = -\frac{\rho^{[O]}}{\rho^{[z]}} \frac{\partial p^{[z]}}{\partial x} \tag{4.2}$$

47

and

$$\frac{\partial w^{[z]}}{\partial t} + u^{[z]}\frac{\partial w^{[z]}}{\partial x} + \frac{w^{[z]}}{\varepsilon}\frac{\partial w^{[z]}}{\partial r} = -\frac{\rho^{[O]}}{\rho^{[z]}}\frac{1}{\varepsilon}\frac{\partial p^{[z]}}{\partial r}, \tag{4.3}$$

where $z = I, O$. The dimensionless kinematic conditions, at the interface $r = R(x, t)$ and $r = S(x, t)$, are given by

$$w^{[z]} = \frac{\partial R}{\partial t} + u^{[z]}\frac{\partial R}{\partial x}, \tag{4.4}$$

where $z = I, O$ and

$$w^{[z]} = \frac{\partial S}{\partial t} + u^{[z]}\frac{\partial S}{\partial x}, \tag{4.5}$$

where $z = O$, respectively. The dimensionless normal stress conditions, at the interfaces $r = S(x, t)$ and $r = R(x, t)$, are

$$p^{[O]} = \frac{\kappa^{[I]}}{We}, \quad \text{where} \quad \kappa^{[I]} = \frac{\left(1 + \varepsilon^2 \left(\frac{\partial S}{\partial x}\right)^2\right)^{-\frac{1}{2}}}{S} - \frac{\frac{\partial^2 S}{\partial x^2}}{\left(1 + \varepsilon^2 \left(\frac{\partial S}{\partial x}\right)^2\right)^{\frac{3}{2}}} \tag{4.6}$$

and

$$p^{[I]} - p^{[O]} = \frac{\sigma\kappa^{[O]}}{We}, \quad \text{where} \quad \kappa^{[O]} = \frac{\left(1 + \varepsilon^2 \left(\frac{\partial R}{\partial x}\right)^2\right)^{-\frac{1}{2}}}{R} - \frac{\frac{\partial^2 R}{\partial x^2}}{\left(1 + \varepsilon^2 \left(\frac{\partial R}{\partial x}\right)^2\right)^{\frac{3}{2}}} \tag{4.7}$$

respectively. Here $\sigma = \sigma^{[I]}/\sigma^{[O]}$ is the ratio of surface tension between the inner and outer fluid interfaces, $We = \rho^{[O]}U^2 a/\sigma^{[O]}$ is the Weber number and $\rho = \rho^{[I]}/\rho^{[O]}$ is the density ratio of the inner fluid to the outer fluid. The steady state solutions of the uniform velocities are $\mathbf{u^{[I]}} = \mathbf{u^{[O]}} = (0, 0, 1)$, which imply $S_0 = 1$ and $R_0 = \chi$.

4.2 Linear Instability Analysis

We now consider the linear temporal instability analysis of an inviscid compound liquid jet. The evolution of the jet depends on the length scale $x = O(1)$, but the disturbances along the jet are much smaller and are comparable to ε when $x = O(1)$. In other words, we can say that the disturbances are typically of the order of jet radius a. Similar to the approach used in previous chapter, we consider the traveling short waves of the form $exp(ik\overline{x} + \lambda\overline{t})$, where $k = k(x) = O(1)$ and $\lambda = \lambda(x) = O(1)$ are the frequency and wavenumber of disturbances. Additionally, $\overline{x} = x/\varepsilon$ and $\overline{t} = t/\varepsilon$ are small length and time scales. Thus, we have a multiple scale formulation as the perturbations grow along the jet having wavelength of $O(\varepsilon)$. Now we introduce small time dependent perturbations to the steady state solutions which take the form

$$u^{[z]} = 1 + \delta\overline{u^{[z]}}(r)\exp(\lambda\overline{t} + ik\overline{x}), \tag{4.8}$$

$$w^{[z]} = 0 + \delta\overline{w^{[z]}}(r)\exp(\lambda\overline{t} + ik\overline{x}), \tag{4.9}$$

$$p^{[z]} = p_0^{[z]}(x) + \delta\overline{p^{[z]}}(r)\exp(\lambda\overline{t} + ik\overline{x}), \tag{4.10}$$

$$R = \chi + \delta\overline{R}\exp(\lambda\overline{t} + ik\overline{x}), \tag{4.11}$$

$$S = 1 + \delta\overline{S}\exp(\lambda\overline{t} + ik\overline{x}). \tag{4.12}$$

where $0 < \delta << \varepsilon$. Substituting the expansions $(4.8) - (4.12)$ into the equations $(4.1) - (4.7)$ yield at leading order, or $O(\delta/\varepsilon)$,

$$ik\overline{u^{[z]}} + \frac{\partial \overline{w^{[z]}}}{\partial r} + \frac{\overline{w^{[z]}}}{r} = 0, \tag{4.13}$$

$$(\lambda + ik)\overline{u^{[z]}} = -((\delta_{\mathbf{Iz}})\frac{1}{\rho} + \delta_{\mathbf{Oz}})\overline{p^{[z]}}ik, \tag{4.14}$$

$$(\lambda + ik)\overline{w^{[z]}} = -((\delta_{\mathbf{Iz}})\frac{1}{\rho} + \delta_{\mathbf{Oz}})\frac{\partial \overline{p^{[z]}}}{\partial r}, \tag{4.15}$$

$$\overline{w^{[z]}} = (\lambda + ik)\overline{R} \quad \text{for} \quad z = I, O, \tag{4.16}$$

$$\overline{w^{[z]}} = (\lambda + ik)\overline{S} \quad \text{for} \quad z = O, \tag{4.17}$$

$$\overline{p^{[I]}} - \overline{p^{[O]}} = \frac{\sigma}{We}(k^2 - \frac{1}{R_0^2})\overline{R}, \tag{4.18}$$

$$\overline{p^{[O]}} = \frac{1}{We}(k^2 - \frac{1}{S_0^2})\overline{S}, \tag{4.19}$$

where $\delta_{\mathbf{Iz}}$ is the Kronecker delta symbol with free index z. Using (4.14) and (4.15) to eliminate $\overline{p^{[z]}}$, we get $\overline{w^{[z]}} = \frac{1}{ik}\frac{\partial \overline{u^{[z]}}}{\partial r}$ and substituting this result in (4.13), so that we have

$$\frac{\partial^2 \overline{u^{[z]}}}{\partial r^2} + \frac{1}{r}\frac{\partial \overline{u^{[z]}}}{\partial r} - k^2\overline{u^{[z]}} = 0, \tag{4.20}$$

50

which has solution

$$\overline{u}^{[z]} = C^{[z]} I_0(kr) + D^{[z]} K_0(kr). \tag{4.21}$$

By using the value of $\overline{u}^{[z]}$, we are able to get

$$\overline{w}^{[z]} = \frac{1}{i}(C^{[z]} I_1(kr) - D^{[z]} K_1(kr)). \tag{4.22}$$

By using (4.14) in (4.21), yields

$$\overline{p}^{[z]} = \frac{-(\lambda + ik)}{ik((\delta_{Iz})\rho + \delta_{\mathbf{Oz}})}(C^{[z]} I_0(kr) + D^{[z]} K_0(kr)), \tag{4.23}$$

where $I_0(kr)$, $I_1(kr)$ and $K_0(kr)$, $K_1(kr)$ are the modified Bessel functions of first and second kind respectively. To avoid the singularities, and to ensure finite values at $r = 0$, we require that $D^{[I]}$ will be equal to zero.

Substituting the values of $\overline{w}^{[z]}$ in (4.16) and (4.17), yields

$$\frac{1}{i}(C^{[I]} I_1(k\chi) - D^{[I]} K_1(k\chi)) = (\lambda + ik)\overline{R}, \tag{4.24}$$

$$\frac{1}{i}(C^{[O]} I_1(k\chi) - D^{[O]} K_1(k\chi)) = (\lambda + ik)\overline{R}, \tag{4.25}$$

$$\frac{1}{i}(C^{[O]} I_1(k) - D^{[O]} K_1(k)) = (\lambda + ik)\overline{S}. \tag{4.26}$$

51

Similarly, using the values of $\overline{p}^{[z]}$ from equation (4.23) in equations (4.18) and (4.19), we get

$$\frac{-(\lambda + ik)}{ik\rho}(C^{[I]}I_0(k\chi)) + \frac{(\lambda + ik)}{ik}(C^{[O]}I_0(k\chi) + D^{[O]}K_0(k\chi)) \tag{4.27}$$

$$= \frac{\sigma}{We}(k^2 - \frac{1}{\chi^2})\overline{R},$$

$$\frac{-(\lambda + ik)}{ik}(C^{[O]}I_0(k\chi) + D^{[O]}K_0(k\chi)) = \frac{1}{We}(k^2 - 1)\overline{S}. \tag{4.28}$$

By eliminating the $C^{[I]}, C^{[O]}, D^{[O]}, \overline{R}$ and $\overline{S}$ from equations $(4.24) - (4.28)$, we are able to arrive at following dispersion relation:

$$\frac{\lambda'^4}{k^2} \left[(I_1(k\chi)K_1(k)I_0(k)K_0(k\chi) - I_1(k\chi)I_0(k\chi)K_0(k)K_1(k)) \right.$$

$$+ \rho \left(K_1(k\chi)I_0(k)I_0(k\chi)K_1(k) + I_1(k\chi)K_1(k)K_0(k)I_0(k\chi)) \right] +$$

$$\frac{\lambda'^2}{kWe} \left[\beta \left(I_1(k\chi)K_1(k\chi)K_1(k)I_0(k) + I_1(k\chi)I_1(k\chi)K_1(k)K_0(k)) \right. \right.$$

$$+ \rho \alpha \left(K_1(k\chi)K_1(k)I_0(k\chi)I_1(k) + I_1(k\chi)I_0(k\chi)K_1(k)K_1(k)) \right. +$$

$$\alpha \left(I_1(k\chi)I_0(k\chi)K_1(k)K_1(k) + I_1(k\chi)K_0(k\chi)K_1(k)I_1(k)) \right] -$$

$$+\frac{\alpha\beta}{We^2} \left(I_1(k\chi)K_1(k\chi)I_I(k)K_1(k) - I_1(k)I_0(k\chi)K_1(k\chi)K_1(k)) \right) = 0. \tag{4.29}$$

In the above dispersion relation, we have

$$\alpha \; = \; k^2 - 1, \quad \beta \; = \; \sigma \, (k^2 - \tfrac{1}{\chi^2})$$

and $\lambda' = \lambda + ik$. If we take the long wavelength limit of (4.29), that is $k \longrightarrow 0$, we obtain the following eigenvalue relation:

$$\lambda'^4 - \frac{k^2}{2We}[(\frac{\chi^2}{\rho} + (1 - \mu^2))(1 - k^2) + \frac{\sigma\chi k^2}{\rho}(\frac{1}{\chi^2} - k^2)]\lambda'^2 + \frac{k^4\sigma\chi}{4\rho We^2}$$

$$(1 - k^2)(\frac{1}{\chi^2} - k^2)(1 - \chi^2) = 0 \tag{4.30}$$

We note that (4.30) is identical to the dispersion relation found by Uddin [87] as shown in chapter two of this thesis.

4.3 Results and discussion

The dispersion relation (4.29) is a quartic equation in λ' for the given values of k and since only even powers of λ' appear, therefore we may use the quadratic formula to obtain solutions for λ'. We now discuss the numerical results obtained by solving equation (4.29). In Fig. 4.1, we plot the growth rate of disturbances for the given value of wavenumber k. Here, we present the comparison between the full dispersion relation and the dispersion relation obtained by Uddin [87] in a long wavelength limit. As anticipated it shows a good agreement for $k \ll 1$ and there is a slight variation for $k = O(1)$ values with the full dispersion relation predicting slightly lower values for the growth rate for all wavenumbers.

The growth rate of disturbances versus the wavenumber k for two different values of the surface tension ratio σ and the density ratio ρ have been shown in Figs. 4.2 and 4.3
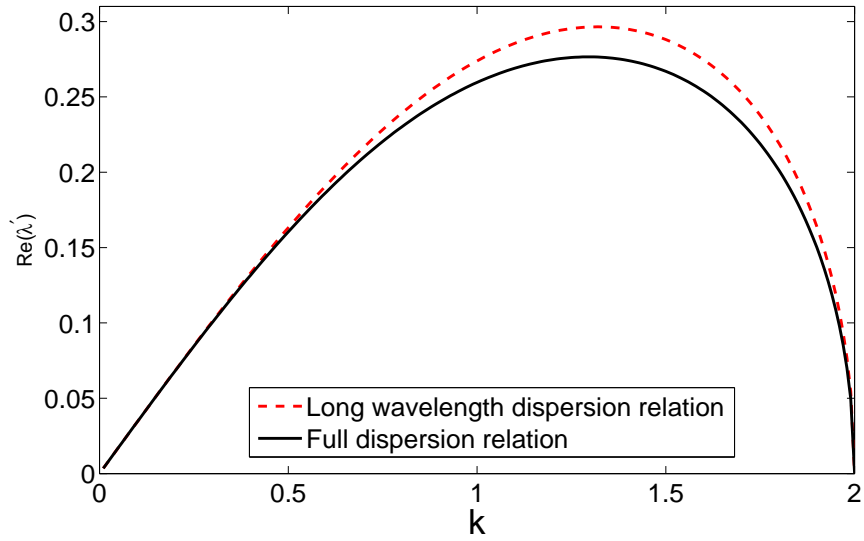
Figure 4.1: Growth rate of disturbances versus wavenumber, The parameters are $We = 10$, $\sigma = 1$, $\rho = 1$, and $\chi = 0.5$
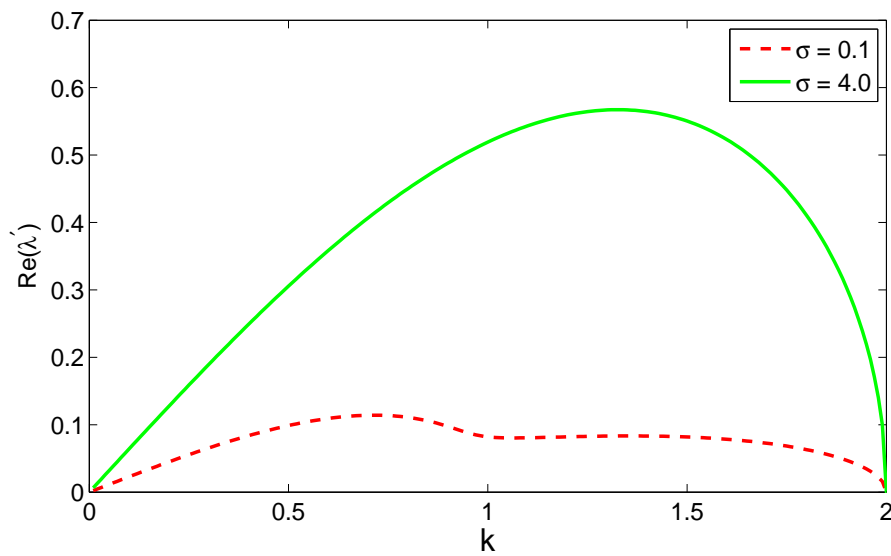
Figure 4.2: Growth rate of disturbances versus wavenumber for two different surface tension ratios, The parameters are $We = 10$, $\rho = 1$, and $\chi = 0.5$
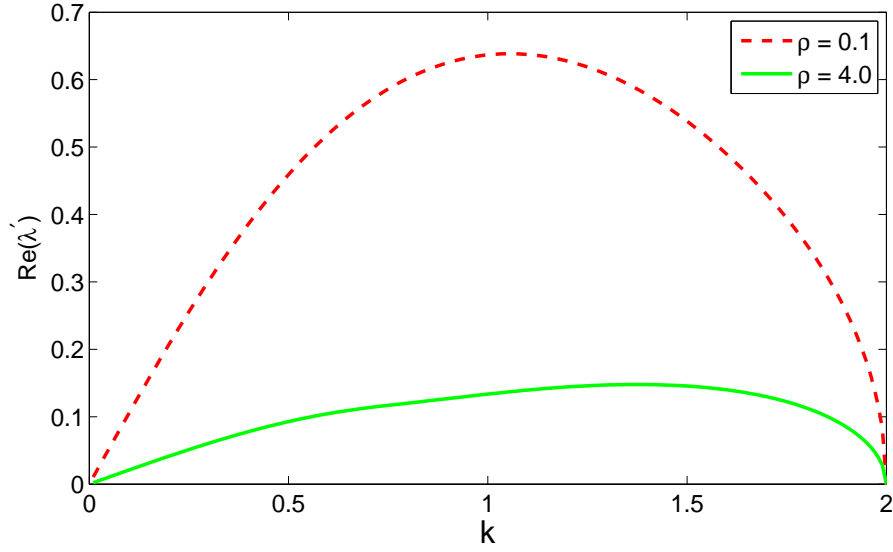
Figure 4.3: Growth rate of disturbances versus wavenumber for two different density ratios, The parameters are $We = 10$, $\sigma = 1$, and $\chi = 0.5$

respectively. We can clearly notice that the growth rate of disturbances increases with the increase in surface tension ratio σ at the interfaces and the lower growth rates are found for the higher value of the density ratio ρ. Figures. 4.4 and 4.5 give us the growth rate of disturbances for two different values of the the Weber number and inner to outer radii ratio χ respectively. It is seen that the growth rate of disturbances reduces at the larger value of the Weber number. In addition, we analyze from the Fig. 4.5 that the cut-off wavenumber and growth rate of disturbances become large by decreasing the inner to outer radii ratio χ.
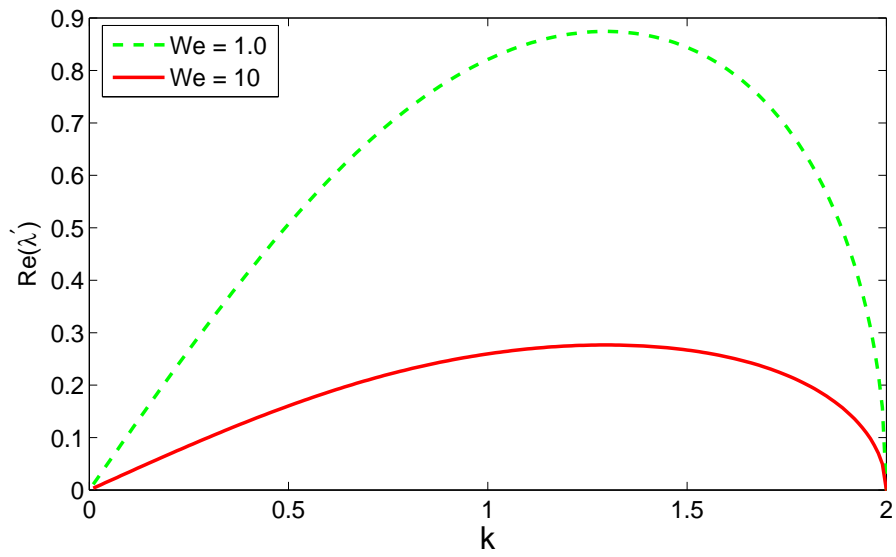
Figure 4.4: Growth rate of disturbances versus wavenumber for two different values of Weber number, The parameters are $\sigma = 1$, $\rho = 1$, and $\chi = 0.5$
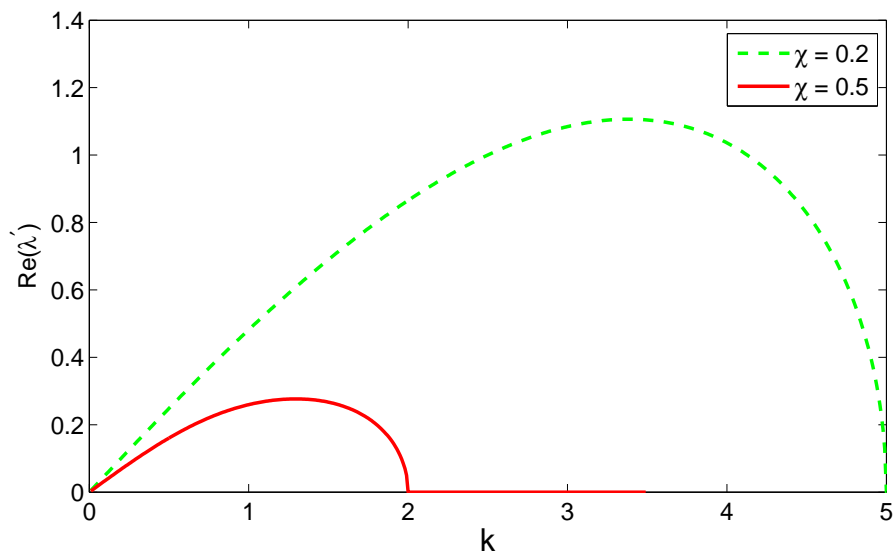
Figure 4.5: Growth rate of disturbances versus wavenumber for two different radii ratios, The parameters are $We = 10$, $\sigma = 1$, and $\rho = 1$

CHAPTER 5

TWO DIMENSIONAL INVISCID COMPOUND JET FALLING UNDER GRAVITY

5.1 Introduction

In the previous chapter, we have performed the linear instability analysis of a two dimensional inviscid compound jet but we ignored the effects of gravity on the dynamics of the jet. Here, we will consider the same compound jet but we will investigate how gravity affects the behavior of the compound jet falling in a vertical direction. We start with the dimensionless equations found by Uddin [86] and Mohsin *et al.* [55] in which the dimensionless continuity and the Euler equations are given by

$$\frac{\partial u^{[z]}}{\partial x} + \varepsilon \frac{\partial w^{[z]}}{\partial r} + \frac{w^{[z]}}{r} = 0, \tag{5.1}$$

$$\frac{\partial u^{[z]}}{\partial t} + u^{[z]} \frac{\partial u^{[z]}}{\partial x} + \frac{w^{[z]}}{\varepsilon} \frac{\partial u^{[z]}}{\partial r} = -\frac{\rho^{[O]}}{\rho^{[z]}} \frac{\partial p^{[z]}}{\partial x} + \frac{1}{F^2} \tag{5.2}$$

and

$$\frac{\partial w^{[z]}}{\partial t} + u^{[z]}\frac{\partial w^{[z]}}{\partial x} + \frac{w^{[z]}}{\varepsilon}\frac{\partial w^{[z]}}{\partial r} = -\frac{\rho^{[O]}}{\rho^{[z]}}\frac{1}{\varepsilon}\frac{\partial p^{[z]}}{\partial r}, \tag{5.3}$$

where $z = I, O$. The dimensionless kinematic conditions, at the interface $r = R(x,t)$ and $r = S(x,t)$, are given by

$$w^{[z]} = \frac{\partial R}{\partial t} + u^{[z]}\frac{\partial R}{\partial x}, \tag{5.4}$$

where $z = I, O$ and

$$w^{[z]} = \frac{\partial S}{\partial t} + u^{[z]}\frac{\partial S}{\partial x}, \tag{5.5}$$

where $z = O$, respectively. The dimensionless normal stress conditions, at the interfaces $r = S(x,t)$ and $r = R(x,t)$, are

$$p^{[O]} = \frac{\kappa^{[I]}}{We}, \quad \text{where} \quad \kappa^{[I]} = \frac{\left(1 + \varepsilon^2\left(\frac{\partial S}{\partial x}\right)^2\right)^{-\frac{1}{2}}}{S} - \frac{\frac{\partial^2 S}{\partial x^2}}{\left(1 + \varepsilon^2\left(\frac{\partial S}{\partial x}\right)^2\right)^{\frac{3}{2}}} \tag{5.6}$$

and

$$p^{[I]} - p^{[O]} = \frac{\sigma\kappa^{[O]}]}{We}, \quad \text{where} \quad \kappa^{[O]} = \frac{\left(1 + \varepsilon^2\left(\frac{\partial R}{\partial x}\right)^2\right)^{-\frac{1}{2}}}{R} - \frac{\frac{\partial^2 R}{\partial x^2}}{\left(1 + \varepsilon^2\left(\frac{\partial R}{\partial x}\right)^2\right)^{\frac{3}{2}}} \tag{5.7}$$

respectively.

5.2 Steady State Solutions

We use the same set of steady state equations which we have discussed in chapter three (obtained using an asymptotic method). The steady state equations are given by

$$\frac{\partial}{\partial x}\left(R_0^2 u_0^{[I]}\right) = 0, \tag{5.8}$$

58

$$\frac{\partial}{\partial x}\left((S_0^2 - R_0^2)u_0^{[O]}\right) = 0, \tag{5.9}$$

$$u_0^{[I]}\frac{\partial u_0^{[I]}}{\partial x} = -\frac{1}{\rho We}\frac{\partial}{\partial x}\left(\frac{\sigma}{R_0} + \frac{1}{S_0}\right) + \frac{1}{F^2} \tag{5.10}$$

and

$$u_0^{[O]}\frac{\partial u_0^{[O]}}{\partial x} = -\frac{1}{We}\frac{\partial}{\partial x}\left(\frac{1}{S_0}\right) + \frac{1}{F^2}, \tag{5.11}$$

where $\sigma = \sigma^{[I]}/\sigma^{[O]}$ is the ratio of surface tension between inner and outer fluid interfaces, $We = \rho^{[O]}U^2 a/\sigma^{[O]}$ is the Weber number, $\rho = \rho^{[I]}/\rho^{[O]}$ is the density ratio of the inner fluid to the outer fluid and $F = U/\sqrt{Lg}$ is the Froude number, which gives a measure of the relative importance of gravitational forces. Equations $(5.8) - (5.11)$ are a system of nonlinear ordinary differential equations with unknowns $u_0^{[I]}$, $u_0^{[O]}$, R_0 and S_0. To solve this set of equations, we specify initial conditions at the nozzle, that is, $u_0^{[I]} = u_0^{[O]} = S_0 = 1$ and $R_0 = \chi$. By using the initial conditions and dropping subscripts zeros from the variables for ease of convenience, we integrate the system of equations and then apply Newton's method to obtain a spatially non-uniform steady state solution for the inviscid compound jet which falls vertically downwards under the influence of gravity. We present the steady state solutions, for various values of the Weber number, for the inner and outer radii of the compound jet in Fig. 5.1. We notice that an increase in the Weber number leads to slightly rapid decay of jet radii along the jet.

5.3   Linear Instability Analysis

We now consider the linear temporal instability analysis of an inviscid compound liquid jet falling under the influence of gravity. The evolution of the jet depends on the length scale $x = O(1)$, but the disturbances along the jet are much smaller and are comparable
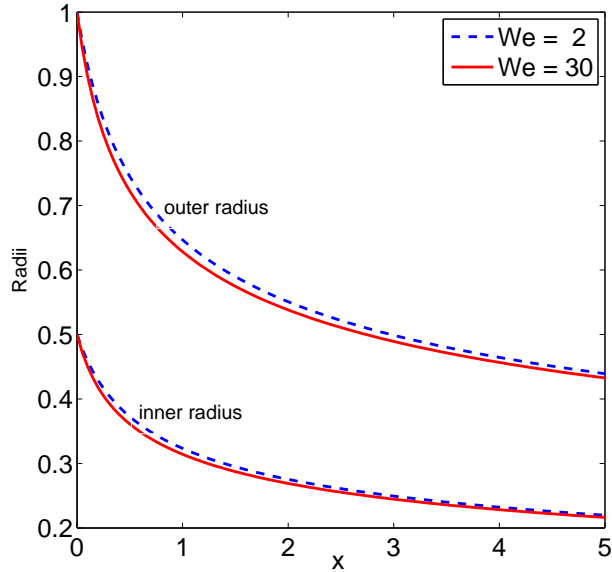
Figure 5.1: The steady state solutions for inner and outer jet radii for various Weber numbers. Other parameters are $\rho = 1$, $\sigma = 1$, $\chi = 0.5$ and $We = 100$.

to ε when $x = O(1)$. In other words, we can say that the disturbances are typically of the order of jet radius a. We consider the traveling short waves of the form $exp(ik\overline{x} + \lambda\overline{t})$, where $k = k(x) = O(1)$ and $\lambda = \lambda(x) = O(1)$ are the frequency and wavenumber of disturbances. Additionally, $\overline{x} = x/\varepsilon$ and $\overline{t} = t/\varepsilon$ are small length and time scales. Thus, we have a multiple scale formulation as the perturbations grow along the jet having wavelength of $O(\varepsilon)$. Now we introduce small time dependent perturbations to the steady state solutions which take the form

$$u^{[z]} = u_0^{[z]}(x) + \delta\overline{u^{[z]}}(r)\exp(\lambda\overline{t} + ik\overline{x}),$$ (5.12)

$$w^{[z]} = w_0^{[z]}(x) + \delta\overline{w^{[z]}}(r)\exp(\lambda\overline{t} + ik\overline{x}),$$ (5.13)

$$p^{[z]} = p_0^{[z]}(x) + \delta\overline{p^{[z]}}(r)\exp(\lambda\overline{t} + ik\overline{x}),$$ (5.14)

60

$$R = R_0(x) + \delta\overline{R}\exp(\lambda\overline{t} + ik\overline{x}), \tag{5.15}$$

$$S = S_0(x) + \delta\overline{S}\exp(\lambda\overline{t} + ik\overline{x}). \tag{5.16}$$

where $0 < \delta << \varepsilon$. We substitute the expansions $(5.12) - (5.16)$ into the equations $(5.1) - (5.7)$ yield at leading order, or $O(\delta/\varepsilon)$,

$$ik\overline{u^{[z]}} + \frac{\partial\overline{w^{[z]}}}{\partial r} + \frac{\overline{w^{[z]}}}{r} = 0, \tag{5.17}$$

$$(\lambda + iku_0^{[z]})\overline{u}^{[z]} = -\left((\delta_{\mathbf{Iz}})\frac{1}{\rho} + \delta_{\mathbf{Oz}}\right)\overline{p^{[z]}}ik, \tag{5.18}$$

$$(\lambda + iku_0^{[z]})\overline{w}^{[z]} = -\left((\delta_{\mathbf{Iz}})\frac{1}{\rho} + \delta_{\mathbf{Oz}}\right)\frac{\partial\overline{p^{[z]}}}{\partial r}, \tag{5.19}$$

$$\overline{w^{[z]}} = (\lambda + iku^{[z]})\overline{R} \quad \text{for} \quad z = I, O, \tag{5.20}$$

$$\overline{w^{[z]}} = (\lambda + iku_0^{[z]})\overline{S} \quad \text{for} \quad z = O, \tag{5.21}$$

$$\overline{p^{[I]}} - \overline{p^{[O]}} = \frac{\sigma}{We}\left(k^2 - \frac{1}{R_0^2}\right)\overline{R}, \tag{5.22}$$

$$\overline{p^{[O]}} = \frac{1}{We}\left(k^2 - \frac{1}{S_0^2}\right)\overline{S}, \tag{5.23}$$

where $\delta_{\mathbf{Iz}}$ is the Kronecker delta symbol with free index z. Using (5.18) and (5.19) to eliminate $\overline{p^{[z]}}$ we get $\overline{w^{[z]}} = \frac{1}{ik}\frac{\partial \overline{u^{[z]}}}{\partial r}$ and substituting this result in (5.17), we have

$$\frac{\partial^2 \overline{u^{[z]}}}{\partial r^2} + \frac{1}{r}\frac{\partial \overline{u^{[z]}}}{\partial r} - k^2 \overline{u^{[z]}} = 0, \tag{5.24}$$

which has solution

$$\overline{u}^{[z]} = C^{[z]} I_0(kr) + D^{[z]} K_0(kr). \tag{5.25}$$

By using the value of $\overline{u}^{[z]}$, we are able to get

$$\overline{w}^{[z]} = \frac{1}{i}(C^{[z]} I_1(kr) - D^{[z]} K_1(kr)). \tag{5.26}$$

By using (5.18) in (5.25), yields

$$\overline{p}^{[z]} = \frac{-(\lambda + ik)u_0^{[z]}}{ik((\delta_{Iz})\rho + \delta_{\mathbf{Oz}})}(C^{[z]} I_0(kr) + D^{[z]} K_0(kr)), \tag{5.27}$$

where $I_0(kr)$, $I_1(kr)$ and $K_0(kr)$, $K_1(kr)$ are the modified Bessel functions of first and second kind respectively. To avoid the singularities, and to ensure finite values at $r = 0$, we require that $D^{[I]}$ will be equal to zero. Substituting the values of $\overline{w}^{[z]}$ in (5.20) and (5.21), yield

$$\frac{1}{i}(C^{[I]} I_1(kR_0) - D^{[I]} K_1(kR_0)) = (\lambda + iku_0^{[I]})\overline{R}, \tag{5.28}$$

$$\frac{1}{i}(C^{[O]} I_1(kR_0) - D^{[O]} K_1(kR_0)) = (\lambda + iku_0^{[O]})\overline{R}, \tag{5.29}$$

$$\frac{1}{i}(C^{[O]}I_1(kS_0) - D^{[O]}K_1(kS_0)) = (\lambda + iku_0^{[O]})\overline{S}. \tag{5.30}$$

Similarly, using the values of $\bar{p}^{[z]}$ from equation (5.27) in equations (5.22) and (5.23), we get

$$\frac{-(\lambda + iku_0^{[I]})}{ik\rho}(C^{[I]}I_0(kR_0)) + \frac{(\lambda + iku_0^{[O]})}{ik}(C^{[O]}I_0(kR_0) + D^{[O]}K_0(kR_0)) \tag{5.31}$$

$$= \frac{\sigma}{We}(k^2 - \frac{1}{R_0^2})\overline{R},$$

$$\frac{-(\lambda + iku_0^{[O]})}{ik}(C^{[O]}I_0(kR_0) + D^{[O]}K_0(kR_0)) = \frac{1}{We}(k^2 - \frac{1}{S_0^2})\overline{S}. \tag{5.32}$$

By eliminating the $C^{[I]}, C^{[O]}, D^{[O]}, \overline{R}$ and $\overline{S}$ from equations $(5.28) - (5.32)$ and removing subscripts from $u_0^{[I]}, u_0^{[O]}, R_0$, and S_0 for ease of convenience, we are able to arrive (after lengthy algebra) at following dispersion relation:

$$\frac{\lambda'^4}{k^2} \left[(I_1(kR)K_1(kS)I_0(kS)K_0(kR) - I_1(kR)I_0(kR)K_0(kS)K_1(kS)) \right.$$

$$\left. + \rho \left(K_1(kR)I_0(kS)I_0(kR)K_1(kS) + I_1(kR)K_1(kS)K_0(kS)I_0(kR)) \right] + \right.$$

$$\frac{\lambda'^3}{k} \left[2i\rho a_1(K_1(kR)I_0(kR)I_0(kS)K_1(kS) - I_1(kS)K_0(kS)K_1(kS)I_0(kR)) \right] +$$

$$\frac{\lambda'^2}{kWe} \left[\beta \left(I_1(kR)K_1(kR)K_1(kS)I_0(kS) + I_1(kR)I_1(kR)K_1(kS)K_0(kS)) \right. \right.$$

$$\left. + \rho \, \alpha \, (K_1(kR)K_1(kS)I_0(kR)I_1(kS) + I_1(kR)I_0(kR)K_1(kS)K_1(kS)) + \right.$$

63

$$\alpha\ (\ I_1(kR)I_0(kR)K_1(kS)K_1(kS) + I_1(kR)K_0(kR)K_1(kS)I_1(kS)\ ) - We$$

$$\rho\ a_1^2\ k(I_1(kR)K_1(kS)K_0(kS)I_0(kR) + K_1(kR)I_0(kR)I_0(kS)K_1(kS))\ ] -$$

$$\frac{2i\lambda'}{We}[a_1\rho\alpha(K_1(kS)K_1(kR)I_1(kS)I_0(kR) - I_1(kR)K_1(kS)K_1(kS)I_0(kR))\ ]$$

$$+\frac{\alpha\beta}{We^2}\ (I_1(kR)K_1(kR)I_I(kS)K_1(kS) - I_1(kS)I_0(kR)K_1(kR)K_1(kS)) +$$

$$\frac{\rho\alpha k a_1^2}{We}\ (K_1(kS)I_1(kR)I_0(kR)K_1(kS) - I_1(kS)K_1(kR)I_0(kR)K_1(kS))\ =\ 0. \quad (5.33)$$

In the above dispersion relation, we have

$$a_1 = (u^{[I]} - u^{[O]}), \quad \alpha\ =\ k^2 - \tfrac{1}{S^2}, \quad \beta\ =\ \sigma\ (k^2 - \tfrac{1}{R^2})$$

and $\lambda' = \lambda + iku^{[O]}$. If we take the long wavelength limit of (5.33) that is $k \longrightarrow 0$, we obtain the following eigenvalue relation:

$$[4RS]\lambda'^4 - [8RS(ik(u^{[O]} - u^{[I]}))]\lambda'^3$$

$$+\left[\frac{2ikR^3}{\rho We}\left(\frac{ik}{S^2} - ik^3\right) + \sigma S\left(\frac{ik}{R^2} - ik^3\right) - (4RS(ik(u^{[O]} - u^{[I]}))^2)\right]\lambda'^2$$

$$+\left[\frac{2ikR(\frac{ik}{S^2} - ik^3)}{We}(S^2 - R^2)\right]\lambda'^2 + \left[\frac{4k^2R(\frac{ik}{S^2} - ik^3)(u^{[O]} - u^{[I]})}{We}(S^2 - R^2)\right]\lambda'$$
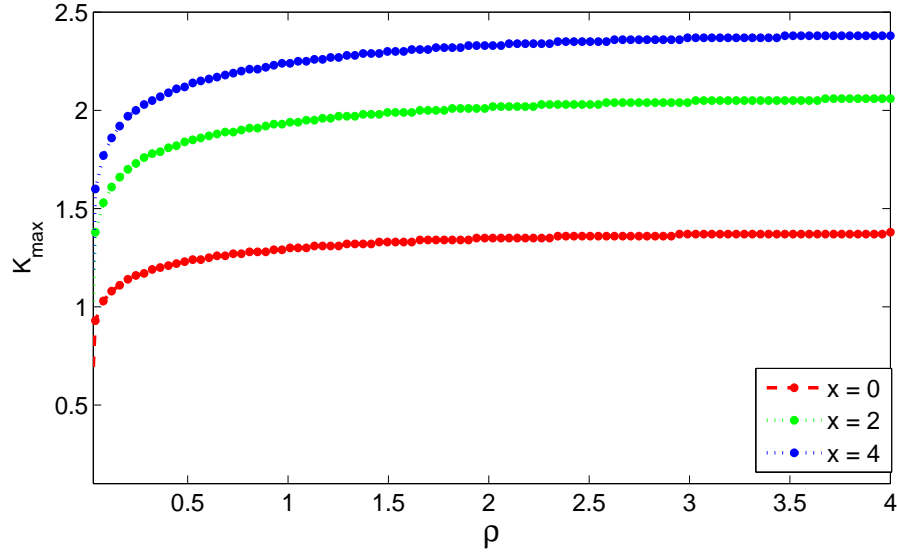
Figure 5.2: Maximum wavenumber versus surface density ratios at different locations of the compound jet. The other parameters are $We = 10$, $\sigma = 1$, $F = 1$ and $\chi = 0.5$

$$+\frac{R(\frac{ik}{S^2} - ik^3)}{We}\left(2k^2(u^{[O]} - u^{[I]}))^2 - \frac{\sigma k^2 R(\frac{ik}{R^2} - ik^3)}{\rho We}\right)(S^2 - R^2) = 0. \qquad (5.34)$$

We note that (5.34) is identical to the dispersion relation found by the author [55].

5.4   Results and discussion

The dispersion relation (5.33) can be solved with the help of Muller's method [58]. The coefficients of this equation depend on x which is axial distance along the compound jet. It is generally known that there is a wavenumber k which corresponds to the maximum value of the growth rate of disturbances and we call it most unstable mode K_{max}. This is the wavenumber where liquid jet breakup and we can find droplet size by the help of this value of wavenumber. In this analysis, we will see how gravity alters the most unstable mode and the maximum growth rate of disturbance of a two dimensional compound liquid jet.

65
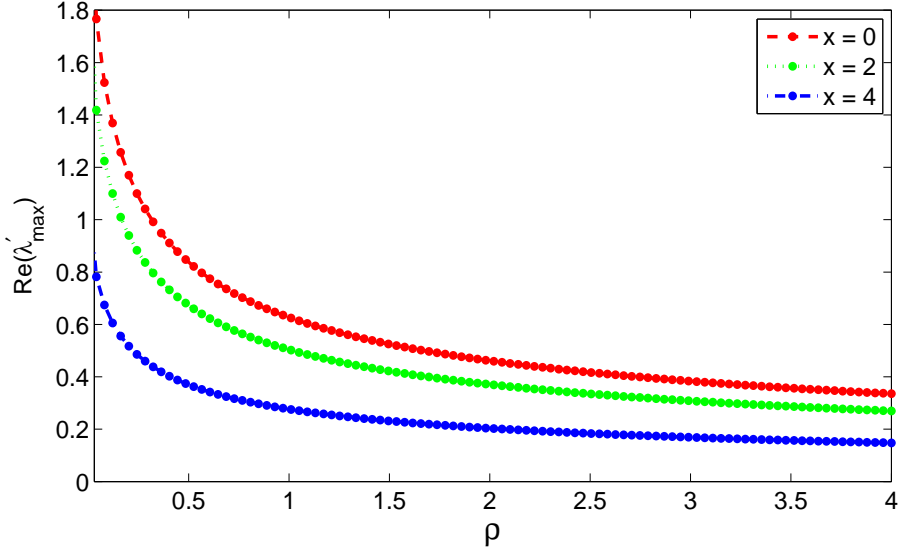
Figure 5.3: Maximum growth rate of disturbances versus surface density ratios at different locations of the compound jet. The other parameters are $We = 10$, $\sigma = 1$, $F = 1$ and $\chi = 0.5$

As the compound jet is accelerating in the vertical direction, therefore steady state solutions are the function of x that is axial distance along the jet. Hence, the coefficients of dispersion relation are affected as we move down the jet and obviously it will have a strong influence on the breakup and the droplet size.

To examine the impact of gravity on the surface of compound jet, we display the maximum wavenumber and maximum growth rate for the given values of density ratio ρ at different location of the jet in the Figs. 5.2 and 5.3 respectively. It is observed that the maximum wavenumber always increases gradually along the jet as we increase the density ratio ρ but an increase in ρ leads to decrease the maximum growth rate of disturbances. We show the similar graphs for the given values of the surface tension ratio σ in Figs. 5.4 and Fig. 5.5.

We find the large difference in the maximum wavenumber which is due to competing mode propagating along the jet as discussed in chapter three. It can be seen that there is a jump in the values of the maximum wavenumber K_{max} at $\sigma = 0.23$, and K_{max} increases
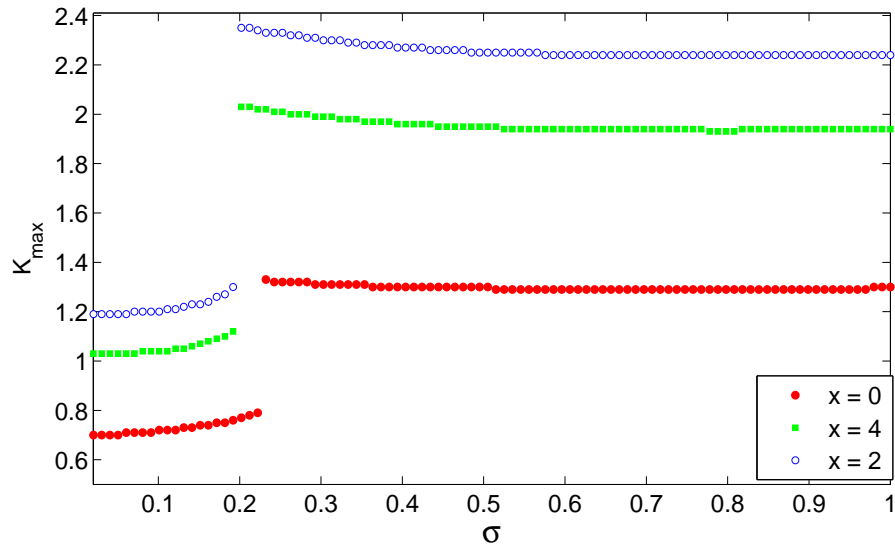
Figure 5.4: Maximum wavenumber versus surface tension ratios at different locations of the compound jet. The other parameters are $We = 10$, $\rho = 1$, $F = 1$ and $\chi = 0.5$
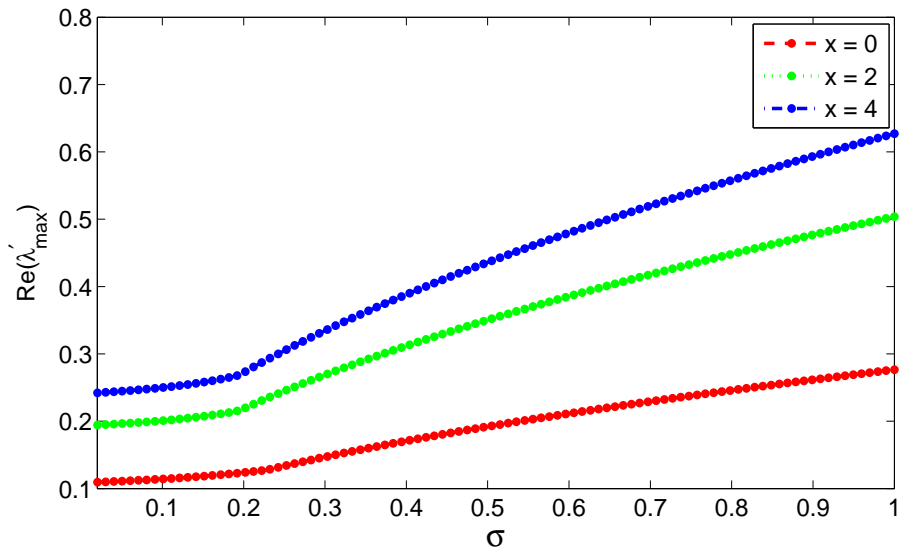
Figure 5.5: Maximum growth rate of disturbances versus surface tension ratios at different locations of the compound jet. The other parameters are $We = 10$, $\rho = 1$, $F = 1$ and $\chi = 0.5$
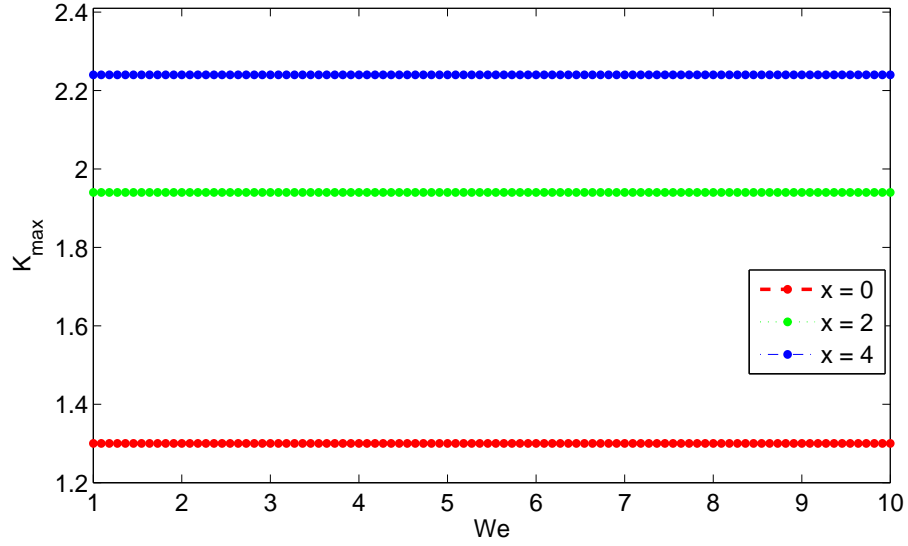
Figure 5.6: Maximum wavenumber versus Weber number at different locations of the compound jet. The other parameters are $\sigma = 1$, $\rho = 1$, $F = 1$ and $\chi = 0.5$

when $\sigma < 0.23$ and it decrease slightly when $\sigma > 0.23$. The trend is similar for all values of x. The growth rate of disturbance λ_{max} increases with σ and x. We also perform the same analysis for the case of Weber number in Figs. 5.6 and 5.7. We observe that the maximum wavenumber is unchanged by varying the Weber number and there is reduction in the maximum value of the growth rate as we increase the Weber number. The maximum growth rate together with most unstable wavenumber increase with the axial distance x.

In Figs. 5.8 and 5.9, we show the maximum wavenumber and its associated maximum growth rate of disturbances for two different values of the surface tension ratio σ against the axial length of the jet respectively. It is found that the maximum wavenumber and its associated maximum growth rate increase along the jet and produce the same effects as we increase σ. The maximum wavenumber versus the axial length of the jet for two different values of ρ is shown in Fig. 5.10, and similarly the maximum growth rate of disturbances versus axial length of the jet is depicted in Fig. 5.11. Here, it is clearly notice that the maximum wavenumber and its associated maximum growth rate increase

68
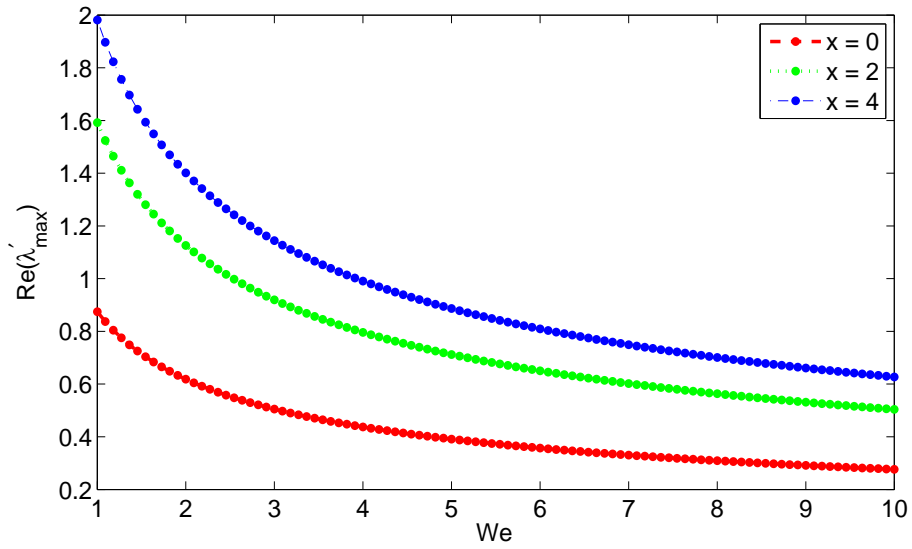
Figure 5.7: Maximum growth rate of disturbances versus Weber number at different locations of the compound jet. The other parameters are $\sigma = 1$, $\rho = 1$, $F = 1$ and $\chi = 0.5$
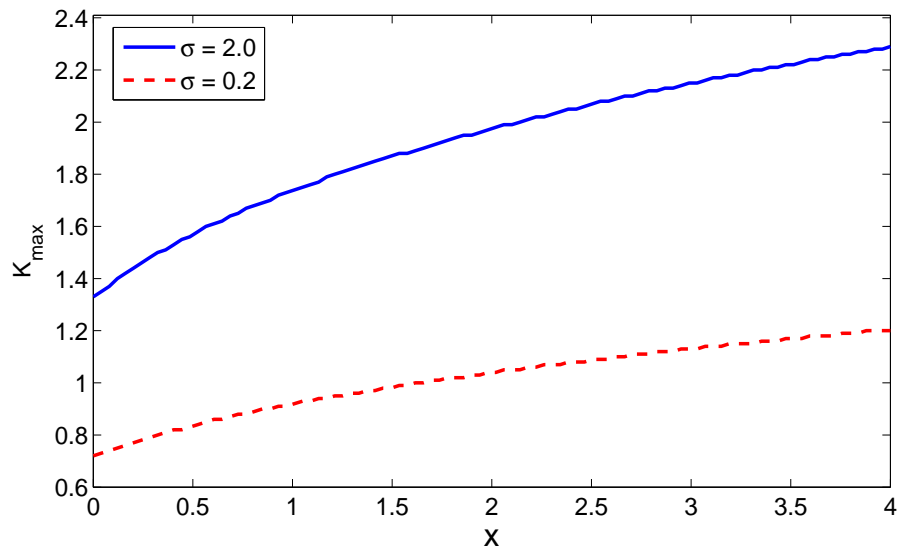
Figure 5.8: Maximum wavenumber versus the axial length of the jet for two different surface tension ratios. The other parameters are $We = 10$, $\rho = 1$, $F = 1$ and $\chi = 0.5$
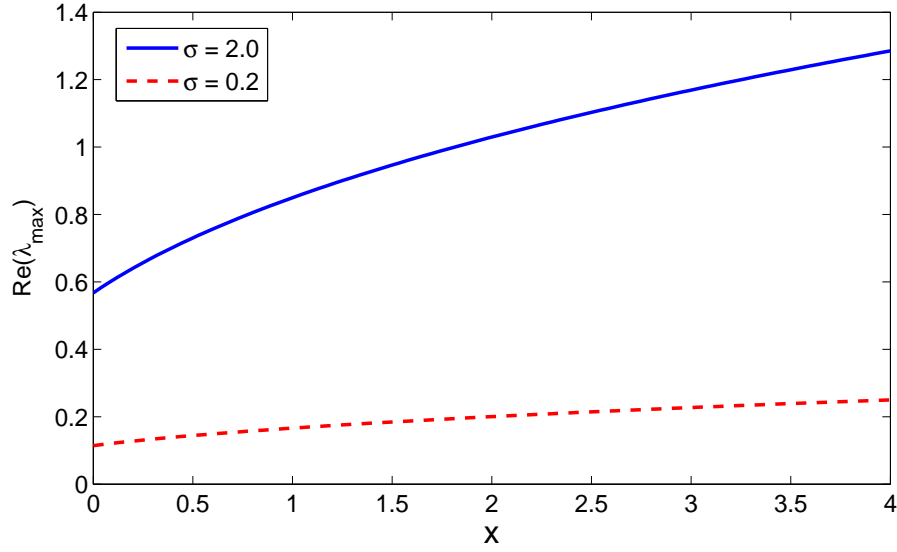
Figure 5.9: Maximum growth rate of disturbances versus the axial length of the jet for two different surface tension ratios. The other parameters are $We = 10$, $\rho = 1$, $F = 1$ and $\chi = 0.5$

along the jet and the most unstable wavenumber increases with the increase in ρ, while the the maximum value of growth rate of disturbances decreases by increasing the inner to outer density ratio ρ. Therefore, we can say that there will be smaller droplets if we increase the density ratio and longer jet are produced if the density ratio ρ between the fluids is higher. From the Figs. 5.12 and 5.13, we can see that the values of the maximum wavenumber and the maximum growth rate increase by decreasing the radii ratio χ and increase along the jet. It is important to note that in all these figures the curves corresponding to $x = 0$ is equivalent to the zero-gravity case and therefore the influence of gravity can be seen in comparison.

Finally, we will use the results of our linear instability analysis and aim to determine the profile of waves traveling along the inner and outer interface to investigate the breakup lengths of inviscid compound jet falling under gravity. In order to find the breakup length, we require time t which we will obtain by integrating the inverse of steady state velocities (in equations $(5.10) - (5.11)$) over the entire length of compound jet. Mathematically
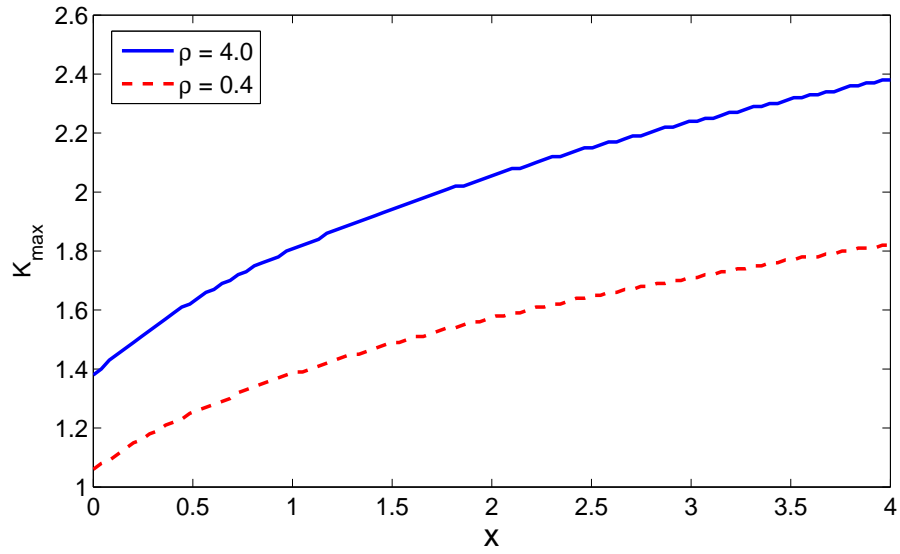
Figure 5.10: Maximum wavenumber versus the axial length of the jet for two different density ratios. The other parameters are $We = 10$, $\sigma = 1$, $F = 1$ and $\chi = 0.5$
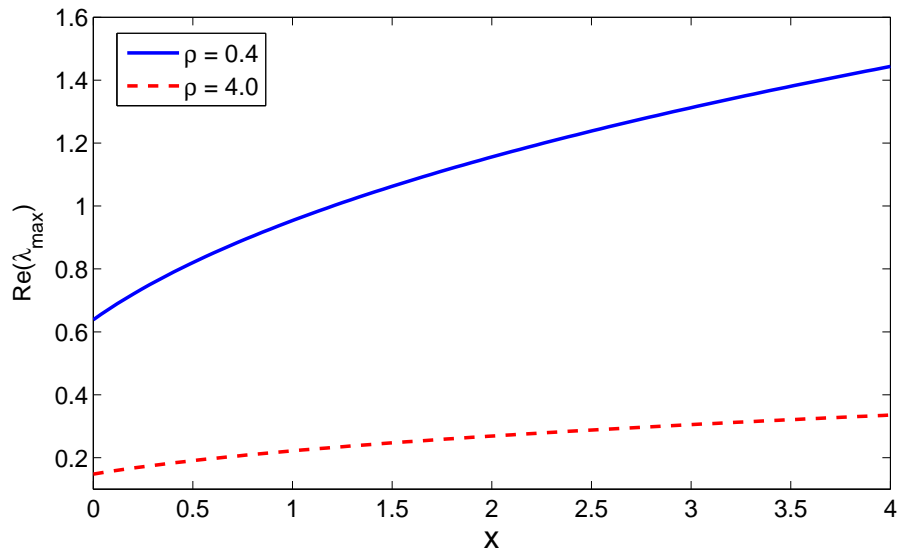
Figure 5.11: Maximum growth rate of disturbances versus the axial length of the jet for two different density ratios. The other parameters are $We = 10$, $\sigma = 1$, $F = 1$ and $\chi = 0.5$
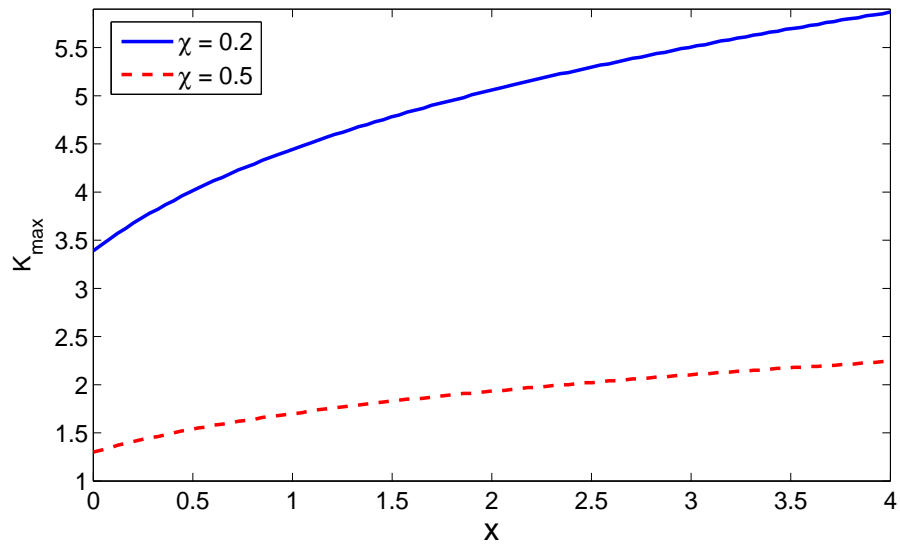
Figure 5.12: Maximum wavenumber versus the axial length of the jet for two different radii ratios. The other parameters are $We = 10$, $\rho = 1$, $F = 1$ and $\sigma = 1$
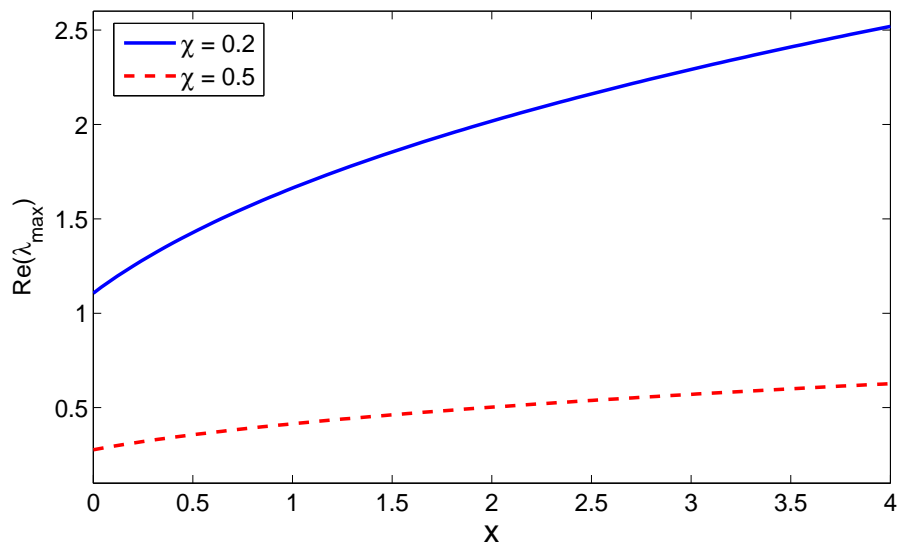
Figure 5.13: Maximum growth rate of disturbances versus the axial length of the jet for two different radii ratios. The other parameters are $We = 10$, $\rho = 1$, $F = 1$ and $\sigma = 1$

it can be expressed as $t = \int_0^x \frac{1}{u(s)} ds$. This integral will be solved with the help of the Trapezoidal rule in MATLAB. Using the results obtained in previous section to plot R and S and choosing a value for ε and δ, we can determine the breakup length l_b. The breakup length is the location of the compound jet where, either inner and outer interface touch or inner radius R approaches to zero. The profiles of the compound jet falling under gravity have been shown in Fig. 5.14. The first profile is the example of inner jet breakup where the inner radius R reaches to zero, while the second profile depicts the outer jet breakup because in this case, instead of inner radius R approaches to zero, the outer interface meets with inner one. The breakup lengths l_b are determined by varying χ for two different values of the Weber number and manifested in Fig. 5.15. It is observed that breakup length increases with the increase in χ and decreases by decreasing the Weber number. We also notice the qualitative change in the jet breakup that we have outer jet breakup and the reason for this fact is the formation of neck which allow outer interface to meet with inner interface. We can compare our results to the breakup lengths obtained by the author [55]. Particularly, at $\rho = 1$, $\sigma = 1$, $F = 1$, $\delta = 0.002$, $\varepsilon = 0.01$, $\chi = 0.6$ and $We = 20$, the breakup length was found $l_b = 42$ (see Fig. 3.4). In this analysis, using the same parameter values, the breakup length we have $l_b = 45$ which seems to be a good agreement. There is small difference in breakup length because we consider two dimensional compound jet as compare to the one dimensional model. Therefore, we can say that our results are more accurate due to the addition of flow in a radial direction of the compound jet. As we know that the liquid jet breakup is inherently nonlinear phenomena, therefore linear theory cannot provide the accurate picture of later stages of breakup but it provides a good prediction of breakup lengths and breakup times [26].
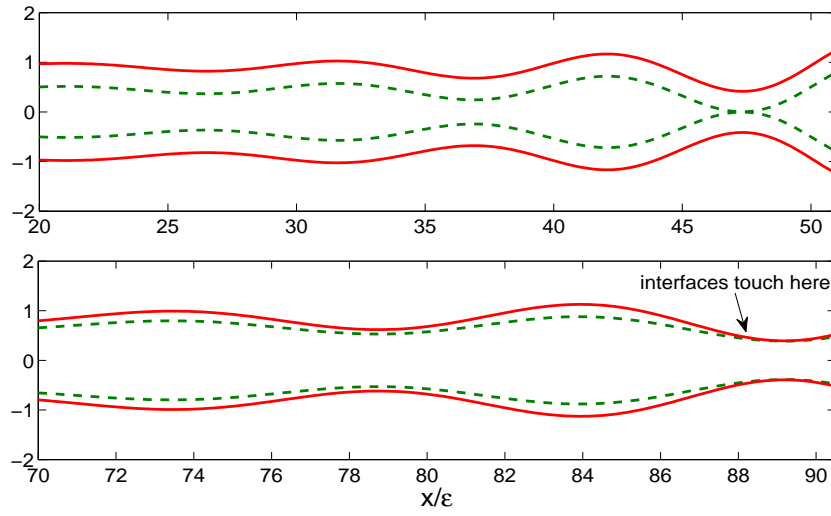
Figure 5.14: Profiles of an inviscid compound jet. The parameters used here are $\chi = 0.62$ (*first*), $\chi = 0.88$ (*second*), $\sigma = 1$, $\varepsilon = 0.01$, $\rho = 1$, $F = 1$, $We = 20$ and $\delta = 0.002$
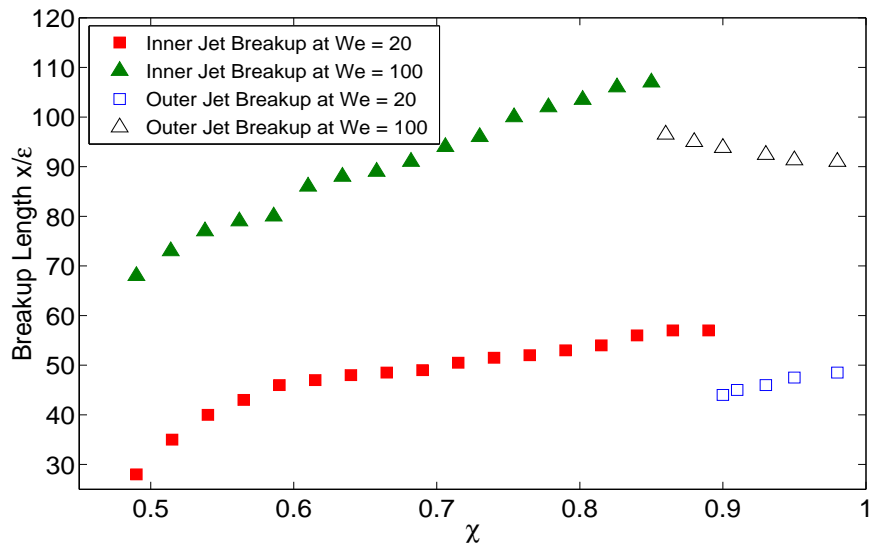
Figure 5.15: Theoretical breakup lengths of compound jet. The parameters used here are $\sigma = 1$, $\varepsilon = 0.01$, $\rho = 1$, $F = 1$ and $\delta = 0.002$

CHAPTER 6

INVISCID COMPOUND JET MOVING IN AN

AMBIENT GAS

The instability of an inviscid axisymmetric two dimensional uniform compound jet moving in a surrounding will be discussed in this chapter. We will see how the density of a surrounding gas modifies the dynamics of a compound jet, in particular the growth rate of unstable waves. Firstly, we formulate the governing equations of the compound jet in the presence of surrounding gas and then we will determine the linear stability of the resulting set of equations.

6.1 Problem Formulation

We consider an inviscid axisymmetric compound jet which emerges from a concentric tube with the exit velocity U and moves in a surrounding gas. The outer radius of the compound jet is denoted by a and the inner radius is denoted by χa, where $0 < \chi < 1$. It is assumed that the compound jet, after issuing from a circular orifice, falls in a vertical direction. It is also assumed that all the fluids are incompressible and immiscible. The geometry of the compound jet is described in a cylindrical coordinate system (r, θ, x), where r is the radial component, θ is an azimuthal component and x is the length of the jet. As we are

assuming axisymmetric flow, the azimuthal components are taken to be zero. Therefore, the velocity vector describing the flow can be written as $\mathbf{u}^{[z]} = (w^{[z]}, 0, u^{[z]})$, where the superscript $z = I, O$ and A refer to the inner fluid, the outer fluid and the surrounding gas respectively. Here we denote $r = R(x, t)$ as the interface of the inner fluid with the outer one, $r = S(x, t)$ as the interface of outer fluid with the surrounding gas, $\sigma^{[I]}$ is the surface tension at the interface $r = R(x, t)$ and $\sigma^{[O]}$ is the surface tension at the interface $r = S(x, t)$. The density of the fluids is denoted by $\rho^{[z]}$, and the pressure and the time are denoted as $p^{[z]}$ and t respectively. In addition, the surface tensions $\sigma^{[I]}$ and $\sigma^{[O]}$ are assumed to be constant at the inner and the outer interface respectively.

The continuity equation and the momentum equation, which describe the resulting dynamics of the compound jet, are given by

$$\frac{\partial u^{[z]}}{\partial x} + \frac{\partial w^{[z]}}{\partial r} + \frac{w^{[z]}}{r} = 0, \tag{6.1}$$

$$\frac{\partial u^{[z]}}{\partial t} + u^{[z]}\frac{\partial u^{[z]}}{\partial x} + w^{[z]}\frac{\partial u^{[z]}}{\partial r} = -\frac{1}{\rho^{[z]}}\frac{\partial p^{[z]}}{\partial x} \tag{6.2}$$

and

$$\frac{\partial w^{[z]}}{\partial t} + u^{[z]}\frac{\partial w^{[z]}}{\partial x} + w^{[z]}\frac{\partial w^{[z]}}{\partial r} = -\frac{1}{\rho^{[z]}}\frac{\partial p^{[z]}}{\partial r}. \tag{6.3}$$

These equations are supplemented by the kinematic conditions and the normal stress conditions. The kinematic conditions, at the interface $r = R(x, t)$, are given by

$$w^{[z]} = \frac{\partial R}{\partial t} + u^{[z]}\frac{\partial R}{\partial x}, \tag{6.4}$$

where $z = I, O$. Similarly, the kinematic conditions, at the interface $r = S(x, t)$, are given by

$$w^{[z]} = \frac{\partial S}{\partial t} + u^{[z]} \frac{\partial S}{\partial x}, \tag{6.5}$$

where $z = O, A$. For inviscid fluids, we have the classical free surface condition of constant pressure and hence zero tangential stress condition. The normal stress conditions, at the interfaces $r = R(x, t)$ and $r = S(x, t)$, are

$$p^{[I]} - p^{[O]} = \sigma^{[I]} \kappa^{[I]} \tag{6.6}$$

and

$$p^{[O]} - p^{[A]} = \sigma^{[O]} \kappa^{[O]}, \tag{6.7}$$

respectively, where $\kappa^{[I]}$ is the curvature of the inner free surface and $\kappa^{[O]}$ is the curvature of the outer free surface, which are given by

$$\kappa^{[I]} = \frac{\left(1 + \left(\frac{\partial R}{\partial x}\right)^2\right)^{-\frac{1}{2}}}{R} - \frac{\frac{\partial^2 R}{\partial x^2}}{\left(1 + \left(\frac{\partial R}{\partial x}\right)^2\right)^{\frac{3}{2}}}, \tag{6.8}$$

$$\kappa^{[O]} = \frac{\left(1 + \left(\frac{\partial S}{\partial x}\right)^2\right)^{-\frac{1}{2}}}{S} - \frac{\frac{\partial^2 S}{\partial x^2}}{\left(1 + \left(\frac{\partial S}{\partial x}\right)^2\right)^{\frac{3}{2}}}. \tag{6.9}$$

We can non-dimensionalize the velocity components with the initial jet velocity U at the tube exit, that is $\overline{w}^{[z]} = w^{[z]}/U$ and $\overline{u}^{[z]} = u^{[z]}/U$, the radial length with the outer jet radius a $\overline{r} = r/a$ and the axial length with a characteristic wavelength L in the axial direction $\overline{x} = x/L$. The time and the pressure are scaled by $\overline{t} = tU/L$ and $\overline{p}^{[z]} = p^{[z]}/\rho^{[O]} U^2$ respectively. By assuming the jet is slender, we define a small parameter ε as

$\varepsilon = a/L << 1$. The dimensionless forms of inner and outer radii of the jet at the nozzle are $R(0, t) = \chi$ and $S(0, t) = 1$ respectively. After dropping the overbars, the resulting dimensionless continuity and Euler equations can be written as

$$\frac{\partial u^{[z]}}{\partial x} + \varepsilon \frac{\partial w^{[z]}}{\partial r} + \frac{w^{[z]}}{r} = 0, \tag{6.10}$$

$$\frac{\partial u^{[z]}}{\partial t} + u^{[z]} \frac{\partial u^{[z]}}{\partial x} + \frac{w^{[z]}}{\varepsilon} \frac{\partial u^{[z]}}{\partial r} = -\frac{\rho^{[O]}}{\rho^{[z]}} \frac{\partial p^{[z]}}{\partial x} \tag{6.11}$$

and

$$\frac{\partial w^{[z]}}{\partial t} + u^{[z]} \frac{\partial w^{[z]}}{\partial x} + \frac{w^{[z]}}{\varepsilon} \frac{\partial w^{[z]}}{\partial r} = -\frac{\rho^{[O]}}{\rho^{[z]}} \frac{1}{\varepsilon} \frac{\partial p^{[z]}}{\partial r}. \tag{6.12}$$

The dimensionless kinematic conditions, at the interface $r = R(x, t)$ and $r = S(x, t)$, are given by

$$w^{[z]} = \frac{\partial R}{\partial t} + u^{[z]} \frac{\partial R}{\partial x}, \tag{6.13}$$

where $z = I, O$ and

$$w^{[z]} = \frac{\partial S}{\partial t} + u^{[z]} \frac{\partial S}{\partial x}, \tag{6.14}$$

where $z = O, A$, respectively. The dimensionless normal stress conditions, at the interfaces $r = S(x, t)$ and $r = R(x, t)$, are

$$p^{[O]} - \rho^G p^{[A]} = \frac{\kappa^{[I]}}{We}, \quad \text{where} \quad \kappa^{[I]} = \frac{\left(1 + \varepsilon^2 \left(\frac{\partial S}{\partial x}\right)^2\right)^{-\frac{1}{2}}}{S} - \frac{\frac{\partial^2 S}{\partial x^2}}{\left(1 + \varepsilon^2 \left(\frac{\partial S}{\partial x}\right)^2\right)^{\frac{3}{2}}} \tag{6.15}$$

78

and

$$p^{[I]} - p^{[O]} = \frac{\sigma \kappa^{[O]}}{We}, \quad \text{where} \quad \kappa^{[O]} = \frac{\left(1 + \varepsilon^2 \left(\frac{\partial R}{\partial x}\right)^2\right)^{-\frac{1}{2}}}{R} - \frac{\frac{\partial^2 R}{\partial x^2}}{\left(1 + \varepsilon^2 \left(\frac{\partial R}{\partial x}\right)^2\right)^{\frac{3}{2}}} \tag{6.16}$$

respectively. Here $\sigma = \sigma^{[I]}/\sigma^{[O]}$ is the ratio of surface tension between inner and outer fluid interfaces, $\rho^G = \rho^{[A]}/\rho^{[O]}$ is the density ratio of gas to the outer fluid, $We = \rho^{[O]}U^2 a/\sigma^{[O]}$ is the Weber number and $\rho = \rho^{[I]}/\rho^{[O]}$ is the density ratio of the inner fluid to the outer fluid. The steady states of inner and outer fluid are $(0, 0, 1)$ and for the surrounding gas is $(0, 0, 0)$, which means $S_0 = 1$ and $R_0 = \chi$.

6.2 Linear Instability Analysis

We now perform the linear temporal instability analysis of an inviscid compound liquid jet moving in a surrounding gas. We therefore introduce small time dependent perturbations to the steady state which take the form

$$u^{[z]} = (\delta_{\mathbf{Iz}} + \delta_{\mathbf{Oz}})1 + \delta \overline{u^{[z]}}(r) \exp(\lambda \bar{t} + ik\bar{x}), \tag{6.17}$$

$$w^{[z]} = 0 + \delta \overline{w^{[z]}}(r) \exp(\lambda \bar{t} + ik\bar{x}), \tag{6.18}$$

$$p^{[z]} = p_0^{[z]}(x) + \delta \overline{p^{[z]}}(r) \exp(\lambda \bar{t} + ik\bar{x}), \tag{6.19}$$

$$R = \chi + \delta \overline{R} \exp(\lambda \bar{t} + ik\bar{x}), \tag{6.20}$$

79

$$S = 1 + \delta \overline{S} \exp(\lambda \overline{t} + ik\overline{x}). \tag{6.21}$$

where $0 < \delta << \varepsilon$. Substituting the expansions $(6.17)-(6.21)$ into the non-dimensionalized form of equations $(6.10) - (6.16)$ yields at leading order, or $O(\delta/\varepsilon)$,

$$ik\overline{u^{[z]}} + \frac{\partial \overline{w^{[z]}}}{\partial r} + \frac{\overline{w^{[z]}}}{r} = 0, \tag{6.22}$$

$$(\lambda + ik(\delta_{\mathbf{Iz}} + \delta_{\mathbf{Oz}}))\overline{u^{[z]}} = -((\delta_{\mathbf{Iz}})\frac{1}{\rho} + (\delta_{\mathbf{Az}})\frac{1}{\rho^G} + \delta_{\mathbf{Oz}})\overline{p^{[z]}}ik, \tag{6.23}$$

$$(\lambda + ik(\delta_{\mathbf{Iz}} + \delta_{\mathbf{Oz}}))\overline{w^{[z]}} = -((\delta_{\mathbf{Iz}})\frac{1}{\rho} + (\delta_{\mathbf{Az}})\frac{1}{\rho^G} + \delta_{\mathbf{Oz}})\frac{\partial \overline{p^{[z]}}}{\partial r}, \tag{6.24}$$

$$\overline{w^{[z]}} = (\lambda + iku)\overline{R} \quad \text{for} \quad z = I, O, \tag{6.25}$$

$$\overline{w^{[z]}} = (\lambda + ik\delta_{\mathbf{Oz}})\overline{S} \quad \text{for} \quad z = O, A, \tag{6.26}$$

$$\overline{p^{[I]}} - \overline{p^{[O]}} = \frac{\sigma}{We}\left(k^2 - \frac{1}{R_0^2}\right)\overline{R}, \tag{6.27}$$

$$\overline{p^{[O]}} - \overline{p^{[A]}} = \frac{1}{We}\left(k^2 - \frac{1}{S_0^2}\right)\overline{S}. \tag{6.28}$$

where $\delta_{\mathbf{Iz}}$, $\delta_{\mathbf{Oz}}$ and $\delta_{\mathbf{Az}}$ are the Kronecker delta symbols with free index z.

Using (6.23) and (6.24) to eliminate $\overline{p^{[z]}}$ we get $\overline{w^{[z]}} = \frac{1}{ik}\frac{\partial \overline{u^{[z]}}}{\partial r}$ and substituting this

result in (6.22), we have

$$\frac{\partial^2 \overline{u^{[z]}}}{\partial r^2} + \frac{1}{r}\frac{\partial \overline{u^{[z]}}}{\partial r} - k^2 \overline{u^{[z]}} = 0, \tag{6.29}$$

which has solution

$$\overline{u}^{[z]} = C^{[z]} I_0(kr) + D^{[z]} K_0(kr). \tag{6.30}$$

By using the value of $\overline{u}^{[z]}$, we are able to get

$$\overline{w}^{[z]} = \frac{1}{i}(C^{[z]} I_1(kr) - D^{[z]} K_1(kr)). \tag{6.31}$$

By using (6.23) in (6.30), yields

$$\overline{p}^{[z]} = \frac{-(\lambda + ik(\delta_{\mathbf{Iz}} + \delta_{\mathbf{Oz}}))}{ik(\delta_{Iz}\rho + \delta_{Az}\rho^G + \delta_{\mathbf{Oz}})}(C^{[z]} I_0(kr) + D^{[z]} K_0(kr)), \tag{6.32}$$

where $I_0(kr)$ and $K_0(kr)$ are the modified Bessel functions of first and second kind respectively. To avoid the singularities, and to ensure finite values at $r = 0$, we require that $D^{[I]}$ and $C^{[A]}$ will be equal to zero.

Substituting the values of $\overline{w}^{[z]}$ in (6.25) and (6.26) yield

$$\frac{1}{i}(C^{[I]} I_1(k\chi) - D^{[I]} K_1(k\chi)) = (\lambda + ik)\overline{R}, \tag{6.33}$$

$$\frac{1}{i}(C^{[O]} I_1(k\chi) - D^{[O]} K_1(k\chi)) = (\lambda + ik)\overline{R}, \tag{6.34}$$

$$\frac{1}{i}(C^{[O]} I_1(k) - D^{[O]} K_1(k)) = (\lambda + ik)\overline{S}, \tag{6.35}$$

$$\frac{1}{i}(-D^{[A]}K_1(k)) = (\lambda)\overline{S}. \tag{6.36}$$

Similarly, using the values of $\overline{p}^{[z]}$ from equation (6.32) in equations (6.27) and (6.28), we get

$$\frac{-(\lambda + ik)}{ik\rho}(C^{[I]}I_0(k\chi)) + \frac{(\lambda + ik)}{ik}(C^{[O]}I_0(k\chi) + D^{[O]}K_0(k\chi)) \tag{6.37}$$
$$= \frac{\sigma}{We}(k^2 - \frac{1}{\chi^2})\overline{R},$$

$$\frac{-(\lambda + ik)}{ik}(C^{[O]}I_0(k\chi) + D^{[O]}K_0(k\chi)) + \frac{\lambda}{ik\rho^G}(D^{[A]}K_0(k\chi)) \tag{6.38}$$
$$= \frac{1}{We}(k^2 - 1)\overline{S}.$$

By eliminating the $C^{[I]}, C^{[O]}, D^{[O]}, D^{[A]}, \overline{R}$ and $\overline{S}$ from equations $(6.33) - (6.38)$, we are able to arrive (after lengthy algebra) at following dispersion relation:

$$\frac{\lambda'^4}{k^2}\ [\ (I_1(k\chi)K_1(k)I_0(k)K_0(k\chi) - I_1(k\chi)I_0(k\chi)K_0(k)K_1(k))$$

$$+ \rho\ (\ K_1(k\chi)I_0(k)I_0(k\chi)K_1(k) + I_1(k\chi)K_1(k)K_0(k)I_0(k\chi)) +$$

$$\rho\ \rho^G(\ K_1(k\chi)I_1(k)K_0(k)I_0(k\chi) - I_1(k\chi)K_1(k)K_0(k)I_0(k\chi)) +$$

$$\rho^G\ (\ I_1(k\chi)K_0(k)I_1(k)K_0(k\chi) + I_1(k\chi)K_1(k)K_0(k)I_0(k\chi))\ ] +$$

$$\frac{\lambda'^3}{k}[\rho^G(I_1(k)K_1(k\chi)K_0(k)I_0(k\chi) - I_1(k\chi)I_0(k\chi)K_0(k)K_1(k))$$

82

$$-2\ \rho\ \rho^G(K_1(k\chi)I_0(k)K_1(k)I_0(k\chi) + I_1(k\chi)K_1(k)K_0(k)I_0(k\chi))]$$

$$\frac{\lambda'^2}{kWe}\ [\ \beta\ (I_1(k\chi)K_1(k\chi)K_1(k)I_0(k) + I_1(k\chi)I_1(k\chi)K_1(k)K_0(k))$$

$$+\ \rho\ \alpha\ (K_1(k\chi)K_1(k)I_0(k\chi)I_1(k) + I_1(k\chi)I_0(k\chi)K_1(k)K_1(k))\ +$$

$$\rho^G\ \beta\ (\ I_1(k\chi)K_1(k\chi)I_1(k)K_0(k) - I_1(k\chi)I_1(k\chi)K_1(k)K_0(k))\ +$$

$$\alpha\ (\ I_1(k\chi)I_0(k\chi)K_1(k)K_1(k) + I_1(k\chi)K_0(k\chi)K_1(k)I_1(k)\ )\ -$$

$$We\rho^G k(I_1(k\chi)K_0(k)I_0(k\chi)K_1(k) + I_1(k\chi)K_0(k\chi)I_1(k)K_0(k))\ +$$

$$We\rho\rho^G kI_0(k\chi)(I_1(k\chi)K_1(k)K_0(k)\ - K_1(k\chi)I_1(k)K_0(k))]\ +$$

$$\frac{2i\lambda'}{We}[\rho^G\ \beta\ (I_1(k\chi)K_1(k\chi)I_1(k)K_0(k) - I_1(k\chi)I_1(k\chi)K_1(k)K_0(k))]$$

$$+\frac{\alpha\beta}{We^2}\ (I_1(k\chi)K_1(k\chi)I_I(k)K_1(k) - I_1(k)I_0(k\chi)K_1(k\chi)K_1(k))\ +$$

$$\frac{\beta\rho^G k}{We}(I_1(k\chi)K_0(k)I_1(k\chi)K_1(k) - I_1(k\chi)K_1(k\chi)I_1(k)K_0(k))\ = 0. \qquad (6.39)$$
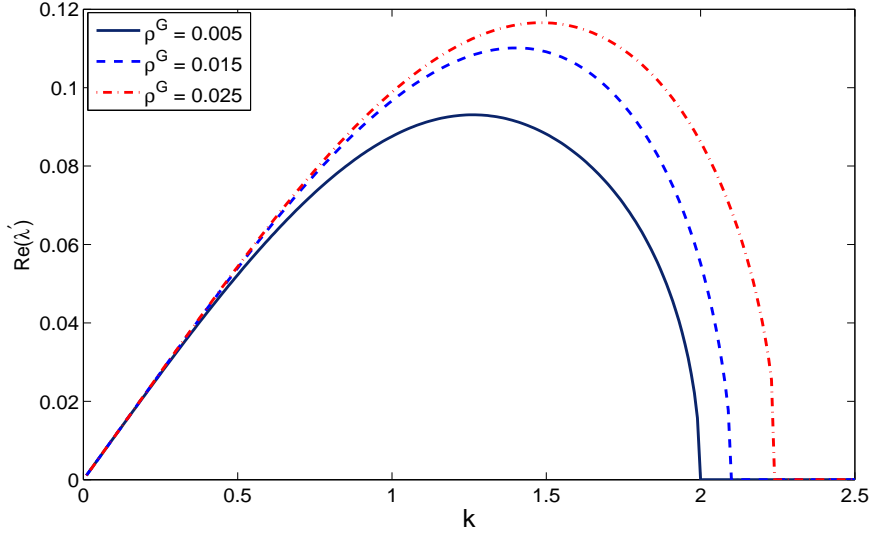
Figure 6.1: Growth rate of disturbance λ'_{max} against the wavenumber for various values of gas-to-shell liquid density ratio. The other parameters are $We = 10$, $F = 1$, $\rho = 1$, $\sigma = 1$ and $\chi = 0.5$.

In the above dispersion relation we have

$$\alpha = k^2 - 1, \quad \beta = \sigma \left(k^2 - \tfrac{1}{\chi^2}\right)$$

and $\lambda' = \lambda + ik$.

6.3 Results and discussion

As we are investigating the instability in temporal mode, therefore we solve dispersion relation (6.39) for λ' using Ferrari's method [4]. The numerical results of the equation (6.39), for given values of wavenumber k, are displayed in Fig. 6.1. These curves are showing the growth rate of disturbances versus wavenumber k for various values of gas to shell liquid density ratio ρ^G. We see that the cut-off wavenumber and the growth rate of disturbances become large by increasing ρ^G which is in agreement with Lin [48].
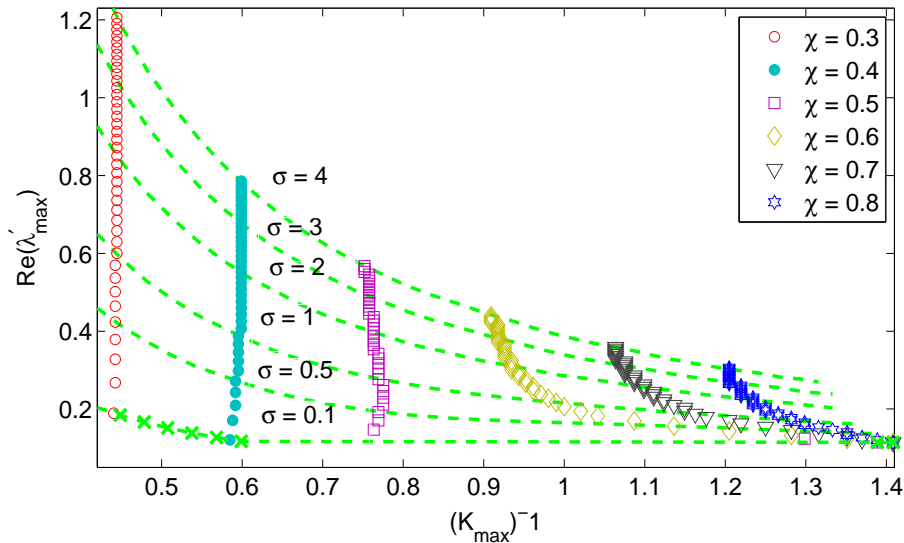
Figure 6.2: Maximum growth rate $[Re(\lambda')]_{max}$ against inverse maximum wavenumber $(k_{max})^{-1}$, for various values of σ and χ. The other parameters are $We = 100$, $F = 1$, $\rho^G = 0.001$ and $\rho = 1$. The symbols are for $\sigma = 0.1 - 4$, while the dashed lines are for $\chi = 0.1 - 0.9$.

In order to explore the effects of the radii ratio χ and surface tension ratio σ in the presence of ambient gas, we plot the set of curves, for inverse wavenumber and its associated maximum growth rate, in the Figs. 6.2 and 6.3. These set of curves are obtained by keeping σ fixed and varying χ and vice versa. It is important to mention that the rest of parameters are kept fixed. Here, the curves for fixed χ and variable σ are presented by symbols, while the dashed lines are obtained by keeping σ fixed and varying χ. We observe that the dashed lines are continuous in nature for $\sigma \geqslant 0.5$, but there are some discontinuities found in the small values of σ. On the other hand, the symbolic curves for fixed χ and variable σ are vertical in nature for small values of χ and take an arc shape for the large values of χ.

In Fig. 6.2, for the case $\rho^G = 0.001$ (typically for a jet composed of water surrounded by air we have $\rho^G = 0.001$), we find some discontinuities for smaller surface tension ratios σ which is due to the competing wave modes which propagate along the compound jet as discussed in chapter five of this thesis. In this case, for $\sigma = 0.1$, no mode exist between
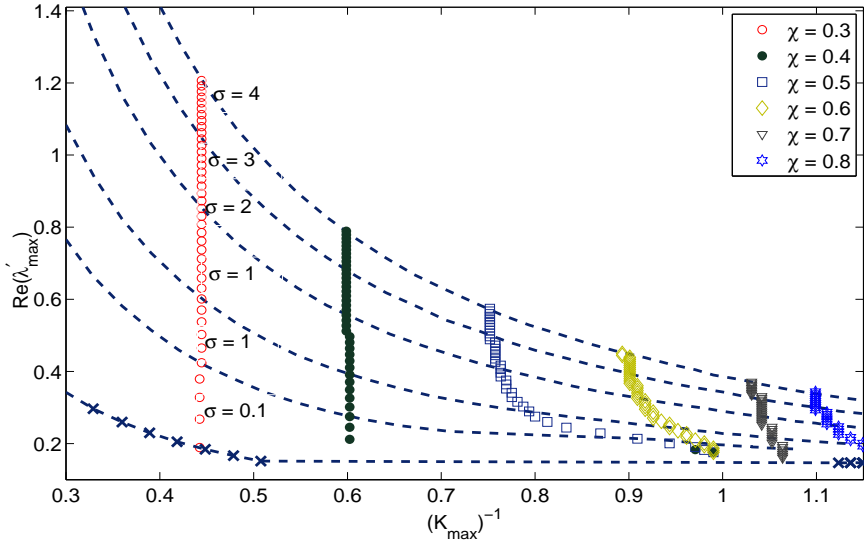
Figure 6.3: Maximum growth rate $[Re(\lambda')]_{max}$ against inverse maximum wavenumber $(k_{max})^{-1}$, for various values of σ and χ. The other parameters are $We = 100$, $F = 1$, $\rho^G = 0.005$ and $\rho = 1$. The symbols are for $\sigma = 0.1 - 4$, while the dashed lines are for $\chi = 0.1 - 0.9$.

$0.58 < k_{max} < 1.33$. From further inspection of Fig. 6.2, we also notice that, at $\chi = 0.5$, there is no mode lying between $0.78 < k_{max} < 1.28$. Moreover, the maximum growth rate of disturbance and its corresponding maximum wavenumber increase with the increase in fixed σ for all variable χ but reduce with the increase in fixed χ for larger values of σ, while, for smaller values of σ, the most unstable wavenumber increases in the case of a smaller fixed χ. In Fig. 6.3, similar set of curves are shown for the case where $\rho^G = 0.005$. Again, we find the discontinuities at smaller values of σ which means that there is no mode lying between $0.51 < k_{max} < 1.2$ and no mode existing between $0.6 < k_{max} < 0.98$ for $\chi = 0.4$. By examining Figs. 6.2 and 6.3, we conclude that the the most unstable wavenumber with its corresponding maximum growth rate increase by increasing the gas to liquid density ratio ρ^G at all values of the surface tension ratio σ, inner to outer radii ratio χ and along the axial length x of the compound jet. Therefore, we can say that the droplet size and breakup length of the jet will reduce due to the presence of ambient gas density.

CHAPTER 7

INFLUENCE OF GRAVITY ON INVISCID COMPOUND JET MOVING IN AN AMBIENT GAS

In this chapter, we incorporate the aerodynamics effects on an inviscid compound jet which is falling vertically downwards under the influence of gravity. We formulate the governing equations which describe the evolution of the interfaces of the compound jet. We then use an asymptotic expansion to derive a set of one dimensional equations that describe the steady state of the jet. We than consider the temporal instability of the jet around this steady state. Moreover, we investigate how key parameters, including surrounding gas density, alter the growth rate and most unstable wavenumber. Lastly, an approximation is used to estimate the breakup lengths of the jet and make a comparison with experimental data.

7.1   Problem Formulation

We consider an inviscid axisymmetric compound jet which emerges from a concentric tube with the exit velocity U and moves in a surrounding gas. The outer radius of the compound

jet is denoted by a and the inner radius is denoted by χa, where $0 < \chi < 1$. It is assumed that the compound jet, after issuing from a circular orifice, falls in a vertical direction under the influence of gravity. It is also assumed that all the fluids are incompressible and immiscible. The geometry of the compound jet is described in a cylindrical coordinate system (r, θ, x), where r is the radial component, θ is an azimuthal component and x is the length of the jet. As we are assuming axisymmetric flow, the azimuthal components are taken to be zero. Therefore, the velocity vector describing the flow can be written as $\mathbf{u^{[z]}} = (w^{[z]}, 0, u^{[z]})$, where the superscript $z = I, O$ and A refer to the inner fluid, the outer fluid and the surrounding gas respectively. Here we denote $r = R(x, t)$ as the interface of inner fluid with the outer one, $r = S(x, t)$ as the interface of outer fluid with the surrounding gas, $\sigma^{[I]}$ is the surface tension at the interface $r = R(x, t)$ and $\sigma^{[O]}$ is the surface tension at the interface $r = S(x, t)$. The density of the fluids is denoted by $\rho^{[z]}$, and the pressure and the time are denoted as $p^{[z]}$ and t respectively. The gravity is taken as $\mathbf{g} = (0, 0, g)$. In addition, the surface tensions $\sigma^{[I]}$ and $\sigma^{[O]}$ are assumed to be constant at the inner and the outer interface respectively.

The continuity equation and the momentum equation, which describe the resulting dynamics of the compound jet, are given by

$$\frac{\partial u^{[z]}}{\partial x} + \frac{\partial w^{[z]}}{\partial r} + \frac{w^{[z]}}{r} = 0, \tag{7.1}$$

$$\frac{\partial u^{[z]}}{\partial t} + u^{[z]} \frac{\partial u^{[z]}}{\partial x} + w^{[z]} \frac{\partial u^{[z]}}{\partial r} = -\frac{1}{\rho^{[z]}} \frac{\partial p^{[z]}}{\partial x} + (\delta_{\mathbf{Iz}} + \delta_{\mathbf{Oz}}) g \tag{7.2}$$

and

$$\frac{\partial w^{[z]}}{\partial t} + u^{[z]} \frac{\partial w^{[z]}}{\partial x} + w^{[z]} \frac{\partial w^{[z]}}{\partial r} = -\frac{1}{\rho^{[z]}} \frac{\partial p^{[z]}}{\partial r}, \tag{7.3}$$

where $\delta_{\mathbf{Iz}}$ and $\delta_{\mathbf{Oz}}$ are the Kronecker delta symbols with free index z. These equations are supplemented by the kinematic conditions and the normal stress conditions. The kinematic conditions, at the interface $r = R(x, t)$, are given by

$$w^{[z]} = \frac{\partial R}{\partial t} + u^{[z]} \frac{\partial R}{\partial x}, \tag{7.4}$$

where $z = I, O$. Similarly, the kinematic conditions, at the interface $r = S(x, t)$, are given by

$$w^{[z]} = \frac{\partial S}{\partial t} + u^{[z]} \frac{\partial S}{\partial x}, \tag{7.5}$$

where $z = O, A$. For inviscid fluids, we have the classical free surface condition of constant pressure and hence zero tangential stress condition. The normal stress conditions, at the interfaces $r = R(x, t)$ and $r = S(x, t)$, are

$$p^{[I]} - p^{[O]} = \sigma^{[I]} \kappa^{[I]}, \tag{7.6}$$

and

$$p^{[O]} - p^{[A]} = \sigma^{[O]} \kappa^{[O]}, \tag{7.7}$$

respectively, where $\kappa^{[I]}$ is the curvature of the inner free surface and $\kappa^{[O]}$ is the curvature of the outer free surface, which are given by

$$\kappa^{[I]} = \frac{\left(1 + \left(\frac{\partial R}{\partial x}\right)^2\right)^{-\frac{1}{2}}}{R} - \frac{\frac{\partial^2 R}{\partial x^2}}{\left(1 + \left(\frac{\partial R}{\partial x}\right)^2\right)^{\frac{3}{2}}}, \tag{7.8}$$

$$\kappa^{[O]} = \frac{\left(1 + \left(\frac{\partial S}{\partial x}\right)^2\right)^{-\frac{1}{2}}}{S} - \frac{\frac{\partial^2 S}{\partial x^2}}{\left(1 + \left(\frac{\partial S}{\partial x}\right)^2\right)^{\frac{3}{2}}}. \tag{7.9}$$

We can non-dimensionalize the velocity components with the initial jet velocity U at the tube exit, that is $\overline{w}^{[z]} = w^{[z]}/U$ and $\overline{u}^{[z]} = u^{[z]}/U$, the radial length with the outer jet radius a $\overline{r} = r/a$ and the axial length with a characteristic wavelength L in the axial direction $\overline{x} = x/L$. The time and the pressure are scaled by $\overline{t} = tU/L$ and $\overline{p}^{[z]} = p^{[z]}/\rho^{[O]}U^2$ respectively. By assuming the jet is slender, we define a small parameter ε as $\varepsilon = a/L << 1$. The dimensionless forms of inner and outer radii of the jet at the nozzle are $R(0,t) = \chi$ and $S(0,t) = 1$ respectively. After dropping the overbars, the resulting dimensionless continuity and Euler equations can be written as

$$\frac{\partial u^{[z]}}{\partial x} + \varepsilon \frac{\partial w^{[z]}}{\partial r} + \frac{w^{[z]}}{r} = 0, \tag{7.10}$$

$$\frac{\partial u^{[z]}}{\partial t} + u^{[z]}\frac{\partial u^{[z]}}{\partial x} + \frac{w^{[z]}}{\varepsilon}\frac{\partial u^{[z]}}{\partial r} = -\frac{\rho^{[O]}}{\rho^{[z]}}\frac{\partial p^{[z]}}{\partial x} + (\delta_{\mathbf{Iz}} + \delta_{\mathbf{Oz}})\frac{1}{F^2} \tag{7.11}$$

and

$$\frac{\partial w^{[z]}}{\partial t} + u^{[z]}\frac{\partial w^{[z]}}{\partial x} + \frac{w^{[z]}}{\varepsilon}\frac{\partial w^{[z]}}{\partial r} = -\frac{\rho^{[O]}}{\rho^{[z]}}\frac{1}{\varepsilon}\frac{\partial p^{[z]}}{\partial r}. \tag{7.12}$$

The dimensionless kinematic conditions, at the interface $r = R(x,t)$ and $r = S(x,t)$, are given by

$$w^{[z]} = \frac{\partial R}{\partial t} + u^{[z]}\frac{\partial R}{\partial x}, \tag{7.13}$$

where $z = I, O$ and

$$w^{[z]} = \frac{\partial S}{\partial t} + u^{[z]}\frac{\partial S}{\partial x}, \tag{7.14}$$

where $z = O, A$, respectively. The dimensionless normal stress conditions, at the interfaces

$r = S(x, t)$ and $r = R(x, t)$, are

$$p^{[O]} - p^{[A]} = \frac{\kappa^{[I]}}{We}, \quad \text{where} \quad \kappa^{[I]} = \frac{\left(1 + \varepsilon^2 \left(\frac{\partial S}{\partial x}\right)^2\right)^{-\frac{1}{2}}}{S} - \frac{\frac{\partial^2 S}{\partial x^2}}{\left(1 + \varepsilon^2 \left(\frac{\partial S}{\partial x}\right)^2\right)^{\frac{3}{2}}} \qquad (7.15)$$

and

$$p^{[I]} - p^{[O]} = \frac{\sigma^I}{\sigma^O} \frac{\kappa^{[O]]}}{We}, \quad \text{where} \quad \kappa^{[O]} = \frac{\left(1 + \varepsilon^2 \left(\frac{\partial R}{\partial x}\right)^2\right)^{-\frac{1}{2}}}{R} - \frac{\frac{\partial^2 R}{\partial x^2}}{\left(1 + \varepsilon^2 \left(\frac{\partial R}{\partial x}\right)^2\right)^{\frac{3}{2}}} \qquad (7.16)$$

respectively.

7.2 Asymptotic form of steady state solutions

In order to find the steady state solutions, we consider a quiescent gas [73], that is $\mathbf{u}^{[A]} = (0, 0, 0)$, and expand our variables using an asymptotic slender jet steady expansion of the form

$$\{u^{[z]}, w^{[z]}, p^{[z]}\} = \{(\delta_{\mathbf{Iz}} + \delta_{\mathbf{Oz}})u_0^{[z]}(x), 0, p_0^{[z]}(x, r)\}$$

$$+ (\varepsilon r)\{(\delta_{\mathbf{Iz}} + \delta_{\mathbf{Oz}})u_1^{[z]}(x), (\delta_{Iz} + \delta_{Oz})w_1^{[z]}(x), p_1^{[z]}(x)\} + O((\varepsilon r)^2), \qquad (7.17)$$

$$\{R, S\} = \{R_0(x), S_0(x)\} + \varepsilon\{R_1(x), S_1(x)\} + O(\varepsilon^2). \qquad (7.18)$$

Substituting the above asymptotic expansions in the equations $(7.10) - (7.16)$, we find the leading order continuity equation for the inner and outer fluids is

$$w_1^{[z]} = -\frac{1}{2} \frac{\partial u_0^{[z]}}{\partial x}, \qquad (7.19)$$

where $z = I, O$. The leading order kinematic conditions (7.13) and (7.14), at $r = R(x)$ and $r = S(x)$, give

$$\frac{\partial}{\partial x} \left(R_0^2 u_0^{[I]} \right) = 0, \qquad (7.20)$$

and

$$\frac{\partial}{\partial x} \left((S_0^2 - R_0^2) u_0^{[O]} \right) = 0, \qquad (7.21)$$

respectively. The leading order normal stress conditions, at $r = S(x, t)$ and $r = R(x, t)$, yield

$$p_0^{[O]} = \frac{1}{S_0 We} + p_0^{[A]}, \text{ and } p_0^{[I]} = \frac{1}{We} \left(\frac{\sigma}{R_0} + \frac{1}{S_0} \right) + p_0^{[A]} \qquad (7.22)$$

respectively, where $\sigma = \sigma^{[I]}/\sigma^{[O]}$ is the ratio of surface tension between inner and outer fluid interfaces and $We = \rho^{[O]} U^2 a / \sigma^{[O]}$ is the Weber number. By using equations (7.19) and (7.22), the radial momentum equation (7.12) gives $\partial p_0^{[z]}/\partial r = 0$, here $z = I, O$, that is automatically satisfied. Since the surrounding gas is motionless, therefore the axial and radial momentum equations of the gas implies $\partial p_0^{[A]}/\partial x = 0$ and $\partial p_0^{[A]}/\partial r = 0$ respectively. We now substitute equation (7.22) in the axial momentum equation (7.11) for the inner and the outer fluids, which implies

$$u_0^{[I]} \frac{\partial u_0^{[I]}}{\partial x} = -\frac{1}{\rho We} \frac{\partial}{\partial x} \left(\frac{\sigma}{R_0} + \frac{1}{S_0} \right) + \frac{1}{F^2} \qquad (7.23)$$

and

$$u_0^{[O]} \frac{\partial u_0^{[O]}}{\partial x} = -\frac{1}{We} \frac{\partial}{\partial x} \left(\frac{1}{S_0} \right) + \frac{1}{F^2}, \qquad (7.24)$$

where $\rho = \rho^{[I]}/\rho^{[O]}$ is the density ratio of the inner fluid to the outer fluid and $F = U/\sqrt{Lg}$ is the Froude number, which gives a measure of the relative importance of gravitational forces. Equations (7.20), (7.21), (7.23), and (7.24) are a system of nonlinear ordinary differential equations with unknowns $u_0^{[I]}$, $u_0^{[O]}$, R_0 and S_0. To solve this set of equations we specify initial conditions at the nozzle, that is $u_0^{[I]} = u_0^{[O]} = S_0 = 1$ and $R_0 = \chi$. By using initial conditions and dropping subscripts from the variables for ease of convenience, we integrate the system of equations and then apply Newton's method to obtain a spatially non-uniform steady state solution for the inviscid compound jet, which moves in a gas and falls vertically downwards under the influence of gravity. We already calculate the steady state solutions of the above set of equations in chapter five of this thesis.

7.3 Linear Instability Analysis

We now consider the linear temporal instability analysis of an inviscid compound liquid jet moving in a surrounding gas. The evolution of the jet depends on length scale $x = O(1)$, but the disturbances along the jet are much smaller and are comparable to ε when $x = O(1)$. In other words, we can say that the disturbances are typically of the order of jet radius a. We consider the traveling short waves of the form $exp(ik\overline{x} + \lambda\overline{t})$, where $k = k(x) = O(1)$ and $\lambda = \lambda(x) = O(1)$ are the frequency and wavenumber of disturbances. Additionally, $\overline{x} = x/\varepsilon$ and $\overline{t} = t/\varepsilon$ are small length and time scales. Thus, we have a multiple scale formulation as the perturbations grow along the jet having wavelength of $O(\varepsilon)$. Now we introduce small time dependent perturbations to the steady state solutions which take the form

$$u^{[z]} = (\delta_{\mathbf{Iz}} + \delta_{\mathbf{Oz}})u_0^{[z]}(x) + \delta\overline{u^{[z]}}(r)\exp(\lambda\overline{t} + ik\overline{x}), \tag{7.25}$$

$$w^{[z]} = (\delta_{\mathbf{Iz}} + \delta_{\mathbf{Oz}})w_0^{[z]}(x) + \delta\overline{w^{[z]}}(r)\exp(\lambda\overline{t} + ik\overline{x}), \tag{7.26}$$

93

$$p^{[z]} = p_0^{[z]}(x) + \delta\overline{p^{[z]}}(r)\exp(\lambda\overline{t} + ik\overline{x}), \tag{7.27}$$

$$R = R_0(x) + \delta\overline{R}\exp(\lambda\overline{t} + ik\overline{x}), \tag{7.28}$$

$$S = S_0(x) + \delta\overline{S}\exp(\lambda\overline{t} + ik\overline{x}). \tag{7.29}$$

where $0 < \delta << \varepsilon$. Substituting the expansions $(7.25 - 7.29)$ into the non-dimensionalized form of equations $(7.10) - (7.16)$ yields at leading order,or $O(\delta/\varepsilon)$,

$$ik\overline{u^{[z]}} + \frac{\partial\overline{w^{[z]}}}{\partial r} + \frac{\overline{w^{[z]}}}{r} = 0, \tag{7.30}$$

$$(\lambda + ik(\delta_{\mathbf{Iz}} + \delta_{\mathbf{Oz}})u_0^{[z]})\overline{u}^{[z]} = -((\delta_{\mathbf{Iz}})\frac{1}{\rho} + (\delta_{\mathbf{Az}})\frac{1}{\rho^G} + \delta_{\mathbf{Oz}})\overline{p^{[z]}}ik, \tag{7.31}$$

$$(\lambda + ik(\delta_{\mathbf{Iz}} + \delta_{\mathbf{Oz}})u_0^{[z]})\overline{w}^{[z]} = -((\delta_{\mathbf{Iz}})\frac{1}{\rho} + (\delta_{\mathbf{Az}})\frac{1}{\rho^G} + \delta_{\mathbf{Oz}})\frac{\partial\overline{p^{[z]}}}{\partial r}, \tag{7.32}$$

$$\overline{w^{[z]}} = (\lambda + iku_0^{[z]})\overline{R} \quad\text{for}\quad z = I, O, \tag{7.33}$$

$$\overline{w^{[z]}} = (\lambda + ik(\delta_{\mathbf{Oz}})u_0^{[z]})\overline{S} \quad\text{for}\quad z = O, A, \tag{7.34}$$

$$\overline{p^{[I]}} - \overline{p^{[O]}} = \frac{\sigma}{We}(k^2 - \frac{1}{R_0^2})\overline{R}, \tag{7.35}$$

$$\overline{p^{[O]}} - \overline{p^{[A]}} = \frac{1}{We}(k^2 - \frac{1}{S_0^2})\overline{S}, \tag{7.36}$$

where $\delta_{\mathbf{Iz}}$, $\delta_{\mathbf{Oz}}$ and $\delta_{\mathbf{Az}}$ are the Kronecker delta symbols with free index z and $\rho^G = \rho^{[A]}/\rho^{[O]}$ is the density ratio of gas to the outer fluid

Using (7.31) and (7.32) to eliminate $\overline{p^{[z]}}$ we get $\overline{w^{[z]}} = \frac{1}{ik}\frac{\partial \overline{u^{[z]}}}{\partial r}$ and substituting this result in (7.30), we have

$$\frac{\partial^2 \overline{u^{[z]}}}{\partial r^2} + \frac{1}{r}\frac{\partial \overline{u^{[z]}}}{\partial r} - k^2 \overline{u^{[z]}} = 0, \tag{7.37}$$

which has solution

$$\overline{u}^{[z]} = C^{[z]} I_0(kr) + D^{[z]} K_0(kr). \tag{7.38}$$

By using the value of $\overline{u}^{[z]}$, we are able to get

$$\overline{w}^{[z]} = \frac{1}{i}(C^{[z]} I_1(kr) - D^{[z]} K_1(kr)). \tag{7.39}$$

By using (7.31) in (7.38), yields

$$\overline{p}^{[z]} = \frac{-(\lambda + ik(\delta_{\mathbf{Iz}} + \delta_{\mathbf{Oz}})u_0^{[z]})}{ik(\delta_{Iz}\rho + \delta_{Az}\rho^G + \delta_{\mathbf{Oz}})}(C^{[z]} I_0(kr) + D^{[z]} K_0(kr)), \tag{7.40}$$

where $I_0(kr)$ and $K_0(kr)$ are the modified Bessel functions of first and second kind respectively. To avoid the singularities, and to ensure finite values at $r = 0$, we require that $D^{[I]}$ and $C^{[A]}$ will be equal to zero.

Substituting the values of $\overline{w}^{[z]}$ in (7.33) and (7.34), yields

$$\frac{1}{i}(C^{[I]} I_1(kR_0) - D^{[I]} K_1(kR_0)) = (\lambda + iku_0^{[I]})\overline{R}, \tag{7.41}$$

$$\frac{1}{i}(C^{[O]}I_1(kR_0) - D^{[O]}K_1(kR_0)) = (\lambda + iku_0^{[O]})\overline{R}, \tag{7.42}$$

$$\frac{1}{i}(C^{[O]}I_1(kS_0) - D^{[O]}K_1(kS_0)) = (\lambda + iku_0^{[O]})\overline{S}, \tag{7.43}$$

$$\frac{1}{i}(-D^{[A]}K_1(kS_0)) = (\lambda)\overline{S}. \tag{7.44}$$

Similarly, using the values of $\overline{p}^{[z]}$ from equation (7.40) in equations (7.35) and (7.36), we get

$$\frac{-(\lambda + iku_0^{[I]})}{ik\rho}(C^{[I]}I_0(kR_0)) + \frac{(\lambda + iku_0^{[O]})}{ik}(C^{[O]}I_0(kR_0) + D^{[O]}K_0(kR_0)) \tag{7.45}$$
$$= \frac{\sigma}{We}(k^2 - \frac{1}{R_0^2})\overline{R},$$

$$\frac{-(\lambda + iku_0^{[O]})}{ik}(C^{[O]}I_0(kR_0) + D^{[O]}K_0(kR_0)) + \frac{\lambda}{ik\rho^G}(D^{[A]}K_0(kR_0)) \tag{7.46}$$
$$= \frac{1}{We}(k^2 - \frac{1}{S_0^2})\overline{S}.$$

By eliminating the $C^{[I]}, C^{[O]}, D^{[O]}, D^{[A]}, \overline{R}$ and $\overline{S}$ from equations $(7.41) - (7.46)$ and removing subscripts from $u_0^{[I]}$, $u_0^{[O]}$, R_0, and S_0 for ease of convenience, we are able to arrive (after lengthy algebra) at following dispersion relation:

$$\frac{\lambda'^4}{k^2} \left[(I_1(kR)K_1(kS)I_0(kS)K_0(kR) - I_1(kR)I_0(kR)K_0(kS)K_1(kS)) \right.$$

$$+ \rho \left(K_1(kR)I_0(kS)I_0(kR)K_1(kS) + I_1(kR)K_1(kS)K_0(kS)I_0(kR) \right) +$$

$$\rho \rho^G (\ K_1(kR)I_1(kS)K_0(kS)I_0(kR) - I_1(kR)K_1(kS)K_0(kS)I_0(kR)) +$$

$$\rho^G \ (\ I_1(kR)K_0(kS)I_1(kS)K_0(kR) + I_1(kR)K_1(kS)K_0(kS)I_0(kR)) \ ] +$$

$$\frac{\lambda'^3}{k}[\rho^G u^{[O]}(I_1(kS)K_1(kR)K_0(kS)I_0(kR) - I_1(kR)I_0(kR)K_0(kS)K_1(kS))$$

$$+2 \ a_2\rho \ \rho^G(K_1(kR)I_0(kS)K_1(kS)I_0(kR) + I_1(kR)K_1(kS)K_0(kS)I_0(kR))$$

$$+2i\rho a_1(K_1(kR)I_0(kR)I_0(kS)K_1(kS) - I_1(kS)K_0(kS)K_1(kS)I_0(kR))] +$$

$$\frac{\lambda'^2}{kWe} \ [\ \beta \ (I_1(kR)K_1(kR)K_1(kS)I_0(kS) + I_1(kR)I_1(kR)K_1(kS)K_0(kS))$$

$$+ \ \rho \ \alpha \ (K_1(kR)K_1(kS)I_0(kR)I_1(kS) + I_1(kR)I_0(kR)K_1(kS)K_1(kS)) +$$

$$\rho^G \ \beta \ (\ I_1(kR)K_1(kR)I_1(kS)K_0(kS) - I_1(kR)I_1(kR)K_1(kS)K_0(kS)) +$$

$$\alpha \ (\ I_1(kR)I_0(kR)K_1(kS)K_1(kS) + I_1(kR)K_0(kR)K_1(kS)I_1(kS) \ ) - We$$

$$\rho \ a_1^2 \ k(I_1(kR)K_1(kS)K_0(kS)I_0(kR) + K_1(kR)I_0(kR)I_0(kS)K_1(kS)) -$$

$$We\rho^G(u^{[O]})^2k(I_1(kR)K_0(kS)I_0(kR)K_1(kS) + I_1(kR)K_0(kR)I_1(kS)K_0(kS))$$

$$+We\rho\rho^G a_3 kI_0(kR)(I_1(kR)K_1(kS)K_0(kS) \ - K_1(kR)I_1(kS)K_0(kS))] +$$

$$\frac{2i\lambda'}{We}[a_1\rho\alpha(K_1(kS)K_1(kR)I_1(kS)I_0(kR) - I_1(kR)K_1(kS)K_1(kS)I_0(kR))$$

$$+\rho^G \ \beta \ u^{[O]} \ (I_1(kR)K_1(kR)I_1(kS)K_0(kS) - I_1(kR)I_1(kR)K_1(kS)K_0(kS))$$

$$+Wek \ \rho \ \rho^G \ a_4 \ I_0(kR)(K_1(kR)I_1(kS)K_0(kS) - I_1(kR)K_1(kS)K_0(kS)) \ ]$$

$$+\frac{\alpha\beta}{We^2} \ (I_1(kR)K_1(kR)I_I(kS)K_1(kS) - I_1(kS)I_0(kR)K_1(kR)K_1(kS)) +$$

$$\frac{\rho\alpha ka_1^2}{We} \ (K_1(kS)I_1(kR)I_0(kR)K_1(kS) - I_1(kS)K_1(kR)I_0(kR)K_1(kS)) +$$

$$\frac{\beta\rho^G k(u^{[O]})^2}{We}(I_1(kR)K_0(kS)I_1(kR)K_1(kS) - I_1(kR)K_1(kR)I_1(kS)K_0(kS)) +$$

$$\rho \ \rho^G(ka_1 u^{[O]})^2 I_0(kR)(K_1(kR)I_1(kS)K_0(kS) - I_1(kR)K_1(kS)K_0(kS)) = 0. \quad (7.47)$$

In the above dispersion relation we have

$$a_1 = (u^{[I]} - u^{[O]}), \quad a_2 = (u^{[I]} - 2u^{[O]}), \quad a_3 = ((u^{[I]} - u^{[O]})^2 + (u^{[O]})^2 + 4u^{[O]} \ (u^{[I]} - u^{[O]})),$$

$$a_4 = ((u^{[O]})^2 \ (u^{[I]} - u^{[O]}) - u^{[O]} \ (u^{[I]} - u^{[O]})^2), \quad \alpha \ = \ k^2 - \tfrac{1}{S^2}, \quad \beta \ = \ \sigma \ (k^2 - \tfrac{1}{R^2}),$$

and $\lambda^{'} = \lambda + iku^{[O]}$.

7.4   Results and discussion

The dispersion relation (7.47) is a quartic equation in $\lambda^{'}$ for the given values of k and it can be solved with the aid of Ferrari's method. The coefficients of this equation depend on x, which is the axial distance along the compound jet. The solution of equation (7.47) gives us two types of growing modes, but we will focus on the mode with the largest growth rate with the reasoning that this mode is responsible for breakup [76, 55].

As the compound jet, which is emerging in an ambient gas, is accelerating in the vertical direction, the steady state solutions are function of x which is axial distance along the jet. Hence, the coefficients of dispersion relation are altered as we move down the jet and, this will have a strong influence on the breakup and droplet size.

Now we start our investigation and see how the ambient gas affects on the compound jet which is falling under the influence of gravity. Therefore, for three different values of ρ^G, the plots of maximum wavenumber versus axial length of the jet are shown in Fig. 7.1 and similarly the plots of maximum growth rate of disturbance versus axial length of the jet are depicted in Fig. 7.2. Here, it is clearly noticeable that the maximum wavenumber and its associated maximum growth rate increase along the jet and produce the same effects as we increase ρ^G. This implies that the breakup lengths and drop sizes will be shorter due to the presence of gravity and ambient gas. To elaborate further, the influence of ambient gas on the surface of a compound liquid jet, we produce the maximum wavenumber and associated maximum growth rate for given values of ρ^G at different locations along the jet in the Figs. 7.3 and 7.4. It is observed that the maximum wavenumber, together with the maximum growth rate, always increases gradually along the jet as we increase the ρ^G.

In order to explore the effects of radii ratio χ and surface tension ratio σ in the presence of ambient gas we plot the set of curves, for inverse wavenumber and its associated maximum growth rate, in the Figs. 7.5 and 7.6. These set of curves are obtained by keeping σ fixed and varying χ and vice versa. It is important to mention that the rest of parameters are kept fixed in Figs. 7.5 and 7.6. Here, the curves for fixed χ and variable σ are presented by symbols, while the dashed lines are obtained by keeping σ fixed and varying χ. With reference to the Figs. 7.5 and 7.6, we observe that the dashed lines are continuous in nature for $\sigma \geqslant 0.5$, but there are some discontinuities found in the small values of σ. On the other hand, the symbolic curves for fixed χ and variable σ are vertical in nature for small values of χ and take an arc shape for the large values of χ.

In Fig. 7.5, we have two sets of diagrams which are obtained at two different locations of the jet, *that is*, at $x = 1$ and $x = 2$. It can be clearly seen that the most unstable wavenumber and its associated maximum growth increase as x increases which implies that the droplet sizes will be reduced and shorter jets will be formed due to the presence of gravity. We find some discontinuities for smaller surface tension ratios σ, that is, for $\sigma = 0.1$, no mode exist between $0.27 < k_{max} < 0.62$ at $x = 1$ and $0.2 < k_{max} < 0.46$ at $x = 2$. From inspection of Fig. 7.5, we also notice that, at $\chi = 0.5$, there is no mode lying between $0.34 < k_{max} < 0.59$ at $x = 1$ and $0.26 < k_{max} < 0.44$ at $x = 2$.

Furthermore, the maximum growth rate of disturbance and its corresponding maximum wavenumber increase with the increase in fixed σ for all variable χ but it reduce with the increase in fixed χ for larger values of σ, while, for smaller values of σ, the most unstable wavenumber increases in the case of a smaller fixed χ. Similar set of diagrams are demonstrated in Fig. 7.6 for the case where $\rho^G = 0.005$. Again, we find the discontinuities at smaller values of σ which means there is no mode lying between $0.24 < k_{max} < 0.53$ at $x = 1$ and $0.18 < k_{max} < 0.42$ at $x = 2$ and no mode existing between $0.39 < k_{max} < 0.48$ at $x = 1$ and $0.27 < k_{max} < 0.37$ at $x = 2$ for $\chi = 0.5$. By examining Figs. 7.5 and 7.6,
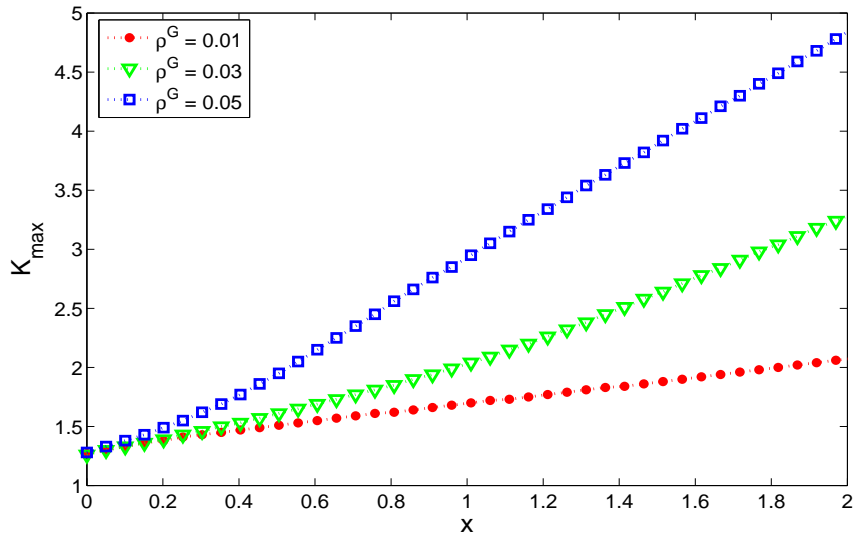
Figure 7.1: Maximum wavenumber k_{max} against the axial length of the jet for various values of gas-to-shell liquid density ratio. The other parameters are $We = 10$, $F = 1$, $\rho = 1$, $\sigma = 1$ and $\chi = 0.5$.
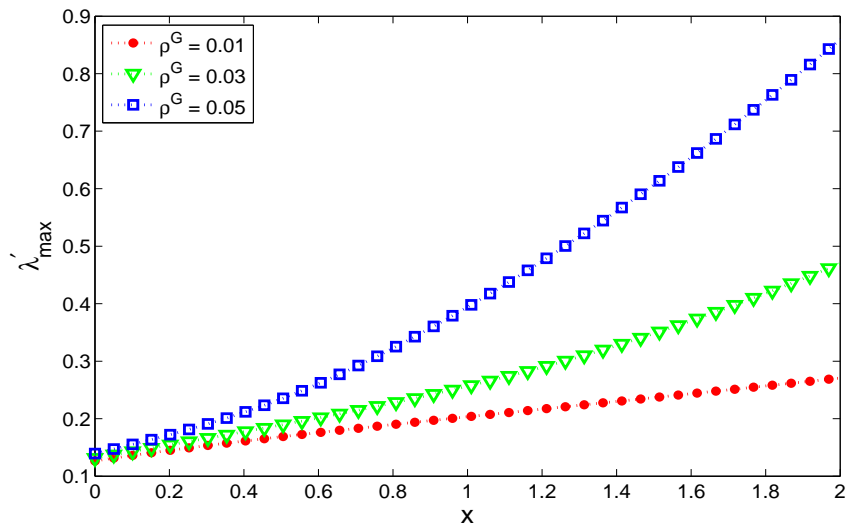
Figure 7.2: Maximum growth rate of disturbance λ'_{max} against the axial length of the jet for various values of gas-to-shell liquid density ratio. The other parameters are $We = 10$, $F = 1$, $\rho = 1$, $\sigma = 1$ and $\chi = 0.5$.
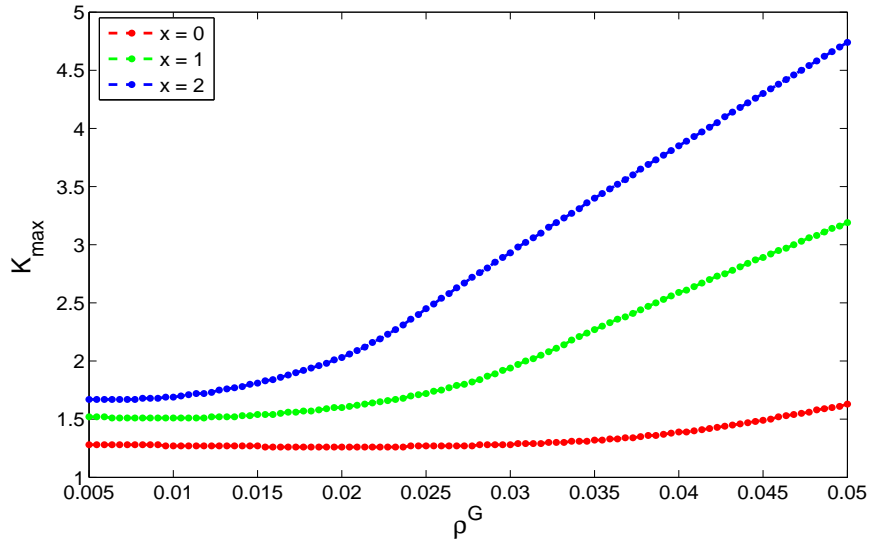
Figure 7.3: Maximum wavenumber k_{max} against gas-to-shell liquid density ratios at various locations of jet. The other parameters are $We = 10$, $F = 1$, $\rho = 1$, $\sigma = 1$ and $\chi = 0.5$.
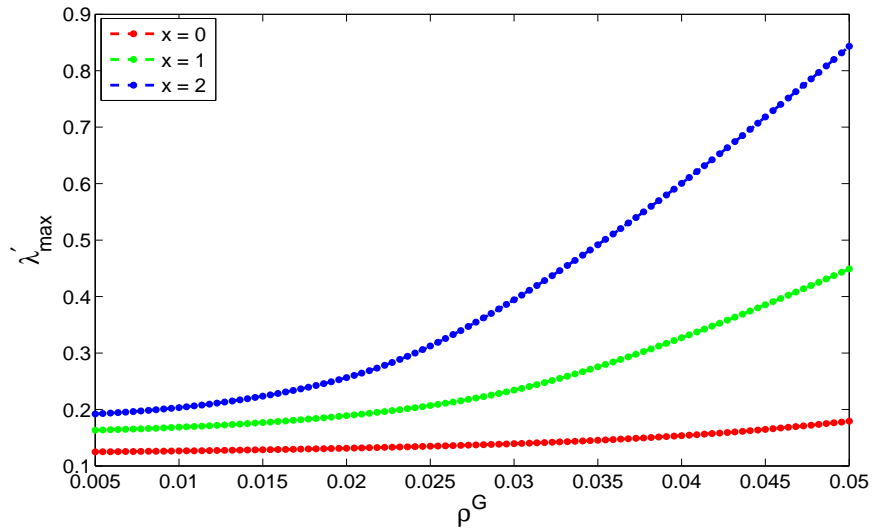
Figure 7.4: Maximum growth rate of disturbance against gas-to-shell liquid density ratios at various locations of jet. The other parameters are $We = 10$, $F = 1$, $\rho = 1$, $\sigma = 1$ and $\chi = 0.5$.
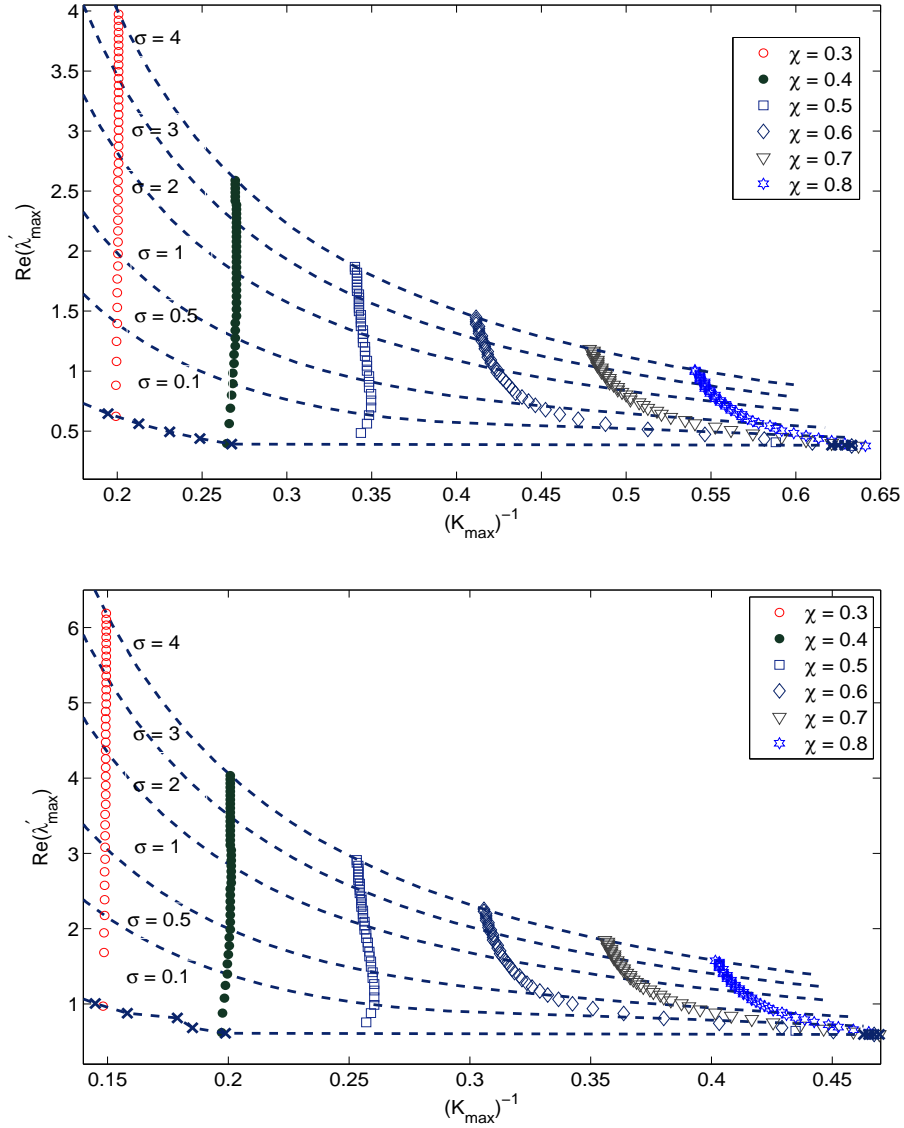
Figure 7.5: Maximum growth rate $[Re(\lambda')]_{max}$ against inverse maximum wavenumber $(k_{max})^{-1}$, for various values of σ and χ. The graphs from top to bottom represent $x = 1$ and $x = 2$ respectively. The other parameters are $We = 100$, $F = 1$, $\rho^G = 0.005$ and $\rho = 1$. The symbols are for $\sigma = 0.1 - 4$, while the dashed lines are for $\chi = 0.1 - 0.9$.
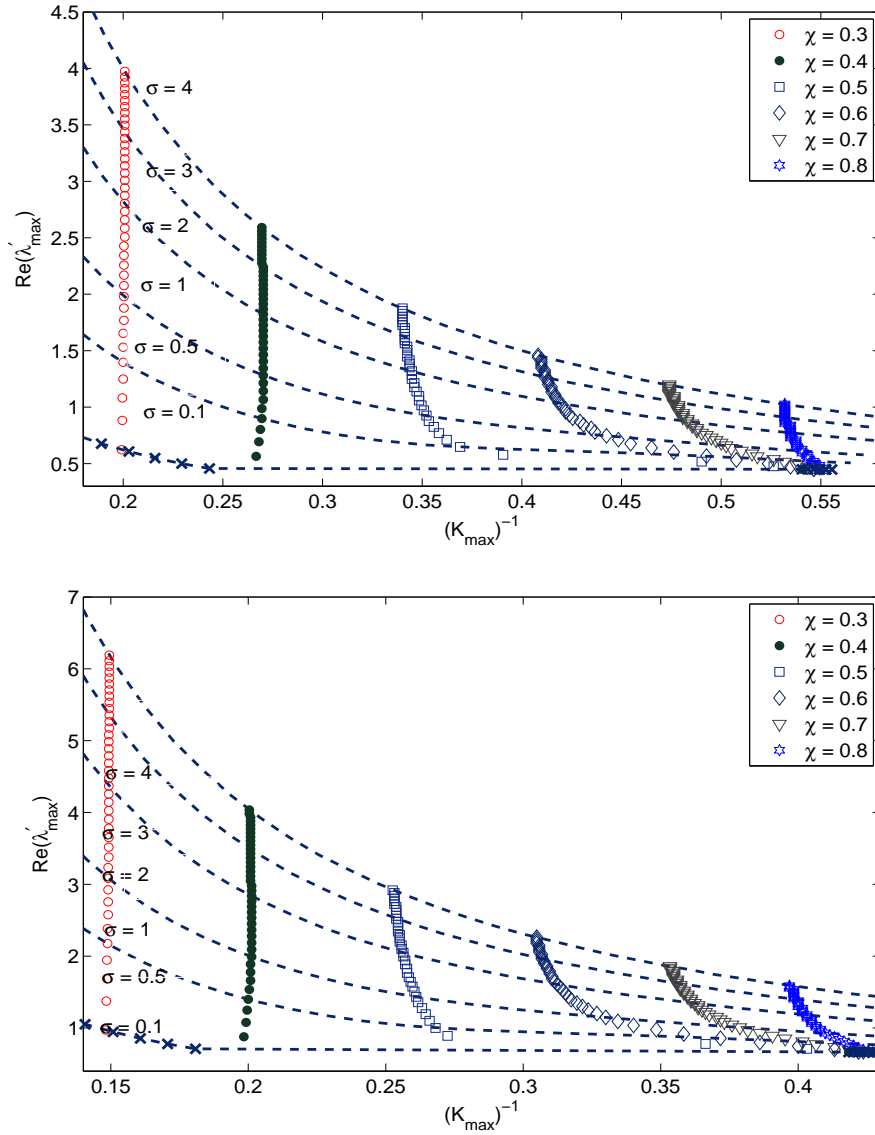
Figure 7.6: Maximum growth rate $[Re(\lambda')]_{max}$ against inverse maximum wavenumber $(k_{max})^{-1}$, for various values of σ and χ. The graphs from top to bottom represent $x = 1$ and $x = 2$ respectively. The other parameters are $We = 100$, $F = 1$, $\rho^G = 0.005$ and $\rho = 1$. The symbols are for $\sigma = 0.1 - 4$, while the dashed lines are for $\chi = 0.1 - 0.9$.

we conclude that the the most unstable wavenumber with its corresponding maximum growth rate increase by increasing the gas to liquid density ratio ρ^G at all values of surface tension ratio σ, inner to outer radii ratio χ and along the axial length x of the compound jet. Therefore it is quite clear that the breakup lengths and droplet sizes of an inviscid compound jet falling under gravity are reduced due to the presence of ambient gas and the effects of gravity.

Finally, we will use the results of our linear instability analysis to determine the breakup lengths of inviscid compound jet falling under gravity in the presence of ambient gas. We note that linear theory is only valid for small disturbances and as such fails near the vicinity of the breakup. However, as disturbances grow exponentially in temporal analysis, linear theory may be used to provide an estimate of breakup lengths. We use an approach similar to Mohsin $et\ al.$ [55] whereby we determine the breakup times of the liquid jet by plotting (7.23) and (7.24) to estimate the location of breakup. Using the results obtained in previous section to plot R and S and choosing a value for ε and δ, we can determine the breakup length l_b. The breakup length is the location of the compound jet, where either the inner and the outer interface touch or the inner radius R approaches to zero. The breakup lengths l_b are determined by varying ρ^G for two different values of inner to outer radii ratio χ and are shown in Fig. 7.7. It may be observed that breakup lengths decrease with an increase in ρ^G and conversely increase when we increase the inner to outer radii ratio χ. This implies that the presence of ambient gas will shorten the length of compound jet.

We can compare our results here to that presented by Hertz & Hermanrud [33], although we note that in their experiment the jet issues horizontally and does not fall vertically under gravity. For the experimental values considered by Hertz & Hermanrud [33], we have $\rho = 1$, $\sigma = 0$, $We = 9.38$, $\rho^G = 0$, $F = \infty$ and $\chi = 0.488$. In this case we see that the same inner and outer fluid and we have $(k_{max})^{-1} = 1.41$ which is the
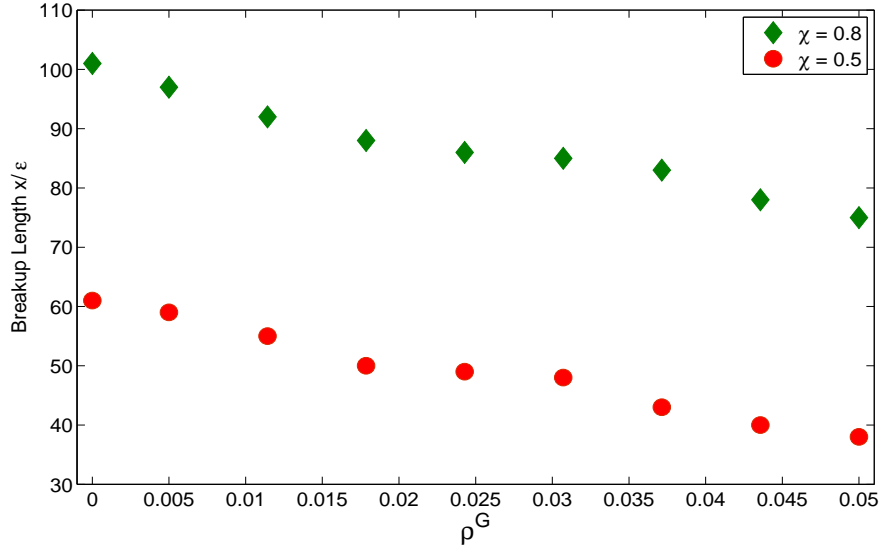
Figure 7.7: A graph of breakup length against ρ^G, for different inner to outer radii ratios χ. The other parameters are $\delta = 0.002$, We $= 100$, $F = 1$, $\varepsilon = 0.01$, $\sigma = 1$ and $\rho = 1$.

same value found by Sanz & Masueger [76] and Hertz & Hermanrud [33]. For the case of two different inner and outer fluids, where $\rho = 1$, $\sigma = 2.6$, $We = 33.8$, $\rho^G = 0.001$ and $\chi = 0.488$, we have $(k_{max})^{-1} = 0.625 - 0.704$ when the Froude number F is varied between $1 - 5$. The experimental value of $(k_{max})^{-1}$ calculated from [33] is 0.64 for the first wave, whereas $(k_{max})^{-1} = 0.6$ is the mean value along the jet which agrees qualitatively with our results for large Froude numbers.

CHAPTER 8

VISCOUS COMPOUND LIQUID JET

In the preceding chapters of this thesis, we have discussed the instability of an inviscid compound liquid jet in several scenarios. Now, we will examine the dynamics and instability of a viscous compound jet issuing from a co-axial cylinder and falling vertically downwards with the constant velocity.

8.1 Problem Formulation

The generalized form of the continuity equation and the Navier-Stokes equation for a viscous compound jet will be,

$$\nabla \cdot \mathbf{u}^{[z]} = 0, \tag{8.1}$$

$$\rho^{[z]} \left(\frac{\partial}{\partial t} + \mathbf{u}^{[\mathbf{z}]} \cdot \nabla \right) \mathbf{u}^{[\mathbf{z}]} = -\nabla p^{[k]} + \mu^{[z]} \nabla \cdot \mathbf{T}^{[\mathbf{z}]}, \tag{8.2}$$

where $\mathbf{T} = \nabla \mathbf{U} + (\nabla \mathbf{U})^T$ is the deformation tensor, $p^{[z]}$ is the pressure, $\rho^{[z]}$ is the density and $\mu^{[z]}$ is the viscosity of inner and outer fluids. The superscript $z = 1$ and $z = 2$ denote the inner and outer fluid respectively. In addition, both the fluids are assumed to be incompressible and immiscible. Since the flow is axisymmetric, so there will be no flow

along the azimuthal direction θ and velocity profile will be $\mathbf{u^z} = (w^{[z]}, 0, u^{[z]})$. Therefore the continuity equation and Navier-Stoke equations are formulated as,

$$w_r^{[z]} + u_x^{[z]} + \frac{w^{[z]}}{r} = 0 \tag{8.3}$$

and

$$\rho^{[z]} \left(u_t^{[z]} + u^{[z]} u_x^{[z]} + w^{[z]} u_r^{[z]} \right) = -p_x^{[k]} + \mu^{[z]} \left(u_{xx}^{[z]} + \frac{1}{r}(r u_r^{[z]})_r \right), \tag{8.4}$$

$$\rho^{[z]} \left(w_t^{[z]} + u^{[z]} w_x^{[z]} + w^{[z]} w_r^{[z]} \right) = -p_r^{[k]} + \mu^{[z]} \left(w_{xx}^{[z]} + (\frac{r w_{rr}^{[z]}}{r})_r \right). \tag{8.5}$$

The kinematic conditions of a viscous compound jet are given by

$$w^{[1]}(R, x, t) = R_t + u^{[1]}(R, x, t)R_x \ , \quad w^{[2]}(R, x, t) = R_t + u^{[2]}(R, x, t)R_x \tag{8.6}$$

and

$$w^{[2]}(S, x, t) = S_t + u^{[2]}(S, x, t)S_x. \tag{8.7}$$

Tangential stress conditions for inner and outer interface of viscous compound jet can be written as

$$2\mu^{[2]} R_x (w_r^{[2]} - u_x^{[2]}) + \mu^{[2]}(1 - (R_x)^2)(u_r^{[2]} - w_x^{[2]}) = 2\mu^{[1]} R_x (w_r^{[1]} - u_x^{[1]}) \ +$$
$$\mu^{[1]}(1 - (R_x)^2)(u_r^{[1]} - w_x^{[1]}), \tag{8.8}$$

$$2\mu^{[2]} S_x (w_r^{[2]} - u_x^{[2]}) + \mu^{[2]}(1 - (S_x)^2)(u_r^{[2]} - w_x^{[2]}) = 0 \tag{8.9}$$

and the normal conditions are given by

$$2\mu^{[2]}u_x^{[2]}(S_x)^2 + 2\mu^{[2]}w_r^{[2]} - 2\mu^{[2]}(u_r^{[2]} + w_x^{[2]})S_x + (p^A - p^{[2]})(1 + (S_x)^2)$$
$$= -\sigma^{[2]}\kappa_2(1 + (S_x)^2), \tag{8.10}$$

$$2\mu^{[2]}u_x^{[2]}(S_x)^2 + 2\mu^{[2]}w_r^{[2]} - 2\mu^{[2]}(u_r^{[2]} + w_x^{[2]})S_x + (p^{[1]} - p^{[2]})(1 + (R_x)^2)$$
$$-2\mu^{[1]}u_x^{[1]}(R_x)^2 - 2\mu^{[1]}w_r^{[1]} - 2\mu^{[1]}(u_r^{[1]} + w_x^{[1]})R_x = \sigma^{[1]}\kappa_1(1 + (R_x)^2), \tag{8.11}$$

here

$$\kappa_1 = \frac{1}{\Gamma_R R} - \frac{R_{xx}}{\Gamma_R^3} \tag{8.12}$$

and

$$\kappa_2 = \frac{1}{\Gamma_S S} - \frac{S_{xx}}{\Gamma_S^3} \tag{8.13}$$

are the radii of the curvature for inner and outer fluid interfaces with $\Gamma_R = (1 + (R_x)^2)^{1/2}$ and $\Gamma_S = (1 + SR_x)^2)^{1/2}$. Assuming no slip condition therefore the velocities at the shared interface $r = R(x, t)$ are continuous that is

$$u^{[1]} \cdot \mathbf{n} = u^{[2]} \cdot \mathbf{n} \quad \text{and} \quad u^{[1]} \cdot \mathbf{t} = u^{[2]} \cdot \mathbf{t}, \tag{8.14}$$

where $\mathbf{n}$ and $\mathbf{t}$ are the unit normal and tangent vectors to the interface $r = R(x, t)$. The governing equations $(8.1) - (8.13)$ can be non-dimensionalised with the help of following

scaling

$$
\bar{x} = \frac{x}{L}, \quad \bar{u}^{[z]} = \frac{u^{[z]}}{U}, \quad \bar{w}^{[k]} = \frac{w^{[z]}L}{Ua},
$$
$$
\bar{t} = \frac{tU}{L}, \quad \bar{r} = \frac{r}{a}, \quad \bar{p}^{[z]} = \frac{p^{[z]}}{\rho^{[2]}U^2},
$$

where U is the exit velocity of the jet, a is the outer jet radius and L is the typical axial length of the jet. Moreover, we let $\frac{a}{L} = \varepsilon << 1$ which is the slender jet assumption. The dimensionless continuity and Navier-Stokes equations are given by

$$
w_r^{[z]} + u_x^{[z]} + \frac{w^{[z]}}{r} = 0, \tag{8.15}
$$

$$
\frac{\rho^{[z]}}{\rho^{[2]}} \left(u_t^{[z]} + u^{[z]}u_x^{[z]} + w^{[z]}u_r^{[z]} \right) = -p_x^{[z]} + \frac{\mu^{[z]}}{\mu^{[2]}Re} \left(u_{xx}^{[z]} + \varepsilon^{-2}\frac{1}{r} \left(ru_r^{[z]} \right)_r \right), \tag{8.16}
$$

$$
\frac{\rho^{[z]}}{\rho^{[2]}} \left(w_t^{[z]} + u^{[z]}w_x^{[z]} + w^{[k]}w_r^{[z]} \right) = -\varepsilon^2 p_r^{[k]} + \frac{\mu^{[k]}}{\mu^{[2]}Re} \left(w_{xx}^{[z]} + \varepsilon^2 \left((w_r^{[z]}/r) - (w^{[z]}/r^2) + w_{rr}^{[k]} \right) \right), \tag{8.17}
$$

where $Re = \rho^{[2]}LU/\mu^{[2]}$ is the Reynolds number. The kinematic conditions used at the two jet interfaces $r = R(x,t)$ and $r = S(x,t)$ will take the form

$$
w^{[1]}(R,x,t) = R_t + u^{[1]}(R,x,t)R_x \quad , \quad w^{[2]}(R,x,t) = R_t + u^{[2]}(R,x,t)R_x \tag{8.18}
$$

and

$$
w^{[2]}(S,x,t) = S_t + u^{[2]}(S,x,t)S_x. \tag{8.19}
$$

110

The dimensionless tangential stress conditions at each interface are given by

$$\frac{1}{\mu}\left(2\varepsilon^2 R_x(w_r^{[2]} - u_x^{[2]}) + (1 - \varepsilon^2(R_x)^2)(u_r^{[2]} - \varepsilon^2 w_x^{[2]})\right) = 2\varepsilon^2 R_x(w_r^{[1]} - u_x^{[1]}) +$$

$$(1 - \varepsilon^2(R_x)^2)(u_r^{[1]} - \varepsilon^2 w_x^{[1]}) \quad \text{at} \quad r = R(x,t), \quad (8.20)$$

$$2\varepsilon^2 S_x(w_r^{[2]} - u_x^{[2]}) + (1 - \varepsilon^2(S_x)^2)(u_r^{[2]} - \varepsilon^2 w_x^{[2]}) = 0 \quad \text{at} \quad r = S(x,t). \quad (8.21)$$

Similarly, the normal stress conditions can be written as

$$\frac{2}{Re(1 + \varepsilon^2(S_x)^2)}\left(\varepsilon^2 u_x^{[2]}(S_x)^2 + w_r^{[2]} - (u_r^{[2]} + \varepsilon^2 w_x^{[2]})S_x\right) + (p^A - p^{[2]})$$

$$= -\frac{1}{We}\left(\frac{1}{\Gamma_S S} - \frac{\varepsilon^2 S_{xx}}{\Gamma_S^3}\right) \quad \text{at} \quad r = S(x,t), \quad (8.22)$$

$$\frac{2}{Re(1 + \varepsilon^2(R_x)^2)}((\varepsilon^2 u_x^{[2]}(R_x)^2 + w_r^{[2]} - (u_r^{[2]} + \varepsilon^2 w_x^{[2]})R_x) - (\varepsilon^2 u_x^{[1]}(R_x)^2$$

$$+w_r^{[1]} - (u_r^{[1]} + \varepsilon^2 w_x^{[1]})R_x)) = (p^{[2]} - p^{[1]}) + \frac{\sigma}{We}\left(\frac{1}{\Gamma_R R} - \frac{\varepsilon^2 R_{xx}}{\Gamma_R^3}\right) \quad \text{at} \quad r = R(x,t),$$

$$(8.23)$$

where $\Gamma_R = (1 + \varepsilon^2(R_x)^2)^{1/2}$ and $\Gamma_S = (1 + \varepsilon^2(S_x)^2)^{1/2}$, $\sigma = \sigma^{[1]}/\sigma_{[2]}$ is the interfacial surface tension, $\rho = \rho^{[1]}/\rho^{[2]}$ is the density ratio, $\mu = \mu^{[1]}/\mu_{[2]}$ is the viscosity ratio and $We = \rho^{[2]}U^2 a/\sigma^{[2]}$ is the Weber number. Now, we will expand all the variables in the form

$$\zeta = \zeta_o + \varepsilon^2 \zeta_2 + \varepsilon^4 \zeta_4 + O(\varepsilon^6)$$

and assuming the leading order axial velocity components of both the fluids are independent of radial direction. Similar expansions are applied by Ramos [69] and Craster *et*

al. [18].

8.2 Leading order solutions

Substituting the expansion in equations $(8.15) - (8.23)$, as a result we obtain the equations into leading order form. The leading order continuity equation is

$$u_{0x}^{[z]} + \frac{1}{r}(rw_0^{[z]})_r = 0, \tag{8.24}$$

writing $u_0^{[z]} = U_i(x,t)$ which implies $w_0^{[z]} = C_z/r - rU_{z_x}/2$ where $C_z = C_z(x,t)$. As the disturbances are assumed to be axisymmetric, we require a condition on the radial velocity such that $w^{[1]} = 0$ at $r = 0$ hence we require $C_1(x,t) = 0$. The leading order kinematic conditions are

$$w_0^{[1]}(R,x,t) = R_t + U_1R_x, \quad w_0^{[1]}(R,x,t) = R_t + U_2R_x, \tag{8.25}$$

$$w_0^{[2]}(S,x,t) = S_t + U_2S_x. \tag{8.26}$$

We can also write these equations as

$$(R^2)_t + (R^2U_1)_x = 0, \tag{8.27}$$

$$(R^2 - S^2)_t + ((R^2 - S^2)U_2)_x = 4C_2. \tag{8.28}$$

112

The velocities of the inner and the outer fluid must be continuous at $r = R(x,t)$ because we are dealing with the viscous fluids which implies

$$u_0^{[1]}(x,t) = u_0^{[2]}(x,t), \quad u_2^{[1]}(R,x,t) = u_2^{[2]}(R,x,t). \tag{8.29}$$

Since we assume that the leading order axial velocities are independent of r, therefore we can take $U_1(x,t) = U_2(x,t) = U(x,t)$, so we have $C_1(x,t) = C_2(x,t) = 0$. The normal stress at $r = S(x,t)$ will be

$$(p^A - p^{[2]}) + \frac{2}{Re} w_{0_r}^{[2]} = -\frac{1}{We}\kappa_2. \tag{8.30}$$

After putting the value of $w_0^{[2]}$ from equation (8.24), we get

$$(p^A - p^{[2]}) + \frac{1}{Re} U_x = -\frac{1}{We}\kappa_2 \tag{8.31}$$

and the normal stress at $r = R(x,t)$ gives

$$(p^{[1]} - p^{[2]}) + \frac{U_x}{Re}(1 - \mu) = -\frac{\sigma}{We}\kappa_1. \tag{8.32}$$

By ignoring the ambient air pressure of the surrounding p^A, we can write the above equations as

$$p^{[2]} = \frac{1}{We}\kappa_2 - \frac{1}{Re}U_x, \tag{8.33}$$

$$p^{[1]} = \frac{1}{We}(\kappa_2 + \sigma\kappa_1) - \frac{\mu}{\rho Re}U_x. \tag{8.34}$$

113

The leading order tangential conditions are

$$u_{0_r}^{[2]} = 0 \quad \text{and} \quad u_{0_r}^{[1]} = 0 \tag{8.35}$$

respectively. The axial equation (8.16) at O(1) is given by

$$\frac{Re\mu^{[2]}}{\mu^{[z]}} \left(\frac{\rho^{[z]}}{\rho^{[2]}}(U_t + UU_x) - p_{0x}^{[z]} \right) - U_{xx} = \frac{1}{r} \left(ru_{2r}^{[z]} \right)_r. \tag{8.36}$$

The general solutions for $u_2^{[1]}$ and $u_2^{[2]}$ will be

$$u_2^{[z]} = A_z(x,t)\frac{r^2}{4} + B_z(x,t)logr + C_z(x,t), \tag{8.37}$$

where

$$A_z(x,t) = \frac{Re\mu^{[2]}}{\mu^{[z]}}(\frac{\rho^{[z]}}{\rho^2}(U_t + UU_x) - p_{0x}^{[z]}) - U_{xx}. \tag{8.38}$$

For the inner fluid, we must have the following conditions

$$u_r^{[1]}(0,x,t) = 0 \quad \text{and} \quad w^{[1]}(0,x,t) = 0. \tag{8.39}$$

In order to avoid the singularity on $u_2^{[1]}$ as $r \longrightarrow 0$, we must take $B_1 = 0$. The tangential stress condition of $O(\varepsilon^2)$ at $r = S(x,t)$ gives

$$2S_{0x}(w_{0r}^{[2]} - U_x) + (u_{2r}^{[2]} + w_{0x}^{[2]}) = 0, \tag{8.40}$$

we substitute the above equation and use (8.37) to obtain the expression for B_2 as

$$B_2 = 3S_0S_{0x}U_x + \frac{S_0^2}{2}U_{xx} - \frac{S_0^2}{2}A_2. \tag{8.41}$$

114

The tangential stress condition at $r = R(x,t)$ gives at $O(\varepsilon^2)$

$$3R_0 R_{0x} U_x + \frac{R_0^2}{2} U_{xx} - \frac{R_0^2}{2} A_2 - B_2 = \mu \left(3R_0 R_{0x} U_x + \frac{R_0^2}{2} U_{xx} - \frac{R_0^2}{2} A_1 \right). \qquad (8.42)$$

Substituting the values of B_2, A_1 and A_2 in equation (8.42), we get

$$(S_0^2 + (\rho - 1)R_0^2)(U_t + UU_x) = -\frac{1}{We}(S_0^2 \kappa_{2x} + \sigma R_0^2 \kappa_{1x})$$
$$+ \frac{3}{Re} \left[((S_0^2 + (\mu - 1)R_0^2)U_x)_x \right]. \qquad (8.43)$$

Removing the subscripts, the final form of momentum equation and kinematic equations are given by

$$(S^2 + (\rho - 1)R^2)(U_t + UU_x) = -\frac{1}{We}(S^2 \kappa_{2x} + \sigma R_0^2 \kappa_{1x})$$
$$+ \frac{3}{Re}[((S^2 + (\mu - 1)R^2)U_x)_x], \qquad (8.44)$$

$$(R^2)_t + (R^2 U_1)_x = 0, \qquad (8.45)$$

$$(R^2 - S^2)_t + ((R^2 - S^2)U_2)_x = 0. \qquad (8.46)$$

8.3   Linear Instability Analysis

In this section we will perform the linear instability analysis of viscous compound jet. For this purpose, we will consider the traveling wave mode of the form $exp(ik\overline{x} + \lambda \overline{t})$ where $\overline{x} = \frac{x}{\varepsilon}$ and $\overline{t} = \frac{t}{\varepsilon}$ are the small time and length scales, k is the wavenumber and λ is the frequency of disturbance. The basic state solutions of above system of equations $(8.44) - (8.46)$ will be $U = S = 1$ and $R = \chi$. Now we will introduce time dependent

perturbations to the steady state solutions which will take the form

$$U = 1 + \delta \exp(\lambda \bar{t} + ik\bar{x})\widehat{U'}, \tag{8.47}$$

$$R = \chi + \delta \exp(\lambda \bar{t} + ik\bar{x})\widehat{R'}, \tag{8.48}$$

$$S = 1 + \delta \exp(\lambda \bar{t} + ik\bar{x})\widehat{S'}, \tag{8.49}$$

where δ is the small amplitude of the wave at the orifice.

To study the effects of viscosity on compound liquid jet we need to rescale the Reynolds number, $\overline{Re} = \varepsilon Re$, as done by Uddin [87] in the case of curved liquid jets otherwise we cannot bring the viscous term into the resulting equations. Moreover, the complete expression of the mean curvature is required to prevent instability to modes with zero wavelength and it is used by many authors, for example Eggers [25], Lee [42] and Garcia & Castellanos [28].

8.3.1   Dispersion Relation

In order to obtain the dispersion relation, substituting the time dependent perturbed solutions $(8.47) - (8.49)$ into equations $(8.44) - (8.46)$ and choosing the linear terms of δ, we are able to get the following result

$$(\lambda + ikU_0)^2 + \frac{3(1 + (\mu - 1)\chi^2)k^2}{(1 + (\rho - 1)\chi^2)Re}(\lambda + ikU_0) -$$
$$\frac{k^2}{2(1 + (\rho - 1)\chi^2)We}[(1 - k^2) + \sigma\chi(1 - k^2\chi^2)] = 0. \tag{8.50}$$

The above dispersion relation can be considered in two different ways, either by spatial instability analysis or by temporal instability analysis. In the case of spatial instability analysis the perturbations grow or decay in space over the jet and we will solve the dispersion relation for k. Here k is taken as a complex, that is, $k = k_r + ik_i$ and λ is

supposed to be imaginary, that is, $\lambda = i\omega$, where k_r is wavenumber, k_i is spatial growth rate and ω is real frequency. In temporal instability analysis the disturbances are assumed to grow in time along the surface of jet. In this case λ is supposed to be complex, that is, $\lambda = \lambda_r + \lambda_i$ and k is taken as a real, where λ_r is the temporal growth rate, λ_i is the frequency and k is the wavenumber. In this section, we perform temporal instability analysis by letting complex λ and real k. Therefore, the dispersion relation will be solved for λ and its solution is given by

$$\lambda_r = -\frac{3(1 + (\mu - 1)\chi^2)k^2}{2(1 + (\rho - 1)\chi^2)Re} +$$

$$\frac{k}{2}\sqrt{(-\frac{3(1 + (\mu - 1)\chi^2)k}{(1 + (\rho - 1)\chi_0^2)Re})^2 + \frac{2}{(1 + (\rho - 1)\chi_0^2)We}[(1 - k^2) + \sigma\chi(1 - k^2\chi^2)]}. \quad (8.51)$$

Differentiating the equation (8.51) with respect to k and then solving for k, we find the wavenumber for which λ_r is maximum. As a result, we have

$$K_{max} = \frac{1}{(2(1 + \sigma\chi^3))^{1/4}}\sqrt{\frac{1 + \sigma\chi}{\sqrt{2(1 + \sigma\chi^3)} + \frac{3Oh(1 + (\mu - 1)\chi_0^2}{\sqrt{1 + (\rho - 1)\chi^2}}}}, \quad (8.52)$$

where Oh is Ohnesorge number which is equal to $Oh = \sqrt{We}/Re$.

8.4 Discussion

The numerical results of equation (8.51) are shown in Figs. $8.1 - 8.6$. In Fig. 8.1, we show the growth rate of disturbances against the wavenumber for three different values of inner to outer jet radii ratio. We notice that the growth rate of disturbances is increased by increasing the inner to outer jet radii ratio. In Figs. 8.2 and 8.3 we analyze the

117
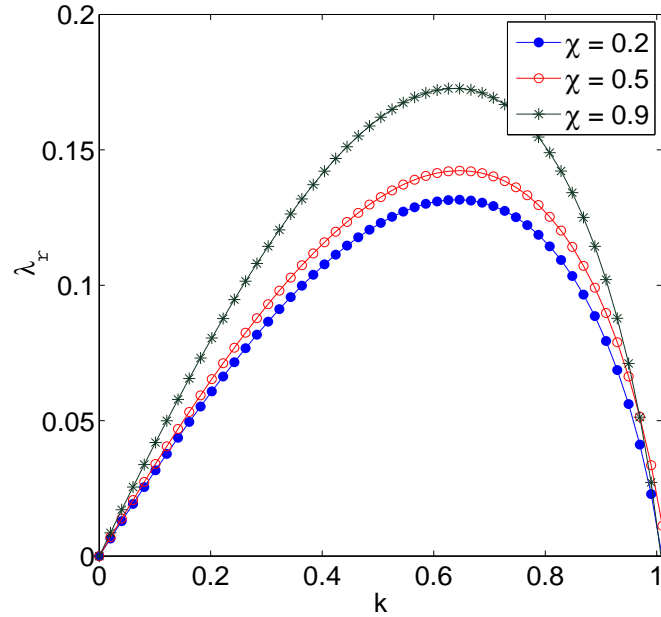
Figure 8.1: Growth rate of disturbances against the wavenumber for two different values of inner to outer radii ratio, where $\rho = 0.5$, $We = 10$, $\overline{Re} = 20$, $\sigma = 0.1$ and $\mu = 0.8$.

behavior of the Reynolds number and density ratio on the growth rate of disturbances and it is clearly seen that the growth rate of disturbances becomes large by increasing the Reynolds number and vice versa for the case of the density ratio. Similar plots are produced for two different values of the Weber number, viscosity ratio and surface tension ratio in Figs. $8.4 - 8.6$ respectively. The increase in the density and the Weber number lead to decrease the growth rate of disturbances, but the growth rate of disturbances and the cut-off wavenumber increase with the increase in surface tension ratio.

The relationship between the maximum growth rate of disturbances and the inner to outer radii ratios for different values of the surface tension ratio is depicted in Fig. 8.7. Here we observe that the maximum growth rate of disturbances increases with the increase in surface tension ratio. In Fig. 8.8, the plots are presented between maximum growth rate of disturbances and the viscosity ratios for different values of Ohnesorge number, here we notice that the increase in Ohnesorge number lead to decrease the maximum growth
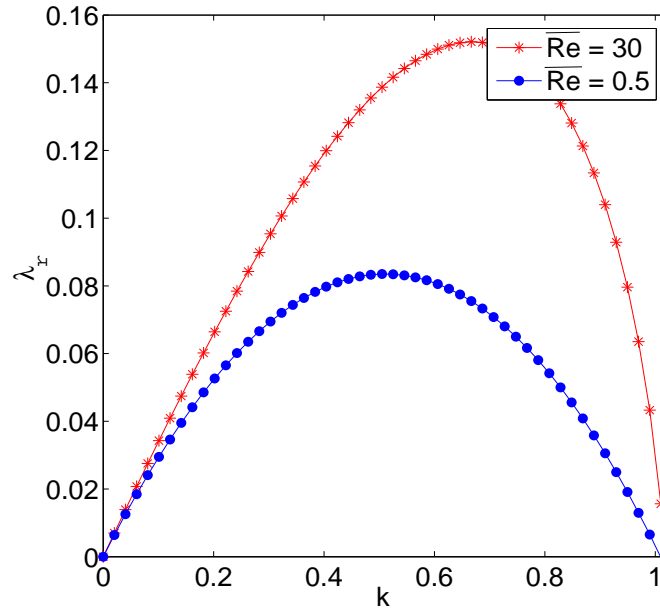
Figure 8.2: Growth rate of disturbances against the wavenumber for two different values of the Reynolds number, where $\chi = 0.5$, $We = 10$, $\sigma = 0.1$, $\rho = 0.5$ and $\mu = 0.8$.
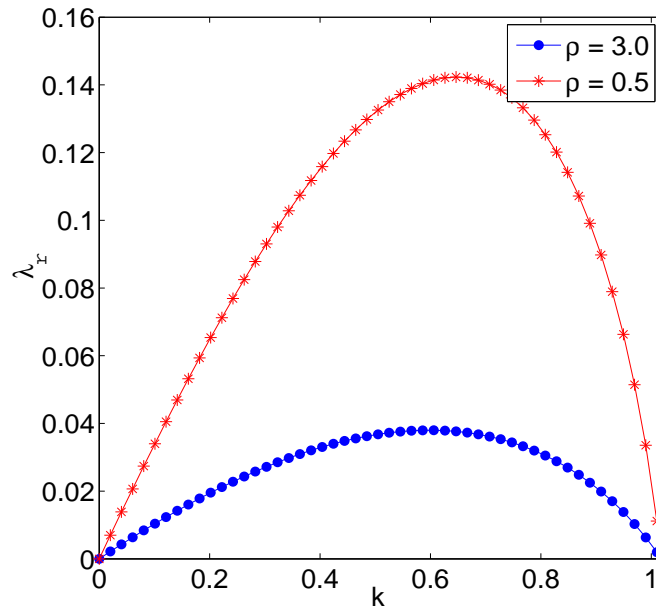
Figure 8.3: Growth rate of disturbances against the wavenumber for two different values of density ratio, where $\sigma = 0.1$, $We = 10$, $\overline{Re} = 20$, $\chi = 0.5$ and $\mu = 0.8$.
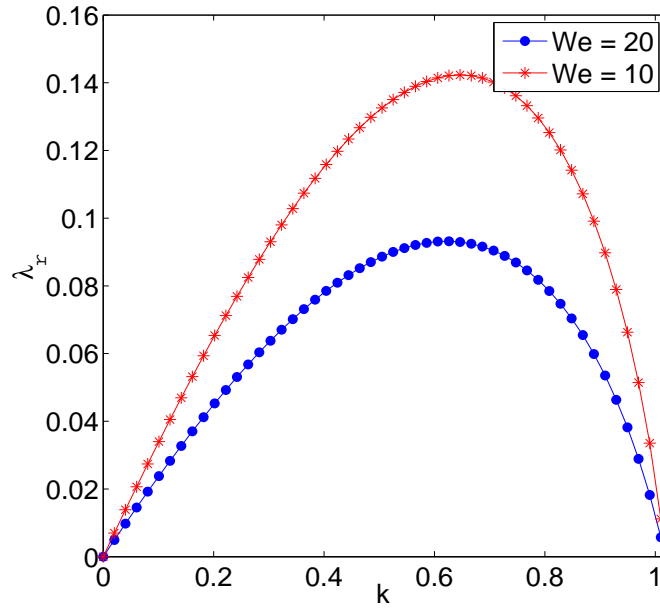
Figure 8.4: Growth rate of disturbances against the wavenumber for two different values of the Weber number, where $\rho = 0.5$, $\chi = 0.5$, $\overline{Re} = 20$, $\sigma = 0.1$ and $\mu = 0.8$.
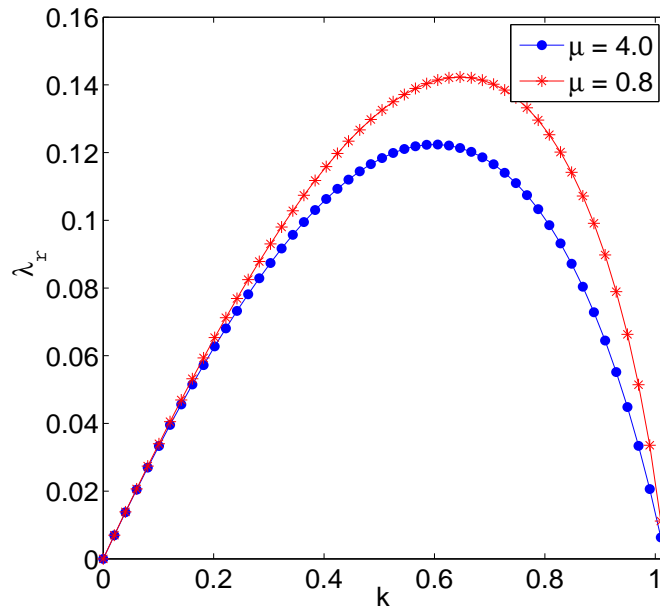
Figure 8.5: Growth rate of disturbances against wavenumber for two different values of the viscosity ratio, where $\rho = 0.5$, $We = 10$, $\overline{Re} = 20$, $\sigma = 0.1$ and $\chi = 0.5$.

120
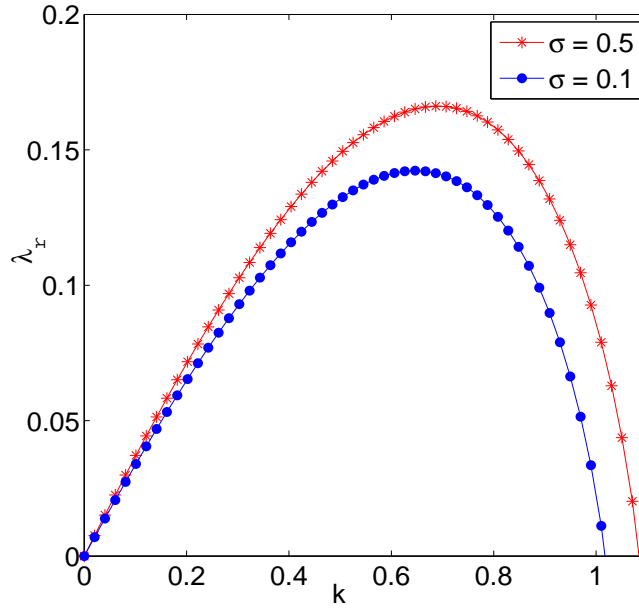
Figure 8.6: Growth rate of disturbances against the wavenumber for two different values of the surface tension ratio, where $\rho = 0.5$, $We = 10$, $\overline{Re} = 20$, $\chi = 0.5$ and $\mu = 0.8$.

rate of disturbances. We also present the graphical results for the maximum growth rate of disturbances against the density ratios for different values of the surface tension ratio in Fig. 8.9 and the maximum growth rate of disturbances against Ohnesorge number for different values of the density ratio in Fig. 8.10. From Fig. 8.9, we can say that the maximum growth rate of disturbances is increased with the surface tension ratio but small effects are noticed with the increase in density ratio as shown in Fig. 8.10. We also check the maximum growth rate of disturbance against the surface tension ratio for different values of the viscosity ratio in Fig. 8.11 and analyze that the maximum growth of disturbance is decreased by increasing the viscosity ratio.

The maximum wavenumber versus inner to outer radii ratio χ for various values of σ is shown in Fig. 8.12. We notice a non-monotonic behavior of a maximum wavenumber for the case of different radii ratios χ. In Fig. 8.13, we present the maximum wavenumber by varying the viscosity ratio μ and Ohnesorge number. We observe that the maximum
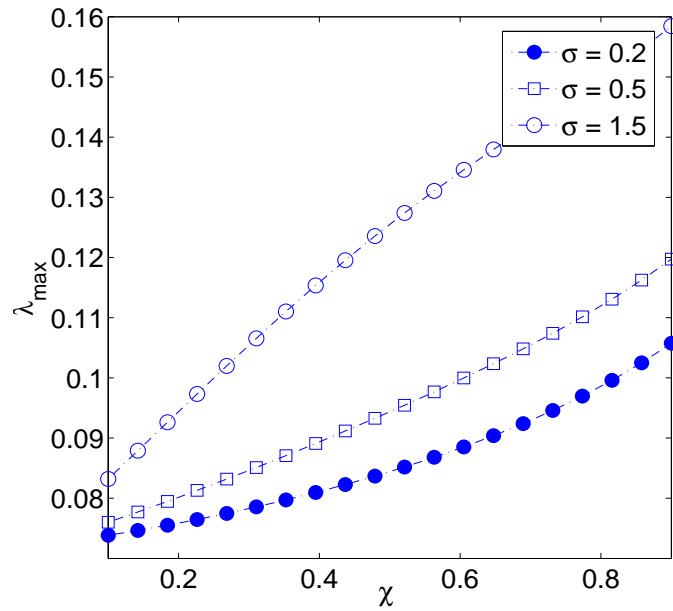
Figure 8.7: Graph showing the maximum growth rate of disturbances against inner to outer radii ratios for different values of the surface tension ratio, where $We = 20$, $Oh = 0.149$, $\rho = 0.5$ and $\mu = 0.5$.
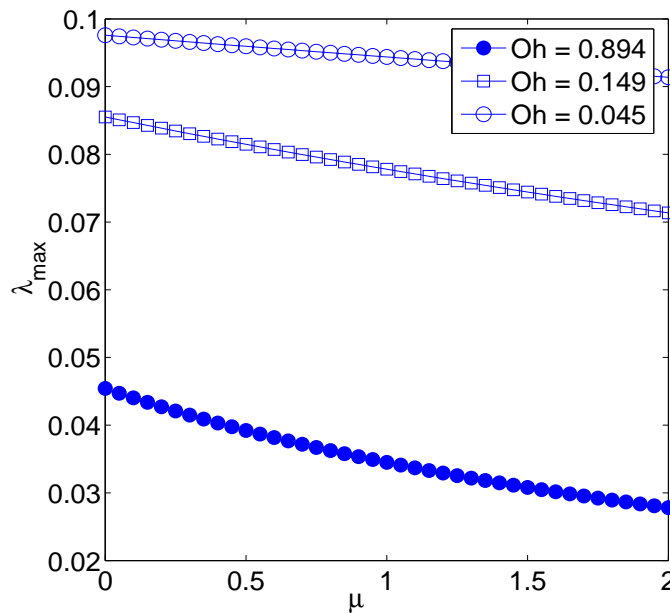
Figure 8.8: Graph showing the maximum growth rate of disturbances against the viscosity ratios for different values of the Ohnesorge number, where $We = 20$, $\sigma = 0.4$, $\rho = 0.5$ and $\chi = 0.6$.
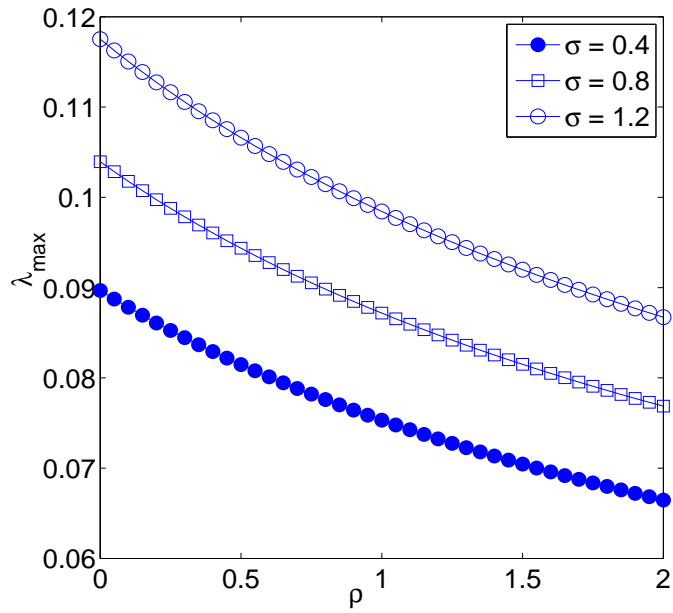
Figure 8.9: Graph showing the maximum growth rate of disturbances against the density ratios for different values of the surface tension ratio, where $We = 20$, $Oh = 0.149$, $\chi = 0.6$ and $\mu = 0.5$.
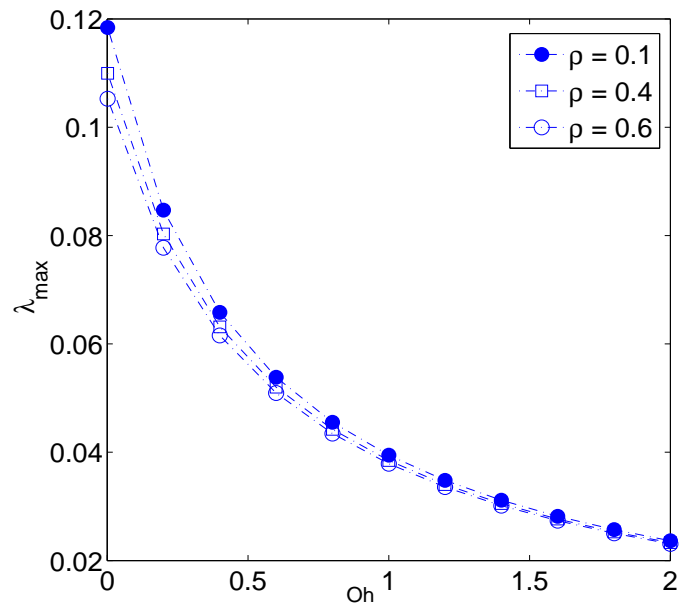
Figure 8.10: Graph showing the maximum growth rate of disturbances against the Ohnesorge number for different values of the density ratio, where $We = 20$, $\sigma = 0.4$, $\chi = 0.6$ and $\mu = 0.5$.
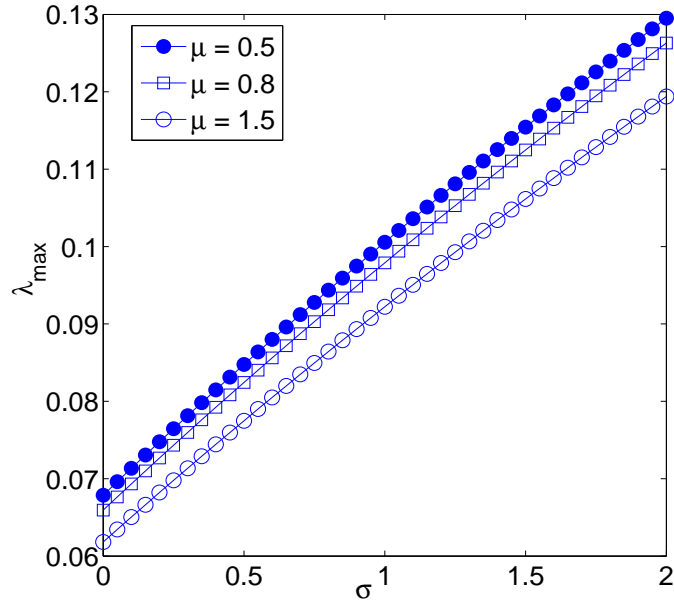
Figure 8.11: Graph showing the maximum growth rate of disturbances against the surface tension ratios for different values of the viscosity ratio, where $We = 20$, $\rho = 0.5$, $\chi = 0.6$ and $Oh = 0.149$.

wavenumber increases with the surface tension ratio σ but reduces with the Ohnesorge number and the viscosity ratioμ. In Fig. 8.14, we display the numerical results between the maximum wavenumber K_{max} and the Ohnesorge number for three different values of the density ratio ρ. We see that k_{max} increases with the density ratio ρ and decreases for the higher values of Ohnesorge number. Furthermore, we provide the numerical results of the K_{max} for the given values of σ and ρ together in Fig. 8.15 and notice that an increase in the values of σ and ρ leads to increase the K_{max} which means the size of the drop becomes smaller as we increase the density ratio between the fluids and the surface tension ratio. From the Fig. 8.16, we can say that higher viscosity ratio μ between the fluids reduces the most unstable mode of disturbances.
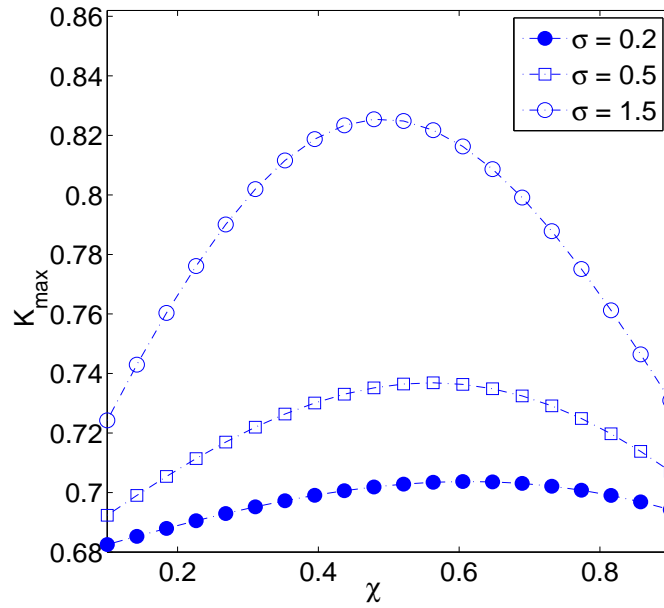
Figure 8.12: Graph showing the maximum wavenumber against inner to outer radii ratios for different values of the surface tension ratio, where $We = 20$, $Oh = 0.149$, $\rho = 0.5$ and $\mu = 0.5$.
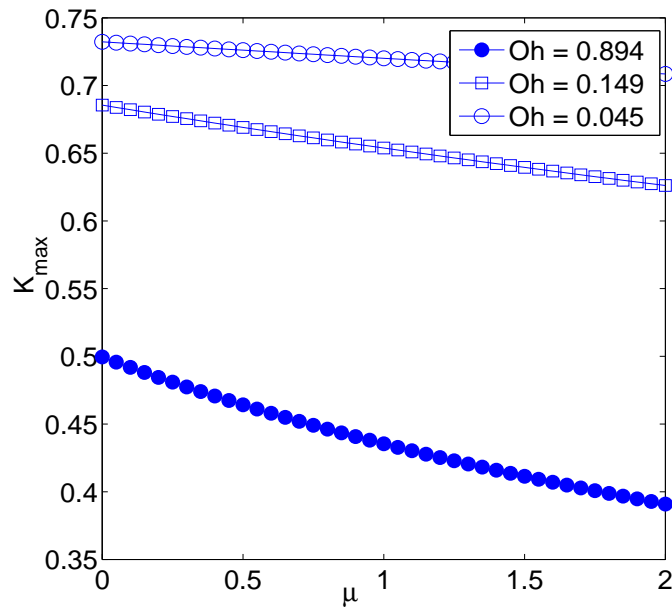
Figure 8.13: Graph showing the maximum wavenumber against viscosity ratios for different values of ohnesorge number, where $We = 20$, $\sigma = 0.4$, $\rho = 0.5$ and $\chi = 0.6$.
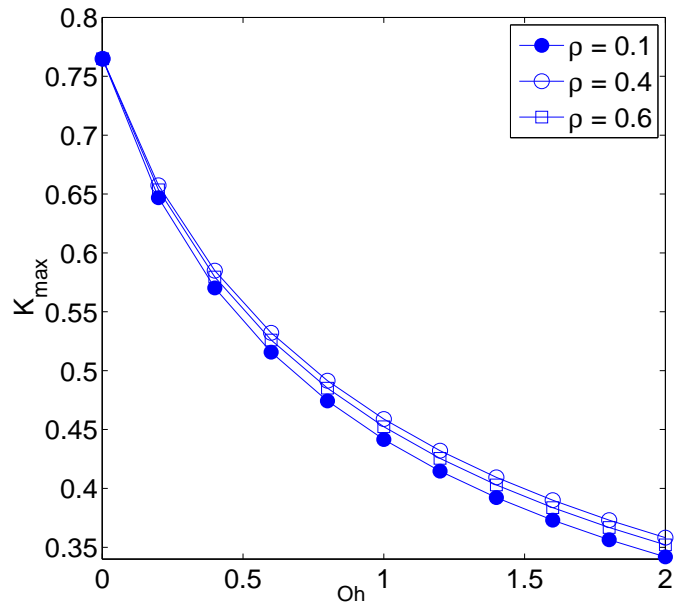
Figure 8.14: Graph showing the maximum wavenumber against the Ohnesorge number for different values of the density ratio, where $We = 20$, $\sigma = 0.4$, $\chi = 0.6$ and $\mu = 0.5$.
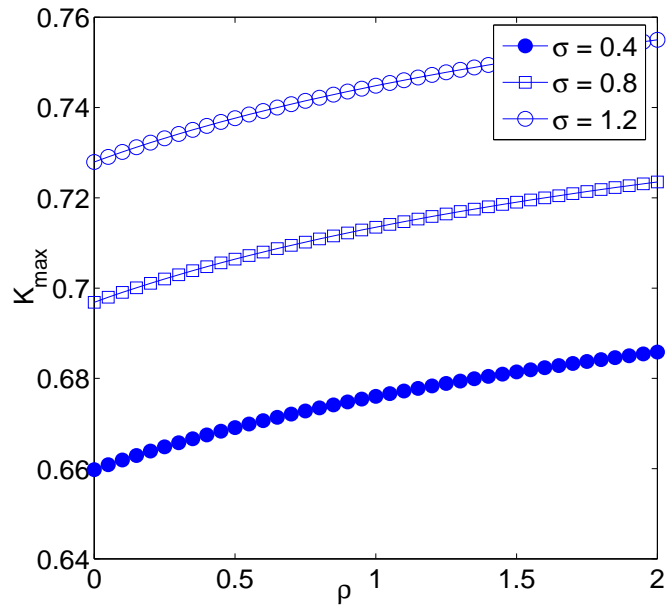
Figure 8.15: Graph showing the maximum wavenumber against the density ratios for different values of the surface tension ratio, where $We = 20$, $Oh = 0.149$, $\chi = 0.6$ and $\mu = 0.5$.
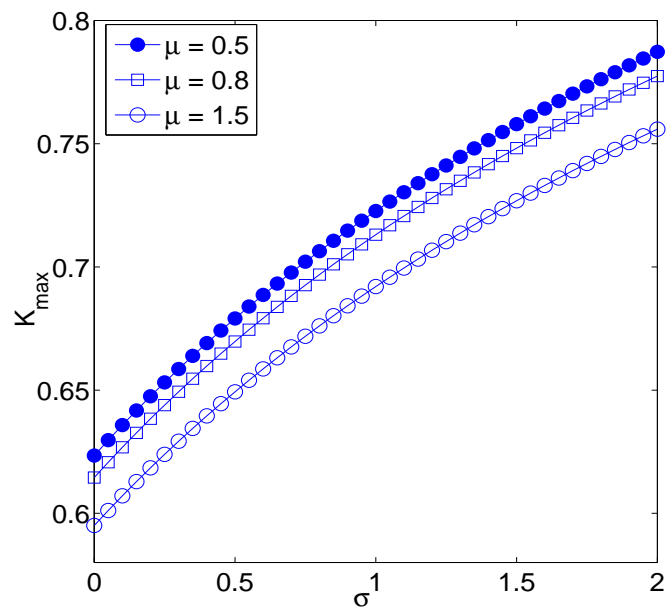
Figure 8.16: Graph showing the maximum wavenumber against the surface tension ratios for different values of the viscosity ratio, where $We = 20$, $\rho = 0.5$, $\chi = 0.6$ and $Oh = 0.149$.

CHAPTER 9

ANALYSIS OF VISCOUS COMPOUND JET

IN THE PRESENCE OF GRAVITY

9.1 Problem Formulation

In this chapter, we will consider the viscous compound jet falling under gravity. Here, we will examine that how gravity affects the instability and breakup of a viscous compound jet. In the presence of gravity, the dimensionless continuity equation and the Navier-Stokes equation can be written as

$$w_r^{[z]} + u_x^{[z]} + \frac{w^{[z]}}{r} = 0, \tag{9.1}$$

$$\frac{\rho^{[z]}}{\rho^{[2]}} \left(u_t^{[z]} + u^{[z]}u_x^{[z]} + w^{[z]}u_r^{[z]} \right) = -p_x^{[z]} + \frac{\mu^{[z]}}{\mu^{[2]}Re} \left(u_{xx}^{[z]} + \varepsilon^{-2}\frac{1}{r}\left(ru_r^{[z]}\right)_r \right) + \frac{1}{F^2}, \tag{9.2}$$

$$\frac{\rho^{[z]}}{\rho^{[2]}} \left(w_t^{[z]} + u^{[z]}w_x^{[z]} + w^{[k]}w_r^{[z]} \right) = -\varepsilon^2 p_r^{[k]} + \frac{\mu^{[k]}}{\mu^{[2]}Re} \left(w_{xx}^{[z]} + \varepsilon^2 \left((w_r^{[z]}//r) - (w^{[z]}/r^2) + w_{rr}^{[k]} \right) \right), \tag{9.3}$$

where $Re = \rho^{[2]} LU/\mu^{[2]}$ is Reynolds number and $F = U/\sqrt{Lg}$ is Froude number.

The kinematic conditions applied at the inner and outer interfaces are

$$w^{[1]}(R, x, t) = R_t + u^{[1]}(R, x, t)R_x \ \text{ and } \ w^{[2]}(R, x, t) = R_t + u^{[2]}(R, x, t)R_x, \quad (9.4)$$

$$w^{[2]}(S, x, t) = S_t + u^{[2]}(S, x, t)S_x. \quad (9.5)$$

The non dimensional tangential stress conditions can be written as

$$\frac{1}{\mu} \left(2\varepsilon^2 R_x(w_r^{[2]} - u_x^{[2]}) + (1 - \varepsilon^2(R_x)^2)(u_r^{[2]} - \varepsilon^2 w_x^{[2]}) \right) = 2\varepsilon^2 R_x(w_r^{[1]} - u_x^{[1]}) \ +$$
$$(1 - \varepsilon^2(R_x)^2)(u_r^{[1]} - \varepsilon^2 w_x^{[1]}) \quad \text{at} \ r = R(x, t), \quad (9.6)$$

$$2\varepsilon^2 S_x(w_r^{[2]} - u_x^{[2]}) + (1 - \varepsilon^2(S_x)^2)(u_r^{[2]} - \varepsilon^2 w_x^{[2]}) = 0 \quad \text{at} \ r = S(x, t) \quad (9.7)$$

and normal stress conditions are given by

$$\frac{2}{Re(1 + \varepsilon^2(S_x)^2)} \left(\varepsilon^2 u_x^{[2]}(S_x)^2 + w_r^{[2]} - (u_r^{[2]} + \varepsilon^2 w_x^{[2]})S_x \right) + (p^A - p^{[2]})$$
$$= -\frac{1}{We} \left(\frac{1}{\Gamma_S S} - \frac{\varepsilon^2 S_{xx}}{\Gamma_S^3} \right) \quad \text{at} \ r = S(x, t), \quad (9.8)$$

$$\frac{2}{Re(1 + \varepsilon^2(R_x)^2)} \left((\varepsilon^2 u_x^{[2]}(R_x)^2 + w_r^{[2]} - (u_r^{[2]} + \varepsilon^2 w_x^{[2]})R_x) - (\varepsilon^2 u_x^{[1]}(R_x)^2 \right.$$
$$+w_r^{[1]} - (u_r^{[1]} + \varepsilon^2 w_x^{[1]})R_x)) = (p^{[2]} - p^{[1]}) + \frac{\sigma}{We} \left(\frac{1}{\Gamma_R R} - \frac{\varepsilon^2 R_{xx}}{\Gamma_R^3} \right) \quad \text{at} \ r = R(x, t),$$

$$(9.9)$$

where $\Gamma_R = (1 + \varepsilon^2(R_x)^2)^{1/2}$ and $\Gamma_S = (1 + \varepsilon^2(S_x)^2)^{1/2}$, $\sigma = \sigma^{[1]}/\sigma_{[2]}$ is the interfacial surface tension, $\rho = \rho^{[1]}/\rho^{[2]}$ is the density ratio, $\mu = \mu^{[1]}/\mu_{[2]}$ is the viscosity ratio and

129

the $We = \rho^{[2]}U^2 a/\sigma^{[2]}$ is the Weber number. We now apply the following expansion

$$\zeta = \zeta_o + \varepsilon^2 \zeta_2 + \varepsilon^4 \zeta_4 + O(\varepsilon^6)$$

and assuming the axial velocity components inner and outer fluids are independent of radial direction. Introducing the above form of expansion in the equations $(9.1) - (9.9)$, the leading order of the continuity equation will be

$$u_{0x}^{[z]} + \frac{1}{r}(rw_0^{[z]})_r = 0, \tag{9.10}$$

writing $u_0^{[z]} = U_k(x,t)$ the above equation implies that $w_0^{[z]} = C_z/r - rU_{k_x}/2$, where $C_z = C_z(x,t)$. Here $C_1(x,t) = 0$ because $w^{[1]} = 0$ at $r = 0$. The leading order kinematic conditions are given by

$$w_0^{[1]}(R,x,t) = R_t + U_1 R_x \ , \ w_0^{[1]}(R,x,t) = R_t + U_2 R_x, \tag{9.11}$$

$$w_0^{[2]}(S,x,t) = S_t + U_2 S_x. \tag{9.12}$$

The above equations can be written in the following form

$$(R^2)_t + (R^2 U_1)_x = 0, \tag{9.13}$$

$$(R^2 - S^2)_t + ((R^2 - S^2)U_2)_x = 4C_2. \tag{9.14}$$

130

The velocities are continuous at the interface $r = R(x, t)$ which requires

$$u_0^{[1]}(x, t) = u_0^{[2]}(x, t) \quad , \quad u_2^{[1]}(R, x, t) = u_2^{[2]}(R, x, t). \tag{9.15}$$

Since the leading order axial velocities are independent of r, so we can write $U_1(x, t) = U_2(x, t) = U(x, t)$ which implies $C_1(x, t) = C_2(x, t) = 0$. The normal stress condition at $r = S(x, t)$ is given by

$$(p^A - p^{[2]}) + \frac{2}{Re} w_{0r}^{[2]} = -\frac{1}{We} \kappa_2. \tag{9.16}$$

By substituting the value of $w_0^{[2]}$ from the equation (9.10), we get

$$(p^A - p^{[2]}) + \frac{1}{Re} U_x = -\frac{1}{We} \kappa_2. \tag{9.17}$$

Similarly, we can write the normal stress at $r = R(x, t)$ as

$$(p^{[1]} - p^{[2]}) + \frac{U_x}{Re}(1 - \mu) = -\frac{\sigma}{We} \kappa_1. \tag{9.18}$$

By ignoring the ambient air pressure of the surrounding p^A, we can write the above equations can be written as

$$p^{[2]} = \frac{1}{We} \kappa_2 - \frac{1}{Re} U_x, \tag{9.19}$$

$$p^{[1]} = \frac{1}{We}(\kappa_2 + \sigma \kappa_1) - \frac{\mu}{\rho Re} U_x. \tag{9.20}$$

131

The leading order tangential conditions are

$$u_{0_r}^{[2]} = 0 \quad \text{and} \quad u_{0_r}^{[1]} = 0. \tag{9.21}$$

respectively. The axial momentum equation (9.2) at O(1) is

$$\frac{Re\mu^{[2]}}{\mu^{[z]}} \left(\frac{\rho^{[z]}}{\rho^{[2]}} (U_t + UU_x - \frac{1}{F^2}) - p_{0x}^{[z]} \right) - U_{xx} = \frac{1}{r} \left(ru_{2r}^{[z]} \right)_r. \tag{9.22}$$

The general solutions for $u_2^{[1]}$ and $u_2^{[2]}$ are

$$u_2^{[z]} = X_z(x, t)\frac{r^2}{4} + Y_z(x, t)logr + Z_k(x, t), \tag{9.23}$$

where

$$X_z(x, t) = \frac{Re\mu^{[2]}}{\mu^z} \left(\frac{\rho^{[z]}}{\rho^{[2]}} (U_t + UU_x - \frac{1}{F^2}) - p_{0x}^{[k]} \right) - U_{xx}. \tag{9.24}$$

The following conditions must be satisfied for the inner fluid

$$u_r^{[1]}(0, x, t) = 0 \quad \text{and} \quad w^{[1]}(0, x, t) = 0 \tag{9.25}$$

and Y_1 must be equal to zero, otherwise there will be singularity at $u_2^{[1]}$ for $r \longrightarrow 0$. The tangential stress condition of $O(\varepsilon^2)$ at $r = S(x, t)$ will be

$$2S_{0x}(w_{0r}^{[2]} - U_x) + (u_{2r}^{[2]} + w_{0x}^{[2]}) = 0. \tag{9.26}$$

Using (9.24) and (9.26), we arrive at the following expression

$$Y_2 = 3S_0S_{0x}U_x + \frac{S_0^2}{2}U_{xx} - \frac{S_0^2}{2}X_2. \tag{9.27}$$

132

The tangential stress condition of $O(\varepsilon^2)$ at $r = R(x,t)$ can be written as

$$3R_0 R_{0x} U_x + \frac{R_0^2}{2} U_{xx} - \frac{R_0^2}{2} X_2 - Y_2 = \mu \left(3R_0 R_{0x} U_x + \frac{R_0^2}{2} U_{xx} - \frac{R_0^2}{2} X_1 \right). \qquad (9.28)$$

Finally, Substitute the values of Y_2, X_1 and X_2 in equation (9.28), we have

$$(S_0^2 + (\rho - 1)R_0^2)(U_t + UU_x) = -\frac{1}{We}(S_0^2 \kappa_{2x} + \sigma R_0^2 \kappa_{1x})$$
$$+ \frac{3}{Re}\left[((S_0^2 + (\mu - 1)R_0^2)U_x)_x\right] + (S_0^2 + (\rho - 1)R_0^2)\frac{1}{F^2}. \qquad (9.29)$$

Removing the subscripts, the final form of momentum equation and kinematic conditions are given by

$$(S^2 + (\rho - 1)R^2)(U_t + UU_x - \frac{1}{F^2}) = -\frac{1}{We}(S^2 \kappa_{2x} + \sigma R_0^2 \kappa_{1x})$$
$$+ \frac{3}{Re}[((S^2 + (\mu - 1)R^2)U_x)_x], \qquad (9.30)$$

$$(R^2)_t + (R^2 U_1)_x = 0, \qquad (9.31)$$

$$(R^2 - S^2)_t + ((R^2 - S^2)U_2)_x = 0. \qquad (9.32)$$

Figure 9.1: Steady state solutions of a viscous compound jet for two different values of the Froude number, where $Re = 20, We = 10, \rho = 0.2, \mu = 0.8, \sigma = 0.6,$ and $\chi = 0.5$.

9.2 Steady State Solutions

By using initial conditions (i.e. $U = S = 1$ and $R = \chi$), equations $(9.30) - (9.32)$ can be written into the steady-state form as,

$$(S^2 + (\rho - 1)R^2)(UU_x - \frac{1}{F^2}) = -\frac{1}{We}(S^2\kappa_{2x} + \sigma R^2\kappa_{1x}) \qquad (9.33)$$
$$+\frac{3}{Re}[((S^2 + (\mu - 1)R^2)U_x)_x],$$

$$R = \frac{\chi}{U^{1/2}} \quad \text{and} \quad S = \frac{1}{U^{1/2}}. \qquad (9.34)$$

To obtain the steady state solutions, we substitute the values of R and S in the equation (9.33) and then apply a second order finite difference scheme to discretize the equation

Figure 9.2: Steady state solutions of a viscous compound jet for two different values of the inner to outer radii ratio, where $Re = 20, We = 10, \rho = 0.2, \mu = 0.8, \sigma = 0.6$, and $F = 1$.
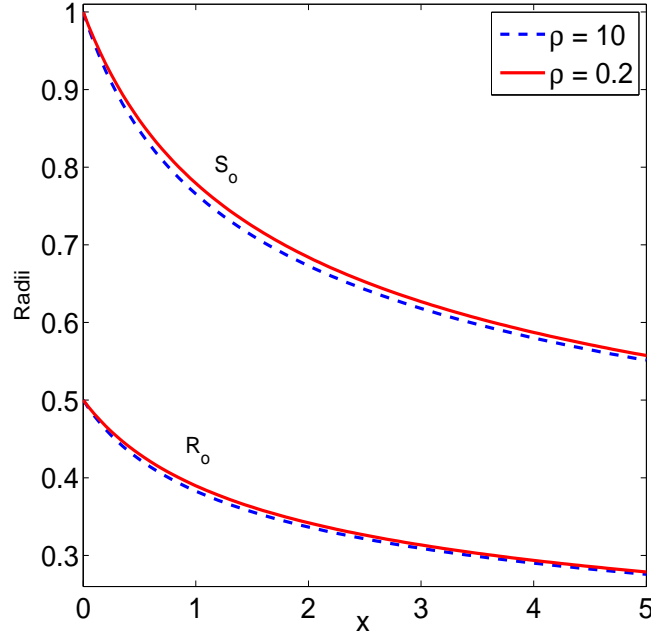
Figure 9.3: Steady state solutions of a viscous compound jet for two different values of the density ratio, where $Re = 20, We = 10, F = 1, \mu = 0.8, \sigma = 0.6,$ and $\chi = 0.5$.

(9.33). We specify the boundary condition at the nozzle as $U(0) = 1$ and downstream boundary condition is obtained by quadratic extrapolation of the last interval mash point. The nonlinear equation (9.33) is solved at each step using a modified Newton's method. It is important to mention that we only compute the Jacobian for the first iteration, so the guess at the next step uses the previous calculated solution. A similar approach is used by Parau [59], for the case of the curved liquid jets. The numerical accuracy can be checked by varying the grid interval ds and mash points N and it was found that the results are dependent of ds and N when $ds \leqslant 0.1$ and $N \geqslant 200$.

The steady state solutions of viscous compound jet falling under gravity have been presented in Figs. $9.1 - 9.7$. Figure. 9.1 show that the inner and outer radii of a viscous compound jet are reduced by decreasing the Froude number that means the velocity of inner and outer column of fluid increases with gravity. The outer radius of the compound
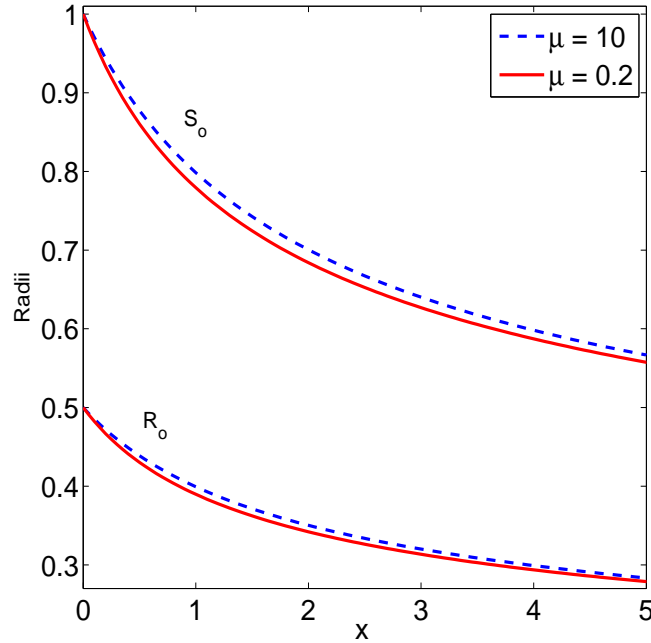
Figure 9.4: Steady state solutions of a viscous compound jet for two different values of the viscosity ratio, where $Re = 20, We = 10, \rho = 0.2, F = 1, \sigma = 0.6$, and $\chi = 0.5$.

jet is not affected by changing the inner radius as shown in Fig. 9.2

Figures $9.3 - 9.5$ depict that the radii of the jet are decreased with the increase in the density ratio, while an increase in the viscosity ratio and surface tension ratio lead to increase the inner and outer radius of the compound jet. We also check the effects of the Reynolds number and the Weber number on the radii of a compound jet and display the graphical results in the Fig. 9.6 and Fig. 9.7 respectively. Clearly, it can be seen that the radii of inner and outer column of the fluid decrease by increasing the Reynolds number and Weber number.

9.3   Linear Instability Analysis

In this section, we will examine the temporal instability of a viscous compound jet falling under the influence of gravity. In order to perform this analysis we will perturb our steady
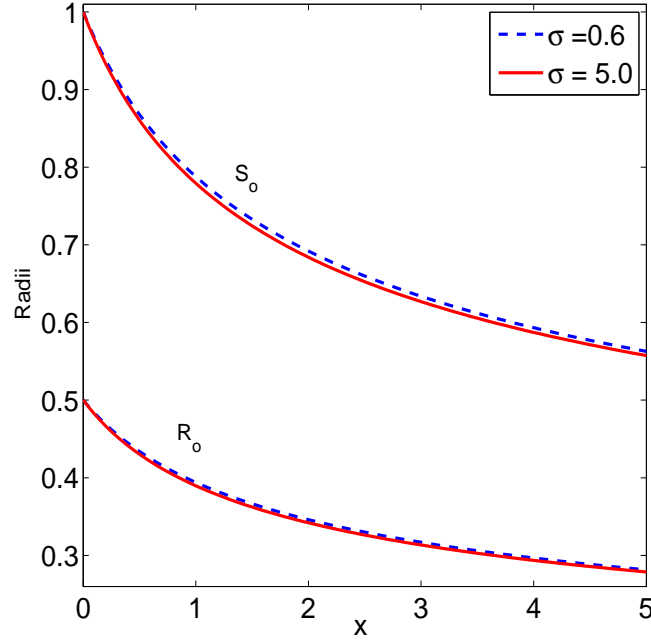
Figure 9.5: Steady state solutions of a viscous compound jet for two different values of the surface tension ratio, where $Re = 20, We = 10, \rho = 0.2, \mu = 0.8, F = 1$, and $\chi = 0.5$.

state solutions by small time dependent disturbances as

$$U = U_0(x) + \delta \exp(\lambda \bar{t} + ik\bar{x})\widehat{U'}, \tag{9.35}$$

$$R = R_0(x) + \delta \exp(\lambda \bar{t} + ik\bar{x})\widehat{R'}, \tag{9.36}$$

$$S = S_0(x) + \delta \exp(\lambda \bar{t} + ik\bar{x})\widehat{S'}. \tag{9.37}$$

where δ is the amplitude of the wave at the nozzle, $k(x)$ is wavenumber, $\lambda(x)$ is the frequency of disturbances, $\bar{x} = \frac{x}{\varepsilon}$ is the small length scale and $\bar{t} = \frac{t}{\varepsilon}$ is the small time scale.

We substitute the equations $(9.35) - (9.37)$ into equations $(9.30) - (9.32)$ and then choose the linear terms in δ, we are able to arrive at the following result

138
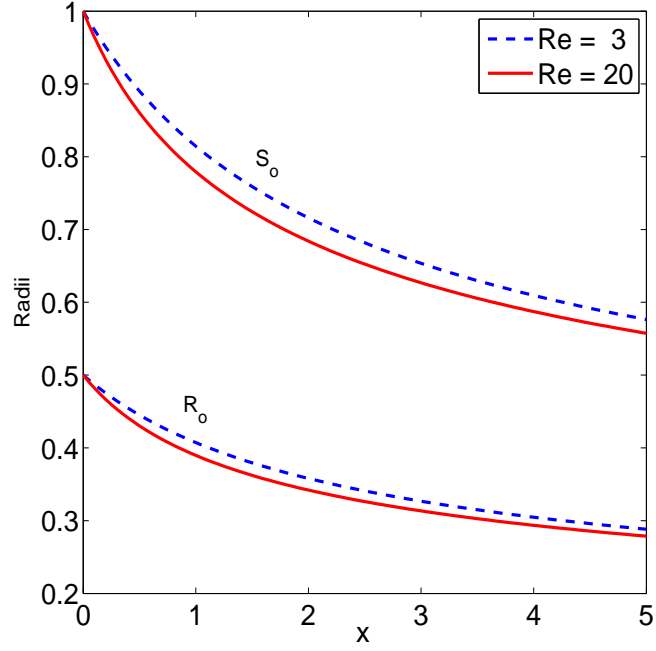
Figure 9.6: Steady state solutions of inner and outer jet radii for two different values of the Reynolds number, where $F = 1, We = 10, \rho = 0.2, \mu = 0.8, \sigma = 0.6$, and $\chi = 0.5$.

$$
\begin{pmatrix}
\alpha\Lambda + \beta(\frac{3k^2}{Re}) & \frac{\sigma}{We}\zeta & \frac{1}{We}\eta \\
\frac{ikR_0^2}{2} & R_0\Lambda & 0 \\
\frac{ik((S_0^2 - R_0^2)}{2} & -R_0\Lambda & -S_0\Lambda
\end{pmatrix}
\cdot
\begin{pmatrix}
\widehat{U'} \\
\widehat{R'} \\
\widehat{S'}
\end{pmatrix}
=
\begin{pmatrix}
0 \\
0 \\
0
\end{pmatrix},
$$

The non-trivial solution of the above system of equations exist only if

$$
\det
\begin{pmatrix}
\alpha\Lambda + \beta(\frac{3k^2}{Re}) & \frac{\sigma}{We}\zeta & \frac{1}{We}\eta \\
\frac{ikR_0^2}{2} & R_0\Lambda & 0 \\
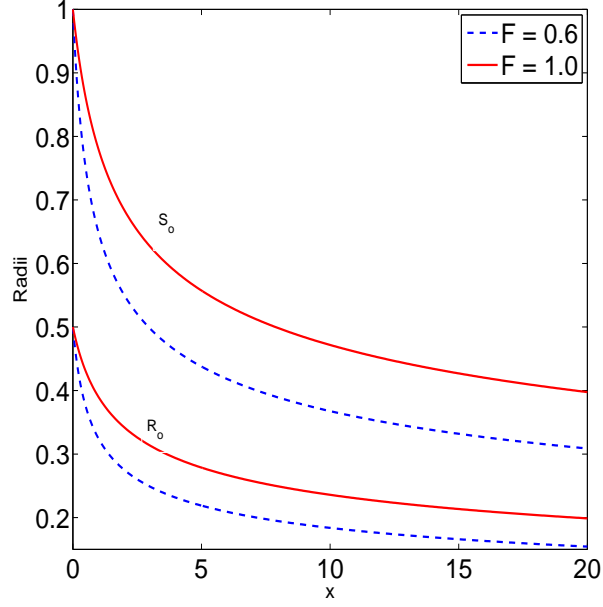\frac{ik((S_0^2 - R_0^2)}{2} & -R_0\Lambda & -S_0\Lambda
\end{pmatrix}
= 0,
$$
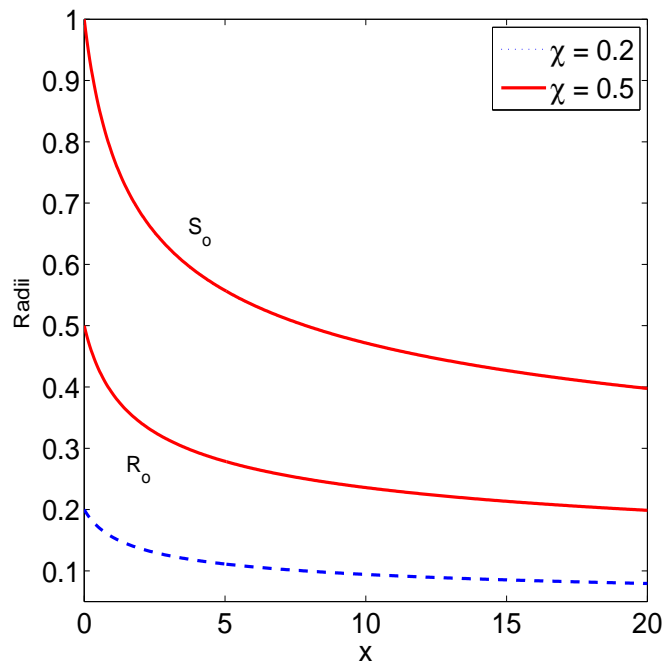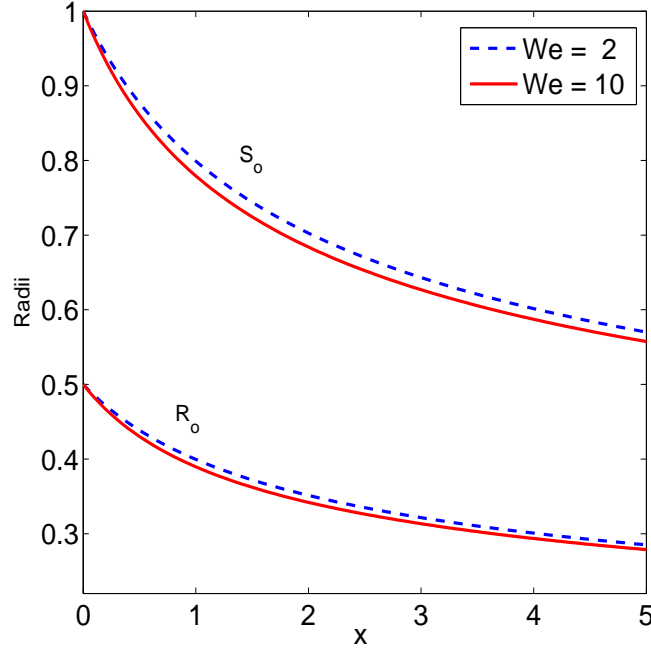
Figure 9.7: Steady state solutions of a viscous compound jet for two different values of the Weber number, where $Re = 20, F = 1, \rho = 0.2, \mu = 0.8, \sigma = 0.6$, and $\chi = 0.5$.

where

$$\Lambda = \lambda + ikU_0, \quad \alpha = S_0^2 + (\rho - 1)R_0^2, \quad \beta = S_0^2 + (\mu - 1)R_0^2,$$

$$\zeta = -ik + ik^3 R_0^2 \quad \text{and} \quad \eta = -ik + ik^3 S_0^2$$

By solving the above determinant, we are able to obtain the following characteristic equation

$$(\lambda + ikU_0)^2 + \frac{3(S_0^2 + (\mu - 1)R_0^2)k^2}{(S_0^2 + (\rho - 1)R_0^2)Re}(\lambda + ikU_0) -$$

$$\frac{k^2}{2(S_0^2 + (\rho - 1)R_0^2)We}[S_0(1 - k^2 S_0^2) + \sigma R_0(1 - k^2 R_0^2)] = 0. \tag{9.38}$$

The solution of equation (9.38) will be

$$\lambda_r = -\frac{3(S_0^2 + (\mu - 1)R_0^2)k^2}{2(S_0^2 + (\rho - 1)R_0^2)Re} +$$

(9.39)

$$\frac{k}{2}\sqrt{(-\frac{3(S_0^2 + (\mu - 1)R_0^2)k}{(S_0^2 + (\rho - 1)R_0^2)Re})^2 + \frac{2}{(S_0^2 + (\rho - 1)R_0^2)We}[S_0(1 - k^2S_0^2) + \sigma R_0(1 - k^2R_0^2)]}.$$

Now, we will differentiate the equation (9.39) with respect to k and then solve it for k to find the wavenumber for which λ_r is maximum. Therefore we have

$$K_{max} = \frac{1}{(2(\sigma R_0^3 + S_0^3))^{1/4}}\sqrt{\frac{\sigma R_0 + S_0}{\sqrt{2(\sigma R_0^3 + S_0^3)} + \frac{3Oh(S_0^2 + (\mu - 1)R_0^2)}{\sqrt{S_0^2 + (\rho - 1)R_0^2}}}},$$

(9.40)

where Oh is the Ohnesorge number which is equal to $Oh = \sqrt{We}/\overline{Re}$.

9.3.1 Discussion

In this section we discuss the numerical results which are obtain from equations (9.39) and (9.40). By substituting $k = K_{max}$ in equation (9.39) we will get the expression for maximum growth rate of disturbances of a viscous compound jet falling under gravity.

In the Fig. 9.8, we show the relationship between the maximum growth of disturbances and the viscosity ratio at three different locations of the viscous compound jet. It is observed that maximum growth rate of disturbances decreases with the increase in the viscosity ratio. Similarly, the graphical results have been shown for the maximum growth rate of disturbances against the Ohnserge number and density ratios in Figs. 9.9 and 9.10 respectively. Here we analyze that the maximum growth rate of disturbance is decreased by increasing the Ohnserge number and the density ratio. We also examined the effects of surface tension ratio on the maximum growth rate of disturbances in Fig. 9.11 and
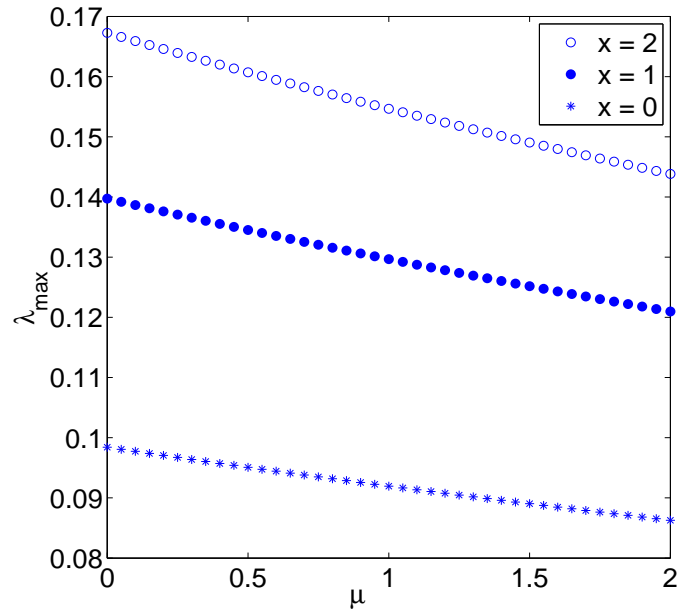
Figure 9.8: Maximum growth rate of disturbances against the viscosity ratios, where $\chi = 0.5$, $We = 10$, $Oh = 0.158$, $\rho = 0.5$, $\sigma = 0.1$, and $F = 1$.

notice that an increase in surface tension leads to increase the maximum growth rate of disturbances.

Similarly, we plot the maximum wavenumber against the viscosity ratio and the Ohnesorge number at three different locations of a viscous compound jet in Figs. 9.12 and 9.13 respectively. It can be seen that the maximum wavenumber is decreased by increasing the viscosity ratio and the Ohnesorge number. In the Fig. 9.14, the numerical results are displayed for the maximum wavenumber against the density ratio at three different location of the jet. Here we observe that an increase in density ratio leads to increase the maximum wavenumber. Moreover, the maximum wavenumber is increased with the increase in the surface tension ratio as shown in Fig. 9.15.

In the Fig. 9.16, we plot the maximum growth rate of disturbances against the axial length of the compound jet for two different values of the Froude number. It is noticed that the maximum growth rate is reduced with the increase in Froude number but it
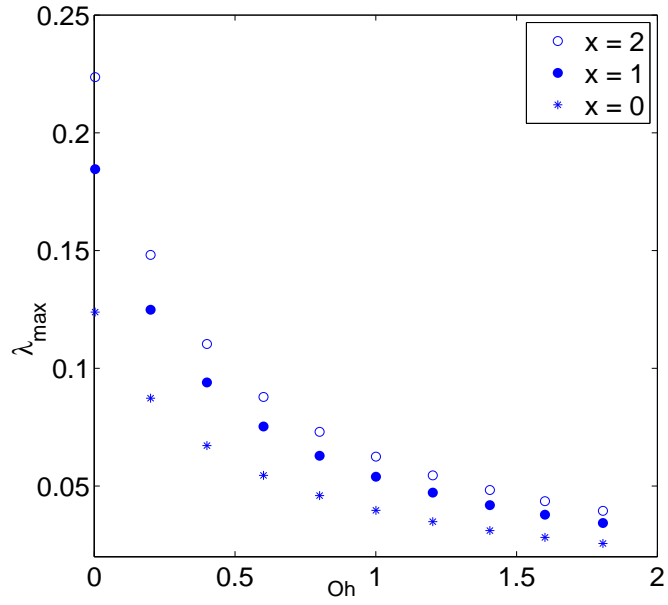
Figure 9.9: Maximum growth rate of disturbances against the Ohnesorge number, where $\chi = 0.5$, $We = 10$, $\sigma = 0.1$, $\rho = 0.5$, $\mu = 0.8$, and $F = 1$.
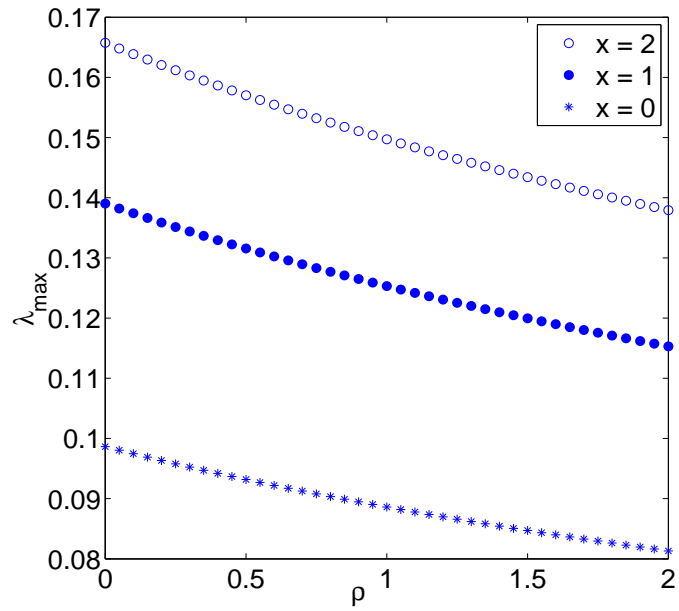
Figure 9.10: Maximum growth rate of disturbances against the density ratios, where $\chi = 0.5$, $We = 10$, $Oh = 0.158$, $\sigma = 0.5$, $\mu = 0.8$, and $F = 1$.
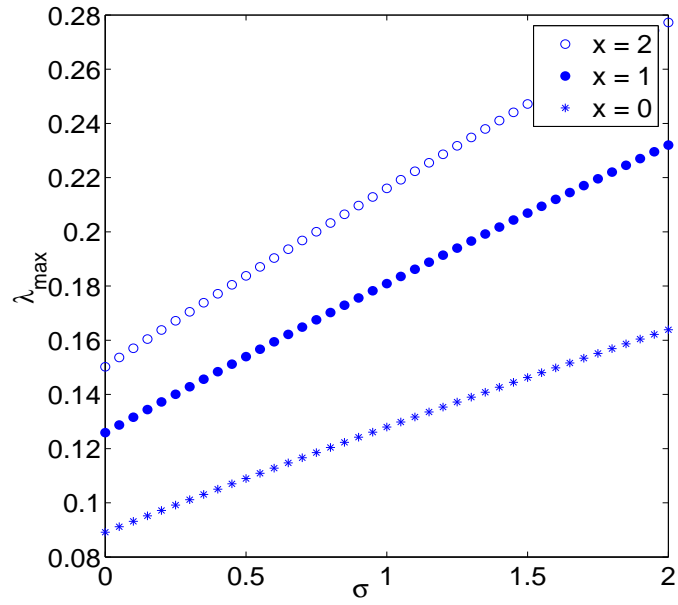
Figure 9.11: Plots of maximum growth rate of disturbance against surface tensions ratios, where $\chi = 0.5$, $We = 10$, $Oh = 0.158$, $\rho = 0.5$, $\mu = 0.8$, and $F = 1$.
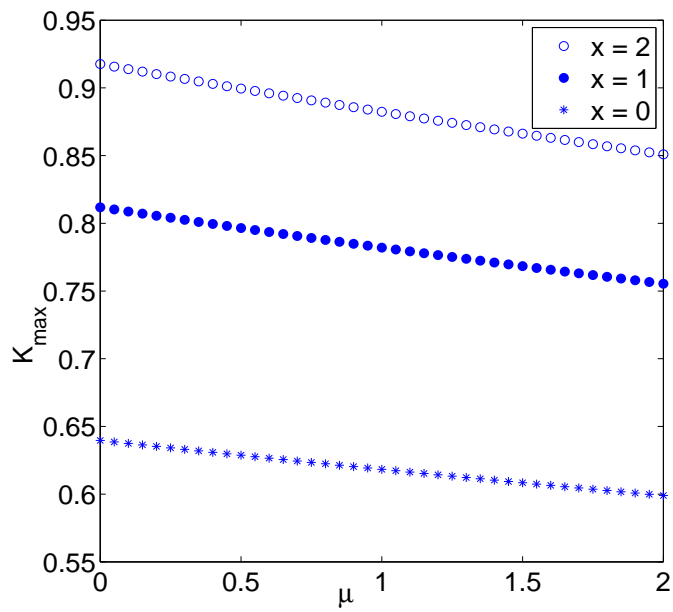
Figure 9.12: Maximum wavenumber against the viscosity ratios, where $\chi = 0.5$, $We = 10$, $Oh = 0.158$, $\rho = 0.5$, $\sigma = 0.1$, and $F = 1$.
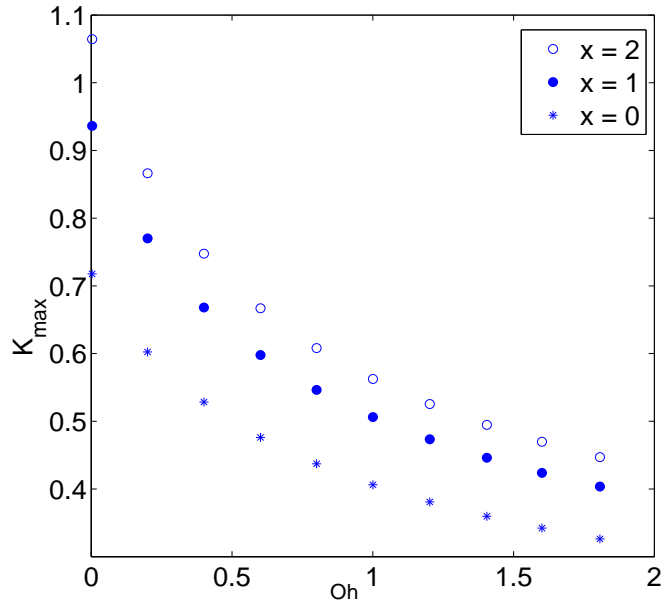
Figure 9.13: Plots of maximum wavenumber against Ohnesorge numbers, where $\chi = 0.5$, $We = 10$, $\sigma = 0.1$, $\rho = 0.5$, $\mu = 0.8$, and $F = 1$.
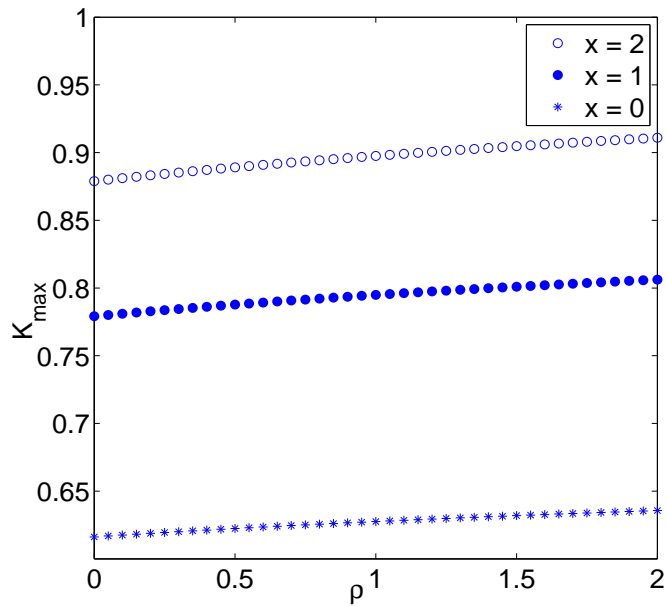
Figure 9.14: Maximum wavenumber against the density ratios, where $\chi = 0.5$, $We = 10$, $Oh = 0.158$, $\sigma = 0.1$, $\mu = 0.8$, and $F = 1$.
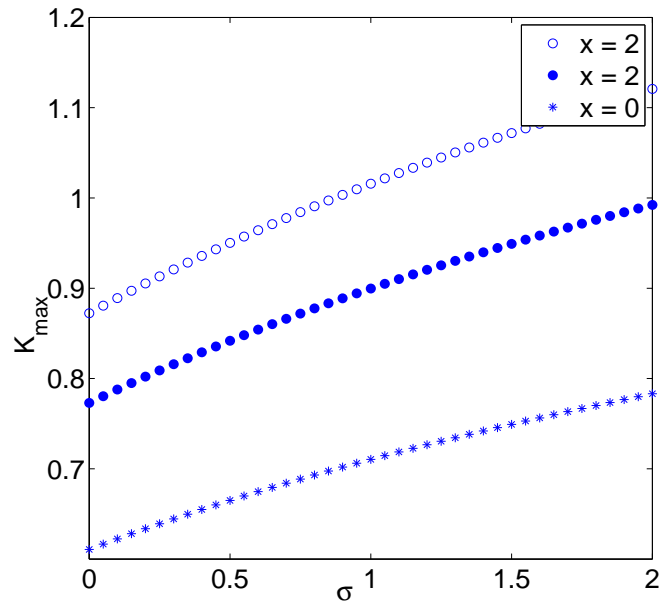
Figure 9.15: Maximum wavenumber against the surface tensions ratios, where $\chi = 0.5$, $We = 10$, $Oh = 0.158$, $\rho = 0.5$, $\mu = 0.8$, and $F = 1$.
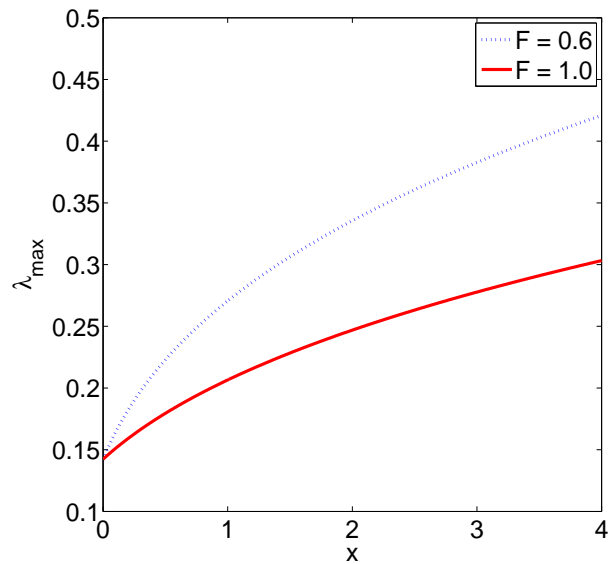
Figure 9.16: Maximum growth rate of disturbances against the axial length of a compound jet for two different values of Froude number, where $\chi = 0.5$, $We = 10$, $Oh = 0.158$, $\rho = 0.5$, $\mu = 0.8$, and $\sigma = 0.1$.
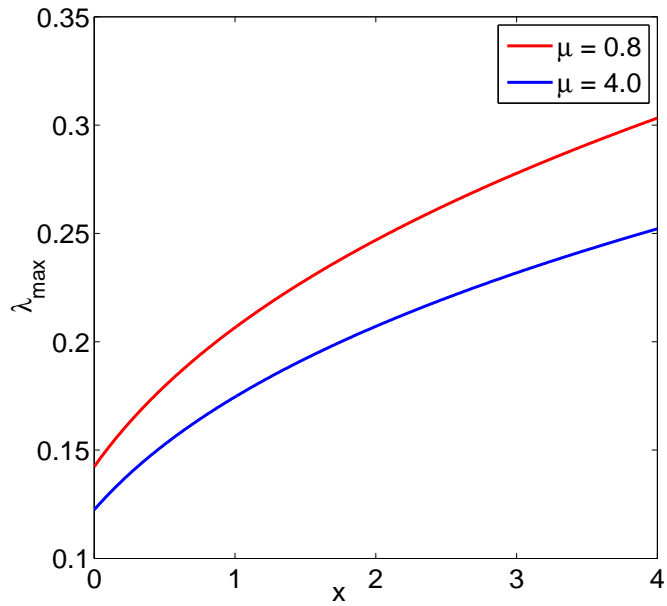
Figure 9.17: Maximum growth rate of disturbances against the axial length of a compound jet for two different values of viscosity ratio, where $\chi = 0.5$, $We = 10$, $Oh = 0.158$, $\rho = 0.5$, $\sigma = 0.1$, and $F = 1$.
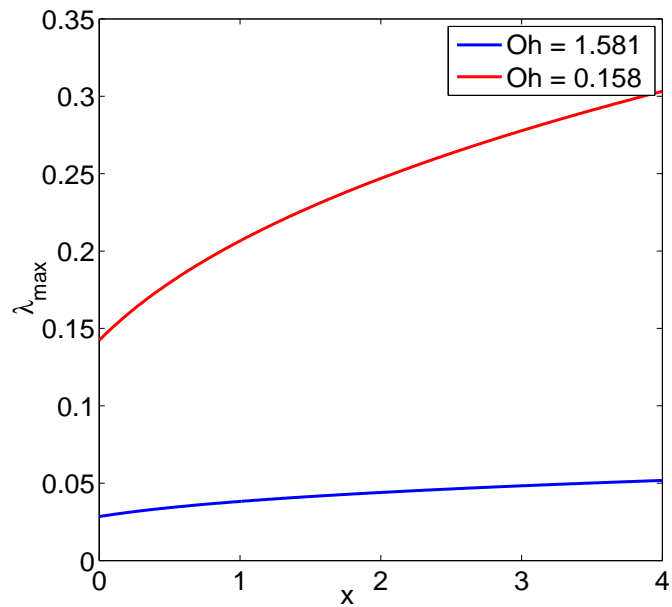
Figure 9.18: Maximum growth rate of disturbances against the axial length of the compound jet for two different values of the Ohnesorge number, where $\chi = 0.5$, $We = 10$, $\sigma = 0.1$, $\rho = 0.5$, $\mu = 0.8$, and $F = 1$.

147
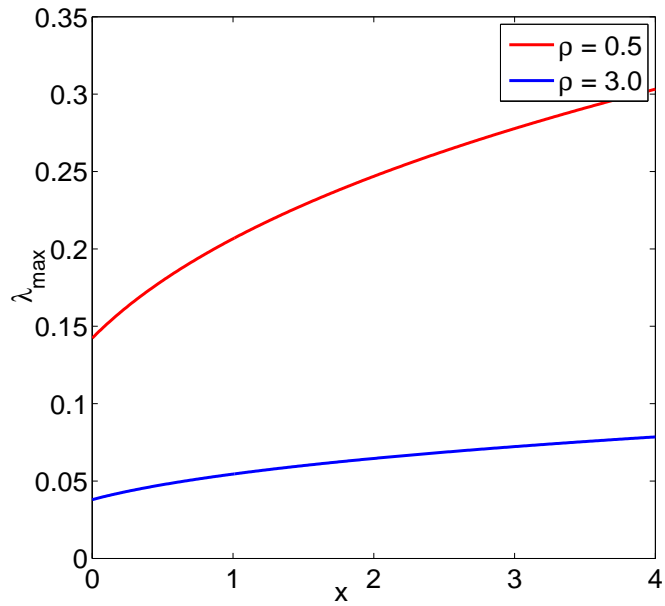
Figure 9.19: Maximum growth rate of disturbances against the axial length of the compound jet for two different values of the density ratio, where $\chi = 0.5$, $We = 10$, $Oh = 0.158$, $\sigma = 0.1$, $\mu = 0.8$, and $F = 1$.
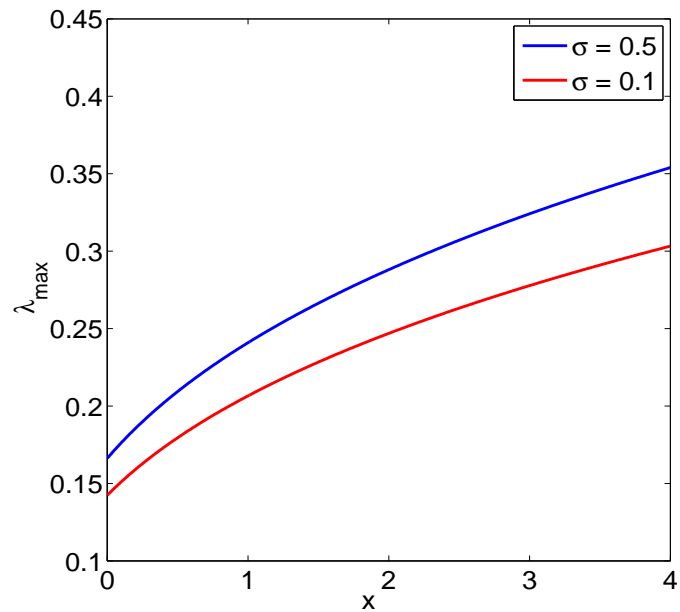
Figure 9.20: Maximum growth rate of disturbance against the axial length of the compound jet for two different values of the surface tension ratio, where $\chi = 0.5$, $We = 10$, $Oh = 0.158$, $\rho = 0.5$, $\mu = 0.8$, and $F = 1$.
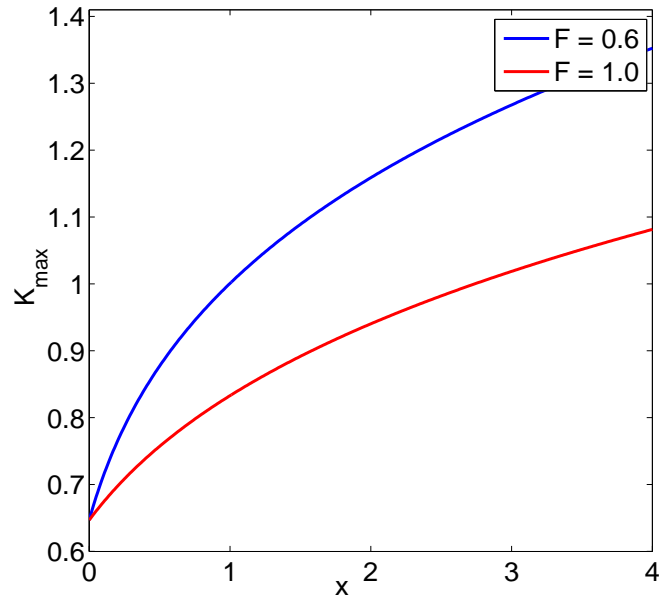
Figure 9.21: Maximum wavenumber against the axial length of the compound jet for two different values of the Froude number, where $\chi = 0.5$, $We = 10$, $Oh = 0.158$, $\rho = 0.5$, $\mu = 0.8$, and $\sigma = 0.1$.
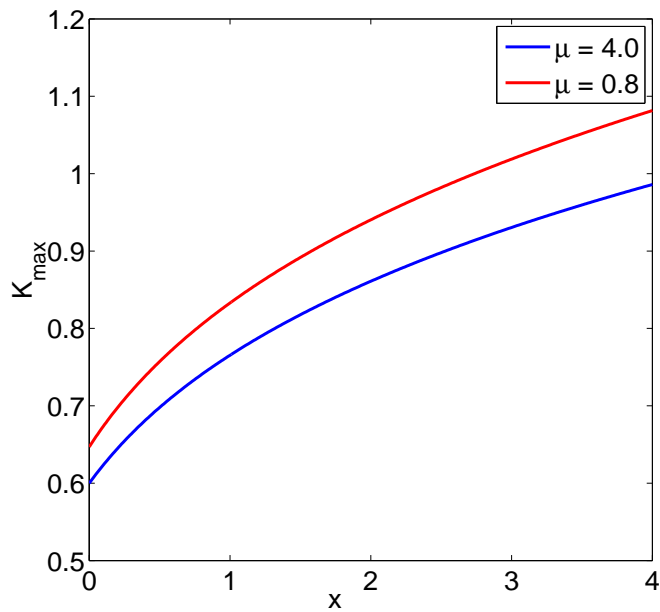
Figure 9.22: Maximum wavenumber against the axial length of the compound jet for two different values of the viscosity ratio, where $\chi = 0.5$, $We = 10$, $Oh = 0.158$, $\rho = 0.5$, $\sigma = 0.1$, and $F = 1$.
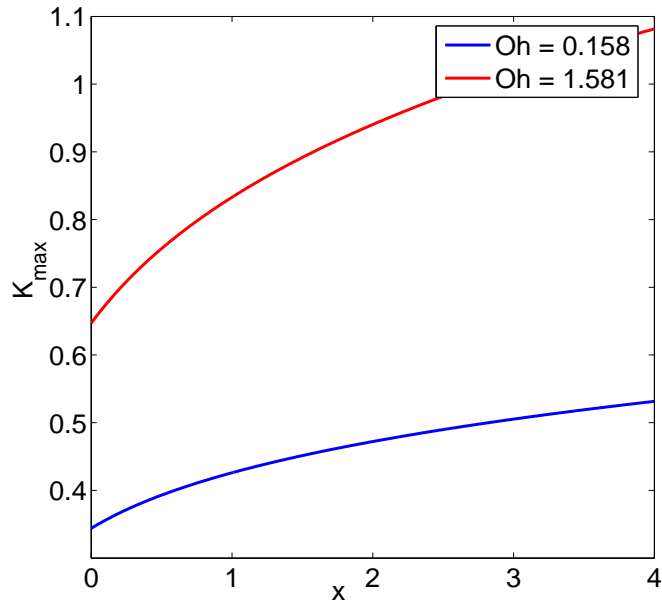
Figure 9.23: Maximum wavenumber against the axial length of the compound jet for two different values of the Ohnesorge number, where $\chi = 0.5$, $We = 10$, $\sigma = 0.1$, $\rho = 0.5$, $\mu = 0.8$, and $F = 1$.

increases along the jet. The plots between the maximum growth rate of disturbances and the axial length of the compound jet for two different values of the viscosity ratio and the Ohnesorge number have been displayed in Figs. 9.17 and 9.18 respectively. It is observed that the maximum growth rate of disturbances is decreased along the jet by increasing the viscosity ratio and the Ohnesorge number. Similar plots are presented for two different values of the density ratio and the surface tension ratio in Figs. 9.19 and 9.20 respectively. It is found that the increase in the density ratio leads to decrease the maximum growth rate of disturbances along the jet but the surface tension ratio raises the maximum growth rate of disturbances over the entire length of the jet.

The curves in Fig. 9.21 are produced for maximum wavenumber against the axial length of compound jet for two different values of the Froude number. Here we can see that the maximum wavenumber is decreased by increasing the Froude number. Figures 9.22 and
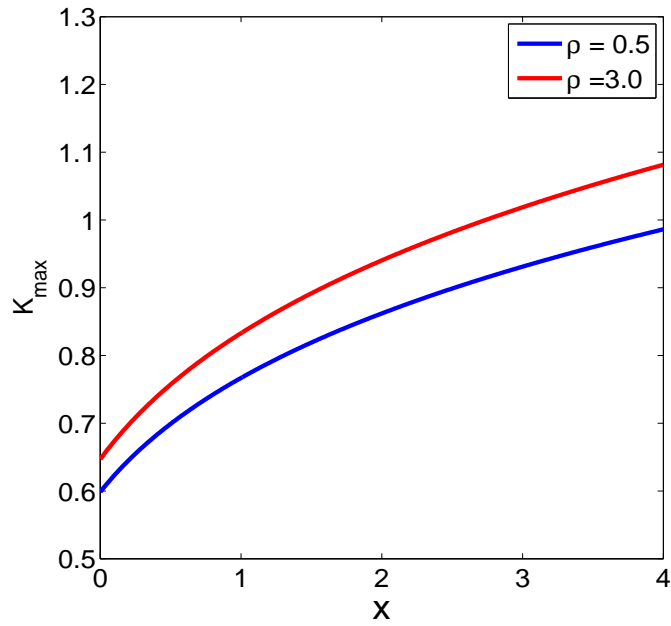
Figure 9.24: Maximum wavenumber against the axial length of a compound jet for two different values of the density ratio, where $\chi = 0.5$, $We = 10$, $Oh = 0.158$, $\sigma = 0.1$, $\mu = 0.8$, and $F = 1$.
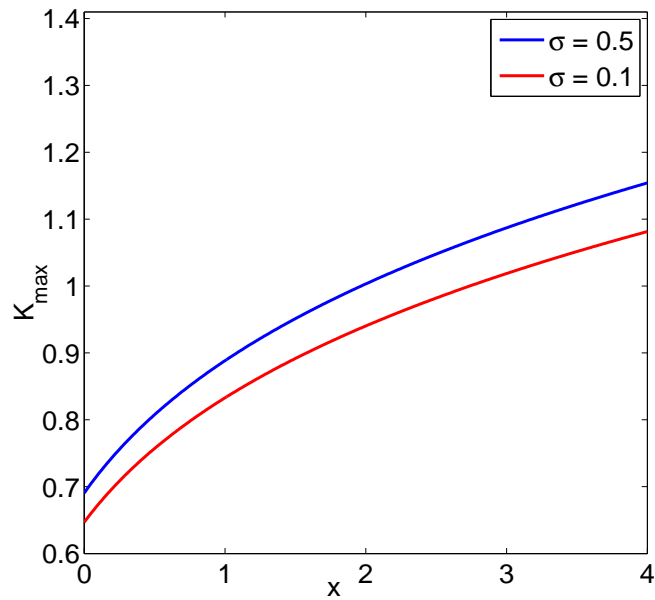
Figure 9.25: Maximum wavenumber against the axial length of a compound jet for two different values of the surface tension ratio, where $\chi = 0.5$, $We = 10$, $Oh = 0.158$, $\rho = 0.5$, $\mu = 0.8$, and $F = 1$.
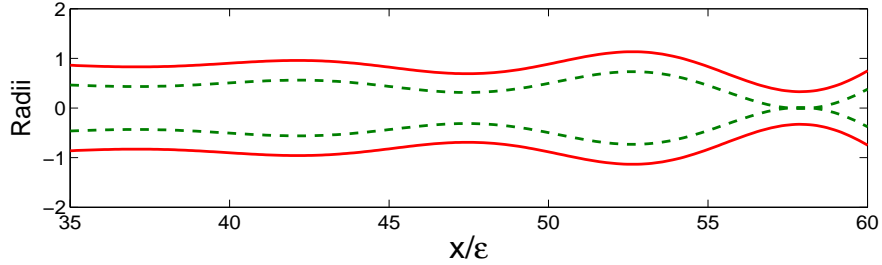
Figure 9.26: Profiles of a viscous compound jet. The parameters used here are $\sigma = 1$, $\varepsilon = 0.01$, $\rho = 0.3$, $\chi = 0.5$, $We = 50$, $Oh = 0.224$, $\mu = 4$ and $\delta = 0.01$

9.23 show that the increase in the viscosity ratio and the Ohnesorge number decrease the maximum wavenumber along the jet. In Figs. 9.24 and 9.25, it is observed that the maximum wavenumber increases down the jet for the higher values of the density ratio and the surface tension ratio.

9.3.2   Breakup lengths

Finally, we investigate the breakup lengths of viscous compound jet falling under the action of gravity. In order to find the breakup length we require time t which we will obtain by integrating the inverse of steady state velocity over the entire length of compound jet. Mathematically, it can be expressed as

$$t = \int_0^x \frac{1}{u(s)} \, \mathrm{d}s. \tag{9.41}$$

The above integral will be solved with the help of the Trapezoidal rule in MATLAB.

152
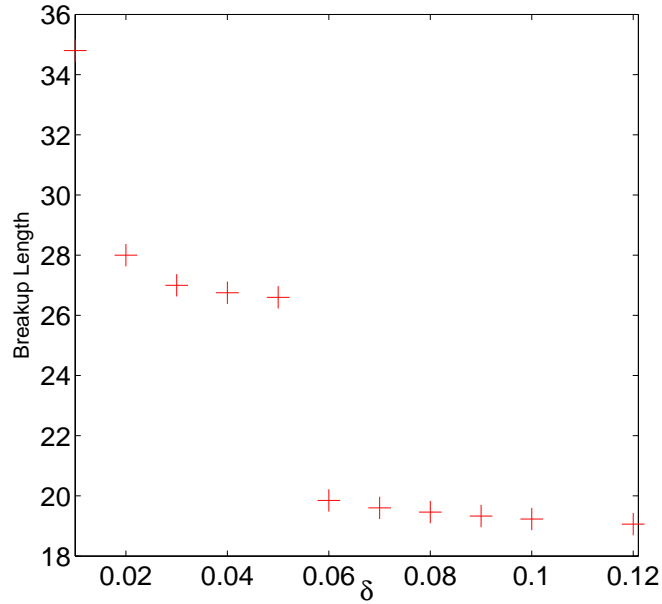
Figure 9.27: Breakup length of the compound jet for different disturbance amplitudes, where $\sigma = 0.5$, $\rho = 0.3$, $\mu = 0.6$, $\chi = 0.5$, $Oh = 0.141$, $F = 1$, $\varepsilon = 0.01$ and $We = 50$

The profile of compound liquid jet has been shown in Fig. 9.26. The breakup lengths of a viscous compound jet against the amplitudes of disturbances are presented in Fig. 9.27. Here we can say that the breakup length of the jet is decreased by increasing the amplitude of disturbance. Therefore, the compound liquid jet takes less time to breakup for higher amplitudes of disturbance. We also notice in Fig. 9.27 that there are number of discontinuities, notably near $\delta = 0.01$ and $\delta = 0.05$. These are caused by a change in the location of breakup due to the growth of disturbances. In the Fig. 9.28, we obtain the breakup length against the surface tension ratio and compare the results with the zero gravity case. We find the shorter breakup lengths in the presence of gravity which implies that zero gravity delays the breakup of compound liquid jet. Moreover, the increase in surface tension ratio leads to decrease the breakup length.

The effects of the viscosity ratio on the breakup of compound jet for two different values of the Weber number are also considered in Fig. 9.29. It is noticed that breakup length

153
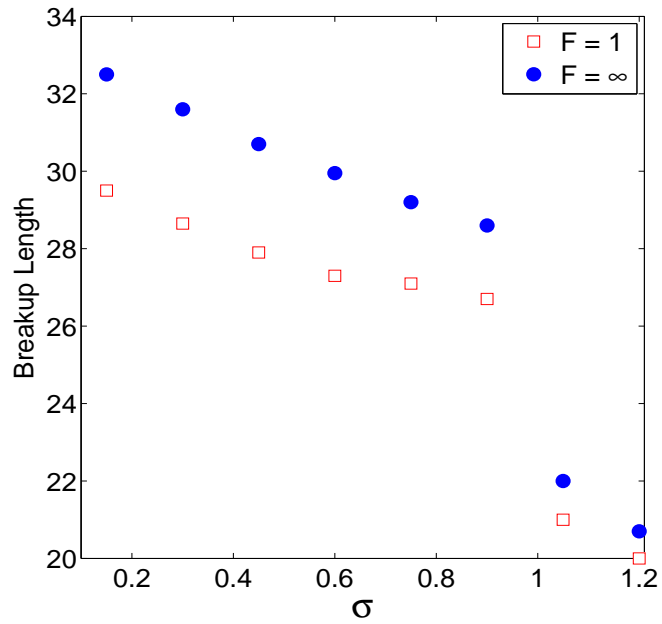
Figure 9.28: Breakup length of the compound jet for different values of the surface tension ratio, where $\rho = 0.3$, $\mu = 0.6$, $\chi = 0.5$, $Oh = 0.224$, $\varepsilon = 0.01$, $\delta = 0.01$ and $We = 20$

increases with the increase in viscosity ratio and the Weber number. In the Fig. 9.30, we analyze the effects of the density ratio on the jet breakup for two different values of the disturbances amplitude. We find that the breakup length of a viscous compound jet increases with the density ratio.
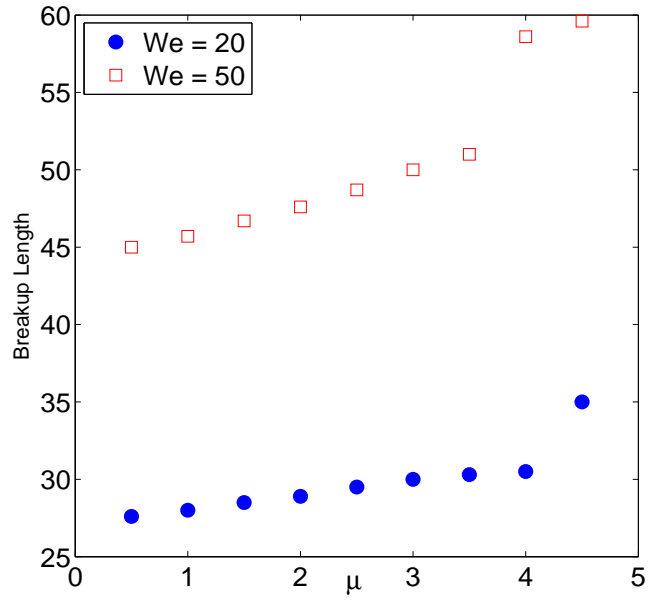
Figure 9.29: Breakup length of the compound jet for different values of the viscosity ratio, where $\rho = 0.3$, $\sigma = 0.5$, $\chi = 0.5$, $Oh = 0.224$, $F = 1$, $\varepsilon = 0.01$ and $\delta = 0.01$
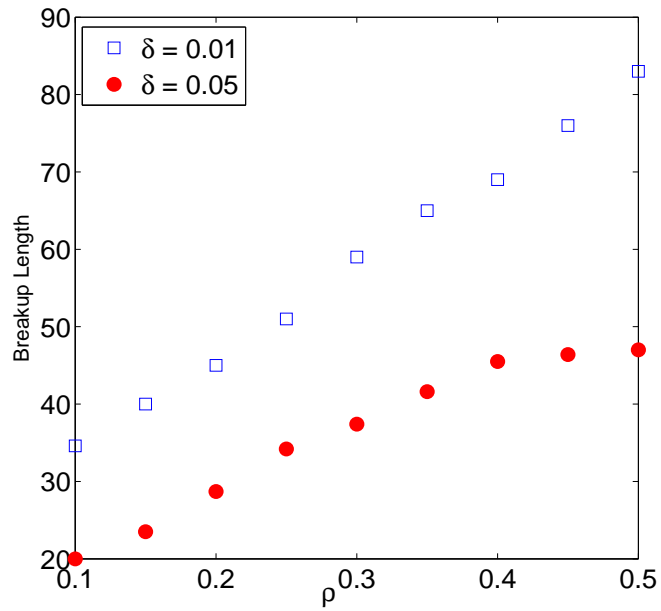
Figure 9.30: Breakup length of the compound jet for different values of the density ratio, where $\mu = 0.3$, $\sigma = 0.5$, $\chi = 0.5$, $Oh = 0.333$, $F = 1$, $\varepsilon = 0.01$, $\delta = 0.01$, and $We = 100$
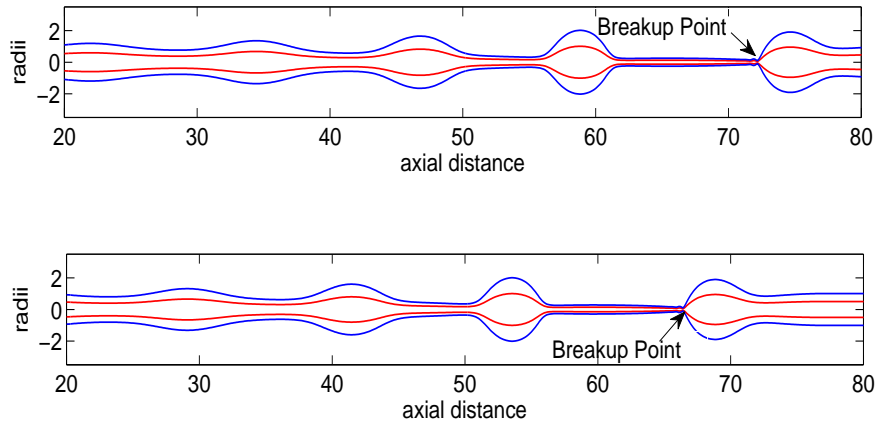
Figure 9.31: Breakup of a viscous compound jet for different values of density ratio, $\rho = 1$ ($First$) and $\rho = 0.8$ ($Second$). The parameters used here are $\sigma = 1$, $K = 0.70$, $Re = 2100$, $\mu = 1$, $F = 0.7$, $We = 30$, $\varepsilon = 0.01$ and $\delta = 0.01$

9.4 Nonlinear Analysis

In the previous section, we performed the linear instability analysis. Now, we are looking to obtain the nonlinear temporal solutions of a viscous compound jet falling under the gravity. In order to solve the nonlinear system of unsteady partial differential equations $(9.30) - (9.32)$, we include the expressions for the pressure with full curvature κ_z instead of leading order pressure terms. It is necessary for the correct reproduction of equilibrium shape in the numerical simulations. A justification of retaining higher order pressure term is provided by number of authors (for example, Eggers [25], Lee [42], and Garcia & Castellanos [28]). The initial conditions for a viscous compound jet were given by steady state solutions which we have calculated in the previous section. The imposed upstream boundary conditions at the nozzle are given by

$$U(0,t) = 1 + \delta \, cos\left(\frac{Kt}{\varepsilon}\right), \quad R(0,t) = \chi \;\; \text{and} \;\; S(0,t) = 1 \tag{9.42}$$
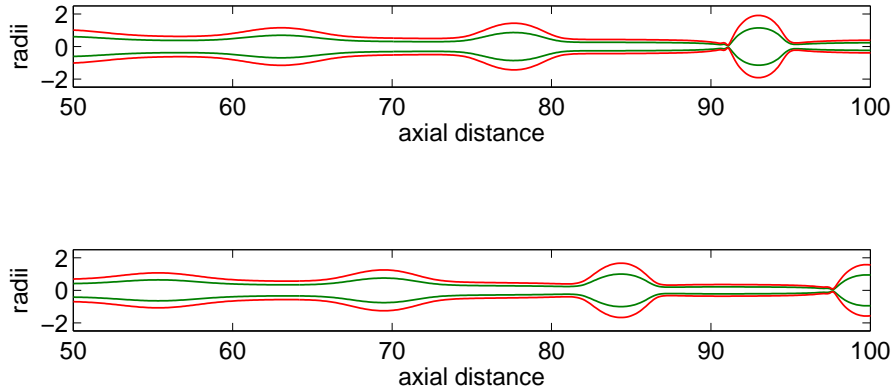
Figure 9.32: Profiles of a viscous compound jet for different values of viscosity ratio, $\mu = 0.5$ ($First$) and $\mu = 1.0$ ($Second$). The parameters used here are $\sigma = 1$, $K = 0.65$, $\rho = 1$, $Re = 1000$, $We = 20$, $F = 0.8$, $\varepsilon = 0.01$ and $\delta = 0.01$

where δ is dimensionless initial amplitude and K is the wavenumber of imposed sinusoidal disturbance. The downstream boundary conditions for U, R and S are obtained by quadratic extrapolation of last interval mesh points. In this numerical simulation of the evolution of compound jet, our stopping criteria was taken to be the time at which the minimum dimensionless jet radius was 0.05. Therefore we took the location of this minimum point to be the location of breakup.

In Fig. 9.31, we show the breakup of a viscous compound jet for different values of density ratio ρ and we observe that the compound jet take more time to breakup for the case of larger density ratio between the fluids. The profiles of the compound jet with more viscous core region than the fluid of shell region and vice versa are presented in Fig. 9.32. The first profile shows the breakup for the case of less viscous core fluid than that of the shell liquid while the second profile depicts the breakup for the case when inner fluid is more viscous than the outer fluid. It is noticed that there is a thinner ligament connecting the droplet and longer jets are produced for the case of large viscosity ratio.

157

The profile of the outer jet breakup is presented in the Fig. 9.33.

From Fig. 9.34, we can see that the compound jet falling under the gravity will be longer and more stable for small disturbance wavenumber but if we increase the wavenumber at the nozzle the compound jet falling without the influence of gravity takes more time to breakup as compare to the compound jet falling with gravity. It is also noticed that the wavenumber at which the breakup time is minimal decreases by increasing the Froude number.

The non-dimensional compound droplets and core droplets against the disturbances amplitude δ are manifested in Fig. 9.35. It is clearly noticed that the drop sizes become larger for the case of zero gravity. Moreover, we can see that the size of droplet increases with the increase in disturbances amplitude δ. In Fig. 9.36, we show the breakup time of a viscous compound jet falling under the gravity against the surface tension ratios for different values of the viscosity ratios. It is observed that the compound jet take more time to breakup for the case of large viscosity ratio. In addition, the increase in the surface tension ratio σ leads to shorten the length of the viscous compound jet.

The breakup time of the compound jet against the density ratio for different values of the disturbance amplitude δ is manifested in Fig. 9.37. We can see that the the compound jet falling under the gravity takes more to breakup for the higher density ratio between the inner and outer fluids whereas for the large value of the disturbance amplitude δ we find the shorter jets. From the Fig. 9.38, we observe that the size of the droplet reduces by varying wavenumber K. In addition, the droplet becomes larger for the higher viscosity ratios. We also measure the droplet size for the given values of the density ratio at different disturbance amplitudes in the Fig. 9.39. Here, we can notice that the droplet becomes smaller for the higher values of the density ratio and the disturbance amplitude. In the Fig. 9.40, we show non-dimensional satellite droplets by varying the viscosity
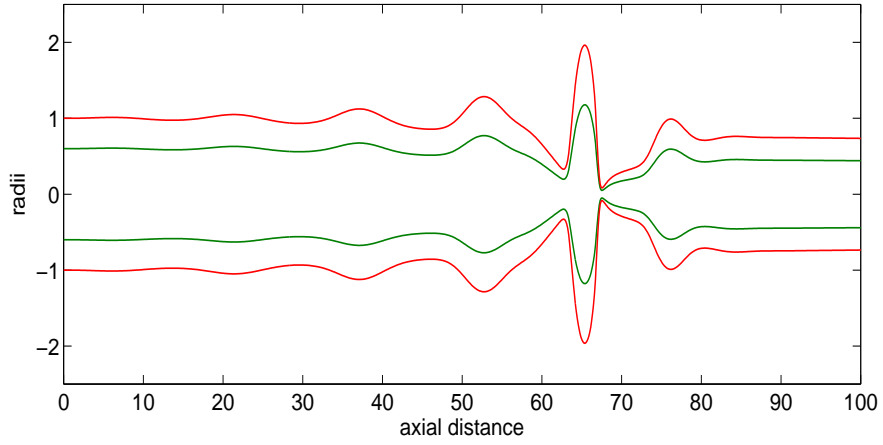
Figure 9.33: Profiles of a viscous compound jet showing the outer jet breakup. The parameters used here are $\sigma = 1$, $K = 0.75$, $\rho = 1$, $We = 30$, $Re = 1100$, $\mu = 1$, $F = 0.8$, $\varepsilon = 0.01$, $\chi = 0.65$ and $\delta = 0.01$
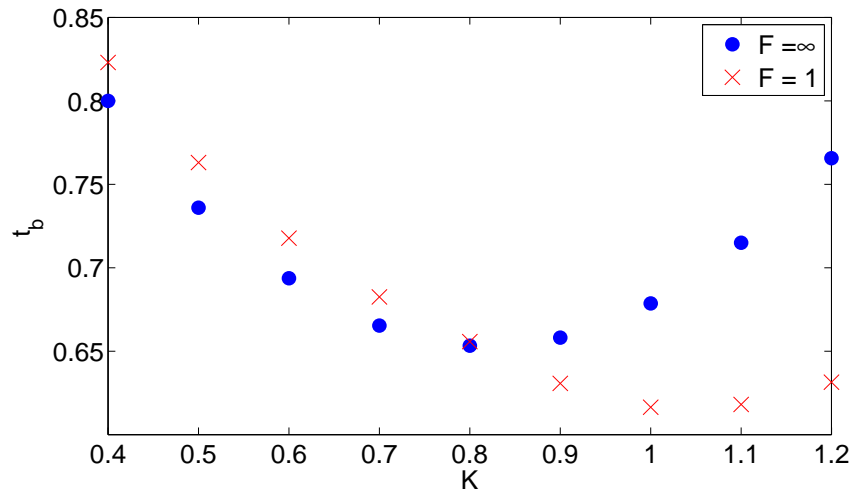
Figure 9.34: Breakup time of compound jet against wavenumber of disturbance at nozzle for different values of Froude number, where $\sigma = 1.0$, $\rho = 1.0$, $\mu = 1$, $\delta = 0.01$, $\varepsilon = 0.01$, $\chi = 0.5$, $Re = 2000$ and $We = 20$.

159
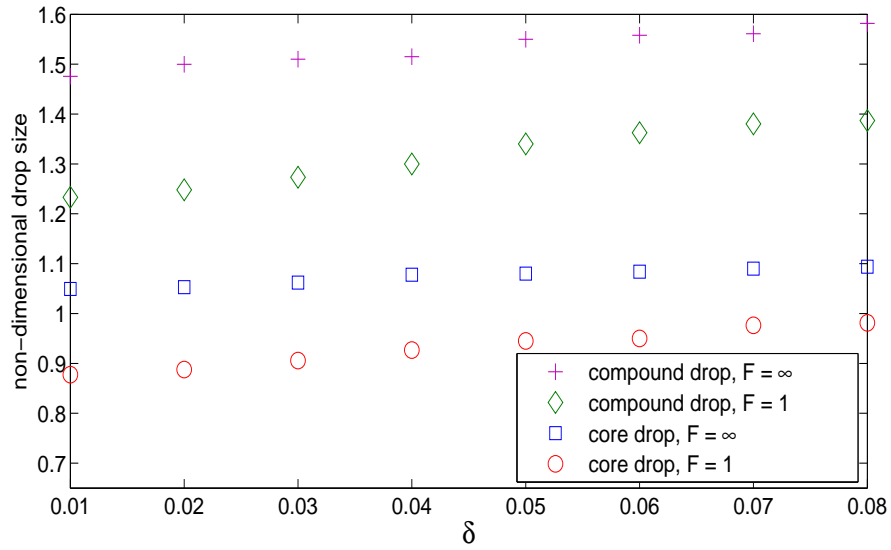
Figure 9.35: Inner and outer droplet sizes when the disturbance amplitude δ is varied. Here, we have $We = 40$, $Re = 3000$ $\sigma = 0.28$, $\rho = 1.2$, $\mu = 1.0$, $\varepsilon = 0.01$, $K = 0.59$ and $\chi = 0.5$
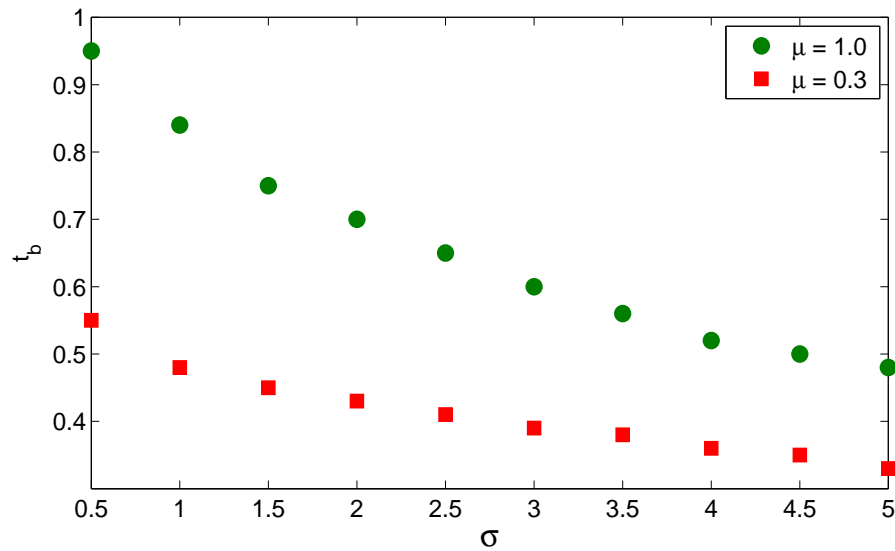
Figure 9.36: Breakup time of compound jet against surface tension ratio for different values of viscosity ratio, where $\rho = 1.0$, $K = 0.68$, $F = 1$, $Re = 900$ $\delta = 0.01$, $\varepsilon = 0.01$, $\chi = 0.5$, and $We = 20$.
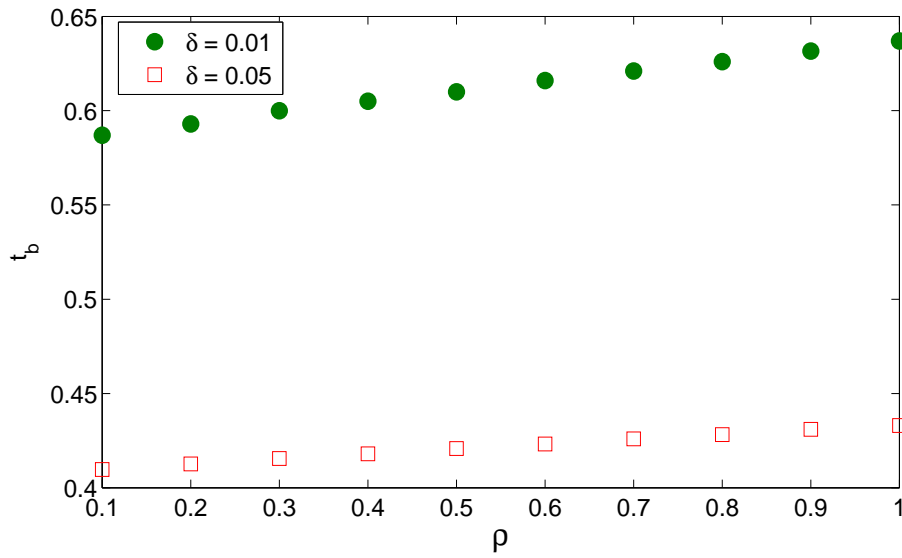
Figure 9.37: Breakup time of compound jet against density ratio for different values of disturbance amplitude, where $\sigma = 1.0$, $F = 1.0$, $K = 0.68$, $Re = 950$, $\varepsilon = 0.01$, $\chi = 0.5$, and $We = 20$.
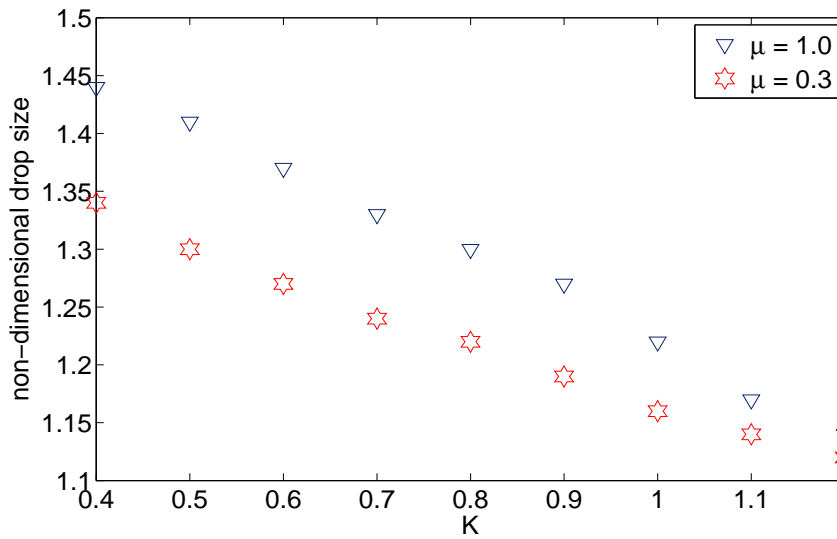
Figure 9.38: Droplet sizes are manifested when the wavenumber is varied for different values of viscosity ratio. Here, we have $We = 50$, $Re = 2100$, $\sigma = 0.5$, $\rho = 1.0$, $F = 0.6$, $\varepsilon = 0.01$, and $\chi = 0.5$

161
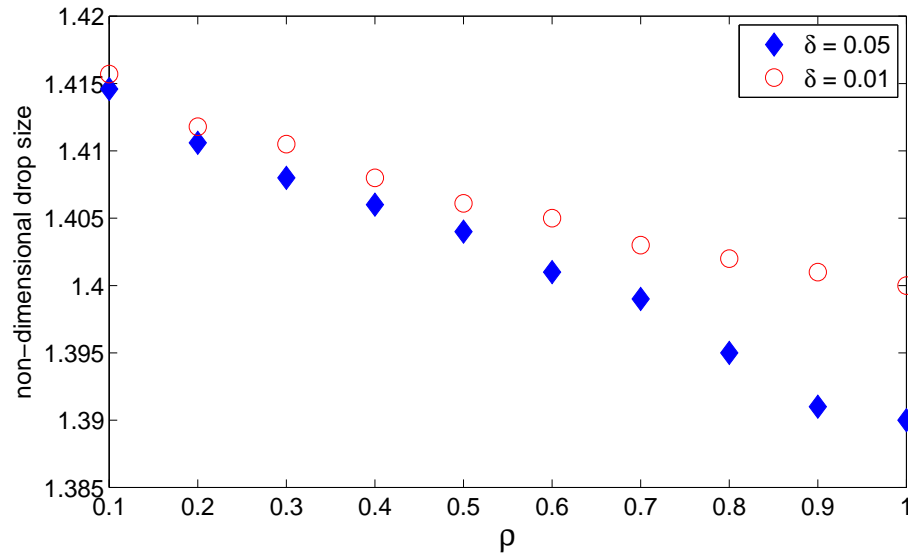
Figure 9.39: Droplet sizes are manifested when the density ratio is varied for different values of disturbance amplitude. Here, we have $We = 30$, $Re = 2500$, $\sigma = 0.28$, $F = 1.0$, $\mu = 1.0$, $\varepsilon = 0.01$, $K = 0.59$ and $\chi = 0.6$

ratio. The satellite droplets are seen to be smaller with the increase in the viscosity ratio μ. Furthermore, it is observed that large values of δ produce larger satellite droplets.
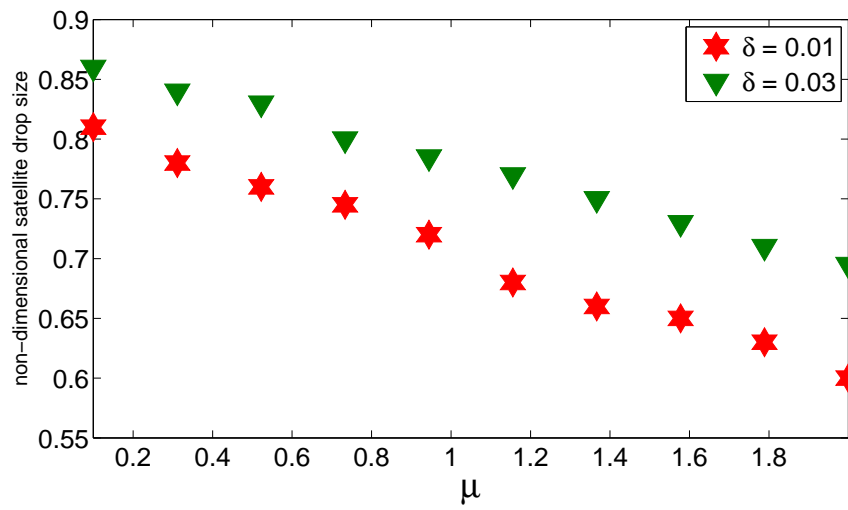
Figure 9.40: Satellite droplets are shown when the viscosity ratio is varied for different values of disturbance amplitude. Here, we have $We = 35$, $Re = 3000$, $\sigma = 0.6$, $F = 1.0$, $\rho = 0.7$, $\varepsilon = 0.01$, $K = 0.59$ and $\chi = 0.6$

CHAPTER 10

CONCLUSIONS AND FUTURE WORK

10.1 Conclusions

In this thesis we have investigated the temporal instability in compound liquid jets. We began our study with the one dimensional axisymmetric inviscid compound jet and extended our analysis into the two dimensional model. We thereafter examined the aerodynamics effects on the instability and breakup of compound jet. We also incorporated the effects of viscosity into the core and annular region, and considered the influence of gravity on the breakup dynamics and drop formation of inviscid and viscous compound jet. Here we summarize the prominent results obtained in this thesis and suggest some projects for the future work.

In chapter one, we gave the detail review on the previous studies of single and compound liquid jets. The linear and nonlinear analysis of one dimensional inviscid compound jet was discussed in chapter two. The dispersion relation obtained by Uddin [87] was reproduced using linear theory and the nonlinear analysis studied by Uddin [87] was reviewed in detail to understand the breakup dynamics and encapsulated drop formation in a compound jet. Chapter three was related with the nonuniform compound liquid jets. An extensive detail of [55] and [86] was given to reveal the key features of the compound jet. It was concluded

that the breakup length of inviscid compound jet increases with the increase in radii ratio χ and decrease for lower values of the Weber number. In addition, the inviscid compound jet takes more time to breakup by decreasing the surface tension ratio and increasing the density ratio. Moreover, the wavenumber at which the breakup time is minimal decrease by increasing the Froude number. Some of these results have been published in *Physics of Fluids*.

We performed the linear temporal instability analysis of two dimensional compound jet in chapter four. A dispersion relation was derived using full set of equation to obtain the most unstable wavenumber and the maximum growth rate of disturbance. We also presented the comparison between the full dispersion relation and the dispersion relation obtained by Uddin [87] in a long wavelength limit. As anticipated it showed a good agreement for $k << 1$ and there is a slight variation for $k = O(1)$ values with the full dispersion relation predicting slightly lower values for the growth rate.

In chapter five, we studied the effects of gravity on the instability and the breakup of two dimensional compound jet. The steady state solutions were found first and thereafter we considered linear temporal instability using full set of equations. We estimated the theoretical breakup lengths by extending our linear analysis which seems to be more accurate than the one dimensional analysis of Mohsin *et al.* [55] due to the presence of radial flow of the compound jet.

An inviscid compound liquid jet emerging in an ambient gas was considered in chapter six. Linear instability analysis gave us an eigenvalue relation which revealed that the maximum growth rate of disturbance and the cut-off wavenumber became larger due to the aerodynamics effects. In addition, the droplet size became smaller because of the ambient gas density.

Using linear theory, the influence of the surrounding gas on the instability of a compound jet falling under gravity has been discussed in chapter seven. The steady sate solutions have been used in the dispersion relation to examine the instability of the jet at different locations along the jet. The maps are plotted to depict the behavior of gas-to-shell density ratios by varying inner-to-outer radii ratios and surface tension ratios together along the compound jet. It is found that, for each value of σ and χ, the growth rate of disturbance becomes larger by increasing ρ^G (density ratio between the outer fluid and the surrounding gas) and, the most unstable wavenumber increases with the increase in ρ^G. In addition, we determined an estimate for the breakup lengths by extending our linear analysis and observed that the shorter jets were generated for the higher values of ρ^G.

In chapter eight, we considered viscous compound jet and governing equations were reduced to one dimension by using asymptotic method. By considering the disturbances in temporal mode, we first found a dispersion relation. Thereafter, we analyzed that the maximum growth rate of disturbances and the most unstable wavenumber is increased by increasing the surface tension ratio and the Ohnesorge number and decreased by increasing the viscosity ratio. The most unstable wavenumber increases with density ratio but maximum growth rate of disturbances decreases by increasing the density ratio. In addition, the increase in inner radius lead to increase the maximum growth rate but most unstable wavenumber increases when $\chi < 0.5$ and decreases when $\chi > 0.5$.

In chapter nine, we examined the effects of gravity on the viscous compound jet falling vertically downward. Newton's method is developed to solve the nonlinear set of differential equations for steady state solutions which implies that the radii of viscous compound jet decrease by decreasing the Froude number. The maximum growth rate of compound jet decreases along the jet if we increase the the viscosity ratio, the density ratio, the Froude number and the Ohnesorge number, but it increases by increasing the surface

166

tension ratio. The most unstable wavenumber along the compound jet is seen to increase with the density ratio and the surface tension ratio. The most unstable wavenumber decreases along the compound jet by increasing the viscosity ratio, the Froude number and the Ohnesorge number. We also produced the breakup lengths of viscous compound jet falling under gravity. The breakup length of the viscous compound jet falling under gravity is decreased for higher amplitude disturbances δ. By increasing the Weber number leads to increase the breakup length. The breakup length increases by increasing the density ratio and decreases for higher surface tension ratios. Moreover, it is observed that the viscous compound jet takes less time to breakup in the presence of gravity. We thereafter applied a numerical method, based on finite difference scheme, on one dimensional system of partial differential equations to find the breakup time, main drop sizes and the satellites droplets. From the results, we concluded that the reduction in surface tension ratio σ and increase in viscosity ratio μ and density ratio ρ lead to produce longer jets. In addition, the optimum wavenumber and the size of main droplet decrease due to the presence of gravity, while the size of satellite droplets reduces with the increase in viscosity ratio.

10.2 Future Work

This thesis is related with the axisymmetric compound liquid jets. The idea can be extended towards the non-axisymmetric compound jets. The linear analysis can be performed to investigate the non-axisymmetric disturbance around the jet particularly for the case of compound jet emerging in a surrounding gas. We can also investigate the spatial instability of inviscid and viscous compound jet falling under the influence of gravity. An example of solving dispersion relation (3.26) in a spatial mode is shown in Fig. 10.1. In this case, k is taken as complex that is $k = k_r + ik_i$ and λ is supposed to be imaginary that is $\lambda = -i\omega$. We plot the spatial growth rate k_i for the given values of the real frequency
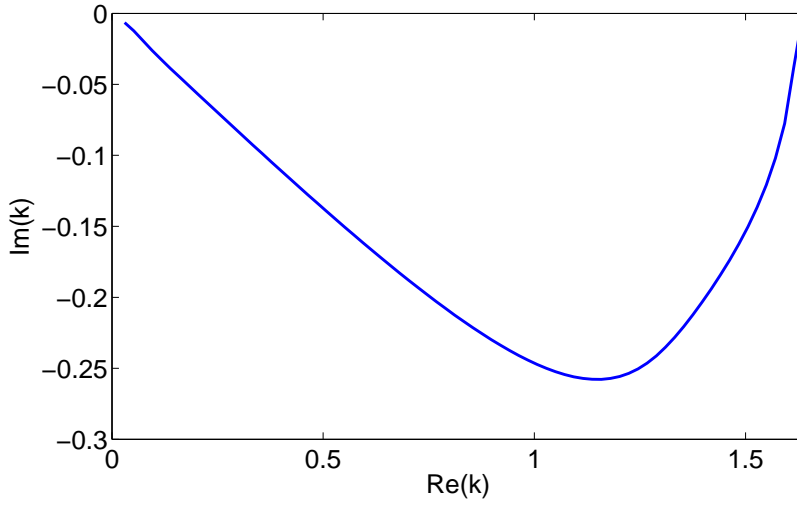
Figure 10.1: Growth rate of disturbances versus the wavenumber at the nozzle, The parameters used here are $We = 20$, $\sigma = 1$, $\rho = 1$, and $\chi = 0.6$

ω.

Linear and nonlinear analysis of a viscous compound jet can also be performed by adding the surfactants in the inner and outer columns of viscous compound jet. Furthermore, a detailed examination of the stability of a compound jet incorporating temporal-spatial analysis (similar to that considered by Kalliadasis *et al.* [37] and Ruyer-Quil *et al.* [75]) along with a comparison with numerical simulations to identify the regimes, where breakup of the jet is caused by the inner and outer interface touching, will be the subject of future work. The absolute instability in a compound liquid jet moving in a surrounding gas is not yet considered which is very important for the case of slow moving jets.

We have discussed the nonlinear analysis of one dimensional inviscid and viscous compound liquid jets using finite difference scheme based on Lax-Wendroff method. A boundary element method can be applied on a two dimensional compound jet to examine the nonlinearity in the breakup and post rupture behaviour in more detail. For this purpose,

we can extend the analysis of Hilbing & Heister [35] who developed boundary element method to study a single liquid jet.

Appendix A

Temporal and spatial instability of a non-axisymmetric compound jet falling under gravity in the ambient gas

The temporal and spatial instability of a non-axisymmetric compound liquid jet which is moving in the surrounding gas and falling vertically under the action of gravity is considered. We are currently working on this paper and are planing to submit in the *Physics of Fluids*.

Abstract

Droplet generated from the rupture of a compound jet can be used to produce encapsulated droplets which have applications in a wide variety of industrial processes. In this paper, we examine the instability of a three dimensional inviscid compound jet falling vertically downwards in a surrounding gas under the influence of gravity. The steady state equations are derived using an asymptotic method and linear instability is determined using a multiple scales approach. The results are analysed to investigate how the

170

gas-to-shell density ratio affects key features of the jet.

A.1 Introduction

Whether it is the investigation of single liquid jets or compound liquid jets, surface insta-
bilities play an important role in the jet breakup. The liquid jet emerging from the orifice
is inherently unstable and continuous growing disturbances lead to the disintegration of
the jet into droplets. In the case of single jets the free interface exists between the fluid
and surrounding gas, but in compound liquid jet there are two interfaces: one separates
the inner and outer immiscible fluid and the other one lies between the outer fluid and
the surrounding gas. A compound liquid jet contains core and annular regions; the fluid
flow in the core region is totally encased by the annulus of second liquid. Like the single
jets, compound jets have many applications in scientific developments and are important
in many practical processes, such as particle encapsulation and food manufacturing [30],
capsule production in pharmaceutics [5, 15], targeted delivery of drugs [36, 52] and ink
jet printing [33].

Hertz & Hermanrud [33] performed the first experiment in the field of compound liquid
jets. They produced a compound jet by forcing a core fluid to emerge from a nozzle below
a stationary immiscible shell liquid. Sanz & Masueger [76] investigated the linear temporal
instability analysis of one dimensional inviscid compound jet. They found two types of
growing modes - namely, stretching mode and squeezing mode - and concluded that the
stretching mode has much larger growth rate than that of squeezing mode. This work
is further extended by Radev & Tchavdarov [67], Shkadov & Sisoev [81] and Chauhan
et al. [12]. It is essential to mention that the theoretical work of all these authors agree
qualitatively with the experimental study of Hertz & Hermanrud [33]. The temporal
instability of a viscous compound jet has been discussed by Chauhan *et al*. [13]. Uddin
& Decent [86] presented the non linear dynamic of an invisicd compound jet falling under

171

gravity. More recently, Mohsin *et al.* [55] examined the influence of gravity on an inviscid compound jet. They used a slender jet approximation to determine a one dimensional model which describes the radial and velocity displacements of the inner and outer free surfaces. In addition, they analysed the effects of key parameters in the presence of gravity and estimated the location of breakup.

The purpose of this article is to incorporate the aerodynamics effects on a nonaxisymmetric inviscid compound jet which is falling vertically downwards under the influence of gravity. Although, Rou *et al.* [73] investigated the effects of ambient gas on a uniform compound jet but they did not take into account the presence of gravity which accelerates the jet in the vertical direction. In this paper, we aim to examine the behavior and instability of an inviscid compound liquid jet which falls vertically under gravity in the presence of a surrounding gas. We formulate the governing equations which describe the evolution of free surfaces of the compound jet. We then use an asymptotic expansions to derive a set of 1D equations that describe the jet. We solve this set of equations using Newton's method to determine a steady state. Thereafter, we consider the temporal and spatial instability of the jet around this steady state. Furthermore, we investigate how key parameters, including surrounding gas density, alter the growth rate and most unstable wavenumber.

A.2   Problem Formulation

We consider an inviscid nonaxisymmetric compound jet which emerges from a concentric tube with the exit velocity U and moves in a surrounding gas. The outer radius of the compound jet is denoted by a and the inner one is denoted by χa, where $0 < \chi < 1$. It is assumed that the compound jet, after issuing from a circular orifice, falls in a vertical direction under the influence of gravity. It is also assumed that all the fluids are incompressible and immiscible. The geometry of the compound jet is described in a

172

cylindrical coordinate system (r, θ, x), where r is the radial component, θ is an azimuthal component and x is the length of the jet. The velocity vector describing the flow can be written as $\mathbf{u}^{[z]} = (w^{[z]}, v^{[z]}, u^{[z]})$, where the subscript $z = I$ is for the inner fluid, $z = O$ is for the outer fluid and $z = A$ is for the surrounding gas. Here we denote $r = R(x, t)$ as the interface of inner fluid with the outer one, $r = S(x, t)$ as the interface of outer fluid with the surrounding gas, $\sigma^{[I]}$ is the surface tension at the interface $r = R(x, t)$ and $\sigma^{[O]}$ is the surface tension at the interface $r = S(x, t)$. The density of the fluids is denoted by $\rho^{[z]}$, and the pressure and the time are denoted as $p^{[z]}$ and t respectively. The gravity is taken as $\mathbf{g} = (0, 0, g)$. In addition, the surface tensions $\sigma^{[I]}$ and $\sigma^{[O]}$ are assumed to be constant at the inner and the outer interface respectively.

The continuity equation and the Euler equation, which describe the resulting dynamics of the compound jet, are given by

$$\frac{\partial u^{[z]}}{\partial x} + \frac{\partial w^{[z]}}{\partial r} + \frac{w^{[z]}}{r} + \frac{1}{r}\frac{\partial v^{[z]}}{\partial \theta} = 0, \tag{A.1}$$

$$\frac{\partial u^{[z]}}{\partial t} + u^{[z]}\frac{\partial u^{[z]}}{\partial x} + w^{[z]}\frac{\partial u^{[z]}}{\partial r} + \frac{v^{[z]}}{r}\frac{\partial u^{[z]}}{\partial \theta} = -\frac{1}{\rho^{[z]}}\frac{\partial p^{[z]}}{\partial x} + (\delta_{\mathbf{Iz}} + \delta_{\mathbf{Oz}})g, \tag{A.2}$$

$$\frac{\partial v^{[z]}}{\partial t} + u^{[z]}\frac{\partial v^{[z]}}{\partial x} + w^{[z]}\frac{\partial v^{[z]}}{\partial r} + \frac{v^{[z]}}{r}\frac{\partial v^{[z]}}{\partial \theta} + \frac{v^{[z]}w^{[z]}}{r} = -\frac{1}{\rho^{[z]}}\frac{1}{r}\frac{\partial p^{[z]}}{\partial \theta} \tag{A.3}$$

and

$$\frac{\partial w^{[z]}}{\partial t} + u^{[z]}\frac{\partial w^{[z]}}{\partial x} + w^{[z]}\frac{\partial w^{[z]}}{\partial r} + \frac{v^{[z]}}{r}\frac{\partial w^{[z]}}{\partial \theta} - \frac{(v^{[z]})^2}{r} = -\frac{1}{\rho^{[z]}}\frac{\partial p^{[z]}}{\partial r}, \tag{A.4}$$

where $\delta_{\mathbf{Iz}}$ and $\delta_{\mathbf{Oz}}$ are the Kronecker delta symbols with free index z. These equations are supplemented by the kinematic conditions and the normal stress conditions. The

173

kinematic conditions, at the interface $r = R(x, t)$, are given by

$$w^{[z]} = \frac{\partial R}{\partial t} + u^{[z]} \frac{\partial R}{\partial x} + \frac{v^{[z]}}{r} \frac{\partial R}{\partial \theta}, \tag{A.5}$$

where $z = I, O$. Similarly, the kinematic conditions, at the interface $r = S(x, t)$, are given by

$$w^{[z]} = \frac{\partial S}{\partial t} + u^{[z]} \frac{\partial S}{\partial x} + \frac{v^{[z]}}{r} \frac{\partial S}{\partial \theta}, \tag{A.6}$$

where $z = O, A$. For inviscid fluids, we have the classical free surface condition of constant pressure and hence zero tangential stress condition. The normal stress conditions, at the interfaces $r = R(x, t)$ and $r = S(x, t)$, are

$$p^{[I]} - p^{[O]} = \sigma^{[I]} \kappa^{[I]}, \tag{A.7}$$

and

$$p^{[O]} - p^{[A]} = \sigma^{[O]} \kappa^{[O]}, \tag{A.8}$$

respectively, where $\kappa^{[I]}$ is the curvature of the inner free surface and $\kappa^{[O]}$ is the curvature of the outer free surface, which are given by

$$\kappa^{[I]} = \frac{\partial}{\partial x} \left(-\frac{1}{E^{[I]}} \frac{\partial R}{\partial x} \right) + \frac{\partial}{\partial r} \left(\frac{r}{E^{[I]}} \right) + \frac{\partial}{\partial \theta} \left(-\frac{1}{r E^{[I]}} \frac{\partial R}{\partial \theta} \right), \tag{A.9}$$

$$\kappa^{[O]} = \frac{\partial}{\partial x} \left(-\frac{1}{E^{[O]}} \frac{\partial S}{\partial x} \right) + \frac{\partial}{\partial r} \left(\frac{r}{E^{[O]}} \right) + \frac{\partial}{\partial \theta} \left(-\frac{1}{r E^{[O]}} \frac{\partial S}{\partial \theta} \right), \tag{A.10}$$

where

$$E^{[I]} = \left(1 + \left(\frac{\partial R}{\partial x} \right)^2 + \frac{1}{r^2} \left(\frac{\partial R}{\partial \theta} \right)^2 \right)^{\frac{1}{2}}, \tag{A.11}$$

$$E^{[O]} = \left(1 + \left(\frac{\partial S}{\partial x}\right)^2 + \frac{1}{r^2}\left(\frac{\partial S}{\partial \theta}\right)^2\right)^{\frac{1}{2}}. \tag{A.12}$$

We can non-dimensionalize the velocity components with the initial jet velocity U at the tube exit, so we have $\overline{w}^{[z]} = w^{[z]}/U$, $\overline{v}^{[z]} = v^{[z]}/U$ and $\overline{u}^{[z]} = u^{[z]}/U$, the radial length with the outer jet radius a that is $\overline{r} = r/a$ and the axial length with a characteristic wavelength L in the axial direction as $\overline{x} = x/L$. The time and the pressure are scaled by $\overline{t} = tU/L$ and $\overline{p}^{[z]} = p^{[z]}/\rho^{[O]}U^2$ respectively. By assuming the jet is slender, we define a small parameter ε as $\varepsilon = a/L << 1$. The dimensionless forms of inner and outer radii of the jet at the nozzle are $R(0,t) = \chi$ and $S(0,t) = 1$ respectively. After dropping the overbars, the resulting dimensionless continuity and Euler equations can be written as

$$\frac{\partial u^{[z]}}{\partial x} + \frac{1}{\varepsilon}\frac{\partial w^{[z]}}{\partial r} + \frac{1}{\varepsilon}\frac{w^{[z]}}{r} + \frac{1}{\varepsilon r}\frac{\partial v^{[z]}}{\partial \theta} = 0, \tag{A.13}$$

$$\frac{\partial u^{[z]}}{\partial t} + u^{[z]}\frac{\partial u^{[z]}}{\partial x} + \frac{w^{[z]}}{\varepsilon}\frac{\partial u^{[z]}}{\partial r} + \frac{v^{[z]}}{\varepsilon r}\frac{\partial u^{[z]}}{\partial \theta} = -\frac{1}{\rho^{[z]}}\frac{\partial p^{[z]}}{\partial x} + (\delta_{\mathbf{Iz}} + \delta_{\mathbf{Oz}})\frac{1}{F^2}, \tag{A.14}$$

$$\frac{\partial v^{[z]}}{\partial t} + u^{[z]}\frac{\partial v^{[z]}}{\partial x} + \frac{w^{[z]}}{\varepsilon}\frac{\partial v^{[z]}}{\partial r} + \frac{v^{[z]}}{\varepsilon r}\frac{\partial v^{[z]}}{\partial \theta} + \frac{v^{[z]}w^{[z]}}{\varepsilon r} = -\frac{1}{\rho^{[z]}}\frac{1}{\varepsilon r}\frac{\partial p^{[z]}}{\partial \theta} \tag{A.15}$$

and

$$\frac{\partial w^{[z]}}{\partial t} + u^{[z]}\frac{\partial w^{[z]}}{\partial x} + \frac{w^{[z]}}{\varepsilon}\frac{\partial w^{[z]}}{\partial r} + \frac{v^{[z]}}{\varepsilon r}\frac{\partial w^{[z]}}{\partial \theta} - \frac{(v^{[z]})^2}{\varepsilon r} = -\frac{1}{\rho^{[z]}}\frac{1}{\varepsilon}\frac{\partial p^{[z]}}{\partial r}. \tag{A.16}$$

The dimensionless kinematic conditions, at the interface $r = R(x,t)$ and $r = S(x,t)$, are given by

$$w^{[z]} = \frac{\partial R}{\partial t} + u^{[z]}\frac{\partial R}{\partial x} + \frac{v^{[z]}}{\varepsilon r}\frac{\partial R}{\partial \theta}, \tag{A.17}$$

where $z = I, O$ and

$$w^{[z]} = \frac{\partial S}{\partial t} + u^{[z]}\frac{\partial S}{\partial x} + \frac{v^{[z]}}{\varepsilon r}\frac{\partial S}{\partial \theta}, \tag{A.18}$$

where $z = O, A$, respectively. The dimensionless normal stress conditions, at the interfaces $r = S(x, t)$ and $r = R(x, t)$, are

$$p^{[O]} - p^{[A]} = \frac{1}{We}\frac{\partial}{\partial x}\left(-\frac{\varepsilon^2}{E^{[O]}}\frac{\partial S}{\partial x}\right) + \frac{\partial}{\partial r}\left(\frac{r}{E^{[O]}}\right) + \frac{\partial}{\partial \theta}\left(-\frac{1}{rE^{[O]}}\frac{\partial S}{\partial \theta}\right) \tag{A.19}$$

and

$$p^{[I]} - p^{[O]} = \frac{\sigma^I}{\sigma^O}\frac{1}{We}\frac{\partial}{\partial x}\left(-\frac{\varepsilon^2}{E^{[I]}}\frac{\partial R}{\partial x}\right) + \frac{\partial}{\partial r}\left(\frac{r}{E^{[I]}}\right) + \frac{\partial}{\partial \theta}\left(-\frac{1}{rE^{[I]}}\frac{\partial R}{\partial \theta}\right) \tag{A.20}$$

respectively, where

$$E^{[I]} = \left(1 + \varepsilon^2\left(\frac{\partial R}{\partial x}\right)^2 + \frac{1}{r^2}\left(\frac{\partial R}{\partial \theta}\right)^2\right)^{\frac{1}{2}} \tag{A.21}$$

and

$$E^{[O]} = \left(1 + \varepsilon^2\left(\frac{\partial S}{\partial x}\right)^2 + \frac{1}{r^2}\left(\frac{\partial S}{\partial \theta}\right)^2\right)^{\frac{1}{2}}. \tag{A.22}$$

A.3   Asymptotic form of steady state solutions

In order to find the steady state solutions, we consider a quiescent gas as in [73], that is $\mathbf{u}^{[A]} = (0, 0, 0)$, and expand our variables using an asymptotic slender jet steady expansion of the form

$$\{u^{[z]}, v^{[z]}, w^{[z]}, p^{[z]}\} = \{(\delta_{\mathbf{Iz}} + \delta_{\mathbf{Oz}})u_0^{[z]}(x), 0, 0, p_0^{[z]}(x, r, \theta)\}$$

$$+(\varepsilon r)\{(\delta_{\mathbf{Iz}} + \delta_{\mathbf{Oz}})u_1^{[z]}(x, \theta), 0, (\delta_{Iz} + \delta_{Oz})w_1^{[z]}(x, \theta), p_1^{[z]}(x, \theta)\} + O((\varepsilon r)^2), \tag{A.23}$$

$$\{R, S\} = \{R_0(x), S_0(x)\} + \varepsilon\{R_1(x, \theta), S_1(x, \theta)\} + O(\varepsilon^2). \tag{A.24}$$

Substituting the above asymptotic expansions in the equations $(A.13 - A.20)$, we find the leading order continuity equation for the inner and outer fluids is

$$w_1^{[z]} = -\frac{1}{2}\frac{\partial u_0^{[z]}}{\partial x}, \tag{A.25}$$

where $z = I, O$. The leading order kinematic conditions (A.17) and (A.18), at $r = R(x)$ and $r = S(x)$, give

$$\frac{\partial}{\partial x}\left(R_0^2 u_0^{[I]}\right) = 0, \tag{A.26}$$

and

$$\frac{\partial}{\partial x}\left((S_0^2 - R_0^2)u_0^{[O]}\right) = 0, \tag{A.27}$$

respectively. The leading order normal stress conditions, at $r = S(x,t)$ and $r = R(x,t)$, yield

$$p_0^{[O]} = \frac{1}{S_0 We} + p_0^{[A]}, \text{ and } p_0^{[I]} = \frac{1}{We}\left(\frac{\sigma}{R_0} + \frac{1}{S_0}\right) + p_0^{[A]} \tag{A.28}$$

respectively, where $\sigma = \sigma^{[I]}/\sigma^{[O]}$ is the ratio of surface tension between inner and outer fluid interfaces and $We = \rho^{[O]}U^2 a/\sigma^{[O]}$ is the Weber number. By using equations (A.25) and (A.28), the radial momentum equation (A.16) gives $\partial p_0^{[z]}/\partial r = 0$ and azimuthal momentum equation (A.15) gives $\partial p_0^{[z]}/\partial\theta = 0$ here $z = I, O$, that is automatically satisfied. Since the surrounding gas is motionless, therefore the axial, azimuthal and radial momentum equations of the gas implies $\partial p_0^{[A]}/\partial x = 0$, $\partial p_0^{[A]}/\partial\theta = 0$ and $\partial p_0^{[A]}/\partial r = 0$ respectively. We now substitute equation (A.28) in the axial momentum equation (A.14)

for the inner and the outer fluids, which implies

$$u_0^{[I]} \frac{\partial u_0^{[I]}}{\partial x} = -\frac{1}{\rho We} \frac{\partial}{\partial x} \left(\frac{\sigma}{R_0} + \frac{1}{S_0} \right) + \frac{1}{F^2} \tag{A.29}$$

and

$$u_0^{[O]} \frac{\partial u_0^{[O]}}{\partial x} = -\frac{1}{We} \frac{\partial}{\partial x} \left(\frac{1}{S_0} \right) + \frac{1}{F^2}, \tag{A.30}$$

where $\rho = \rho^{[I]}/\rho^{[O]}$ is the density ratio of the inner fluid to the outer fluid and $F = U/\sqrt{Lg}$ is the Froude number, which gives a measure of the relative importance of gravitational forces. Equations $(A.26)$, $(A.27)$, $(A.29)$, and $(A.30)$ are a system of nonlinear ordinary differential equations with unknowns $u_0^{[I]}$, $u_0^{[O]}$, R_0 and S_0. To solve this set of equations we specify initial conditions at the nozzle, that is, $u_0^{[I]} = u_0^{[O]} = S_0 = 1$ and $R_0 = \chi$. By making use of initial conditions and dropping subscripts from the variables for ease of convenience, we integrate the system of equations and then apply Newton's method to obtain a spatially non-uniform steady state solution for the inviscid compound jet, which moves in a gas and falls vertically downwards under the influence of gravity.

A.4   Linear Instability Analysis

We now consider the linear temporal instability analysis of an inviscid compound liquid jet moving in a surrounding gas. The evolution of the jet depends on length scale $x = O(1)$, but the disturbances along the jet are much smaller and are comparable to ε when $x = O(1)$. In other words we can say that the disturbances are typically of the order of jet radius a. We consider the traveling short waves of the form $exp(ik\bar{x} + \lambda \bar{t})$, where $k = k(x) = O(1)$ and $\lambda = \lambda(x) = O(1)$ are the frequency and wavenumber of disturbances. Additionally, $\bar{x} = x/\varepsilon$ and $\bar{t} = t/\varepsilon$ are small length and time scales. Thus, we have a multiple scale formulation as the perturbations grow along the jet having wavelength of

$O(\varepsilon)$. Now we introduce small time dependent perturbations to the steady state solutions which take the form

$$u^{[z]} = (\delta_{\mathbf{Iz}} + \delta_{\mathbf{Oz}})u_0^{[z]}(x) + \delta\overline{u^{[z]}}(r)\exp(\lambda\bar{t} + ik\bar{x}), \tag{A.31}$$

$$v^{[z]} = (\delta_{\mathbf{Iz}} + \delta_{\mathbf{Oz}})v_0^{[z]}(x) + \delta\overline{v^{[z]}}(r)\exp(\lambda\bar{t} + ik\bar{x}), \tag{A.32}$$

$$w^{[z]} = (\delta_{\mathbf{Iz}} + \delta_{\mathbf{Oz}})w_0^{[z]}(x) + \delta\overline{w^{[z]}}(r)\exp(\lambda\bar{t} + ik\bar{x}), \tag{A.33}$$

$$p^{[z]} = p_0^{[z]}(x) + \delta\overline{p^{[z]}}(r)\exp(\lambda\bar{t} + ik\bar{x}), \tag{A.34}$$

$$R = R_0(x) + \delta\overline{R}\exp(\lambda\bar{t} + ik\bar{x}), \tag{A.35}$$

$$S = S_0(x) + \delta\overline{S}\exp(\lambda\bar{t} + ik\bar{x}). \tag{A.36}$$

where $0 < \delta << \varepsilon$. Substituting the expansions $(A.31 - A.36)$ into the non-dimensionalized form of equations $(A.13 - A.20)$ yields at leading order, or $O(\delta/\varepsilon)$,

$$ik\overline{u^{[z]}} + \frac{\partial\overline{w^{[z]}}}{\partial r} + \frac{\overline{w^{[z]}}}{r} = 0, \tag{A.37}$$

$$(\lambda + ik(\delta_{\mathbf{Iz}} + \delta_{\mathbf{Oz}})u_0^{[z]})\overline{u^{[z]}} = -((\delta_{\mathbf{Iz}})1/\rho + (\delta_{\mathbf{Az}})1/\rho^G + \delta_{\mathbf{Oz}})\overline{p^{[z]}}ik, \tag{A.38}$$

179

$$(\lambda + ik(\delta_{\mathbf{Iz}} + \delta_{\mathbf{Oz}})u_0^{[z]})\overline{v}^{[z]} = -((\delta_{\mathbf{Iz}})1/\rho + (\delta_{\mathbf{Az}})1/\rho^G + \delta_{\mathbf{Oz}})\overline{p^{[z]}}ik, \qquad (A.39)$$

$$(\lambda + ik(\delta_{\mathbf{Iz}} + \delta_{\mathbf{Oz}})u_0^{[z]})\overline{w}^{[z]} = -(\delta_{\mathbf{Iz}}\rho + \delta_{\mathbf{Az}}\rho^G)\frac{\partial\overline{p^{[z]}}}{\partial r}, \qquad (A.40)$$

$$\overline{w^{[z]}} = (\lambda + iku_0^{[z]})\overline{R} \quad \text{for} \quad z = I, O, \qquad (A.41)$$

$$\overline{w^{[z]}} = (\lambda + ik(\delta_{\mathbf{Oz}})u_0^{[z]})\overline{S} \quad \text{for} \quad z = O, A, \qquad (A.42)$$

$$\overline{p^{[I]}} - \overline{p^{[O]}} = \frac{\sigma}{We}(k^2 - \frac{1}{R_0^2})\overline{R}, \qquad (A.43)$$

$$\overline{p^{[O]}} - \overline{p^{[A]}} = \frac{1}{We}(k^2 - \frac{1}{S_0^2})\overline{S}, \qquad (A.44)$$

where $\delta_{\mathbf{Iz}}$, $\delta_{\mathbf{Oz}}$ and $\delta_{\mathbf{Az}}$ are the Kronecker delta symbols with free index z and $\rho^G = \rho^{[A]}/\rho^{[O]}$ is the density ratio of gas to the outer fluid. Using $(A.38)$ and $(A.40)$ to eliminate $\overline{p^{[z]}}$ we get $\overline{w^{[z]}} = \frac{1}{ik}\frac{\partial\overline{u^{[z]}}}{\partial r}$ and similarly $(A.38)$ and $(A.39)$ gives $\overline{v^{[z]}} = \frac{\overline{u^{[z]}}}{rk}$. By substituting these result in $(A.37)$, we have

$$\frac{\partial^2\overline{u^{[z]}}}{\partial r^2} + \frac{1}{r}\frac{\partial\overline{u^{[z]}}}{\partial r} - (m^2 + k^2)\overline{u^{[z]}} = 0, \qquad (A.45)$$

which has solution

$$\overline{u}^{[z]} = C^{[z]}I_m(kr) + D^{[z]}K_m(kr). \qquad (A.46)$$

By using the value of $\overline{u}^{[z]}$, we are able to get

$$\overline{w}^{[z]} = \frac{1}{ik}(C^{[z]}I'_m(kr) - D^{[z]}K'_m(kr)). \tag{A.47}$$

By using $(A.38)$ in $(A.46)$, yields

$$\overline{p}^{[z]} = \frac{-(\lambda + ik(\delta_{\mathbf{Iz}} + \delta_{\mathbf{Oz}})u_0^{[z]})}{ik(\delta_{Iz}\rho + \delta_{\mathbf{Az}}\rho^G + \delta_{\mathbf{Oz}})}(C^{[z]}I_m(kr) + D^{[z]}K_m(kr)), \tag{A.48}$$

where $I_m(kr)$ and $K_m(kr)$ are the modified Bessel functions of first and second kind respectively. To avoid the singularities, and to ensure finite values at $r = 0$, we require that $D^{[I]}$ and $C^{[A]}$ will be equal to zero.

Substituting the values of $\overline{w}^{[z]}$ in $(A.41)$ and $(A.42)$, yields

$$\frac{1}{ik}(C^{[I]}I'_m(kR_0) - D^{[I]}K'_m(kR_0)) = (\lambda + iku_0^{[I]})\overline{R}, \tag{A.49}$$

$$\frac{1}{ik}(C^{[O]}I'_m(kR_0) - D^{[O]}K'_m(kR_0)) = (\lambda + iku_0^{[O]})\overline{R}, \tag{A.50}$$

$$\frac{1}{ik}(C^{[O]}I'_m(kS_0) - D^{[O]}K'_m(kS_0)) = (\lambda + iku_0^{[O]})\overline{S}, \tag{A.51}$$

$$\frac{1}{ik}(-D^{[A]}K'_m(kS_0)) = (\lambda)\overline{S}. \tag{A.52}$$

Similarly, using the values of $\overline{p}^{[z]}$ from equation $(A.48)$ in equations $(A.43)$ and $(A.44)$, we get

$$\frac{-(\lambda + iku_0^{[I]})}{ik\rho}(C^{[I]}I_m(kR_0)) + \frac{(\lambda + iku_0^{[O]})}{ik}(C^{[O]}I_m(kR_0) + D^{[O]}K_m(kR_0)) \quad (A.53)$$
$$= \frac{\sigma}{We}(k^2 - \frac{1}{R_0^2})\overline{R},$$

$$\frac{-(\lambda + iku_0^{[O]})}{ik}(C^{[O]}I_m(kR_0) + D^{[O]}K_m(kR_0)) + \frac{\lambda}{ik\rho^G}(D^{[A]}K_m(kR_0)) \quad (A.54)$$
$$= \frac{1}{We}(k^2 - \frac{1}{S_0^2})\overline{S}.$$

By eliminating the $C^{[I]}, C^{[O]}, D^{[O]}, D^{[A]}, \overline{R}$ and $\overline{S}$ from equations $(A.49 - A.54)$ and removing subscripts from $u_0^{[I]}$, $u_0^{[O]}$, R_0, and S_0 for ease of convenience, we are able to arrive (after lengthy algebra) at following dispersion relation:

$$\frac{\lambda'^4}{k^2} \ [\ (I'_m(kR)K'_m(kS)I_m(kS)K_m(kR) - I'_m(kR)I_m(kR)K_m(kS)K_m(kS))$$

$$+ \ \rho \ (\ K'_m(kR)I_m(kS)I_m(kR)K'_m(kS) + I'_m(kR)K'_m(kS)K_m(kS)I_m(kR)) +$$

$$\rho \ \rho^G (\ K'_m(kR)I'_m(kS)K_m(kS)I_m(kR) - I'_m(kR)K'_m(kS)K_m(kS)I_m(kR)) +$$

$$\rho^G \ (\ I'_m(kR)K_m(kS)I'_m(kS)K_m(kR) + I'_m(kR)K'_m(kS)K_m(kS)I_m(kR)) \ ] +$$

$$\frac{\lambda'^3}{k}[\rho^G u^{[O]}(I'_m(kS)K'_m(kR)K_m(kS)I_m(kR) - I'_m(kR)I_m(kR)K_m(kS)K'_m(kS))$$

182

$$+2\ a_2\rho\ \rho^G(K_m^{'}(kR)I_m(kS)K_m^{'}(kS)I_m(kR) + I_m^{'}(kR)K_m^{'}(kS)K_m(kS)I_m(kR))$$

$$+2i\rho a_1(K_m^{'}(kR)I_m(kR)I_m(kS)K_m^{'}(kS) - I_m^{'}(kS)K_m(kS)K_m^{'}(kS)I_m(kR))] +$$

$$\frac{\lambda^{'2}}{kWe}\ [\ \beta\ (I_m^{'}(kR)K_m^{'}(kR)K_m^{'}(kS)I_m(kS) + I_m^{'}(kR)I_m^{'}(kR)K_m^{'}(kS)K_m(kS))$$

$$+\ \rho\ \alpha\ (K_m^{'}(kR)K_m^{'}(kS)I_m(kR)I_m^{'}(kS) + I_m^{'}(kR)I_m(kR)K_m^{'}(kS)K_m^{'}(kS)) +$$

$$\rho^G\ \beta\ (\ I_m^{'}(kR)K_m^{'}(kR)I_m^{'}(kS)K_m(kS) - I_m^{'}(kR)I_m^{'}(kR)K_m^{'}(kS)K_m(kS)) +$$

$$\alpha\ (\ I_m^{'}(kR)I_m(kR)K_m^{'}(kS)K_m^{'}(kS) + I_m^{'}(kR)K_m(kR)K_m^{'}(kS)I_m^{'}(kS)\ ) - We$$

$$\rho\ a_1^2\ k(I_m^{'}(kR)K_m^{'}(kS)K_m(kS)I_m(kR) + K_m^{'}(kR)I_m(kR)I_m(kS)K_m^{'}(kS)) -$$

$$We\rho^G(u^{[O]})^2k(I_m^{'}(kR)K_m(kS)I_m(kR)K_m^{'}(kS) + I_m^{'}(kR)K_m(kR)I_m^{'}(kS)K_m(kS))$$

$$+\ We\rho\rho^G a_3kI_m(kR)(I_m^{'}(kR)K_m^{'}(kS)K_m(kS)\ -\ K_m^{'}(kR)I_m^{'}(kS)K_m(kS))] +$$

$$\frac{2i\lambda^{'}}{We}[a_1\rho\alpha(K_m^{'}(kS)K_m^{'}(kR)I_m^{'}(kS)I_m(kR) - I_m^{'}(kR)K_m^{'}(kS)K_m^{'}(kS)I_m(kR))$$

$$+\rho^G \ \beta \ u^{[O]} \ (I'_m(kR)K'_m(kR)I'_m(kS)K_m(kS) - I'_m(kR)I'_m(kR)K'_m(kS)K_m(kS))$$

$$+Wek \ \rho \ \rho^G \ a_4 \ I_m(kR)(K'_m(kR)I'_m(kS)K_m(kS) - I'_m(kR)K'_m(kS)K_m(kS)) \ ]$$

$$+\frac{\alpha\beta}{We^2} \ (I'_m(kR)K'_m(kR)I'_m(kS)K'_m(kS) - I'_m(kS)I_m(kR)K'_m(kR)K'_m(kS)) \ +$$

$$\frac{\rho\alpha ka_1^2}{We} \ (K'_m(kS)I'_m(kR)I_m(kR)K'_m(kS) - I'_m(kS)K'_m(kR)I_m(kR)K'_m(kS)) \ +$$

$$\frac{\beta\rho^G k(u^{[O]})^2}{We}(I'_m(kR)K_m(kS)I'_m(kR)K'_m(kS) - I'_m(kR)K'_m(kR)I'_m(kS)K_m(kS)) \ +$$

$$\rho\rho^G(ka_1 u^{[O]})^2 I_m(kR)(K'_m(kR)I'_m(kS)K_m(kS) - I'_m(kR)K'_m(kS)K_m(kS)) = 0. \ (\text{A.55})$$

In the above dispersion relation we have

$$a_1 = (u^{[I]} - u^{[O]}), \quad a_2 = (u^{[I]} - 2u^{[O]}), \quad a_3 = ((u^{[I]} - u^{[O]})^2 + (u^{[O]})^2 + 4u^{[O]} \ (u^{[I]} - u^{[O]})),$$

$$a_4 = ((u^{[O]})^2 \ (u^{[I]} - u^{[O]}) - u^{[O]} \ (u^{[I]} - u^{[O]})^2), \quad \alpha \ = \ k^2 - \tfrac{1}{S^2}, \quad \beta \ = \ \sigma \ (k^2 - \tfrac{1}{R^2}),$$

and $\lambda' = \lambda + iku^{[O]}$.
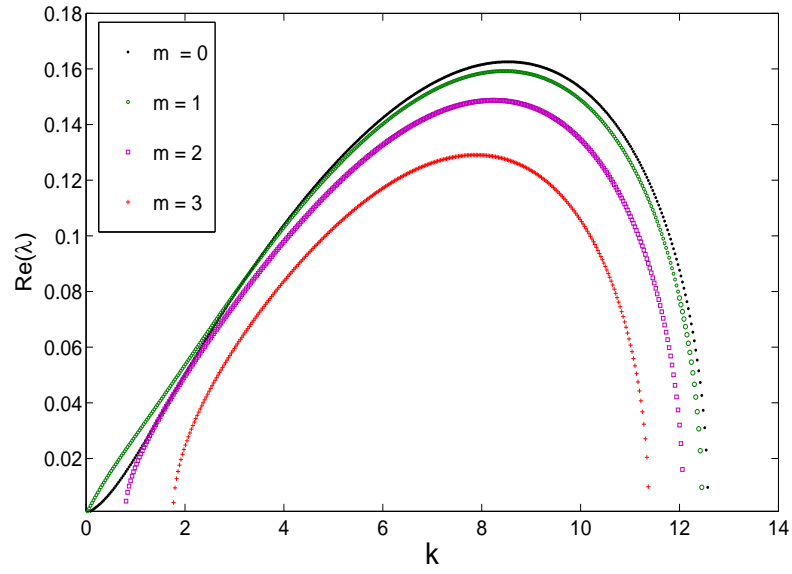
Figure A.1: Growth rate of disturbances versus wavenumber for various values of m, The parameters used here are $We = 30$, $\sigma = 0.5$, $\rho = 1$, and $\chi = 0.3$

A.5 Results and discussion

The dispersion relation $(A.55)$ is a quartic equation in λ' for the given values of k. We aim to solve this dispersion relation numerically in both temporal and spatial growing modes. An example of solving dispersion relation in a temporal mode is shown in Fig. $A.1$.

REFERENCES

[1] Ambravaneswaran, B. and Basaran, O. A., 1999, Effects of insoluble surfactants on the nonlinear deformation and break up of stretching liquid bridges, Phys. Of fluids, 11, 15, 997-1015.

[2] Amini, G. and Dolatabadi, 2011, A., Capillary instability of elliptic liquid jets, Phys. Of fluids, 23, 084109.

[3] Anno, J. N., 1977, The mechanics of liquid jets, Lexington Books.

[4] Bali, N.P., & Iyengar, N., 2005, A Textbook of Engineering Mathematics, Laxmi Publications, India.

[5] Berkland C., Pollauf E., Varde N., Pack D.W., Kim K.K., 2007, Monodisperse Liquid-filled Biodegradable Microcapsules, Pharmaceutical Research, 24(5), 1007–1013.

[6] Baird, M. H. I. and Davidson, J. F., 1962, Annular jets-I: Fluid dynamics, Chem. Eng. Sci., 17, 467-472.

[7] Bechtel, S. E., 1989, The oscillation of slender elliptical inviscid and Newtonain jets: Effects of surface tension, inertia, viscosity and gravity, Trans. ASME, 56, 968.

[8] Bogy, D. B., 1979, Drop formation in a circular liquid jet. Ann. Rev. Fluid Mech., 11, 201-229.

186

[9] Chaudhary, K. C., and Maxworthy, T., 1980b, The nonlinear capillary instability of a liquid jet: Part 2. Experiments on jet behavior before drop formation, J. Fluid Mech., 96, 275.

[10] Chaudhary, K. C., and Maxworthy, T., 1980c, The nonlinear capillary instability of a liquid jet: Part 3. Experiments on satellite formation and control, J. Fluid Mech., 96, 287.

[11] Chaudhary, P. J., Kee, D. D., and Redekopp, L. G., 1980a, The nonlinear capillary instability of a liquid jet: Part 1. Theory, J. Fluid Mech., 96, 257.

[12] Chauhan, A., Maldarelli, C. and Rumchitzki, D. S., 1996, Temporal and spatial instability of an inviscid compound jet, Rheol. Acta, 35, 567-583.

[13] Chauhan, A., Maldarelli, C., Papageorgiou, D. T. and Rumchitzki, D. S., 2000, Temporal instability of compound thread and jets, J. Fluid Mech., 420, 1-25.

[14] Chauhan, A., Maldarelli, C., Papageorgiou, D. T. and Rumchitzki, D. S., 2006, The absolute instability of an inviscid compound jet, J. Fluid Mech., 549, 81-98.

[15] Chen, H.Y., Zhao, Y., & Jiang, L., 2009, Compound-fluidic electrospray: An efficient method for the fabrication of microcapsules with multicompartment structure, Chinese Science Bulletin, 54, 3147–3153.

[16] Chiu, S. and Lin, T., 2008, Breakup of compound liquid jets under periodic excitation at small core-to-shell mass ratio, J. Chinese Inst. Eng., 31, 1-8.

[17] Crane, L. S., Birch, S. and McCormack, P. O., 1964, The effect of mechanical vibration on the breakup of a cylindrical water jet in air, Brit. J. Appl. Phys., 15,743.

[18] Craster, R., V., Matar, O. V. and papageorgiou, D. T., 2003, Pinchoff and satellite formation in compound viscous threads, Phys. Of fluids, 15, 11, 3409-3428.

[19] Craster, R., V., Matar, O. V. and papageorgiou, D. T., 2005, On compound viscous threads with large viscosity contrast, J. Fluid Mech., 533, 95-124.

[20] Decent, S. P., King, A. C., Simmons, M. J. H., Parau, E. I, Wallwork, I. M, Gurney, C. J., and Uddin. J., 2009, The trajectory and stability of a spiralling liquid jet: Viscous theory, Appl. Math. Model., 33 (12):4283 4302.

[21] Donnely, R. J., and Glaberson, W., 1966, Experiments on capillary of liquid jet, Proc. R. Soc. London, Ser. A, 290.

[22] Edgerton, H. E., Hauser, E. A. and Tucker, W. B., 1937, Studies in drop formation as revealed by the high-speed motion cameras, J. Phys. Chem., 41, 1017-1028.

[23] Eggers, J., 1993, Universal pinching of 3D axisymmetric free-surface flow, Phys. Rev. Lett. 71, 22, 3458-3460.

[24] Eggers, J., 1997, Nonlinear dynamics and breakup of free surface flows, Rev. Mod. Physics, 69, 3, 865-929.

[25] Eggers, J., and Dupont, T. F., 1994, Drop formation in one dimensional approximation of a Navier Stokes equation, J. Fluid Mech., 262, 205-221.

[26] Eggers, J. and Villermaux, E.,2008, Physics of liquid jets, Rep. Prog. Phys.,71, 036601.

[27] Finnicum, D. S., Weinstein, S. J. and Ruschak K. J., 1993, The effects of applied pressure on the shape of a two-dimensional liquid curtain falling under the influence of gravity, J. Fluid Mech., 255, 647-665.

[28] Garcia, F., J. and Castellanos, A., 1994, One dimensional models for slender axisymetric viscous liquid jets, Phys. Fluids, 6, 2676-2689.

[29] Goedde, E. F., and Yuen, M. C., 1970, Experiments on liquid jet instability, J. Fluid Mech., 40, 495-511.

[30] Hardas, N., Danviriyakul, S., Foley, J. L., Nawar, W. W. and Chinachoti, P., 2000, Accelerated stability studies of microencapsulated anhydrous milk fat, Lebensm. Wiss. Technol., 33, 506-513.

[31] Harkins, W. D. and Brown, F. E., 1919, The determination of surface tension (free surface energy), and the weight of falling drop, J. Am. Chem. Soc., 41, 499.

[32] Hauser, E. A., Edgerton, H. E. and Tucker, W. B., 1936, The application of high-speed motion picture camera to research on the surface tension of liquids, J. Phys. Chem., 40, 973-988.

[33] Hertz, C. H., and Hermanrud, B., 1983, A liquid compound jet, J. Fluid Mech., 131, 271-287.

[34] Hertzberg L. A., Sweet R. G. and Herzberg, L. A., 1976, Fluorescence-activated cell sorting, sci Am., 234, 97.

[35] Hilbing, J. H. and Heister, S. D., 1996, Droplet size control in liquid jet breakup, Phys Fluids, 8, 1574-1581.

[36] Jung, T., kamm, W., Breitenbach, A., Kaiserling, E., Xiao, J. X. and Kissel, T., 2000, Biodegradable nanoparticles for oral delivery of peptides: Is there a role for polymers to affect mucosal uptake? Eur. J. Pharm. Biopharm., 50, 147-160.

[37] Kalliadasis, S., Ruyer-Quil, C., Scheid, B. and Velarde, M. G., (2012), Falling Liquid Films, Springer London, United Kingdom.

[38] Keller, J. B., Rubinow, S. I., and Tu, Y. O., 1973, Spatial instability of a jet, Phys. Fluids A, 5, 521.

[39] Kendall, J. M., 1986, Experiments on annular liquid jet instability and on the formation of liquid shells, Phys Fluids, 29, 2086-2094.

[40] Kowalewski, T. A., 1996, On the separation of droplets from a liquid jet, Fluid dyn. Res., 17, 121-145.

[41] Kwak, S., and Pozrikidis, C., 2001, Effects of surfactants on the instability of liquid thread or annular layer. Part 1: Quiescent fluids, Int. J. Multiphase Flow, 27,.

[42] Lee, H., C., 1974, Drop formation in a liquid jet, IBM J. Res. Dev. 18 364.

[43] Leib, S. J. and Goldstein, M. E., 1986, The generation of capillary instabilities on a liquid jet. J. Fluid Mech., 168, 479-500.

[44] Lenard, P., 1887, Ueber die schwingungen fallender tropfen, Ann. Physik, 30, 209-243.

[45] Lin, S. P. and Lian, Z. W., 1989, Absolute instability of a liquid jet in gas, Phys. Fluids A., 1, 490-499.

[46] Lin, S. P. and Reitz, R. D., 1998, Drop and spray formation from a liquid jet, Annu. Rev. Fluid mech., 30, 85-105.

[47] Lin, S. P., 1996, Regimes of Jet Breakup and breakup mechanisms (Mathematical Aspects). Appeared in recent advances in spray combustion, Spray atomization and drop burning. Edited by Kuo, K. K., American Institute of Aeronautics and Astronautics, Inc.

[48] Lin, S. P., 2003, Breakup of liquid sheets and jets, Cambridge University Press, United Kingdom.

[49] Lister, J. R., and Stone, H. A., 1998, Capillary breakup of Viscous thread surrounded by another viscous thread, Phys. Fluids, 10,(11), p.2758.

[50] Loscertales ,I. G., Barrero, A., Guerrero, I., Cortijo, R., Marquez, M. and Ganan-calvo, A. M., 2002, Micro/Nano Encapsulation via electicfield coaxial liquid jets, Science, 295, 1695.

[51] Mariotte, E., 1686, Traite du movement des eaux et des autres corps fluids, E. Michal-let parries.

[52] Mathiowitz, E., Jacob, J. S., Jong, Y. S., Carino, G. P., Chickering, D. E., Chaturvedi, P., Santos, C. A., Vijayaraghavan, K., Montgomery, S., Bassett, M. and Morrell, C.,2000, Biologically erodable microsphere as potential oral drug delivery system, Nature (London), 386, 410.

[53] Middleman, S., 1995, Modelling of axisymmetric flows (Dynamics of Films, Jets and Drops), Academic Press, San Diego.

[54] Mohsin, M., Uddin, J., Decent, S. P. and Simmon, M., 2012, Break Up and droplet formation in shear thinning compound liquid jets, IMA J. App. Math.

[55] Mohsin, M., Uddin, J., Decent, S. P. & Afzaal, M. F., 2013. Temporal instability analysis of inviscid compound jets falling under gravity, Phys Fluids, 25, 012103.

[56] Mortanto, W., Baish, S. M., Costner, E. A., Prausnitz, M. R. and Smith, M. K., 2005, Fluid dynamics in conically shaped microneedles, AICHE Journal, 51, 6.

[57] Moseler, M. and Landman, U., 2000, Formation, stability and breakup of nanojets, Science, 289, 1165.

[58] Muller, D. E., 1956, A method for solving algebraic equations using an automatic computer, Math. Comp., 10, 208-215.

[59] Parau, E. I., Decent, S. P., Simmons, M. J. H., Wong, D. C. Y. and King, A. C., 2007, Nonlinear viscous liquid jets from a rotating orifice, J. of Eng. Maths., 57, 159-179.

[60] Peregrine, D. H., Shoker, G., and Symon. A., 1990, The bifurcation of liquid bridges, J. Fluid Mech., 212, 25.

[61] Perrin, B., 2004, Improving insecticides through encapsulation, Pesticide Outlook.

[62] Pimbley, W. T., and Lee, H. C., 1977, Satellite droplet formation in a liquid jet, IBM J. Res. Dev. 21, 21-25.

[63] Plateau, J., 1849, Sur les figures dequilibre dune masse liquid sans pesanteur, Mem. De lAcad. Roy. Belgique, nuvelle ser, 23, 1-59.

[64] Plateau, J., 1873, Statique experimentale et theoretique des liquids soumis aux seules forces moleculaires, Gautheir Villars, Parris,II, 319.

[65] Prausnitz, M. R., 2001, Analysis: Overcoming skins barrier ; The search for effective and user friendly drug delivery, 3,2 233-236

[66] Radev, S. and Gospodinov, P., 1986, Numerical treatment of the steady flow of a liquid compound jet, Int. J. Multiphase Flow, 12, 997-1007.

[67] Radev, S. and Tchavdarov, B., 1988, Linear stability of compound jets, Int. J. Multiphase Flow, 14, 67-79.

[68] Ramos, J. I., 1998, Annular liquid jets and other axisymmetric free-surface flows at high Reynolds numbers, Applied Mathematical and Computations, 22, p.423-452.

[69] Ramos, J. I., 1999, Asymptotic analysis of compound liquid jets at low Reynolds numbers, Applied Mathematical and Computations, 100, p.233-240.

[70] Rayleigh, W. S., 1878, On the instability of jets, Proc. Lond. Math. Soc., 10, 4.

[71] Rayleigh, L., 1891, Some application of photography, Nature London, 44, 177-180.

[72] Rayleigh, W. S., 1899, Investigation in capillarity, Phil. Mag., 48, 321.

[73] Rou, A., Chen, F. and Chang, M., 2009, Linear instability of compound jets with nonaxisymmetric disturbances, Phys Fluids, 21, 012101.

[74] Rutland, D. F., and Jameson, G. J. J., 1970, A nonlinear effect on capillary instability of liquid jets.

[75] Ruyer-Quil, C., Treveleyan, P., Giorgiutti-Dauphine, Duprat, C., and Kalliadasis, S., (2008), Modelling film flows down a fibre, J. Fluid Mech., 603, 431–462

[76] Sanz, A., and Meseguer, J., 1985, One dimensional analysis of compound jet, J. Fluid Mech. 159, 55-68.

[77] Savart, F., 1833, Memoire sur la constitution des veines liquides lancees par des orices circulaires en mince paroi, Annal, Chim., 53, 337.

[78] Schulkes, R. M. S. M., 1993, Dynamics of liquid jets revisited, J. Fluid Mech., 250, 635-650.

[79] Shikhmurzaev, Y. D., 2008, Capillary flows with forming interfaces, Chapman and Hall/CRC.

[80] Shi, X. D., Brenner, M. P. and Nagel, S., 1994, A cascade of structure in a drop falling from a faucet, Science, 265, 219.

[81] Shkadov, V. Y. and Sisoev, G. M., 1996, Instability of two-layer capillary jet, Int. J. Multiphase Flow, 22, 363-377.

[82] Sterling, A. M. and Sleicher, C. A., 1975, The instability of capillary jets, J. Fluid Mech, 68(3):477495.

[83] Suryo, R., Doshi, P. and Basaran, O. A., 2006, Nonlinear dynamics and breakup of liquid jets, Phys. Of fluids, 18, 082107.

[84] Tate, T., 1864, On the magnitude of a drop of liquid formed under different circumstances, Phil Mag., 27, 176.

[85] Tomotika, S., 1935, On the stability of a cylindrical thread of a viscous liquid surrounded by another viscous liquid. Proc. R. Soc. Lond., A, 150, 322-337.

[86] Uddin, J. and Decent, S. P., 2010, Breakup of inviscid compound liquid jets falling under the gravity, J. Phys. A: Math. Theor., 43, 485501.

[87] Uddin, J., 2007, Controlling breakup and droplet formation of single and compound liquid jets, Ph.D thesis, University of Birmingham, United Kingdom.

[88] Weber, C., 1931, Zum Zerfall eines Flussigkeitsstrahles, Z. Angew. Math. Mech.,11, 136-141.

[89] Wilson, H. J., and Rallison, J. M., 1997, Short wave instability of co-extruded elastic liquids with matched viscosities, J. Non-Newtonian Fluid Mech., 72, 237-251.

[90] Yarin, A. L., 1993, Free liquid jets and films: hydrodynamics and rheilogy, Longman.

[91] Yeo, E. S. and Ghazali, M. N., 2008, Numerical simulation of a microchip cooling wth microjet array, Jurnal Mekanikal, 25, 39-49.

[92] Yoshinaga, T. and Maeda, M., 2008, Instability and encapsulation of a compound liquid jet, J. Fluid Sci. Technol, 4, 324-334.

[93] Yuen, M. C., 1968, Nonlinear capillary instability of a liquid jet, J. Fluid Mech., 33, 151-163.